THE UNIVERSITY OF CHICAGO

UNDERSTANDING THE GENERATION OF OLFACTORY BULB BETA OSCILLATIONS THROUGH COMPUTATIONAL MODELING, PHARMACOLOGY, AND ELECTROPHYSIOLOGY OF GRANULE CELLS

A DISSERTATION SUBMITTED TO

THE FACULTY OF THE DIVISION OF THE PHYSICAL SCIENCES

AND

THE FACULTY OF THE DIVISION OF THE BIOLOGICAL SCIENCES

AND THE PRITZKER SCHOOL OF MEDICINE

IN CANDIDACY FOR THE DEGREE OF

DOCTOR OF PHILOSOPHY

GRADUATE PROGRAM IN BIOPHYSICAL SCIENCES

BY

BOLESŁAW LESZEK OSINSKI

CHICAGO, ILLINOIS

MARCH 2018

Dla moich rodziców

For my parents

Copyright Page

Most of Chapters 2 and 3 of this dissertation have appeared in separate publications:

Osinski BL, **Kay LM**. Granule cell excitability regulates gamma and beta oscillations in a model of the olfactory bulb dendrodendritic microcircuit. *J Neurophysiol* 116: 522–39, 2016.

Osinski B, **Kim A**, **Xiao W**, **Mehta NM**, **Kay LM**. Pharmacological manipulation of olfactory bulb granule cell excitability modulates beta oscillations: Testing a model. *bioRxiv* (2017). doi: 10.1101/234625.

Table of Contents

List of Figures

List of Tables

Acknowledgements

This work would not have been possible without the ongoing support and encouragement of my thesis committee consisting of Dr. Nicolas Brunel, Dr. Stephanie Palmer, Dr. Sliman Bensmaia, and my thesis advisor Dr. Leslie Kay. Each member of my committee helped me in more ways than I can list here, so I will be brief. Thank you Nicolas for giving me insight into conductance based modeling of synaptic currents. Thank you Stephanie for sharpening my quantitative analysis chops and getting me excited about neuroscience. Thank you Sliman for helping me when I got stuck and for having me join you on stage for not one but two SFN parties! Thank you Leslie for teaching me to be an experimentalist and a surgeon, and for giving me the independence to satisfy my curiosity.

I would also like to thank Dr. Donald Frederick for his guidance in the early phase of my graduate career, Nisarg Mehta and Vivian Nguyen for keeping the lab from burning down, and Andrew Sheriff, Rui He, Dr. Shane Peace, and Yu Ji for many insightful and fun discussions. I thank Wenxi Xiao, Selina Baeza-Loya, and Cameron Westerback for running some of my experiments and Alex Kim for enduring the cold of the cryostat to slice rat brains. Finally, I would like to thank the Biophysics program at University of Chicago for giving me the freedom and flexibility to choose my own research path.

Abstract

The mammalian olfactory bulb (OB) generates gamma (40 – 100 Hz) and beta (15 – 30 Hz) oscillations of the local field potential (LFP). Beta oscillations occur in response to odorants in learning or odor sensitization paradigms, but their generation mechanism is still poorly understood. When centrifugal inputs to the OB are blocked, beta oscillations disappear, but gamma oscillations persist. These inputs primarily target GABAergic granule cells (GC) in the GC layer (GCL) and regulate their excitability. This leads us to the central question motivating this work: What role does GC excitability play in generating beta oscillations? To answer this question we first developed a computational model incorporating the biophysical properties of the reciprocal dendrodendritic synapses between glutamatergic mitral cells (MC) and GCs. The model predicted that beta oscillations emerge only when inhibition of MCs, due to heightened GC excitability, and the excitation of MCs due to sensory input is sufficiently balanced. Because of this balance of excitation and inhibition, the model predicted that beta oscillations could also be supported in the absence of heightened GC excitability provided that the input strength was also low. The model also predicted that beta oscillations are sustained by voltage dependent calcium channel (VDCC) mediated GABA release, independently of NMDA channels.

We tested the predictions of this model using pharmacology in the OBs of rats. Infusion of scopolamine, a muscarinic antagonist known to decrease GC excitability, decreased or completely suppressed odor-evoked beta in response to a strong stimulus, but increased beta power in response to a weak stimulus, as predicted by our model. APV, an NMDA receptor antagonist, suppressed gamma

oscillations selectively (in OB and piriform cortex), lending support to the model's prediction that beta oscillations can be supported by VDCC currents.

In another set of experiments we recorded extracellular potentials in the GCL of rats using multichannel silicon (Si) probes. Because these were the first recordings of GCs and other GCL interneurons in awake, freely behaving rats, the nature of these experiments was exploratory. We found that many GCL neurons fired at the onset of beta oscillations, which is consistent with our model, because GC excitability increases can be triggered by GC somatic spikes. We also found a rich diversity of excitatory and inhibitory responses that showed odor selectivity and phase locking to different LFP frequency bands. Some responses evolved over the course of multiple days. By classifying responses to different odors using a distance metric analysis, we showed that some cells were better at distinguishing between odors based on their firing rates, while others were better based on spike timing. Intriguingly, the timescales at which most of these spike-timing cells best distinguished between odors were in the theta and beta frequency ranges. In a final set of experiments we trained two rats implanted with Si probes to poke their noses into an odor port to receive sugar pellet rewards. We found that some GCL neurons fired precisely at the time when a rat poked its nose into the odor port, while others fired only at the onset of beta oscillations. In one rat we also found cells that appeared to change their response when reward was discontinued. Together, these experiments lend strong support for the main predictions of the model, and also provide exciting preliminary data for future studies regarding the involvement of GCL neurons in contextual representations of odors during motivated behaviors.

Abbreviations

ADP	Afterdepolarization
AHP	Afterhyperpolarization
AMPA(R)	α-amino-3-hydroxy-5-methyl-4-isoxazolepropionic acid (receptor)
AON	Anterior olfactory nucleus
CDI	Calcium-dependent inactivation
DDI	Dendrodendritic inhibition
GCD	Granule cell dendrites
EPL	External plexiform layer
EPSC	Excitatory postsynaptic current
GABA(R)	γ-Aminobutyric acid (receptor)
GC	Granule cell
GCL	Granule cell layer
GLO	Glomerulus
ILFP	Local field potential calculated from mitral cell inhibitory current
VLFP	Local field potential calculated from mitral cell membrane voltage
IPSC	Inhibitory postsynaptic current
LFP	Local field potential
LLD	Long-lasting depolarization
LLE	Locally linear embedding
MC	Mitral cell
M/T	Mitral/Tufted
MCL	Mitral/Tufted cell layer
NMDA(R)	N-methyl-D-aspartate (receptor)
OB	Olfactory bulb
ORN	Olfactory receptor neuron
PC	Piriform cortex
PING	Pyramidal interneuron network gamma
PRING	Pyramidal resonance interneuron network gamma
SFC	Spike-field coherence
SFD	Spike-frequency deviation
STO	Sub-threshold oscillation
t-SNE	t-distributed stochastic neighbor embedding
VDCC	Voltage dependent calcium channel

Introduction

Local field potential (LFP) oscillations in the mammalian olfactory bulb (OB) represent coordinated neural activity that is dynamically regulated during olfactory processing. These oscillations are classified into three bands: theta (1-12 Hz), gamma (40-100 Hz), and beta (15-30 Hz). The theta rhythm is coupled to respiratory and sniffing frequencies (Rojas-Líbano et al., 2014). The gamma and beta rhythms strongly depend on behavioral context and odor quality (for a review see Kay et al., 2009 and Kay, 2014). The generation mechanism for OB gamma oscillations has been studied extensively and explained from the mechanistic to the functional level (Rall & Shepherd, 1968; Freeman, 1975; Nusser et al., 2001; Friedman & Strowbridge, 2003; Lagier et al., 2004; Bathellier et al., 2006; Rojas-Líbano & Kay, 2008; Brea et al., 2009; Lepousez & Lledo, 2013; Peace et al. 2017), but the generation mechanism for OB beta oscillations has received considerably less attention. Beta oscillations increase in power with the onset of learning in operant tasks (Martin et al., 2004, 2007a; Frederick et al., 2016a) and require intact cortical feedback to the olfactory bulb (Neville and Haberly, 2003a; Martin et al., 2006a) and thus are likely to be involved in mediating the contextual meaning of odors. Beta oscillations are also highly coherent across olfactory and hippocampal regions (Martin et al., 2007b; Gourévitch et al., 2010) and may be involved in the formation or retrieval of olfactory memory as well as initiation of odor-related

actions (Martin and Ravel, 2014). These oscillations overwhelm the olfactory bulb (OB) and pyriform cortex (PC) LFP during odor sampling, and yet they remain mechanistically and functionally enigmatic. The primary aim of this work, and the focus of Chapters 2 & 3, is to better understand the generation of beta oscillations through computational modeling and electrophysiological recordings. As the work progressed we found that OB granule cells (GCs) played a central role in the generation of these oscillations, so a secondary aim of this work emerged, which was to explore and catalogue the responses of these neurons during odor evoked beta oscillations. This is the focus of Chapter 4. Before we present the research we first provide some background on the olfactory bulb and its LFP oscillations.

1. Background on olfactory system LFP oscillations

1.1 Synaptic organization of the olfactory bulb

The OB is a three-layered paleocortex and is part of the limbic system. The outermost layer, called the glomerular layer, is almost completely covered by glomeruli (GLO), which are spherical dendritic structures (visible in Figure 1.1A). The GLO receive odorant stimuli registered by olfactory receptor neurons (ORN) embedded in the nasal sensory epithelium. In rodents, the majority of ORNs express a single type of the over 1000 receptor proteins (Chess et al., 1994; Malnic et al., 1999), and ORNs expressing the same receptor type converge to the same pair of glomeruli (GLO) on opposing sides of a single OB (Mombaerts et al., 1996). Thus, the GLO layer is often represented as an odorant map or mosaic. GLO are innervated by M/T dendrites and contain GABAergic periglomerular cells, which modulate M/T cells as part of the larger class of juxtaglomerular cells, resting in the space between GLO, which can couple one glomerulus to another. This outermost layer is capable of performing contrast enhancement to decorrelate similar olfactory stimulation patterns, and normalization (gain control) so that M/T cells are not overwhelmed by too broad a range of stimulation strengths (Linster & Cleland, 2009).

Below the GLO layer is the mitral/tufted cell layer (MCL), containing the bodies of the principal excitatory output neurons of the OB, the M/T cells. In addition to the apical dendrites that receive inputs from the sensory nerve in the glomeruli, these cells also possess long lateral dendrites spanning almost all the way across the bulb, a morphological feature unique to the OB (Migliore et al., 2014).

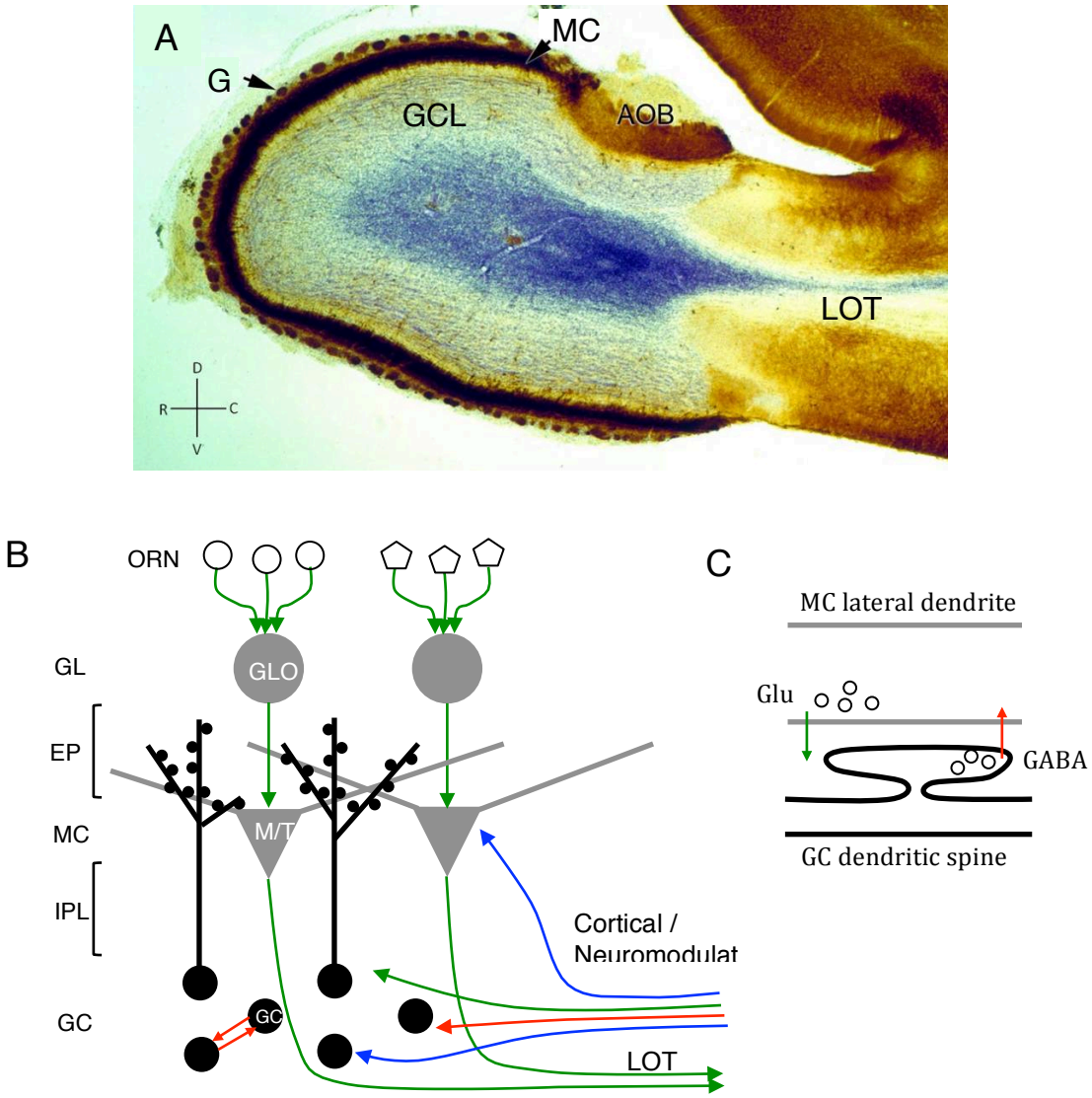

Figure 1.1. OB architecture. (A) Sagittal section through a rodent OB. The olfactory nerve has been removed, although in the anterior surface of the bulb some remnants can be seen. Glomerular layer (GL) and mitral cell layer (MCL) are seen clearly. Axons of mitral cells, stained in blue (Nissl stain), exit the OB through the LOT. AOB: Accessory OB; GCL: Granule cell layer; LOT: Lateral olfactory tract; D, V, R, C: Dorso-Ventral and Rostro-Caudal axes. **(B)** Simplified OB network connectivity. Green, red, and blue arrows represent excitatory, inhibitory, and neuromodulatory synaptic interactions respectively. Glomeruli (GLO) are innervated by olfactory receptor neurons (ORN) expressing only one type of receptor (represented by circle or pentagon). Mitral/Tufted (M/T) cells form reciprocal synapses with spines (small black dots) on granule cell dendrites. Mutual inhibition exists between granule cells (GC). Cortical feedback largely targets GCs. ORN: Olfactory receptor neurons; GL: Glomerular layer; EPL: External plexiform layer; MCL: Mitral cell layer; IPL: Internal plexiform layer; GCL: granule cell layer; LOT: Lateral olfactory tract. **(C)** Zooming in on a reciprocal synapse between a single GC dendritic spine and a MC lateral dendrite. **(A)** adapted from (Elsaesser and Paysan 2007) (publisher: BioMed Central)

The innermost layer of the OB, called the granule cell layer (GCL), contains millions of inhibitory granule cells (GCs), which comprise the most abundant cell type in the OB. Although GCs express GABA receptors (Nusser et al., 2001a)(Fig. 1.1B, red arrows), and the GCL also contains several other inhibitory subtypes, such as Blanes and deep-short-axon cells, the bulk of this work only concerns the excitatory-inhibitory interaction between GCs and MCs, which is depicted schematically in Figure 1.1B. GCs project long proximal dendrites towards M/T cell lateral dendrites. These projections end in a granule cell dendritic tree, which is peppered by small dendritic spines, each of which form reciprocal dendrodendritic synapses with MC lateral dendrites in the external plexiform layer (EPL) (Shepherd, 1972). M/T cells excite GC spines by glutamate release, which in turn inhibit M/T cells by GABA release (Fig. 1.1C). Individual GC spines can release GABA onto MC dendrites in a graded fashion independently of one another, or all at once, depending on the strength of M/T cell input and the spread of GC somatic action potentials (Egger 2005). The graded release of GABA from GC spines depends on Ca^{2+} flow through NMDA receptors (NMDARs) and other voltage-dependent calcium Ca^{2+} channels (VDCCs) expressed on GC spines (Chen et al., 2000; Isaacson & Strowbridge, 1998; Schoppa et al., 1998). The M/T cells project through the lateral olfactory tract (LOT) densely to the anterior olfactory nucleus (AON) and pyriform cortex (PC), among other areas. The PC, like the bulb is also a 3-layered paleocortex. M/T cells also project to many other limbic system regions, including the entorhinal cortex and amygdala.

The OB receives more cortical and neuromodulatory feedback inputs than it sends out, and the majority of this feedback targets the GCL (Fig. 1.1B left-pointing arrows). PC pyramidal cells send excitatory inputs to the OB (Fig. 1.1B green arrows). Interestingly the horizontal limb of the diagonal band of Broca sends both GABAergic (Fig. 1.1B red arrows) and cholinergic (Fig. 1.1B blue arrows) inputs that target GCs. Neuromodulatory systems of all types project to the OB. For example, serotonin from the raphe nuclei, noradrenaline from the locus coeruleus (Devore and Linster, 2012a), and oxytocin from the hypothalamus (Yu et al., 1996). Immediately caudal to the main OB is the accessory OB (AOB), seen in Figure 1.1A. This region also has a similar organization of M/T cells and GCs as the main OB but, curiously enough, may respond in an opposite way to cholinergic modulation (see Chapter 3 *Discussion*).

1.2 A short review of olfactory gamma oscillations

1.2.1 General properties of gamma oscillations

Olfactory bulb gamma oscillations were first recorded by Lord Edgar Douglas Adrian (1942), who noted that they were associated with increased firing of M/T cells. Later research showed that M/T cells tend to fire at a preferred phase of the gamma oscillations (Fig. 1.2A) (Eeckman and Freeman, 1990; Buonviso et al., 2003a; Bathellier et al., 2006). Assuming a phase convention with, the preferred phase of M/T cells is 90^{o}, as shown in Figure 1.2B. M/T cells do not fire on every cycle of the gamma oscillation, and thus individual cells may be highly phase locked to the LFP

while not firing synchronously with each other (Eeckman and Freeman, 1990). Walter Freeman, at the University of California Berkley, was among the first to describe the coupling between gamma oscillations and respiration (Freeman, 1975). This produces a nested theta-gamma coupling that characterizes the intrinsic resting state of the OB LFP, as shown in Figure 1.2C.

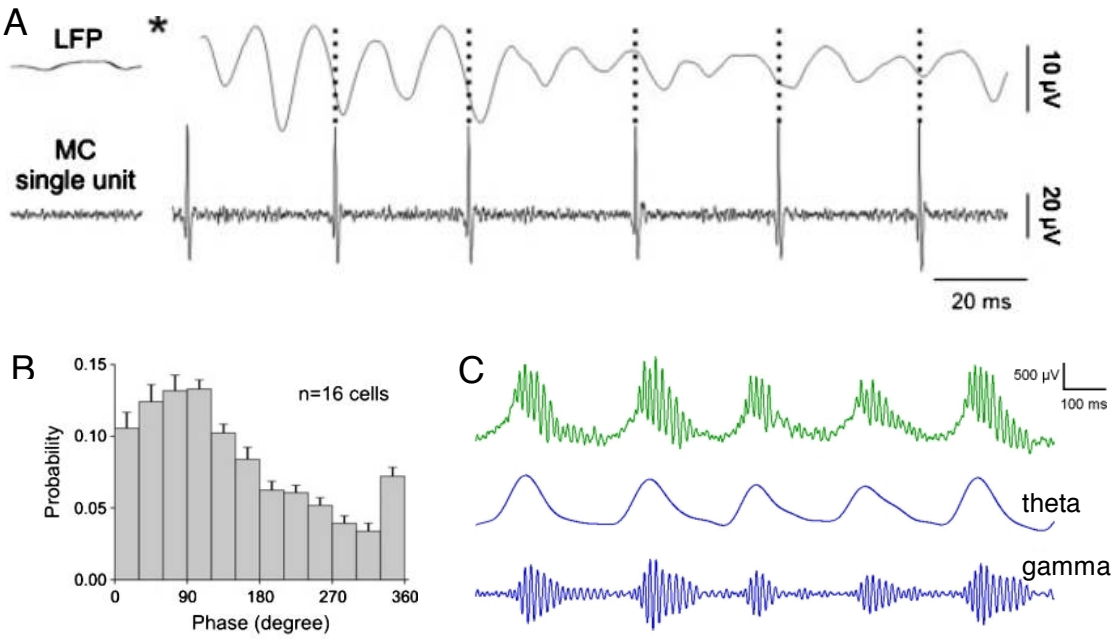

Figure 1.2. Basic properties of gamma oscillations. A: OB LFP (top) and single M/T cell response following olfactory nerve stimulation. Stimulation time indicated by star. MCs tend to fire on descending phase of gamma oscillation. **B:** Spike firing probability of 16 M/T cells for different LFP gamma phases. **C:** Raw (green) LFP (1-475 Hz) recorded from awake, freely behaving rat displays respiration-locked gamma oscillations. The same trace filtered for theta (1 – 12 Hz) and gamma (65 – 100 Hz) frequency ranges are shown in blue. (A) and (B) from Bathellier et al. (2006), (C) from Rojas-Libano & Kay (2008).

1.2.2 Gamma oscillation generation mechanism

It is generally agreed that intrinsic gamma oscillations arises from synaptic currents flowing across the reciprocal dendrodendritic synapses (Rall and

Shepherd, 1968) formed between excitatory glutamatergic mitral cell M/T cell lateral dendrites and inhibitory GABAergic GC distal dendritic spines in the EPL (Fig. 1.1B). These synapses form a negative feedback loop, which bears similarities to a pyramidal-interneuron network gamma (PING) mechanism. Some models of OB oscillations were based on this assumption (Li and Hopfield, 1989). However, PING networks lack cellular resonance properties, such as the intrinsic sub-threshold oscillations (STOs) of MCs (Desmaisons et al., 1999). A computational model by Brea et al. (2009) proposed that MC STOs are capable of driving gamma oscillations. This model resolved some limitations of the PING mechanism, because it supported a stable gamma oscillation frequency in the presence of fluctuating sensory input. Importantly, this model also used graded inhibition, which is a unique feature of the MC-GC synapse (Schoppa et al., 1998a), but this model was not compatible with experimentally recorded low GC firing rates (Cang and Isaacson, 2003a) and did not provide a mechanism for controlling the spatial extent of gamma coherence across the OB. Recently, a network based on inhibition-coupled intrinsic cellular oscillators has been proposed (Peace et al., 2017; Li & Cleland, 2017). In this hybrid network, intrinsic MC STOs are transiently coupled during olfactory stimulation into a coherent oscillatory network controlled by GC-mediated inhibition that periodically resets the slower MC STOs. This gamma generation mechanism, termed pyramidal resonance interneuron network gamma (PRING), exhibits key PING-like properties (e.g., the population oscillation frequency depends on the decay time constant of the GABA(A) receptor conductance), but also retains the dependence on STO dynamics of mitral cells (Li and Cleland, 2017). The PRING mechanism is consistent with

known physiological MC and GC properties, as well as the changes in spatial extent of gamma coherence across the bulb noted by Freeman and Schneider (1982).

1.2.3 Sub-bands of gamma oscillations

Although olfactory LFP oscillations between 40 – 100 Hz are all considered gamma oscillations, many studies suggest that there are distinct sub-bands in this frequency range. Rats trained to discriminate between two odors display high frequency gamma (60 – 100 Hz), dubbed gamma 1, during odor periods and low frequency gamma (40 – 65 Hz), dubbed gamma 2, during the waiting periods (Kay, 2003a). The onset of gamma 1 bursts is tightly locked to inspiration, whereas gamma 2 activity tends to occur between inhalations and during periods of slow breathing in attentive behavior and grooming (Fig. 1.3A). Odor-induced gamma oscillations sweep from high to low frequency on each sniff (Buonviso et al., 2003a; Manabe and Mori, 2013)(Fig. 1.3B). Recordings in rats and mice show that odor inhalation induces early-onset high-frequency burst (~100-Hz) discharges of tufted cells at the middle of inhalation (roughly coinciding with onset of fast high frequency gamma) followed by later-onset low-frequency burst (~45 Hz) discharges of mitral cells (Nagayama et al., 2004; Igarashi et al., 2012). Together, these results suggest that the early-onset fast gamma-oscillations are generated mainly by the tufted cell subsystem, whereas later-onset slow gamma-oscillations are supported mainly by mitral cells.

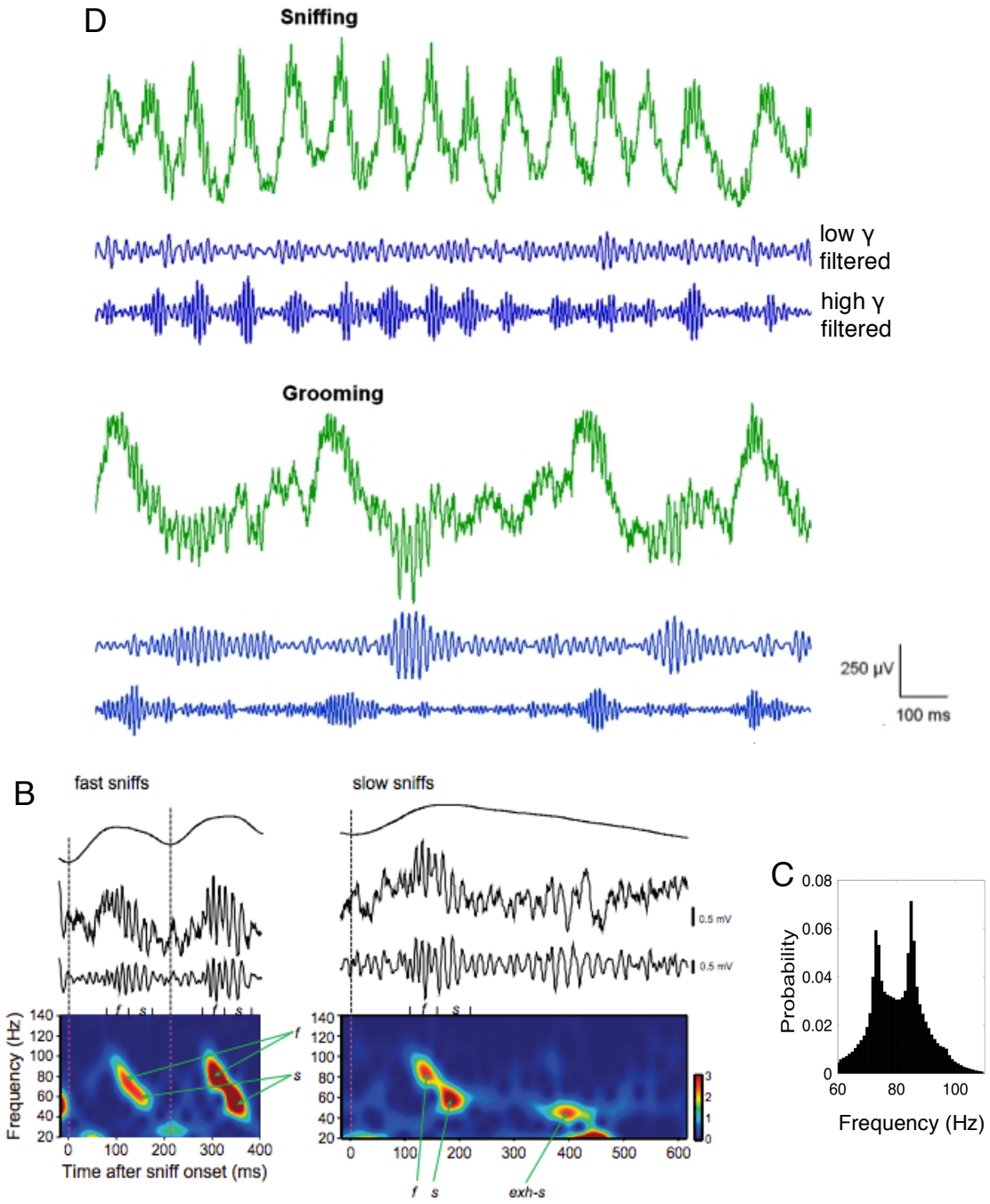

Figure 1.3. Properties of gamma sub-bands. (A) Raw (green) LFP (1-475 Hz) recorded from awake, freely behaving rat. The same trace filtered for low and high gamma frequency ranges are shown in blue. High gamma dominates during fast sniffing, but low gamma is enhanced during grooming. (**B)** Time course of respiration-locked gamma oscillations during two active sniffs (left), and one sniff during resting condition (right). Black traces show respiration rhythm (top), raw LFP (middle), and gamma filtered (40 – 140 Hz) LFP (bottom). Wavelet analysis shows instantaneous gamma frequency sweeping from high to low. Color scale indicates normalized power. Dashed lines indicate sniff onset. *f*: Fast gamma-oscillation; *s*: slow gamma-oscillation; *exh-s*: Slow gamma-oscillation during exhalation. **C:** Frequency distributions of several million gamma wavepackets. (A) from Rojas-Libano & Kay (2008), (B) from Manabe & Mori (2013), (C) from Frederick et al. (2016).

Another distinction been gamma 1 and gamma 2 comes from genetic knockout studies in mice. Interestingly, mice missing the β3 subunit of $GABA_A$ receptors on GCs do not generate gamma 2, suggesting that the switch from gamma 1 to gamma 2 may be initiated by a change in inhibitory coupling of GCs. Recent work suggests that the gamma 1 band itself is also subdivided into two bands, as the distribution of gamma 1 wavepackets has been found to be bimodal (Frederick et al., 2016a; Fig. 1.3C). Because the gamma 1 and gamma 2 nomenclature is not common in the field and the function of these distinct bands is still being researched, we refer to the lower and higher gamma bands as low gamma (40 – 60 Hz) and high gamma (60 – 100 Hz).

1.3 Known properties of Beta oscillations

Unlike gamma oscillations, beta oscillations only occur when an odorant stimulus is presented. Beta oscillations follow gamma oscillations during odor sampling (Martin et al., 2006; Martin & Ravel, 2014; Fig. 1.4A,B). In anesthetized rats gamma and beta oscillations alternate on each sniff, with beta oscillations occurring during exhalation (Buonviso et al., 2003; Cenier et al., 2009; David et al., 2015; Fourcaud-Trocmé et al., 2011). In waking rats, beta oscillations can persist across sniff cycles (as shown in Fig. 1.4A), and can also occur during periods of low respiratory drive in late odor sampling (Martin et al., 2007b; Rojas-Líbano and Kay, 2012). The transition from gamma to beta can be very fast (Fig. 1.4A, top), indicating a state-like transition in a system variable. They can also be very large in amplitude

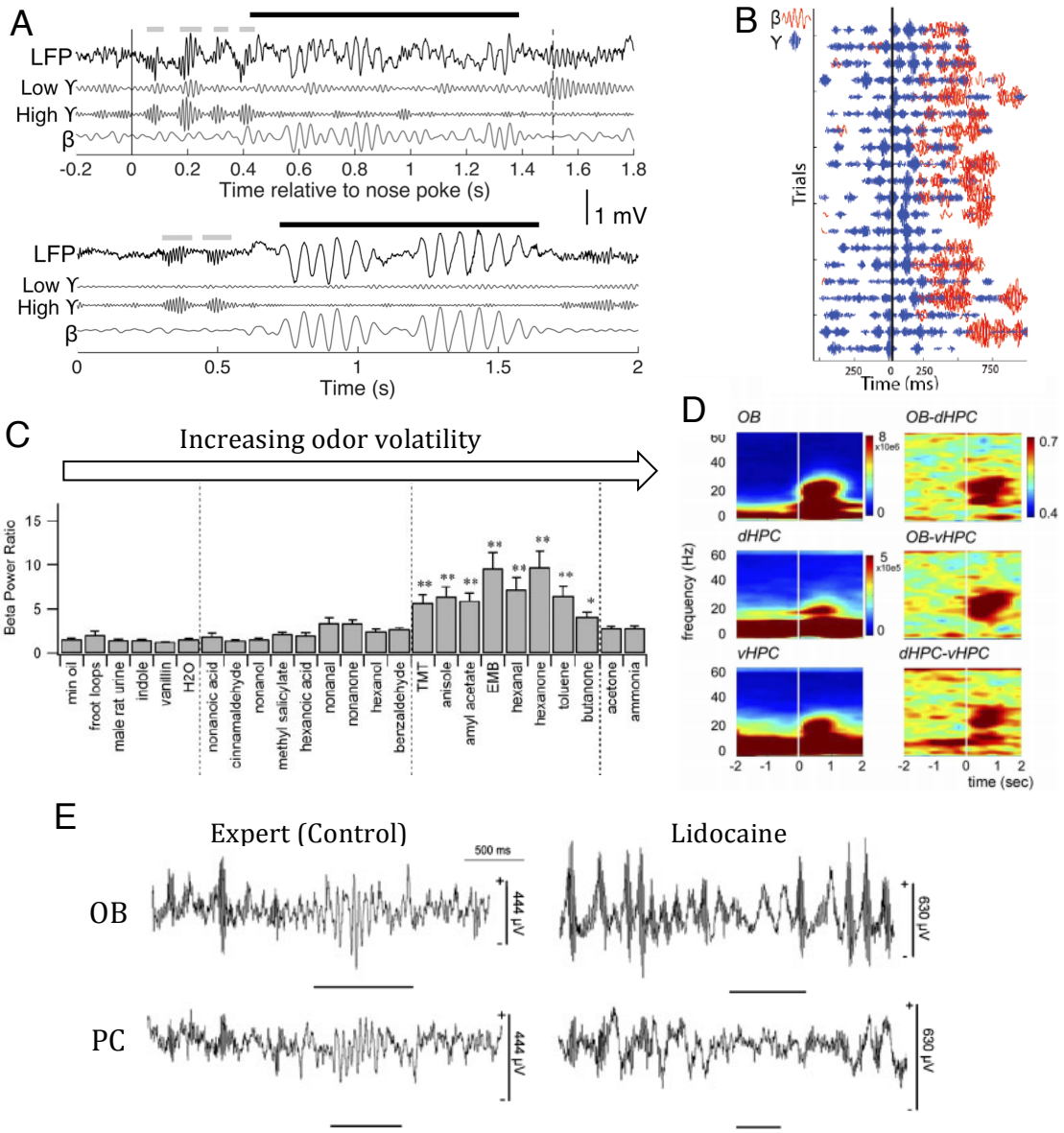

Figure 1.4. Known properties of beta oscillations. (A) Example beta oscillations in 2 different rats. Each plot shows raw (1–300 Hz), low-gamma filtered (Low γ; 40–60 Hz), high-gamma (High γ; 60–100 Hz) filtered, and beta (β; 15–30 Hz) filtered LFP. (*top*) A rat trained in a 2-alternative choice task with diluted high-volatility odors pokes into odor port at time $t = 0$ (black vertical line) and exits after ~1.5 s (dashed black vertical line). Nose poke is followed by 4 sniffs (gray horizontal bars) and a beta oscillation near 24 Hz (black horizontal bar). The onset of beta roughly coincides with the end of the last gamma burst, indicating a very fast transition. *(bottom)* same markings as in *(top)*. A freely behaving rat was presented with a cotton swab soaked in an undiluted high-volatility odor (ethyl butyrate). This odor evokes a large beta oscillation near 18 Hz. **(B)** Gamma (blue) and beta (red) wavepackets are plotted for each trial of a Go-No-Go experiment. Black vertical line marks time at which rat pokes into odor port. **(C)** Normalized OB beta band power induced by odors in order of increasing vapor pressure (volatility). **(D)** Spectrograms show an odor (heptanol) induced increase in beta (15–35 Hz) power (*left*) in OB, and dorsal & ventral parts of the hippocampus (dHPC & vHPC) accompanied by an increase in coherence (*right*) between these regions in the same frequency band. Odor onset is indicated by the vertical white line at 0 s. Color scales represent signal power (μV^2, *right*) and coherence (*left*). **(E)** Example raw LFP signals (1 – 300 Hz) from OB and PC during control (*left*) and lidocaine (*right*) sessions in expert rats. Beta oscillations are extinguished after lidocaine injection into LOT, but gamma oscillations are enhanced. Horizontal bars under each trace indicate odor sampling. (A) from Osinski and Kay (2016), (C) from Lowry and Kay (2007), (D) from Martin et al. (2006).

(Fig. 1.4A, bottom), suggesting the presence of highly synchronized synaptic currents.

Beta oscillation power scales with odor volatility (Lowry & Kay, 2007; Fig. 1.4C), and thus represents to some degree the strength of odor input. But beta oscillations also depend critically on centrifugal feedback into the bulb from other brain regions. When this centrifugal input to the bulb is surgically lesioned (Neville and Haberly, 2003) or pharmacologically blocked by lidocaine injection into the LOT (Martin et al., 2006), beta oscillations are completely extinguished, but gamma oscillations persist and are even enhanced (Fig. 1.4E). Furthermore beta oscillation power increases with the onset of learning in odor discrimination operant tasks (Martin et al., 2004, 2006, 2007; Frederick et al., 2016; Ravel et al., 2003).

The dependence of OB beta oscillations on cortical feedback and increase in power with learning odor associations suggest that these oscillations may be more involved in mediating the subjective contextual meaning of an odor OB rather than the objective representation of an odor during early sensory processing. Beta oscillations are also highly coherent with PC and also the entorhinal cortex and hippocampus (Martin et al., 2007a; Gourévitch et al., 2010; Kay and Beshel, 2010; Fig. 1.4D). This high degree of coherence across the olfacto-cortical-hippocampal network also suggests that beta oscillations may coordinate distinct brain regions to carry out actions associated with odorant meaning.

Although when we began this work there were no existing models of beta oscillations, a few models of beta oscillations from other groups have been published during the course of this work (Fourcaud-Trocmé et al., 2011b; David et

al., 2015a). These models are addressed and compared to our own model in the discussions of Chapters 2 & 3. While there are significant differences between these models and our own, one feature that stands out in common across all the models is the dependence on GC excitability. Because GCs receive the bulk of centrifugal inputs, they gate incoming input to the MCs, and this activity across the dendrodendritic synapses of large MC and GC populations emerges as beta oscillations.

2. Granule cell excitability regulates gamma and beta oscillations in a model of the olfactory bulb dendrodendritic microcircuit

2.1 Introduction

The network mechanism that generates OB beta oscillation has received much less attention than gamma oscillations. Current source density analysis in anaesthetized, tracheotomized rats has shown that while gamma and beta oscillations never occur simultaneously, both oscillations have dipoles centered in the OB external plexiform layer (EPL) (Fig. 2.1A; Neville and Haberly, 2003), suggesting that both oscillations are generated by the same synaptic currents between MC and GC dendrites. More recent analysis has revealed that gamma and beta oscillations may arise from distinct EPL sublaminae (Fourcaud-Trocmé et al., 2014). Nonetheless, it is unclear how dendrodendritic inhibition (DDI) between MCs and GCs can support both gamma and beta frequencies.

An important clue to the origins of beta oscillations comes from lesion experiments. When centrifugal input to the OB is blocked, odor evoked beta oscillations are extinguished or reduced, while gamma oscillations persist and can be enhanced (Gray and Skinner, 1988; Neville and Haberly, 2003; Martin et al., 2006; see Fig. 1.4E). Analogous to cortical feedback control of thalamic reticular nucleus neurons, feedback from MC cortical projection areas primarily targets the GC layer with excitatory synapses onto GABAergic GCs and other interneurons (Balu et al., 2007; Boyd et al., 2012; Kay & Sherman, 2007). Gamma oscillations have been

shown to persist even after GC somata are surgically disconnected from their distal dendrites (Lagier et al., 2004). Thus, there is strong evidence that centrifugal inputs near GC somata may be critical for beta but not gamma generation.

Under certain conditions GCs enter periods of increased excitability following a somatic spike. For example, activation of M1 muscarinic receptors in GCs transforms the afterhyperpolarization (AHP) following GC spikes into an afterdepolarization (ADP) lasting several hundred milliseconds (Fig. 2.1B; Pressler et al., 2007), which may trigger quasipersistent firing modes lasting several seconds (Inoue and Strowbridge, 2008). The GC ADP propagates faithfully into distal dendrites, leading to increased Ca^{2+} influx (Egger et al., 2003). GCs may also undergo a long-lasting depolarization (LLD) that can last well over 1s (Fig. 2.1C) when a GC somatic spike is triggered by strong glomerular input (Egger, 2008a). We propose that a convergence of sensory, cortical, and neuromodulatory inputs onto GCs may help explain the observed dependence of beta oscillations on odorant characteristics and centrifugal feedback.

To test this hypothesis we developed a model of the MC-GC reciprocal dendrodendritic synaptic network with graded inhibition dependent on NMDA and N-type Ca^{2+} currents. In our model we summarize the cortical, local inhibitory/excitatory, and neuromodulatory sources of GC excitability control by a single parameter, $V_{rest,GC}$, the granule cell dendritic (GCD) resting membrane potential. To investigate the individual contributions of NMDA and N-type currents we also create two additional models, one with only NMDA and the other with only N-type channels included in the GCDs. Our model predicts that a sudden

depolarization of the membrane potential of a subpopulation of GCs can drive an increase of Ca^{2+} dependent graded inhibition that will switch the frequency from a gamma to a beta regime. The model also argues that high power beta oscillations observed *in vivo* (Fig. 1.4A) are primarily mediated by N-type currents.

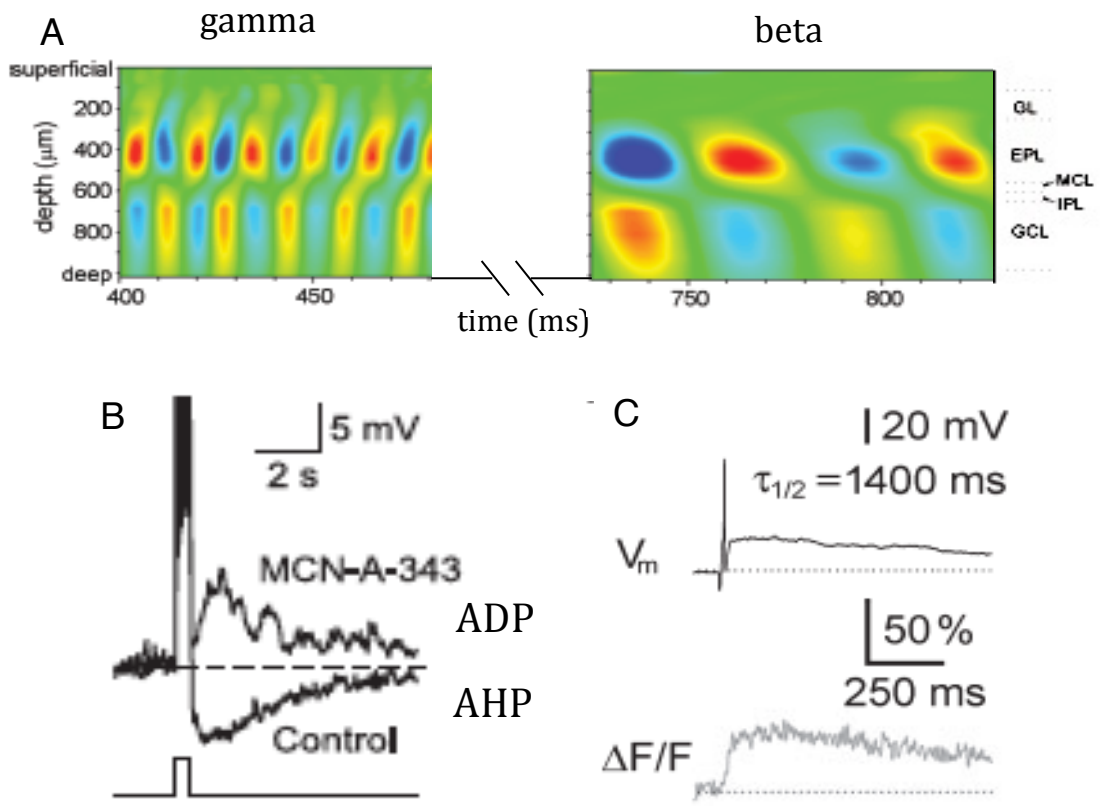

Figure 2.1 Experimental results motivating the model A) CSD analysis of an odor evoked gamma oscillation (left) followed by a beta oscillation (right) shows that both oscillations arise at the same layer of the OB. **B)** Muscarinic agonists convert GC AHP to ADP, which increases GC excitability. **C)** Sufficiently strong glomerular stimulations trigger GC ADP that can last over 1 s. **(A)** from Neville & Haberly (2003), **(B)** from Pressler et al (2007), **(C)** from Egger (2008)

2.2 Methods

2.2.1 Model Architecture

In the rat OB, excitatory MCs form reciprocal dendrodendritic connections between their lateral dendrites and the spines on GCDs. MC lateral dendrites extend broadly across the OB and support bi-directional action potential propagation, allowing MCs and GCs on opposite sides of the OB to be synaptically connected. Our model represents a subset of this network, with 45 MCs and 720 GCDs. Each MC is reciprocally connected to 30% of the GCD population (Fig. 2.2), similar to previous models (De Almeida et al., 2013; Linster et al., 2009), yielding a total of 9,720 MC-GC dendrodendritic synapses. Our model MCs do not represent individual cells, but rather the population of MCs associated with a particular GLO. Although the density of Na^+ channels is known to vary slightly along the length of MC lateral dendrites (Migliore and Shepherd, 2002), in our model all excitatory synaptic weights from MCs to GCs are equal.

Our model architecture is motivated by five key experimental findings: 1) Gamma and beta oscillations both have dipoles centered in the EPL where MC-GC dendrodendritic synapses are formed (Neville and Haberly, 2003a); 2) GCs can release GABA in a graded (spike-independent) fashion dependent on NMDA and VDCC Ca^{2+} currents (Isaacson and Strowbridge, 1998; Schoppa et al., 1998a; Isaacson, 2001); 3) GCs spike at very low rates in awake animals compared to cortical interneurons (Cazakoff et al., 2014); 4) Beta oscillations require intact centrifugal projections to the olfactory bulb (Neville and Haberly, 2003a; Martin et al., 2006a), many of which target the GC layer and regulate GC excitability; 5) GCs

can undergo periods of increased excitability with sustained elevated membrane potentials propagating faithfully into their distal dendrites (Pressler et al., 2007a; Egger, 2008a). We represent all these sources of excitability control by a single parameter, the GCD resting potential $V_{rest,GC}$. Because we have direct control over the excitability of the GCDs, we do not explicitly model the GC soma, whose synaptic integration and bidirectional signal propagation properties are complex and not yet fully understood (Balu et al., 2007; Egger et al., 2005; Inoue & Strowbridge, 2008). Instead, we only model the entire GC dendritic tree as a single unit, which receives inputs from multiple MCs (Fig. 2.2). In the real system, GC dendritic spines can act

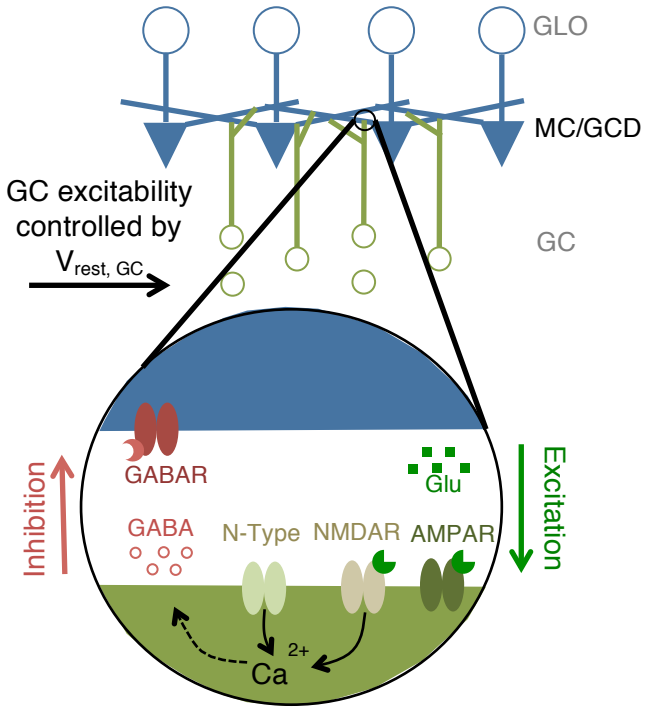

Figure 2.2. Schematic of the reciprocal dendrodendritic MC-GC model. There are 45 MCs, and 720 GCDs. Each MC represents the population of MCs associated with a glomerulus (GLO). The GLO and GC soma, represented by empty circles, are not explicitly modeled. Each MC is randomly connected to 216 GCDs (30% of the population). MCs only express GABARs, while GCs express AMPARs, NMDARs, and N-Type channels. Ca^{2+} flow through NMDA and N-Type receptors drives release of GABA vesicles, modeled as a graded inhibitory current. NMDA and AMPA currents have a spike-triggered activation, which represents the binding of glutamate released from MCs following a spike.

independently of one another and influence each other via low-threshold Ca^{2+} spikes (Egger et al., 2005; Egger, 2008), but this scenario is not captured by our model. Inhibitory coupling between GCs is also omitted for simplicity. All simulations were implemented in MATLAB® R2014b, with a forward Euler integration time step of 0.1 ms. Simulations with forward and backward Euler methods were found to give identical results. The code for has been made available through the ModelDB under accession number 185464 (Hines et al., 2004).

2.2.2 Neuron and Synapse Equations

MCs and GCDs are modeled as single compartments whose membrane potentials evolve in time according to

$$\tau \dot{V} = -V + W_{chan} * I_{chan} + V_{rest} \tag{2.1}$$

where τ is the membrane time constant, W_{chan} is a dimensionless synaptic weight representing the ratio of maximum conductance of a particular channel to the membrane leak conductance (from here on referred to as synaptic weight), I_{chan} is the synaptic current through a particular channel, and V_{rest} is the resting membrane potential. We have chosen units such that resistance = 1, and therefore the currents and membrane voltages are in the same units, but are not in SI units. The critical parameter in this model is $V_{rest,GC}$, the resting potential of the GC dendritic tree. The MCs obey leaky integrate and fire dynamics with a hard threshold 7 mV above resting potential. Probabilistic firing is achieved by introducing noise into the MC external inputs. Although recent experiments have detected regenerative Na^{2+}

spikes in GC dendrites (Bywalez et al., 2015), the GCDs do not fire action potentials in this model.

All synaptic currents in the model are conductance-based currents that obey the general form

$$I = \alpha(t, V, [Ca])[E - V] \tag{2.2}$$

where $\alpha(t, V, [Ca])$ is the product of normalized channel activation and inactivation variables (may depend on time, membrane voltage, and internal calcium concentration $[Ca]$), and E is the Nernst potential of the ionic species flowing through the channel.

Each MC receives two currents: 1) I_{ext}, an external sensory input; 2) I_{GABA}, a graded inhibitory GABA (Cl^-) current from GCs. Each GCD receives three currents: 1) I_{AMPA}, an AMPA (Na^{2+}) current with MC spike-triggered conductance; 2) I_{NMDA}, an NMDA (Ca^{2+}) current with MC spike-triggered conductance and voltage-dependent Mg^{2+} block (Jahr and Stevens, 1990; Baszczak and Kasicki, 2005); 3) I_N, an N-Type (Ca^{2+}) current with voltage-dependent activation and Ca^{2+} dependent inactivation (Amini et al., 1999; Zeng et al., 2009). The mathematical details of the currents are summarized in Table 2.1.

2.2.3 External excitatory input to MCs

Following De Almeida et al. (2013), the external input I_{ext} to each MC is modeled by a continuous variable that represents the average instantaneous firing probability of the population of olfactory sensory neurons innervating a given GLO. We do not model respiration because the inhibitory circuits mediating gamma/beta

MC	**Activation/Inactivation**
$I_{ext,i} = W_{ext,i}[1 + \sigma_{ext}\eta_{ext,i}]$ $W_{ext,i} = \sigma_w \eta_{w,i} + W_{min,ext}$	Continuous
$I_{GABA,i} = \sum_j P_{release,j}[E_{Cl} - V_{MC,i}]$ $P_{release,j} = \frac{[Ca]_j - [Ca]_{baseline,j}}{[Ca]_{th} - [Ca]_{baseline,j}}$, $[0, 1]$ $\tau_{Ca}[\dot{Ca}]_j = -[Ca]_j + \rho_{Ca}(I_{NMDA,j} + I_{N,j})$	$P_{release}$, graded activation
GCD	
$I_{AMPA,j} = \sum_i s_{j,i}(t)[E_{AMPA} - V_{GCD,j}]$ $s_{j,i}(t) = \frac{1}{s_{norm}}\left[e^{-\frac{t-t_{spike,i}}{\tau_{decay}}} - e^{-\frac{t-t_{spike,i}}{\tau_{rise}}}\right]$	$s(t)$, MC spiking activation
$I_{NMDA,j} = \sum_i B(V_{GCD,j}) s_{j,i}(t)[E_{NMDA} - V_{GCD,j}]$ $B(V_{GCD,j}) = \frac{1.0}{1.0 + 0.28[Mg]e^{-0.062\,(V_{GCD,j} - V_{Mg})}}$	$s(t)$, MC spiking activation $B(V_{GCD})$, Voltage - dependent activation
$I_{N,j} = m_{N,j} h_{N,j}[E_{Ca(N),j} - V_{GCD,j}]$ $\tau_{m_{N,j}} \dot{m}_{N,j} = \bar{m}_{N,j} - m_{N,j}$ $\tau_{m_{N,j}} = 18.0e^{-((V_{GCD,j}+70)/25)^2} + 0.3$ $\bar{m}_{N,j} = \frac{1.0}{1.0 + e^{-(V_{GCD,j}+45)/7}}$, $h_{N,j} = \frac{10^{-4}}{10^{-4} + [\mathrm{Ca}]_j}$	m_N, Voltage - dependent activation h_N, $[Ca^{2+}]$ - dependent inactivation

Table 2.1. MC and GCD synaptic current equations. The index *i* always refers to MCs and index *j* always refers to a GCDs. $[Ca^{2+}]$ represents GCD internal calcium concentration.

oscillations are dissociable from those mediating theta (Fukunaga et al., 2014) and because we are interested in investigating the effect that GC excitability alone has on MC synchronization, which to our knowledge has not yet been done. To make MC spike firing probabilistic we include an input noise $\sigma_{ext}\eta_{ext,i}$ where σ_{ext} is a scalar and $\eta_{ext,i}$ is drawn from the standard normal distribution for the *i*'th MC on each

timestep. Each MC represents the average activities of all the MCs innervating a particular GLO and therefore this model does not capture variations in the activity of individual MCs innervating the same GLO. Periglomerular cells, which normally gate sensory inputs to MCs, are not included in the model, because we are interested only in the modulation of MC activity by GCDs. Instead, continuous sensory input is fed directly into MCs. The input weight to the *i*'th MC $W_{ext,i}$ (Table 2.1) is determined by a scalar σ_w, a number $\eta_{w,i}$ chosen randomly from a uniform distribution on [0 1], and a minimum weight $W_{min,ext}$. For most simulations we set σ_{ext} = 0.001 and $W_{min,ext}$ = 0.013, resulting in uniformly distributed free running (uninhibited) MC firing rates between 130 and 150 Hz. These uninhibited firing rates are much higher than experimentally recorded firing rates of individual MCs when inhibition is blocked (Lepousez and Lledo, 2013a). However, each of our model MCs represents a population of MCs associated with an individual GLO, and not a single MC. Thus, high unsynchronized firing rates are expected. Furthermore, our model aims to simulate the beta oscillations induced by high volatility odors, which may bind OSNs quickly and uniformly, causing stronger convergent inputs onto MCs. We find that the network requires this strong external drive in order to generate the full gamma to beta range as GC excitability is varied.

2.2.4 Graded inhibitory input to MCs

We assume a graded form of inhibition from GCDs onto MCs, which is proportional to the probability of GABA vesicle release $P_{release}$. The release

probability is only dependent on intracellular [Ca^{2+}] (Table 2.1). Thus, the AMPA current can only drive graded inhibition indirectly by activating NMDA and N-type channels. Much like MC IPSCs recorded in slice (Schoppa et al., 1998), the time-course of the model MC IPSCs follows the slow exponential decay of NMDA and N-type channels. The proportionality ρ_{Ca} between Ca^{2+} current and Ca^{2+} concentration is chosen such that [Ca^{2+}] is typically between 0.1 and 1 μM, a physiologically realistic range for [Ca^{2+}] in a dendritic spine (Higley and Sabatini, 2012). The threshold for maximum Ca^{2+} release, $[Ca]_{th}$, is chosen so that the maximum $P_{release}$ is near 1 in the high excitability condition. Experiments have shown that DDI is largely unaffected by intracellularly injected Ca^{2+} chelators, suggesting that the GABA release machinery in GC dendrites is tightly coupled to the Ca^{2+} influx following MC spikes (Isaacson, 2001). Because the model N-type current admits a constant Ca^{2+} influx due to nonzero voltage-dependent activation even in the absence of MC spikes there is a constant internal baseline [Ca^{2+}], which we call $[Ca]_{baseline}$ (see *Appendix I* for derivation of $[Ca]_{baseline}$). We subtract $[Ca]_{baseline}$ in the calculation of $P_{release}$ to ensure that tonic inhibition is not released onto MCs in the absence of MC spikes (Fig. 2.3D).

2.2.5 Excitatory and Ca^{2+} currents in GCDs

The model GCDs include AMPAR, NMDA, and N-type currents. The synaptic time course $s(t)$ of the AMPA and NMDA currents is modeled as a difference of exponentials with rise and decay times that represent the opening and closing of the channels following glutamate binding (Brunel and Wang, 2003). The NMDA current

I_{NMDA} also contains an additional voltage-dependent activation $B(V_{dGC})$ (Table 2.1) which represents the Mg^{2+} block as determined by Jahr & Stevens (1990). Because the connections are probabilistic, some GCDs may be connected to as few as 4 MCs while others may be connected to as many as 22. The synaptic weight of the AMPA current $W_{AMPA,GC}$ is chosen such that the magnitude of membrane depolarization for

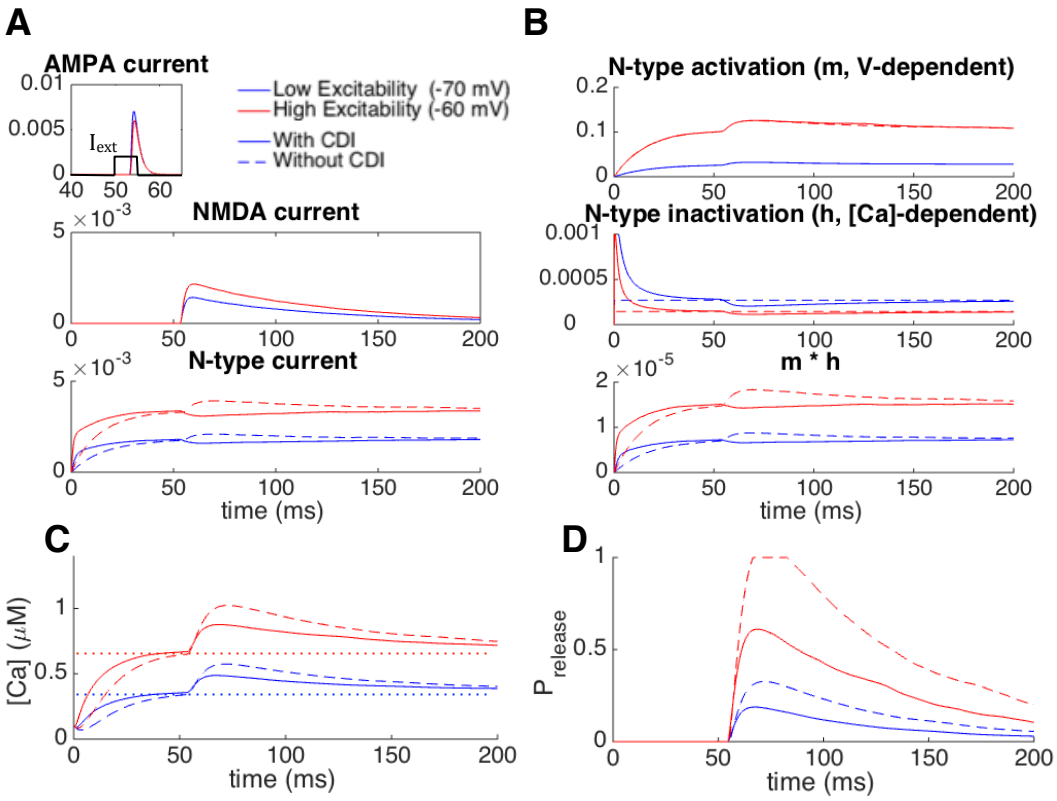

Figure 2.3. Model currents A: AMPA, NMDA, and N-type currents of a single GCD connected to 14 MCs are plotted. A 5 ms long current pulse (I_{ext}, amplitude not to scale) was initiated at t = 50 ms, causing all 14 MCs to fire a single action potential almost simultaneously. The latency of the currents from onset of I_{ext} corresponds to the integration time of the MCs before spikes. Simulations were performed under low ($V_{rest,GC}$ = -70 mV, blue) and high ($V_{rest,GC}$ = -60 mV, red) GC excitability conditions. The N-type current was simulated with (solid lines) and without (dashed lines) CDI. **B:** N-type activation (m) and inactivation (h) variables and their product ($m*h$) for the N-type currents shown in **A** are plotted. CDI is prevented by evaluating h at $[Ca^{2+}]_{baseline}$, leaving it constant. Deflections near t = 0 are transients which can be ignored. CDI greatly reduces the magnitude of the deflections from the baseline in $m * h$, but does not change their overall shape. **C:** Internal $[Ca^{2+}]$ traces resulting from the NMDA and N-type currents shown in part **A** are plotted. Dotted lines indicate $[Ca^{2+}]_{baseline}$ for low and high excitability conditions. **D:** The $P_{release}$ traces derived from the internal $[Ca^{2+}]$ traces shown in part **C** are plotted. Subtraction of $[Ca^{2+}]_{baseline}$ from $[Ca^{2+}]$ ensures that $P_{release}$ is 0 until a MC spike is fired. The presence of CDI significantly decreases $P_{release}$, but does not change the temporal structure of GABA release.

a GCD connected to an average number of 14 MCs is near 7 mV, which is comparable to the experimentally measured average size of AMPA-mediated depolarization of GC dendrites (Cang and Isaacson, 2003a). The experimentally recorded amplitude of NMDA current is usually smaller than the AMPA current, though this is not always the case (Schoppa et al., 1998). For our simulations $W_{NMDA,GC}$ is chosen such that the amplitude of I_{NMDA} is $\sim 1/4$ that of I_{AMPA} (Fig. 2.3A). The NMDA decay time constant is 75 ms in most of our simulations, close to the value reported in physiological concentrations of Mg^{2+} (Isaacson, 2001; Schoppa et al., 1998). With these parameters, GCD membrane depolarization closely resembles that which is seen in experiments, with fast decaying AMPA-mediated and slow decaying NMDA-mediated components.

The N-type current I_N includes a voltage-dependent activation variable, m_N, and a Ca^{2+} dependent inactivation (CDI) variable, h_N. The activation curves of N-type channels reported in the literature are not the same across all neuronal cell types, with half activation voltages ranging from -45 mV (Amini et al., 1999; Zeng et al., 2009) to -3 mV (Evans et al., 2013). To our knowledge the activation curve of N-type channels in OB GCs has not yet been measured. We choose to use a model that begins to activate at relatively low potentials so that I_N is sensitive to increases in GC excitability, which are at most only about 25 mV above the resting potential. This ensures that I_N alone can drive slowly decaying dendrodendritic inhibition when excitability is increased, as has been shown in slice (Isaacson, 2001). For most of our simulations $W_{N,GC}$ is chosen so that the N-type current is approximately 1/3 the magnitude of the NMDA current (Fig. 2.3 A), a choice that is motivated by Ca^{2+}

imaging studies which have shown that although NMDA channels mediate the majority of Ca^{2+} entry, VDCCs still mediate a sizeable portion (Egger, 2008a; Bywalez et al., 2015). $W_{N,GC}$ is so much greater than $W_{NMDA,GC}$ because the product of the N-type activation and inactivation terms is on order of 10^{-5}, while the NMDA activation term is on the order of 1.This model does not include voltage-dependent inactivation. Because in most of our simulations the GC membrane potential does not exceed -40mV and inactivation only becomes significant above -20 mV (Johnston & Wu, 1995; Evans et al., 2013), voltage-dependent inactivation would not make a large contribution here even if it were included.

The effect of CDI is to drive the N-type inactivation variable in the opposite direction of the activation variable, as shown in Figure 2.3B, causing a net negative deflection of I_N shown in Figure 2.3A. Without CDI, both I_{NMDA} and I_N fully contribute to the internal $[Ca^{2+}]$ buildup, resulting in a high amplitude GABA release profile that saturates in the high excitability condition (Fig. 2.3D). When CDI is present I_{NMDA} becomes the dominant source of Ca^{2+} for driving graded inhibition of MCs. Even though CDI significantly reduces the $[Ca^{2+}]$ amplitude and reverses the direction of the N-type current deflection, it does not change the temporal structure of graded inhibition (Fig. 2.3C, D). Therefore, the model is capable of generating the full gamma to beta range with and without CDI as long as the excitatory and inhibitory weights are adjusted accordingly. CDI is included in all subsequent simulations.

Due to low internal Ca^{2+} concentrations, the Nernst potential for Ca^{2+} is sensitive to changes in intracellular Ca^{2+} and is calculated on each step of the simulation by the Nernst equation

$$E_{Ca} = \frac{RT}{zF} ln \frac{[Ca]_{out}}{[Ca]_{in}} \quad (2.3)$$

where R = 8.31 J/(mole * K) is the ideal gas constant, T = 300 K is the temperature, z = 2 is the valence of the Ca^{2+} ion, and F = 96,485 Coul/mole is Faraday's constant. Assuming an extracellular calcium concentration $[Ca]_{out}$= 1.5 mM (Higley and Sabatini, 2012) E_{Ca} is typically near 100 mV.

2.2.6 Simulation and spectral analysis of local field potential

The model is simulated for 700 ms. The LFP is generated by smoothing and averaging the MC IPSCs (ILFP) or MC membrane voltages (VLFP) using MATLAB's built in `smoothts` function with a box filter width of 5 ms. The ILFP and VLFP have nearly identical frequencies, but differ notably in phase and power, which we discuss in Figures 2.4 and 2.5. Only simulation data after 100 ms is used in order to avoid transients due to initial conditions of the simulation. For most of our simulations we only present the ILFP. Recent work has shown that *in vivo* LFPs correlate more strongly with IPSCs and EPSCs than with membrane potentials (Atallah and Scanziani, 2009; Mazzoni et al., 2015). Unless otherwise stated, the power spectra are computed by MATLAB's `fft` function on the mean-subtracted LFP and we report the LFP frequency as the peak frequency of the power spectrum between 7 Hz and 100 Hz. For reference, all power plots indicate the maximum power of the noise floor, which we define as the maximum power of the residual oscillation due to common inputs to MCs when inhibition is removed. In Figure 2.6 we perform a continuous Morlet wavelet transform with MATLAB's `cwt` function in

order to display the instantaneous LFP frequency in response to sudden changes in GC excitability. We use a frequency range of f_{range} = 5 – 80 Hz and the standard frequency–scale relation, f_c*sf/f_{range} (where f_c is central frequency of wavelet and sf is sampling frequency), to define the scale range.

Using the frequency obtained from the FFT of the LFP (LFP_{fq}) we also define a simply spike synchrony measure, which we call the spike-frequency deviation (SFD), as

$$SFD = \left|N_{spikes} - N_{MC}\left(0.6LFP_{fq}\right)\right| \tag{2.4}$$

where N_{spikes} is the actual number of spikes fired in the last 0.6 s of simulation and the second term is the number of spikes that would be fired in 0.6 s if each MC fired at exactly the LFP frequency LFP_{fq}. The deviation is 0 when each MC fires exactly once per LFP oscillation cycle, and is greater than 0, due to the absolute value, when MCs fire more often or less often than once per cycle.

We also compute the spike-field coherence (SFC) using the `coherencycpt` function included in the Chronux version 2.11 toolbox for MATLAB (Bokil et al., 2010a). We used a time-half-bandwidth of 5 with 9 tapers over a frequency range of 5 Hz to 120 Hz. Finite sampling corrections were included, although they did not significantly alter the results. The SFC produces a coherence spectrum between each MC and the LFP, so we report the peak coherence averaged over the 45 MCs. The SFD and SFC measures are both used in Figure 2.5.

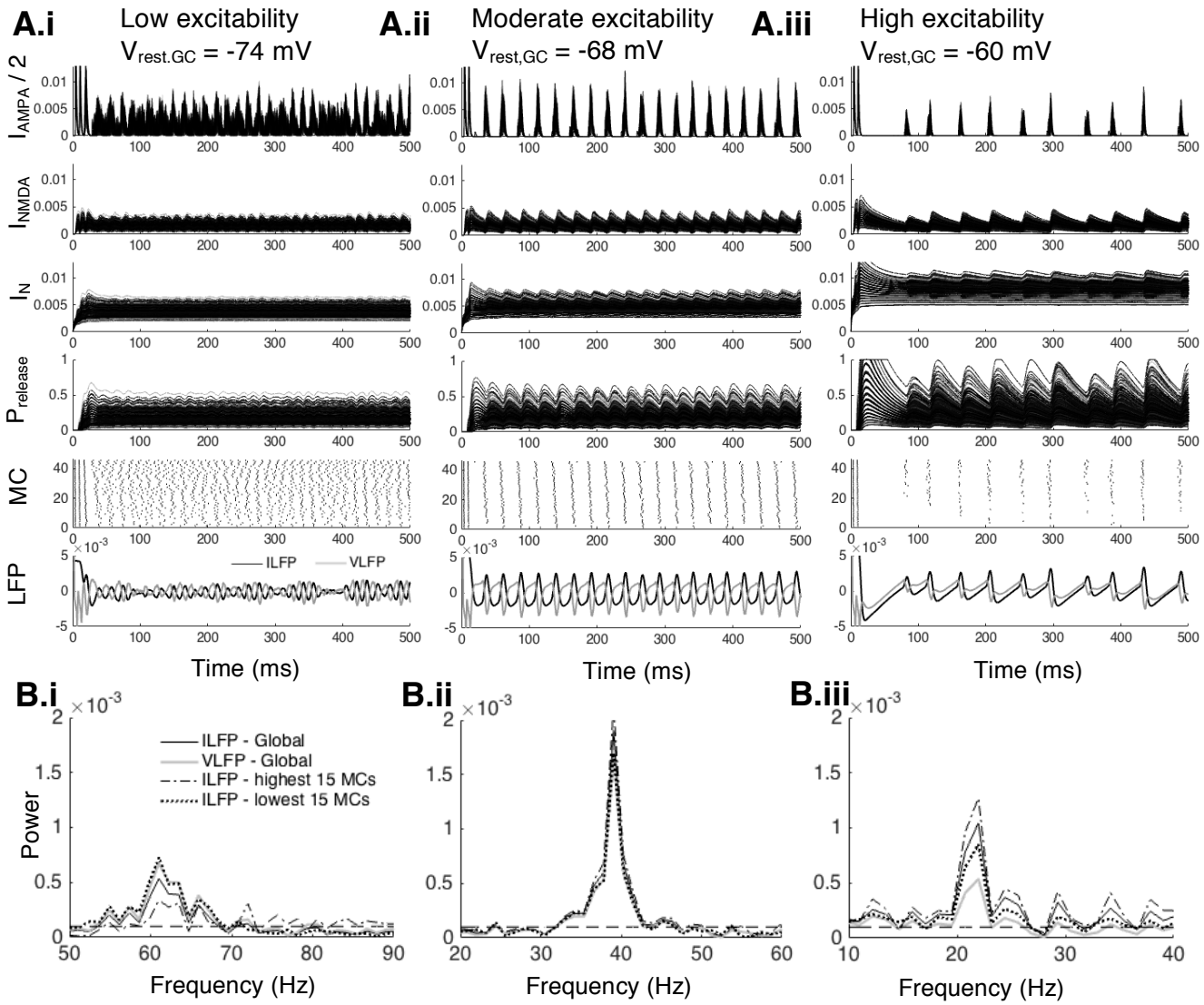

Figure 2.4. Simulations in low, moderate, and high GC excitability regimes A: The MC-GC dendrodendritic network activity was simulated under low (**A.i**), moderate (**A.ii**), and high (**A.iii**) GC excitability conditions in response to constant ORN input current for 500 ms. The top three rows show the AMPA, NMDA, and N-type currents of all 720 GCDs for each condition. The AMPA current is scaled by ½ so that all axes fit on the same scale. The N-type current has a constant offset that increases with $V_{rest,GC}$ due its voltage-dependent activation. The fourth row shows the GABA release probabilities, $P_{release}$, for each of the 720 GCDs resulting from the inward Ca^{2+} currents (I_{NMDA} and I_N). The fifth row shows MC raster plots with cells ordered from bottom to top by increasing input strength. The bottom row shows the LFP calculated from the average MC IPSCS (ILFP, black) and MC membrane voltages (VLFP, gray). **B:** For each of the three conditions power spectra were calculated from the ILFP generated by the global population as well as from the top 15 MCs receiving the strongest external input, the bottom 15 MCs receiving the weakest external input, and the VLFP of the global population. The y-axes of the three plots are the same, but the x axes differ. The horizontal dashed black line indicates the maximum power of the noise floor.

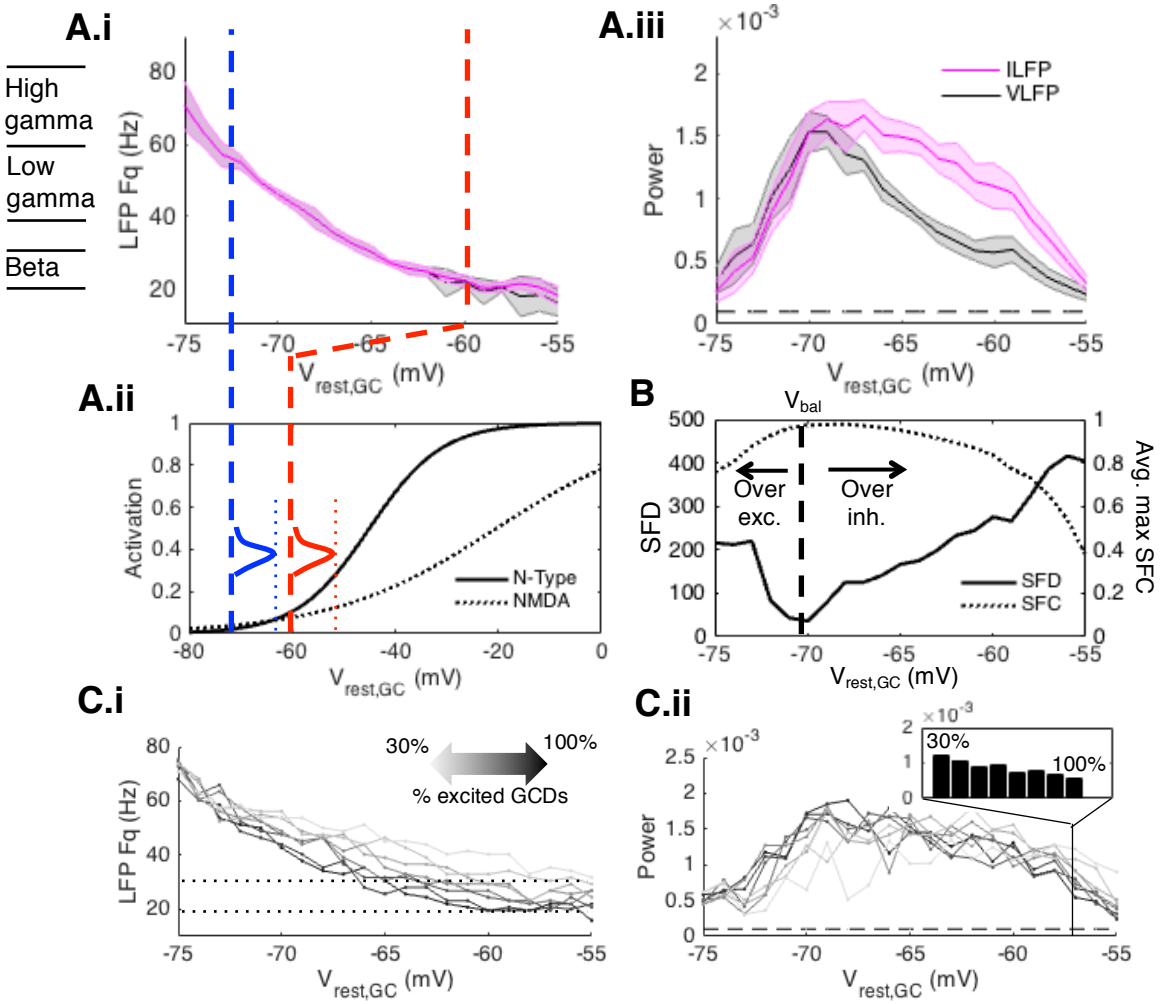

Figure 2.5. Population activity as a function of GC excitability ($V_{rest,GC}$) A.i: The simulated ILFP (pink) and VLFP (black) frequencies of the full model decrease continuously with increased GC excitability, represented by $V_{rest,GC}$. Shaded regions denote the standard deviation from the mean from ten simulations. Approximate frequency ranges for high/low gamma and beta states are indicated to the left. **A.ii:** The voltage-dependent activation curves of N-type and NMDA channels are plotted. A schematic showing the average AMPA depolarization from the GCD resting potential (7mV) is shown for low excitability (blue) and high excitability (red) conditions. In the excited state the depolarization is high enough to significantly activate both NMDA and N-type currents (see where the vertical dotted red line crosses the activation curves). **A.iii:** The power of the ILFP and VLFP from Ai is shown. The horizontal dashed line represents the power of the noise floor, where inhibition can no longer sustain oscillations. **B:** The means of the spike-frequency deviation (SFD, dashed line, left axis) and average maximum spike-field coherence (SFC, dotted curve, right axis) for the simulations in **A** are shown. Standard deviations are omitted for clarity. The minimum of the SFD is marked by the vertical dashed line and labeled V_{bal}. To the left of V_{bal} some MCs are over excited, while to the right of V_{bal} some MCs are over inhibited. The maximum of the SFC spectrum between each MC spike train and the global ILFP was averaged across all 45MCs to obtain each point of the plot. **C.i:** The excitability of a randomly chosen subpopulation of GCDs is varied while holding the remainder at a resting potential of -75 mV. Each of the curves converges to the point where the entire GCD population is in the same state at -75 mV. The parameters for this simulation are shown in Table 2.2. Each of the 7 curves corresponds to a randomly selected subpopulation ranging from 30% (light gray) to 100% (black). Dotted lines indicate the borders of the beta regime. **C.ii:** The peak power of curves in C.i. The black dashed line indicates the maximum power of the noise floor. The inset shows the cross section of power at $V_{rest,GC}$ = -63 mV. The power is highest when only 30% of the GCDs are in a high excitability state.

2.3 Modeling Results

Waking rats and mice show stereotypic transitions from gamma to beta oscillations after a few trials sniffing highly volatile odorants or after learning to correctly discriminate odors in operant tasks (Fig. 1.4A). Both oscillations occur in a single sampling bout, and the switch can be very fast (10-100 ms). This has led us to propose that a fast change in a parameter value, such as GC excitability, could produce a fast change in temporal properties. We propose a mechanism by which the same circuit can generate both gamma and beta oscillations with a fast change in GC excitability.

2.3.1 GC excitability controls LFP frequency through activation of NMDA and N-type currents

We show the activity of the full model under low, moderate, and high GC excitability conditions in Figure 2.4. The model parameters for this simulation are presented in Table 2.2. There is a large variation in synaptic current amplitude among the 720 GCDs (Fig. 2.4A, rows 1-3). This variation is due to differences in the number of MCs connected to each GCD, with the fewest numbering near 4 and the most near 22. GCDs connected to higher numbers of MCs produce higher values of $P_{release}$ and contribute more to the MC IPSCs than GCDs with fewer connections (Fig. 2.4A, fourth row). For the choices of $[Ca]_{th}$ and ρ_{Ca} used in this simulation (see Table 2.2), the maximum GABA release nearly saturates in the high excitability regime ($P_{release}$ = 1; Fig. 2.4A.iii). The N-type current (third row) has a non-zero baseline that

Parameter	Value (units)	Description	Reference
Input			
W_{ext}	See METHODS	Input current weights	N/A
σ_{ext}	5 (mV/R)	Input current variability	N/A
MC			
τ_{MC}	5 (ms^{-1})	MC membrane time constant	De Almeida et al., 2013
$\tau_{AMPA1,MC}$	1 (ms^{-1})	MC AMPA rise time	De Almeida et al., 2013
$\tau_{AMPA2,MC}$	2 (ms^{-1})	MC AMPA decay time	De Almeida et al., 2013
E_{AMPA}	0 (mV)	MC AMPA reversal potential	Brunel & Wang, 2003
$\tau_{GABA1,MC}$	0.5 (ms^{-1})	MC GABA rise time	Brunel & Wang, 2003
$\tau_{GABA2,MC}$	5 (ms^{-1})	MC GABA decay time	Brunel & Wang, 2003
E_{GABA}	-80 (mV)	GABA reversal potential	Cang & Isaacson, 2003
$V_{rest,MC}$	-70 (mV)	MC resting potential	De Almeida et al., 2013*
$V_{th,MC}$	-63 (mV)	MC firing threshold	Cang & Isaacson, 2003
V_{hyper}	-80 (mV)	MC/GCD hyperpolarization potential	De Almeida et al., 2013*
$W_{GABA,MC}$	0.0125	MC GABA inhibitory weight	N/A (Varied in Fig. 6, 8)
GCD			
τ_{GC}	5 (ms^{-1})	GCD membrane time constant	De Almeida et al., 2013
$\tau_{AMPA1,GC}$	1 (ms^{-1})	GCD AMPA rise time	De Almeida et al., 2013
$\tau_{AMPA2,GC}$	2 (ms^{-1})	GCD AMPA decay time	De Almeida et al., 2013
$\tau_{NMDA1,GC}$	2 (ms^{-1})	GCD NMDA rise time	N/A (Varied in Fig. 9)
$\tau_{NMDA2,GC}$	75 (ms^{-1})	GCD NMDA decay time	N/A (Varied in Fig. 9)
τ_{Nmax}	18 (ms^{-1})	GCD N-type activation time constant	Amini et al., 1999
E_{AMPA}	0 (mV)	GC AMPA reversal potential	Brunel & Wang, 2003
E_{NMDA}	0 (mV)	GC NMDA reversal potential	De Almeida et al., 2013
$E_{Ca(N)}$	~ 120 (mV)	GC N-type reversal potential	Calculated each time step
$[Ca]_{out}$	1500 (μ M)	External Ca^{2+} concentration	Zeng et al., 2009
$[Ca]_{th}$	1.5 (μ M)	Ca^{2+} threshold for maximum GABA rel.	N/A
ρ_{Ca}	100	Proportionality between I_{Ca} and $[Ca^{2+}]$	N/A
$V_{rest,GC}$	Varied	GCD resting potential	N/A (Varied in most Figs)
$W_{AMPA,GC}$	0.03	GCD AMPA excitatory weight	Cang & Isaacson, 2003
$W_{NMDA,GC}$	0.04	GCD NMDA excitatory weight	N/A (Varied in Fig. 8)
$W_{N,GC}$	250	GCD N-type excitatory weight	N/A (Varied in Fig. 8)

Table 2.2. Parameters for the full model simulation presented in Figure 2.4.
* Voltages are shifted down by -70 mV from De Almeida et al., 2013, but remain the same relative distance from each other.

increases with $V_{rest,GC}$ due to voltage-dependent activation, and causes tonically elevated internal [Ca^{2+}]. This [Ca^{2+}] baseline is subtracted for each GCD individually so that non-physiological tonic inhibition is prevented (see *Appendix I*).

Spike rasters line up with LFP fluctuations in each frequency range (Fig. 2.4A, fifth row). Field potential can be simulated either from current or voltage (ILFP, VLFP); the two oscillate at the same frequency, but are phase shifted by 180^o (Fig. 2.4A, bottom row). We can understand this phase shift by considering what happens after a MC spike. Immediately following a spike the MC membrane voltage undergoes hyperpolarization, producing a trough in the VLFP. At the same time, GCDs experience a strong inward Ca^{2+} current that in turn triggers a strong MC IPSC, producing a peak in the ILFP.

GC excitability alone can control the frequency of network oscillations through activation of NMDA and N-Type currents. Under low excitability conditions ($V_{rest,GC}$ = -74 mV, Fig. 2.4A.ii) the NMDA and N-type currents are not strongly activated, so inhibition is low and MCs are not fully synchronized across the population. Physiological MCs are known to skip cycles of the gamma oscillation (Lagier et al., 2004, 2007; Bathellier et al., 2006), however our model MCs represent populations of MCs associated with particular glomeruli and thus are expected to fire on each cycle. The MCs receiving the weakest external inputs, towards the bottom of the raster plot in Figure 2.4A.i, are able to synchronize, but those receiving stronger inputs are over-excited and fire multiple spikes per cycle. This produces low amplitude oscillations falling within the high gamma band as shown in the power spectrum (Fig. 2.4B.i). When $V_{rest,GC}$ is increased to -68 mV the network

oscillation frequency falls into the low gamma band. The increased inhibition synchronizes all the MCs (representing populations associated with individual glomeruli), which leads to higher power LFPs (Fig. 2.4A.ii, fifth row & 2.4B.ii). Finally, when $V_{rest,GC}$ is further increased to -60 mV the network oscillates at beta frequencies. The power of this beta state is lower than the low gamma state (Fig. 2.4B.ii), because the MCs receiving the weakest external excitation become over-inhibited and cease firing spikes.

Shifts in the balance of excitation and inhibition to MCs explain the differences in power. When GC excitability, and hence MC inhibition, is low, the least excited MCs generate the largest ILFP signal (Figure 2.4B.i). In contrast, during high GC excitability, the most excited MCs generate the largest ILFP signal (Figure 2.4B.iii). This is because when GC excitability is low the MCs are over excited, firing on average more than one spike per LFP cycle, but when GC excitability is high the MCs are over-inhibited, firing on average less than one spike per LFP cycle. Under moderate GC excitability conditions, excitation and inhibition are balanced such that nearly all the MCs become synchronized and therefore the simulated LFP power of any subset of cells is very close to the global LFP. The maximum synchronization at low gamma frequencies in our model agrees with recordings in awake mice which found that long range LFP coherency and MC spike synchronization occurs at low gamma, but not high gamma frequencies (Lepousez and Lledo, 2013a). We will show later that the balance of excitation and inhibition causing peak power in the low gamma band is primarily a property of the NMDA currents, while N-type currents show a balance of excitation and inhibition in the beta band (see *2.3.5*

Relative contributions of NMDAR- and N-type currents).

2.3.2 Network response to continuous changes in GC excitability

A continuous change in GC excitability is not physiological, but it gives us a qualitative understanding of the relationship between network frequency and GC excitability. As $V_{rest,GC}$ sweeps from -75 mV to -55 mV, LFP frequency changes continuously (Fig. 2.5A.i). The ILFP and VLFP frequencies span the full range from high gamma to beta (approximate frequency ranges indicated to the left) and have nearly identical dependence on $V_{rest,GC}$, differing only in the high excitability condition where over-inhibition tends to make the VLFP frequency slightly lower than the ILFP. The curves are steeper in the gamma than the beta regime, indicating that beta frequencies are more stable with respect to small changes in $V_{rest,GC}$. The decrease in LFP frequency in response to an increase in $V_{rest,GC}$ is caused by activation of NMDA and N-Type currents (Fig. 2.5A.ii). The average AMPA-mediated membrane depolarization (7 mV) from $V_{rest,GC}$ = -73 mV (Fig. 2.5A.ii, blue curve) barely activates the currents (see vertical blue dotted line). However, the same depolarization from $V_{rest,GC}$ = -60 mV (red curve) significantly activates the currents (see vertical red dotted line). Depending on how many MCs are connected to a particular GCD, the AMPA-mediated membrane depolarization can range from approximately 2 mV to 18 mV, thus activating NMDA and N-Type currents to varying degrees.

The ILFP and VLFP power plots overlap much less than their frequencies (Fig. 2.5A.iii). The ILFP and VLFP power values are nearly identical in the high

gamma regime, increasing dramatically with $V_{rest,GC}$ as increased inhibition synchronizes the entire MC population. The power peaks in the low gamma regime, when there is a balance of excitation and inhibition onto MCs such that all MCs are synchronized (as described in Fig. 2.4). Finally, as the system approaches the beta regime, some MCs become over-inhibited and ILFP and VLFP power drops off, with the VLFP falling more sharply than the ILFP. Not all of the oscillations generated by the model are physiological, because we explore a wider parameter space than what is available to the real system; such high power in the low gamma regime is rarely seen *in vivo*. However, this parameter exploration allows us to characterize properties of the system that otherwise may not be understood. In a later section we show the model response to a more physiologically realistic fast change in GC excitability (see *2.3.4 Network response to fast change in GC excitability*).

To show that the power peak in the low gamma band is indeed due to a balance of excitation and inhibition, where the MC population fires close to one spike per cycle, we devise a simple measure that we call the spike-frequency deviation (SFD; see *Methods* Eq. 2.4). The SFD measures the deviation from the number of spikes expected if all MCs fire exactly once per LFP cycle (SFD = 0 if all MCs fire exactly 1 spike per cycle). In addition, we also calculate the spike-field coherence (SFC), which measures the phase locking between spikes and LFPs (see *Methods*). We use the ILFP in calculating the SFD and SFC measures, though using the VLFP produces nearly indistinguishable curves.

The SFC and SFD measure spiking coherence with the LFP and deviations in spike rate, respectively, associated with changing GC excitability (Fig. 2.5B). The

population averaged SFC is at a maximum when SFD is at a minimum and MCs are closest to the balanced condition (V_{bal} ~ -71 mV). MCs are over-excited when $V_{rest,GC} < V_{bal}$ and over-inhibited when $V_{rest,GC} > V_{bal}$. When the number of MC spikes deviates from the number expected at maximum synchrony, the VLFP is decreased, and therefore the SFD looks almost like a mirror reflection of the VLFP. The SFC, on the other hand has a much broader peak similar to the ILFP, because it only measures synchrony, not the number of firing MCs. The peaks of ILFP and VLFP power in Figure 2.5A.iii both correspond to maximally synchronous conditions, but by construction the VLFP is more sensitive to MC spiking, while the ILFP is more sensitive to synchronized current flow. Overall, the ILFP and VLFP are quite similar. However, physiological LFP signals have been shown to follow synaptic currents more closely than membrane voltages (Atallah and Scanziani, 2009; Mazzoni et al., 2015), and so we choose to report the frequency and power of the maximum peak in the ILFP spectrum for the remainder of the paper, unless otherwise stated.

So far we have modulated the excitability of the entire population of GCDs. Such a broad modulation of excitability could potentially be mediated by diffusion of acetylcholine released from cholinergic fibers (Pressler et al., 2007a; Ma and Luo, 2012) or other neuromodulators. However, odorants excite only a fraction of downstream cortical neurons, which in turn feed back onto a subpopulation of GCs (Mouret et al., 2009; Poo & Isaacson, 2009); thus, the excitability of only a subpopulation of GCs may be modulated. We therefore continuously vary the excitability of randomly chosen GCD subpopulations of decreasing size while holding the remainder at a resting potential of -75 mV in Figure 2.5C. Modulating

the excitability of subpopulations as small as 40% produces LFP oscillations that still span the full gamma to beta range (Fig. 2.5C.i). Beta oscillation power is actually higher when the size of the excited GCD population is reduced (inset of Fig. 2.5C.ii). This is because MCs in the beta state are over-inhibited, and reducing the population of excited GCDs reduces inhibition, allowing more MCs to participate in the oscillation. On the other hand, the high and low gamma power is lower for smaller excited GCD populations, because now MCs are not receiving enough inhibition. In the real system, beta power tends to be higher than gamma. Therefore, not only can modulation of the excitability of a GCDs subpopulation generate oscillations that span the high gamma to beta range, but the simulated oscillations appear more physiological.

2.3.3 Beta frequency is highly stable with respect to changes in MC excitation and inhibition

In Figure 2.5 we showed that the ILFP power of the full model peaks in the low gamma band, which corresponds to a state where excitation and inhibition are balanced such that the all the MCs are synchronized. We next explore how network oscillations respond to changes in excitatory-inhibitory balance by directly manipulating MC excitatory and inhibitory weights. Increasing MC excitation, by increasing the minimum excitatory weight $W_{min,ext}$, raises the LFP frequency in the low excitability regime (Fig. 2.6A.i) and dramatically increases the maximum power peak while shifting the peak towards higher excitabilities (Fig. 2.6A.ii). The pink

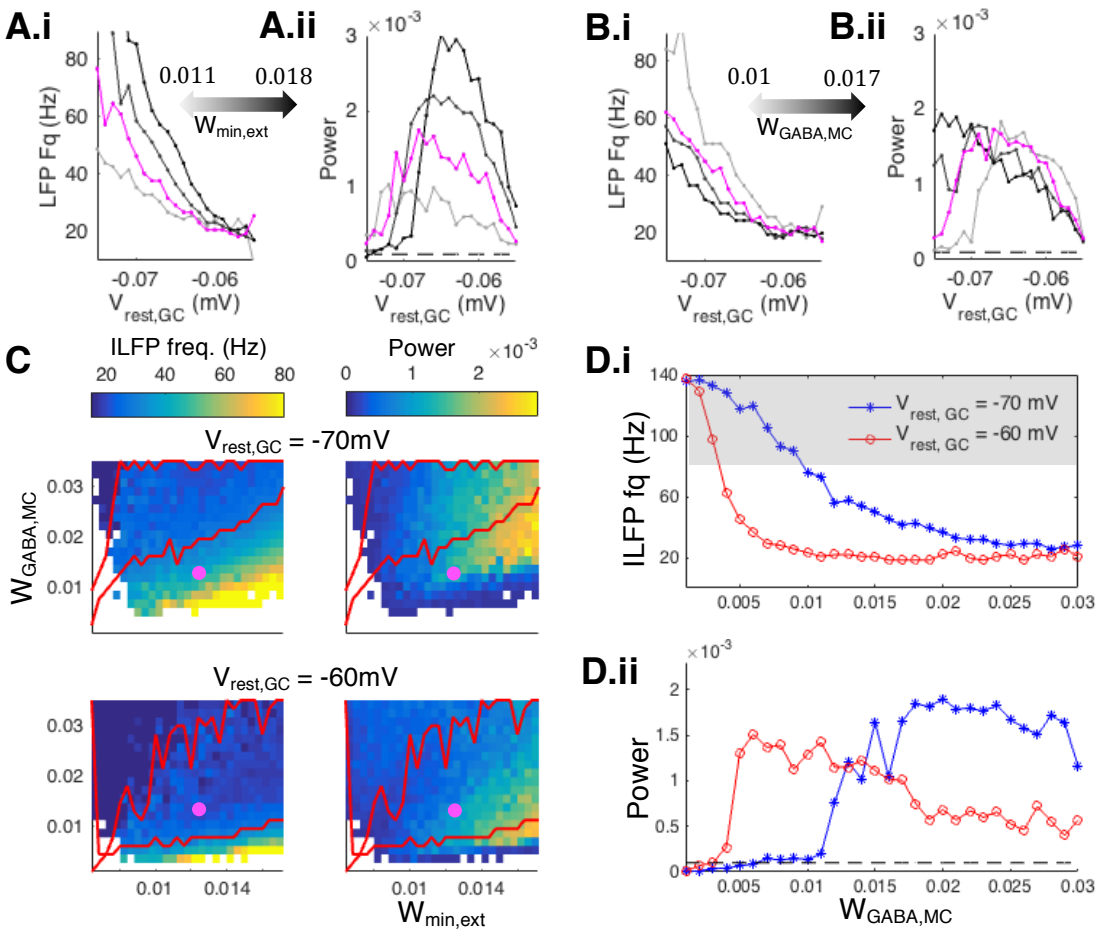

Figure 2.6. Beta oscillation dependence on GC excitability, sensory input, and MC inhibition.
A: The frequency (A.i) and power (A.ii) of the ILFP is plotted for varying strengths of MC excitation ($W_{min,ext}$). The pink curves correspond to parameters used in Figures 4 and 5. **B:** Same as in **A** but strength of MC inhibition ($W_{GABA,MC}$) is varied. $W_{GABA,MC}$ is varied over the same range as $W_{min,ext}$ (0.007), so that the plots in **A** and **B** are visually comparable. **C:** The ILFP frequency (left column) and power (right column) are plotted with $V_{rest,GC}$ = -70 mV (top row) and $V_{rest,GC}$ = -60 mV (bottom row) as the MC inhibitory weight $W_{GABA,MC}$, and minimum excitatory weight $W_{min,ext}$ are varied. Red lines mark the borders of the beta regime (20-30 Hz). Regions where ILFP power is less than or equal to the baseline power are colored white. Pink circles indicate the parameter values used for the simulations in Figures 4 and 5. **D:** Vertical cross sections of the plots in **C** fixed at $W_{min,ext}$ = 0.0134 (pink dot location) are shown for low (blue connected stars, $V_{rest,GC}$ = -70 mV) and high (red connected circles, $V_{rest,GC}$ = -60 mV) excitability conditions. The gray shaded region in **D.i** marks the region where network oscillations are considered part of the noise floor. The horizontal black dashed line in **D.ii** indicates the maximum power of the noise floor.

curve corresponds to $W_{min,ext}$ = 0.0134 (used in Figs. 2.4 and 2.5). Note that the shift is such that the frequency at maximum power is still in the low gamma band, because the balance of excitation is still maintained at low gamma frequencies. Interestingly, the frequency curves converge at beta frequencies because beta frequencies are stable with respect to MC excitation. However, beta power is very sensitive to $W_{min,ext}$. We routinely observe beta oscillations with drastically different amplitudes in awake animals. In particular, low volatility odors produce lower power beta oscillations than high volatility odors (Lowry and Kay, 2007a). In our model, differences in MC excitation are sufficient to explain this phenomenon.

If we hold MC excitation constant and instead vary MC inhibition (Fig. 2.6B), we find that increasing $W_{GABA,MC}$ reduces the ILFP frequency in the low excitability regime and shifts the power peak towards lower excitability (Fig. 2.6B.i). The shift towards lower excitability is such that the peak power is in the low gamma band, much like before. However, unlike changes in $W_{min,ext}$, changes in $W_{GABA,MC}$ do not significantly alter the maximum power amplitude. Excitatory modulation essentially adds energy to the system, setting the overall scale for how high the power can be. Inhibition, on the other hand, gates how much of this power is accessible at a particular frequency. The frequencies in Figure 2.6B.i also converge to beta frequencies in the high excitability regime, indicating that beta frequency is also stable with respect to inhibition.

To further explore the extent of beta regime stability we co-varied MC excitation and inhibition under low and high GC excitability conditions (Fig. 2.6C). The beta frequency is quite stable over a wide parameter range under both low and

high excitability conditions. The gamma regime (blue-green-orange colors on the frequency scale) occupies a sizeable region of parameter space under low excitability, but becomes very narrow under high excitability. Under high excitability, the lower boundary of the beta regime becomes more horizontal, indicating that beta frequency becomes less sensitive to changes in $W_{min,ext}$. The power (Fig. 2.6C, right columns) increases with $W_{min,ext}$ and peaks just outside of the beta regime, in the low gamma regime. These plots show us that overall, beta is less sensitive to changes in excitation and inhibition than gamma. This agrees qualitatively with in vivo recordings which have found beta oscillations to occupy a narrower frequency band than gamma (Neville and Haberly, 2003a; Kay, 2014a)

In this model, inhibition–mediated gamma frequency oscillations only occur below ~80 Hz, because higher frequencies (gray shaded region in Fig. 2.6D.i) are so low in power that they are essentially indistinguishable from the noise floor (dashed line in Fig. 2.6D.ii). Under high excitability (red connected circles), the beta frequency is remarkably stable and insensitive to changes in $W_{GABA,MC}$. However, if $W_{GABA,MC}$ is too low, the network frequency sharply rises and quickly becomes part of the noise floor, which is why the gamma regime is so narrow in the bottom panels of Figure 6C. Under low excitability, as $W_{GABA,MC}$ increases, the frequency falls more gradually through the gamma range until eventually a stable beta frequency is reached (Fig. 2.6D.i blue connected stars).

The power (Fig. 2.6D.ii) exhibits the same low gamma frequency peak as described earlier (Figures 2.4 and 2.5). Pharmacological manipulations in awake mice have shown that gamma oscillation power is reduced by high concentrations of

picrotoxin (a GABA antagonist), but is increased by low concentrations (Lepousez and Lledo, 2013a). The peak in the simulated LFP power vs $W_{GABA,MC}$ curve for low excitability in Figure 2.6D.ii (blue connected stars) can account for such a concentration-dependent effect. If the initial degree of inhibition puts the system just to the right of the peak power (for example $W_{GABA,MC}$ = 0.018 in Figure 2.6D.ii), then a small concentration of picrotoxin would only slightly decrease $W_{GABA,MC}$, thus increasing the power. But a high concentration would put $W_{GABA,MC}$ to the left of the peak, resulting in lower gamma power. It is interesting to note that the concentration-dependent power modulation was restricted primarily to low gamma frequencies in the Lepousez and Lledo (2013) study, and in our model the peak power is in the low gamma band. However, the same study also showed that high concentrations of picrotoxin (represented in our model as a decrease in $W_{GABA,MC}$) reduced gamma frequency, but in our model a decrease in $W_{GABA,MC}$ only increases gamma frequency. Indeed, there are other factors that our model does not include, such as asynchronous GABA release (Bathellier et al., 2006) and sub threshold resonance (Brea et al., 2009), which likely play an important role in gamma generation.

2.3.4 Network response to fast change in GC excitability

In the living system, changes in the excitability of GC dendritic spines leading to activation of dendritic Ca^{2+} channels are not gradual as in Figure 2.5, but occur very rapidly (Egger, 2008; Pressler, et al., 2007). Therefore, we explore how the computational model reacts to such a fast transition. Because the exact cellular

dynamics driving excitability changes in GC dendritic spines are highly complex and still being studied (Egger et al., 2005a; Egger, 2008a; Bywalez et al., 2015), they are beyond the scope of this model. Instead, we simulate a rapid change in the excitability of the entire GC dendritic arbor by forcing $V_{rest,GC}$ to vary from -74 mV to -60 mV following a sigmoid defined as $V_{rest,GC}$ = -74mV + 14mV/(1 + exp(αt)), where α defines the steepness of the transition and t is the time over which the transition occurs.

The speed of transition in $V_{rest,GC}$ may account for the fast changes in frequency we see in waking animals (Fig. 1.4A). For the slowest changes (Fig. 2.7, top two traces) the ILFP frequency changes continuously, while for the fastest changes (bottom two traces) the transition from gamma to beta frequencies is sharp but is accompanied by a large low frequency artifact. The gamma to beta transitions observed in vivo (Fig. 1.4A) are sharp (*i.e.*, there are no intermediate frequencies) but also spectrally clean (*i.e.*, there are no sudden artifacts). Therefore, the closest qualitative match between our model and experimental observation is found in the middle row of Figure 2.7, where the gamma to beta transition is sharp, and no artifacts are produced. The change in excitability does not have to be instantaneous in order to elicit an apparent sharp gamma to beta transition. When the excitability switch is fast, the intermediate values of GC excitability shown in Figures 2.4 and 2.5 are skipped, and therefore high power oscillations in the low gamma regime are skipped. This may explain why high power oscillations in the low gamma band are rarely observed *in vivo* (although see Kay, 2003).

The simulations producing sharp and clean gamma to beta transitions have sigmoidal widths of approximately 60 - 80 ms (Fig. 2.7, middle trace). This is slow relative to the onset of ADP and LLD in individual spines, which is on the order of 1 ms (Pressler et al., 2007a; Egger, 2008a), but relatively fast on a behavioral time scale (*i.e.*, less than one sniff). Thus, our model predicts that the excitability transitions of a population of dendritic spines should take place over roughly 60 - 80 ms to drive a gamma to beta transition during odor sampling.

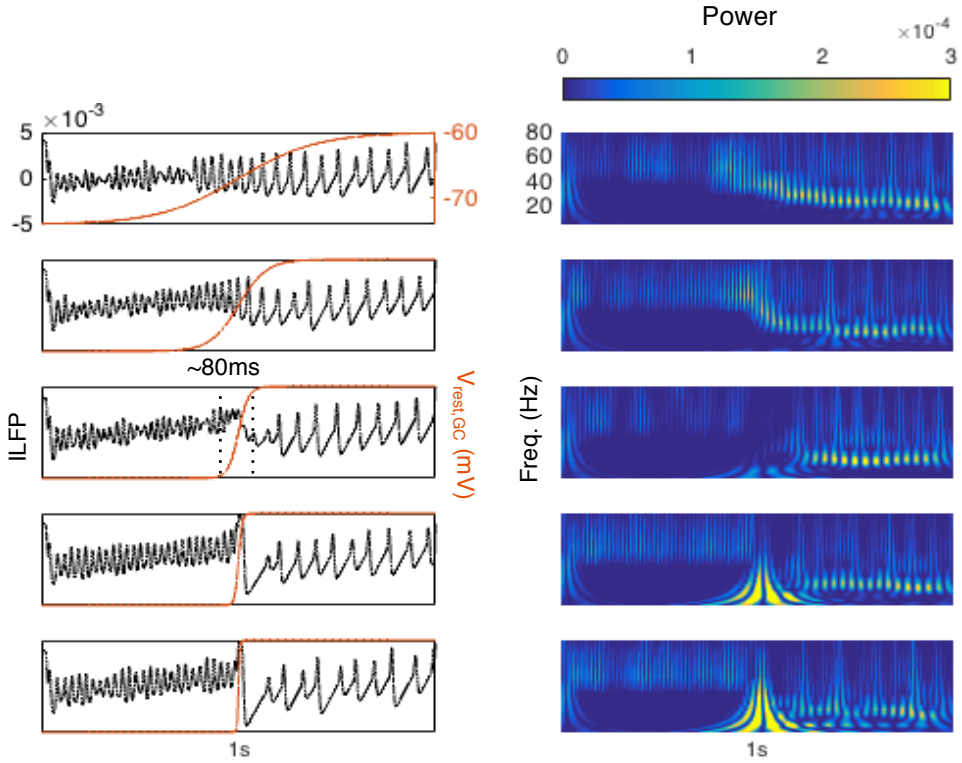

Figure 2.7. Simulated ILFP in response to changing $V_{rest,GC}$. Simulated ILFP (black left y-scale) in response to changing $V_{rest,GC}$ (red right y-scale) from -74 mV to -60 mV over 1s with varying speeds (slowest at top, fastest at bottom). In the middle row, the dotted vertical lines indicate the duration of the excitability transition for that plot, which is roughly 80 ms. (*Right*) A Morlet wavelet transform spectrogram (see Methods) gives the instantaneous frequency (y-axis) and power (color scale) of the ILFP traces.

2.3.5 Relative contributions of NMDA- and N-type currents

In the full model, graded inhibition of MCs is mediated by NMDA and N-type Ca^{2+} currents (Figs. 2.4 & 2.5). Slice studies have shown that Ca^{2+} flow through NDMARs alone can drive DDI (Schoppa et al., 1998). However, with NMDAR current pharmacologically blocked, slowly decaying DDI can also be evoked solely by AMPAR activation under pharmacological conditions that increase GC excitability (Isaacson, 2001), and thus the activation of N- and P/Q- type VDCCs by AMPA-mediated depolarization alone can trigger GABA release. Furthermore, pharmacological manipulations of OB activity in awake mice have shown that odor-evoked beta oscillation frequency and power are not very sensitive to NMDAR antagonists (Fig. 3 in Lepousez & Lledo, 2013), providing evidence that beta oscillations may depend on Ca^{2+} flow through N- and P/Q- type VDCCs, but not through NMDARs.

In order to test the relative contributions of Ca^{2+} flow through NMDARs and VDCCs to the network oscillations we simulate a complete pharmacological block of NMDAR or N-type currents by setting the weight of either current equal to 0 (Fig. 2.8A,B). In these simulations the [Ca^{2+}] threshold for maximum GABA release ($[Ca]_{th}$), the GCD AMPA weight ($W_{AMPA,GC}$), and external inputs to MCs ($W_{min,ext}$) are identical to the full model, but MC inhibition ($W_{GABA,MC}$) and the GCD NMDA/N-Type excitatory weights ($W_{NMDA,GC}$ and $W_{N,GC}$) are varied. For both pure NMDA and pure N-type models $W_{GABA,MC}$ is varied from 0.01 to 0.07. The minimum and maximum $W_{NMDA,GC}$ and $W_{N,GC}$ are chosen such that the transition to the unsynchronized state, where the power is below the noise floor, happens near the midpoint on the

horizontal and vertical axes. This allows for a visual comparison of the two models, despite $W_{N,GC}$ being approximately 10^5 greater than $W_{NMDA,GC}$.

The frequency of both pure models decreases with increased $V_{rest,GC}$, as is evident when comparing the same points from low and high excitability conditions, and both models generate oscillations spanning the gamma to beta range. The power of the pure NMDA model is highest at low gamma frequencies (right panels Fig. 2.8A), and the gamma regime under high excitability is very narrow (bottom left panel Fig. 2.8A), much like in the full model (see Fig. 2.6D). The pure N-type model, on the other hand, generates peak power within the 20 – 30 Hz beta regime (outlined by red lines) and even for frequencies below the beta regime (Fig. 2.8B, bottom right panel). Why does the full model behave more like the pure NMDA model than the pure N-type model? One factor is the CDI of the N-type current by the NMDA Ca^{2+} current, which reduces the N-type current as NMDA current increases. Another factor is the balance of excitation and inhibition. In the pure N-type model there is a balance at beta frequencies, but in the pure NMDA model the balance is in the low gamma regime and the MCs in the beta regime are already over-inhibited. Therefore, when the two pure currents are combined, the MCs continue to be over-inhibited in the beta state and only the peak at low gamma power remains.

The maximum power of the ILFP oscillations generated by the pure NMDA model is much lower than the maximum power of the pure N-Type model (Fig. 2.8A.i, B.i). By systematically exploring parameters we found that the main cause for this difference is the difference in decay time constants of the two models. The

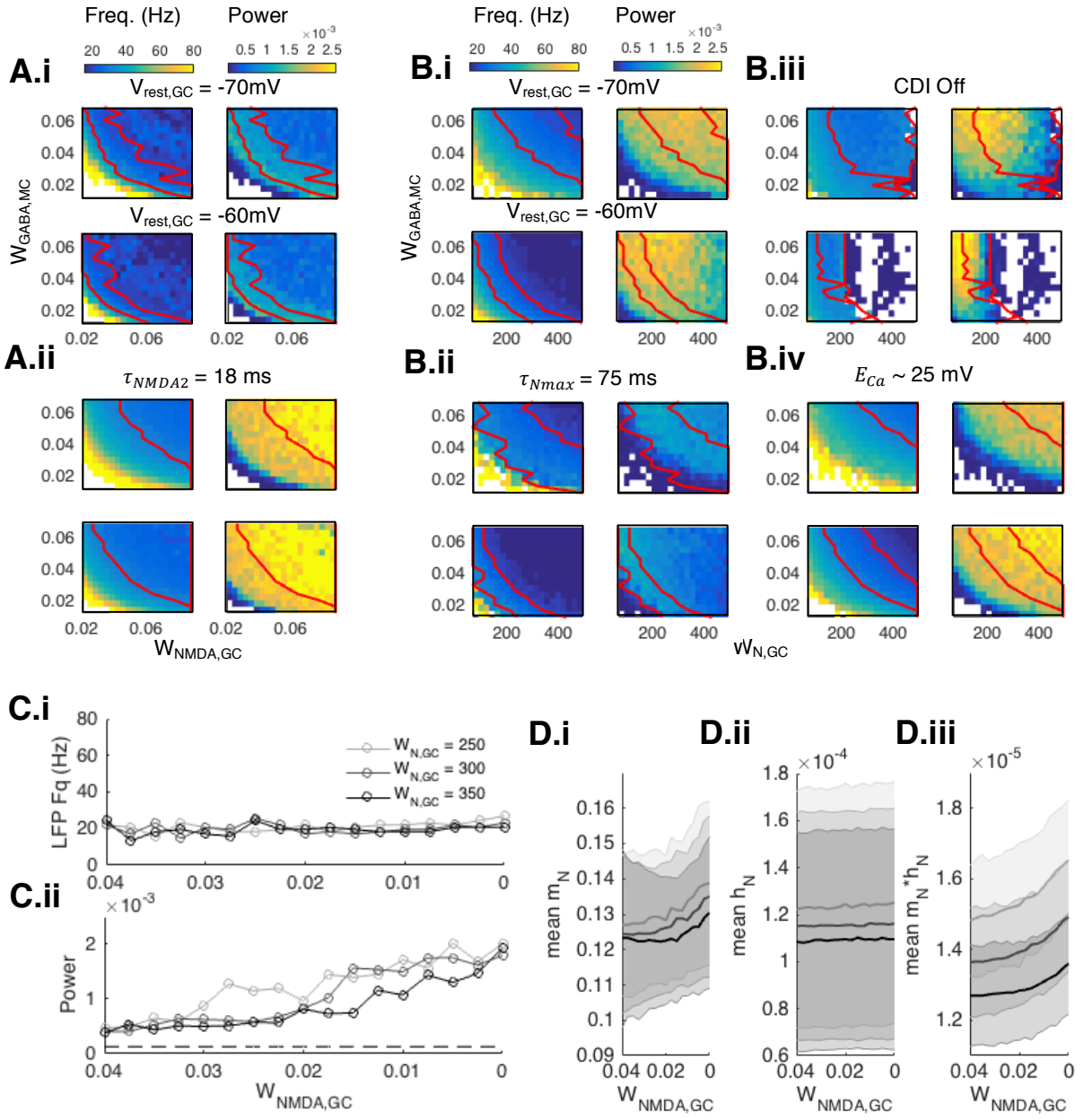

Figure 2.8. Parameter exploration of pure NMDA and N-type models. A: The ILFP frequency (left column) and power (right column) of the pure NMDA model are plotted with $V_{rest,GC}$ = -70 mV (top row) and $V_{rest,GC}$ = -60 mV (bottom row) as the MC inhibitory $W_{GABA,MC}$ and GC excitatory NMDA weights $W_{NMDA,GC}$ are varied. Red lines mark the borders of the beta regime (20-30 Hz). Regions where ILFP power is less than or equal to the baseline power are colored white. In **A.i** we simulated the default NMDA model with τ_{NMDA2} = 75 ms. In **A.ii** we switched the NMDA and N-type constants, so that τ_{NMDA2} = 18 ms. **B:** Same layout as **A**, but for the pure N-type model with τ_{NMDA2} = 18 ms (**B.i**, default N-type model), with τ_{NMDA2} = 75 ms (**B.ii**, switched decay time constant with NMDA model), without CDI (**B.iii**), and with N-type Nernst potential lowered to ~20 mV by reducing the external Ca^{2+} concentration (**B.iv**). **C.i:** A gradual NMDA block was simulated by reducing $W_{NMDA,GC}$ with GCDs fixed at $V_{rest,GC}$ = -60 mV. The maximum frequency during the gradual NMDA block is plotted for three values of $W_{N,GC}$, showing that beta frequency can be sustained by N-type currents as NMDA currents are reduced. **C.ii:** The maximum power of the same three curves increases as $W_{NMDA,GC}$ is decreased because the MCs are over inhibited when $W_{NMDA,GC}$ is maximum. **D.i:** The mean N-type activation (m_N) is shown for the same three curves in **C**. Because m_N is oscillatory we include the shaded regions to indicate the minimum and maximum extent of the oscillations. **D.ii:** Same as in **D.i**, but for N-type inactivation (h_N). **D.iii:** Same as in **D.i**, but for the product (m_N*h_N).

default decay times of the NMDA and N-type currents are τ_{NMDA2} = 75 ms and τ_{Nmax} = 18 ms. If we switch the values of the time constants we find that the pure NMDA power increases dramatically (Fig. 2.8A.ii), while the pure N-type power decreases to levels close to the original pure NMDA model (Fig. 2.8B.ii). The maximum power of the oscillations is inversely proportional to the decay time constant, because inhibitory current pulses with short decay times will decay fully each cycle, causing a high amplitude between peaks and troughs of the inhibitory current oscillation, but for longer decay times the pulses fall off more slowly and the difference between peaks and troughs is smaller. With a shorter decay time the pure NMDA model releases less GABA over time, so higher excitatory/inhibitory weights are required to sustain beta oscillations (note the shift of beta regime towards higher $W_{GABA,MC}$ and $W_{NMDA,GC}$ in Fig 2.8A.ii compared to Fig 2.8A.i). Interestingly, this shift towards higher weights is accompanied by a greater stability in both gamma and beta regimes. Furthermore, the maximum power is shifted into the beta regime, as was the case for the original pure N-type model (Fig. 2.8B.i). Therefore, the peak power at low gamma is not a specific consequence of the NMDA model, but a general consequence of a long time constant.

We explored the sensitivity of the N-type model's frequency and power landscapes to the absence of CDI. Removal of CDI results in dramatically higher graded inhibitory release probability (Fig. 2.3D), which causes the pure N-type model to be highly over-inhibited for large $W_{N,GC}$ in the high excitability condition (bottom panels Fig. 2.8B.iii). Curiously, the absence of CDI caused a broadening of the gamma and beta regimes under low excitability (bottom panels Fig. 2.8B.iii).

This shows that the N-type model has a substantial amount of self induced CDI, and that CDI prevents the inhibitory current from getting too large too quickly as excitability is increased.

We also explored the effect of changing the reversal potential on the frequency and power landscapes. Glutamate receptors such as AMPARs and NMDARs tend to have Nernst potentials near 0 mV, while VDCCs tend to have Nernst potentials at the Ca^{2+} reversal potential, E_{Ca}. In our model E_{Ca} oscillates with the network near 120 mV, because it is calculated on each time step, but its mean value is controlled by the extracellular Ca^{2+} concentration $[Ca]_{out}$ (see Eq. 2.3). When $[Ca]_{out}$ is reduced to 5 μM, the Nernst potential of E_{Ca} oscillates near $\sim$ 25 mV. This manipulation does not significantly alter the maximum power, but it shifts the beta regime of the pure N-type model towards higher weights (Fig 2.8B.iv). This is because a lower (positive) Ca^{2+} reversal potential causes the Ca^{2+} current to reverse more quickly, so that less inhibition is released over time and higher weights are needed to sustain beta oscillations. In contrast, we increased the NMDA reversal potential from 0 to 100 mV (not shown). This also had little effect on the ILFP power, but the beta regime was now shifted towards lower weights, as higher reversal potential allow more graded inhibition to be released.

Our models show that NMDARs or N-type VDCCs alone can mediate graded DDI, confirming what has been found empirically (Isaacson and Strowbridge, 1998; Schoppa et al., 1998a; Isaacson, 2001). Furthermore, they suggest that Ca^{2+} flow through N-type channels may be responsible for generating the high power beta oscillations we record in experiments (Fig. 1.4A) due to the shorter decay time of

the N-type current compared to the NMDA current. The parameter exploration in Figure 2.8A, B also shows that the gamma and beta regimes can always be reached by sufficiently increasing the excitatory/inhibitory weights. There can be multiple paths to generating beta as long as inhibitory current is sufficiently strong. This suggests that potentiation of the MC-GC synapse could lead to beta oscillations, although this is not explicitly modeled here.

We were curious to see how the network responds to a gradual block of the NMDA current, since infusion of pharmacological blockers *in vivo* likely results in only a partial block. Figure 2.8C shows the network response to decreasing $W_{NMDA,GC}$ under high GC excitability conditions ($V_{rest,GC}$ = -60 mV) for three different values of $W_{N,GC}$. For these simulations the MC inhibitory weight $W_{GABA,MC}$ was increased to 0.015 in order to maintain a strong inhibitory current when NMDA is completely removed. We point out that models with higher $W_{GABA,MC}$ still generate the full gamma to beta range (see Fig. 2.6B.i). With this arrangement, the beta frequency is quite stable with decreasing $W_{NMDA,GC}$ (Fig. 2.8C.ii). For the lowest $W_{N,GC}$ the LFP frequency rises out of the low gamma regime as $W_{NMDA,GC}$ approaches 0, but for higher $W_{N,GC}$ the frequency remains in the beta regime even when the NMDA current is completely blocked. Interestingly, the gradual reduction of NMDA current actually increases beta power (Fig. 2.8C.ii), because we are reducing the degree of MC over-inhibition. We saw a similar effect when reducing the fraction of excited GCs in Figure 2.5C.ii.

We also investigated the effect that the gradual NMDA block has on the inactivation of N-type current through CDI. Recall that the inactivation variable, h_N,

has an inverse dependence on internal [Ca^{2+}] (Table 2.1). We expected that a reduction in NMDA current would lower internal [Ca^{2+}], and therefore raise the overall N-type activation by raising h_N. As shown in Figure 2.8D.iii, the overall N-type activation does increase with decreased NMDA current, but not because of an increase in h_N, which is largely flat (Fig. 2.8D.ii). Instead, the voltage-dependent activation variable m_N, is responsible for the overall increased N-type activation, while h_N only reflects the background level of Ca^{2+} influx due to the increased excitatory weights $W_{N,GC}$. The reduction of MC over-inhibition results in more MC spikes, which drives higher GCD membrane depolarization through the AMPA current, thus raising m_N. The increased internal [Ca^{2+}] nearly balances the reduction of [Ca^{2+}] due to blocking the NMDA current, resulting in a nearly flat h_N. These simulated results provide a possible explanation for *in vivo* experiments which have shown that NMDA blockers have little effect on beta frequency (Fig. 3 in Lepousez & Lledo, 2013). Namely, blocking the NMDA current results in a higher activation of N-Type current through reducing MC over-inhibition, which keeps the beta frequency stable. However, there is only partial agreement with the model as these pharmacological experiments also found the beta power to be relatively unchanged while the beta power in the model is sensitive to NMDA current.

2.3.6 Beta frequency dependence on rise and fall time constants of Ca^{2+} currents

In this model the beta frequency emerges as a consequence of strong graded inhibition when the NMDAR and N-type channels are sufficiently activated under

high GC excitability conditions. In Figure 2.8 we showed that the beta regime shifted towards higher W when the decay time constants are decreased. In Figure 2.9 we explore the dependence of the model response on the time constants alone, holding everything else fixed. The literature reports a wide range of MC IPSC decay times, from about 50 ms to several hundred ms, which may reflect varying concentrations of Mg^{2+} at synaptic clefts as well as varying proportions of NMDARs and VDCCs expressed on individual GCDs (Isaacson and Strowbridge, 1998; Schoppa et al., 1998a; Isaacson, 2001; Urban and Sakmann, 2002). As described in the Methods, NMDA activation is governed by two time constants, the rise time τ_{NMDA1} and the decay time τ_{NMDA2}. For simulations in which τ_{NMDA1} is varied, τ_{NMDA2} is fixed at 75 ms (Fig. 2.9A.i, ii), and for simulations in which τ_{NMDA2} is varied, τ_{NMDA1} is fixed at 2 ms (Fig. 2.9A.iii, iv), which are the default values used throughout this work. The NMDA rise and decay times are close to those used in other models (Bathellier et al., 2006; de Almeida et al., 2013a). The N-type model only has one time constant, τ_N. Because τ_N itself is dependent on $V_{rest,GC}$ we vary its maximum value τ_{Nmax}. The default value of τ_{Nmax} = 18 ms is taken from Amini et al. (1999) and Zeng et al. (2009).

NMDA rise times as high as 10 ms have been reported in slice (Schoppa et al., 1998; Isaacson & Strowbridge, 1998). When the rise time τ_{NMDA1} of the pure NMDA model is increased, the LFP frequency is driven down (Fig. 2.9A.i). If the excitability is too low, the slower rise times generate a slower MC IPSC that fails to sufficiently inhibit the MC before a spike is elicited by the constant ORN stimulation. This prohibits MC synchronization, and the frequency shoots upwards while the power

falls to noise floor levels (Fig. 2.9A.ii). For sufficiently fast rise times (< 3 ms) the full gamma to beta range can be generated. Interestingly, longer rise times create higher power in the beta regime because the slower rise time increases the inhibition released over time. Increasing the decay time τ_{NMDA2} also decreases LFP frequency, but for short decay times (< 30 ms) beta oscillations cannot be sustained because the inhibition is not strong enough to sufficiently delay MC spikes (Fig. 2.9A.iii). As τ_{NMDA2} is increased, the LFP frequency in the high excitability condition enters the beta regime. The beta frequency becomes nearly stable after τ_{NMDA2} > 50 ms,

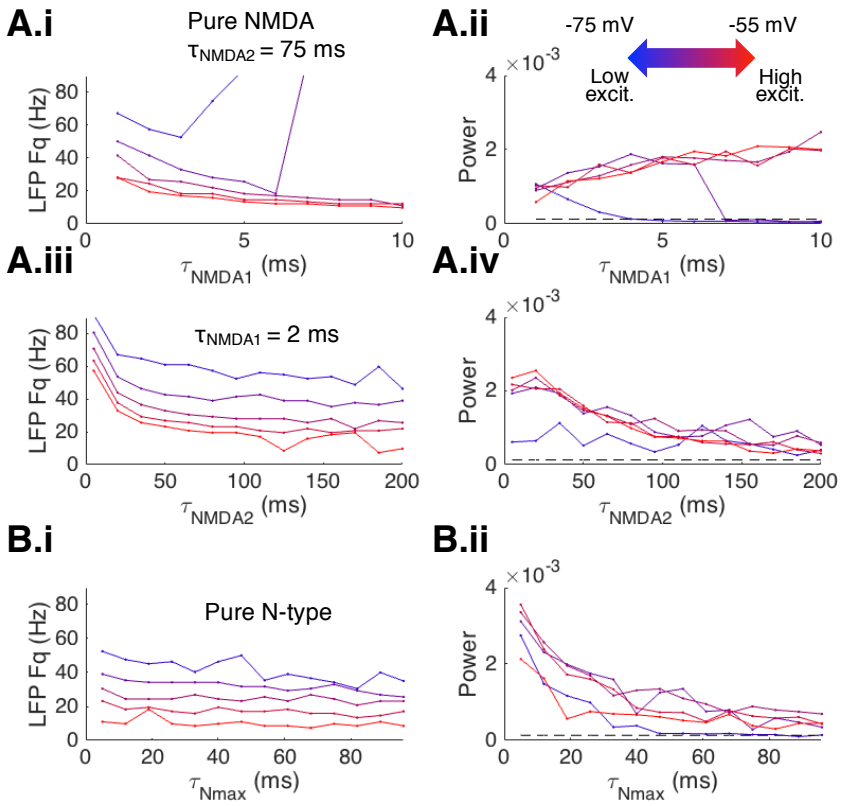

Figure 2.9 Network oscillation dependence on NMDA and N-type time constants . **A:** Dependence of the LFP frequency and power on rise time τ_{NMDA1} and decay time τ_{NMDA2} of the pure NMDA model. In **A.i** and **A.ii** τ_{NMDA2} is fixed at 75 ms. In **A.iii** and **A.iv** τ_{NMDA1} is fixed at 2 ms. **B:** Dependence of the LFP frequency and power on the N-type activation time constant maximum τ_{Nmax} of the pure N-type model. Each plot shows 20 curves calculated for uniformly spaced values of $V_{rest,GC}$ ranging from -75mV (blue) to -55mV (red), as indicated by the color scale.

because lengthening the tail of the inhibitory pulse decay does not significantly change the overall inhibition of MCs each cycle. Therefore, in the pure NMDA model the beta frequency only emerges if the decay time is long enough, but beta is not very sensitive to the exact value.

A slightly different picture arises for the pure N-type model ILFP oscillations; the frequency changes very gradually with a nearly constant slope over the entire range of decay times (Fig. 2.9B.i), and for higher excitabilities the frequency is nearly constant. The NMDA model only showed such constant frequency dependence for τ_{NMDA2} > 50 ms. This difference between the models is due to the absence of separate rise and fall times for the N-type model, which has a single, dynamic time constant that effectively produces rise and fall times that adapt to GC excitability conditions. Therefore, the frequency of pure N-type ILFP oscillations is much more sensitive to GC excitability and choice of inhibitory excitatory weights than to τ_{Nmax}. However, as was shown earlier in Figure 2.8B, the power is quite sensitive to τ_{Nmax} (Fig. 2.9B.ii). We find that both pure NMDA and pure N-type models are capable of generating beta oscillations when graded inhibition is sufficiently strong, but near their physiological parameter regimes the pure N-type model generates higher power beta oscillations that are more invariant to parameter changes.

2.4 Discussion

We demonstrate that GC excitability could play a pivotal role in regulating OB oscillations, thus closely linking ADPs and LLDs in GCs to beta generation. We hypothesized that GC excitability could control the strength of graded inhibition through NMDA and N-type Ca^{2+} currents, allowing MC-GC dendrodendritic synapses to support both gamma and beta oscillations. Our model generates LFP oscillations ranging from high gamma to beta by varying GC excitability over a range of ~15 mV. Gradual increases in GC excitability cause monotonic decreases in LFP frequency due to graded inhibitory release through activation of NMDA and N-type currents (Fig. 2.5). This contrasts with spiking inhibitory systems where increased interneuron excitability leads to increased firing rates and higher synchronization frequencies (Fisahn et al., 2004; Lakatos et al., 2005). Interestingly, beta power increased with smaller GCD populations (Fig. 2.5C), suggesting that high power beta oscillations may only recruit a subpopulation of GCs in high excitability states. Such subpopulations of excited GCs may arise from intrinsic individual GC differences in plateau currents (Egger et al., 2005a) and cortical/neuromodulatory inputs to GCs associated with odor selective MCs (Matsutani and Yamamoto, 2008).

GC excitability exerts control over LFP frequency by shifting the excitation-inhibition balance such that low GC excitability induces over-excitation and high GC excitability induces over-inhibition (Fig. 2.4B). With intermediate GC excitability all the MCs fire at low gamma frequencies (Fig. 2.4, 2.5), reminiscent of type 2 gamma (35-65 Hz) oscillations which have high coherence across the OB and PC *in vivo* (Kay, 2003; Lepousez & Lledo, 2013). We found that maximum power at low gamma

frequencies was primarily due to the long NMDA decay times (Fig. 2.8A). Interestingly, high power low frequency gamma oscillations are routinely seen in slice (Friedman and Strowbridge, 2003; Bathellier et al., 2006; Gire & Schoppa, 2008) where Mg^{2+} concentrations are often low and NMDA currents may contribute more to DDI than they do *in vivo*. A more realistic fast change in GC excitability drives a transition from high gamma to beta, skipping the low gamma regime (Fig. 2.7). A change in GC excitability as slow as 100 ms can produce a sudden switch from gamma to beta frequencies, rather than a gradual shift.

In a pure N-type model, the maximum power is in the beta band and is much higher than the pure NMDA due to its shorter decay time (Fig. 2.8B), suggesting that high power beta oscillations (Fig. 1.4A) triggered by high volatility odors (Lowry and Kay, 2007a) and learning (Ravel et al., 2003; Martin et al., 2006a) may depend on VDCCs more than NMDA currents. Starting with both NMDA and N-type currents, we showed that beta oscillations can be sustained as NMDA is blocked (Fig. 2.8C), in agreement with past experiments (Fig. 3 in Lepousez & Lledo, 2013). Comparison of LFP power between models and experiments should be done with care because our simple model is only a caricature of the LFP, and experimentally recorded LFPs can vary in amplitude depending on electrode position and placement. Because we assume that the same synaptic currents produce both gamma and beta oscillations, we compare the relative size of the beta and gamma oscillations in the model as we do in experiment.

In the full model we found that beta frequencies are more stable than gamma with respect to MC inhibitory and excitatory weights (Fig. 2.6), but beta power

increased dramatically with MC excitatory weight (Fig. 2.6A). If high volatility odorants represent stronger inputs, this may explain the high power beta oscillations produced by these odors (Lowry and Kay, 2007a). In the pure NMDA and N-type models the beta regime became more stable as their excitatory synaptic decay times were shortened (Fig. 2.8). We found that CDI is critical to maintaining beta oscillations in the high excitability of the pure N-type model, since without CDI the MCs became over-inhibited. Finally, long decay times are critical to sustaining beta oscillations in the pure NMDA model, but not the pure N-type model (Fig. 2.9). Together these results argue that the odor-evoked gamma to beta transition could be triggered by an increase in GC excitability, which drives an increase in VDCC-mediated graded inhibition.

2.4.1 Multiple factors may contribute to odor-evoked gamma to beta transition

Our model shows that increased GC excitability can drive beta oscillations, but it is agnostic as to which inputs control GC excitability. Because GC excitability is regulated by centrifugal, neuromodulatory, and local inputs, beta oscillations may be supported by a convergence of inputs onto GCs, which we summarize in Figure 2.10. For example, cholinergic inputs could transform the AHP current to an ADP current (Pressler et al., 2007a) so that cortical inputs could trigger excitability increases in GCs and hence generate odor-evoked beta oscillations. This could potentially explain why beta oscillations are dependent on such varied

circumstances as stimulus characteristics, the state of the animal, and behavioral context (Martin et al., 2006; Lowry & Kay, 2007; Cenier et al., 2008, 2009). Because many factors influence the strength of inhibition, such as the inhibitory/excitatory weights and even the external Ca^{2+} concentration (Fig. 2.8), our model argues that there can be multiple paths to generating beta oscillations, as long as there is sufficiently strong inhibition.

Respiration may also influence beta generation (Fig. 2.10). Fast airflow during inhalation coincides with gamma oscillations and decreased airflow during

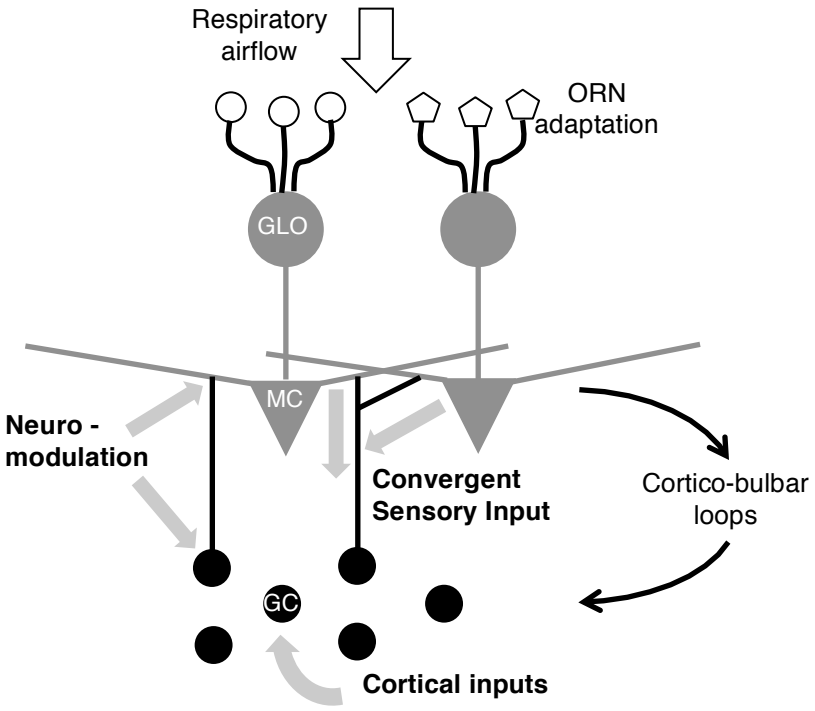

Figure 2.10. Summary of possible factors contributing to the gamma to beta transition. Those that explicitly control GC excitability are marked in bold with gray arrows. GC excitability can be regulated by at least three distinct inputs to GCs, all of which may cooperate in the generation of beta oscillations. Neuromodulatory fibers may target the soma and GC dendritic arbors and gate excitatory inputs from MCs and cortical neurons. Our model summarizes these different sources of GC excitability control by a single parameter, the GC resting potential, to show that GC excitability has a direct influence on the LFP frequency. However, our model does not include respiratory modulation, ORN adaptation, and cortico-bulbar loops, which may also contribute to beta generation.

exhalation coincides with beta oscillations in urethane-anesthetized rats (Cenier et al., 2008, 2009; Fourcaud-Trocmé et al., 2011). Waking rats also slow their respiration during late odor sampling when beta emerges (Rojas-Líbano & Kay, 2012).

The gamma to beta sequence recorded in rats resembles the transition from fast to slow oscillations detected in moth olfactory LFPs associated with firing rate adaptation of peripheral ORNs (Ito et al., 2009). Firing rate adaption also occurs in rat and amphibian ORNs (Laing & MacKay-Sim, 1975; Kurahashi & Menini, 1997; Zufall, 2000). It is possible that ORN firing rate adaptation plays a role in the gamma to beta transition in rats (Fig. 2.10).

2.4.2 Comparison with other theories of olfactory beta generation

Beta oscillations are highly coherent between the OB and PC, and it has been proposed that beta oscillations may be generated by long distance action potential propagation within the loop encompassing MCs, PC pyramidal neurons, and GCs (Neville and Haberly, 2003a; Martin et al., 2006a). However, PC pyramidal neurons also target deep short axon cells which strongly inhibit GCs (Boyd et al., 2012). Furthermore, beta oscillations are also coherent between the OB and the entorhinal cortex and hippocampus (Gourévitch et al., 2010; Kay & Beshel, 2010; Martin et al., 2007), so it is unclear which of these loops would be responsible for beta. Our model generates beta oscillations intrinsically in the OB and relies on centrifugal innervation solely for the regulation of GC excitability, reminiscent of the role that OB input to PC plays in the generating PC oscillations (Freeman, 1968a). The model

predicts beta band directional influence from the OB to other cortical areas as we have shown experimentally (Gourévitch et al., 2010; Kay & Beshel, 2010). Nonetheless, it is possible that a combination of GC excitability regulation and long distance action potential propagation stabilizes the beta frequency.

To our knowledge there are only two other computational models of OB beta (Fourcaud-Trocmé et al., 2011b; David et al., 2015a). Both of these models, like ours, infer that the mutual exclusivity of gamma and beta oscillations suggests a common mechanism, namely the ionic currents at the dendrodendritic MC-GC synapses. The Fourcaud-Trocmé et al. model also uses graded inhibition, but argues that the critical parameter in switching from gamma to beta is the excitatory synaptic conductance to the MCs. The David *et al*. model argues that the switch between gamma and beta depends on non-spiking (graded) and spiking states of the GCs respectively. Our model is closer to the David *et al*. model in spirit as both models assume a switch in the state of the GCs. Although experiments have shown that the majority of DDI is mediated by Ca^{2+} currents through NMDARs and VDCCs (Isaacson and Strowbridge, 1998; Schoppa et al., 1998a; Chen et al., 2000), neither of the other models include Ca^{2+} currents, which are essential to beta generation in our model.

Differences between modeling approaches are to some extent motivated by differences in experimental data. While the other models aim to reproduce experimental data showing gamma to beta transitions within a single sniff in anesthetized rats (Cenier et al., 2009), we reproduce high power beta epochs lasting several sniffs that occur during both learning and passive exposure to high volatility odorants (Fig.1.4A). These models together suggest that beta oscillations arise from

an appropriate convergence of sensory stimulation and centrifugal feedback onto GCs.

Recent current source density analysis has suggested that gamma and beta are generated by distinct sublaminar networks within the EPL (Fourcaud-Trocmé et al., 2014). Distinct sublaminar networks are compatible with our GC excitability-based hypothesis, because different sublaminae may represent distinct developmental stages of GCs with different excitability characteristics (Lepousez et al., 2013; Petreanu & Alvarez-Buylla, 2002).

2.4.3 Limitations of the model

Every model must trade off simplicity with accuracy. We used a standard NMDA current model (Jahr and Stevens, 1990), which does not include CDI, but NMDA channels can also exhibit CDI (Legendre et al., 1993; Zhang et al., 1998), which could dynamically compete with VDCC currents. Our model also excludes the GC soma and relies on graded inhibition alone. However, somatic spikes could propagate through the entire dendritic arbor of a GC to trigger global lateral inhibition of MCs (Mouret et al., 2009a). We do not include this in our model, because it would require simulating bidirectional conductance along GC primary dendrites, the properties of which are still being studied (Egger et al., 2005a; Balu et al., 2007). Nonetheless, our model implicitly depends on GC spikes, because spikes trigger the ADP (Pressler et al., 2007a) or LLD (Egger, 2008a) that provides the mechanism for transition between gamma and beta oscillations. Although GC spikes

have recently been recorded for the first time in awake animals (Cazakoff et al., 2014), they have yet to be recorded during beta oscillations.

Our GCDs are modeled as single compartments, but recent experiments have shown that GC dendritic spines can independently support Na^+ spike generation (Bywalez et al., 2015) and that locally produced Ca^{2+} spikes mediated by T-type VDCCs can spread activity across the entire dendritic arbor to synchronize GABA release from all the dendritic spines of a given GC cell (Egger et al., 2005a). Our model does not capture this fine-grained activity because we aimed to model population activity. However, it remains an interesting and open question how this fine-grained activity influences population activity.

3. Pharmacological manipulation of olfactory bulb granule cell excitability modulates beta oscillations: Testing a model

3.1 Introduction

3.1.1 Model Predictions

In a Chapter 2, I introduced a model that addressed the role of granule cell (GC) excitability in generating beta oscillations (Osinski and Kay, 2016). This model was inspired by three lines of evidence: (1) Beta oscillations cannot be generated without intact centrifugal input to the OB (Fig. 1.4E; Neville and Haberly, 2003; Martin et al., 2006); (2) centrifugal input largely targets the GC layer and synapses onto GCs are perisomatic (Fig 3.1A; Mouret et al. 2009, but see Illig, 2011); (3) GCs can undergo at least two types of long lasting afterdepolarizations, one dependent on GC muscarinic receptor activation (Castillo et al., 1999; Pressler et al., 2007b) and the other on an appropriate convergence of mitral cell (feedforward) and cortical (feedback) inputs onto GCs (Egger et al., 2005b). Another model also predicted that OB beta oscillations can only occur when GCs are in high states of excitability and relied on spiking GCs (David et al., 2015b). Some studies have shown that GCs spike rarely and can release GABA in a graded fashion at the dendrodendritic reciprocal synapse (Schoppa et al., 1998b; Cang and Isaacson, 2003b). We therefore interpreted excitability not as a tendency to spike but rather a tendency to drive graded inhibition (model summarized in Figure 3.1).

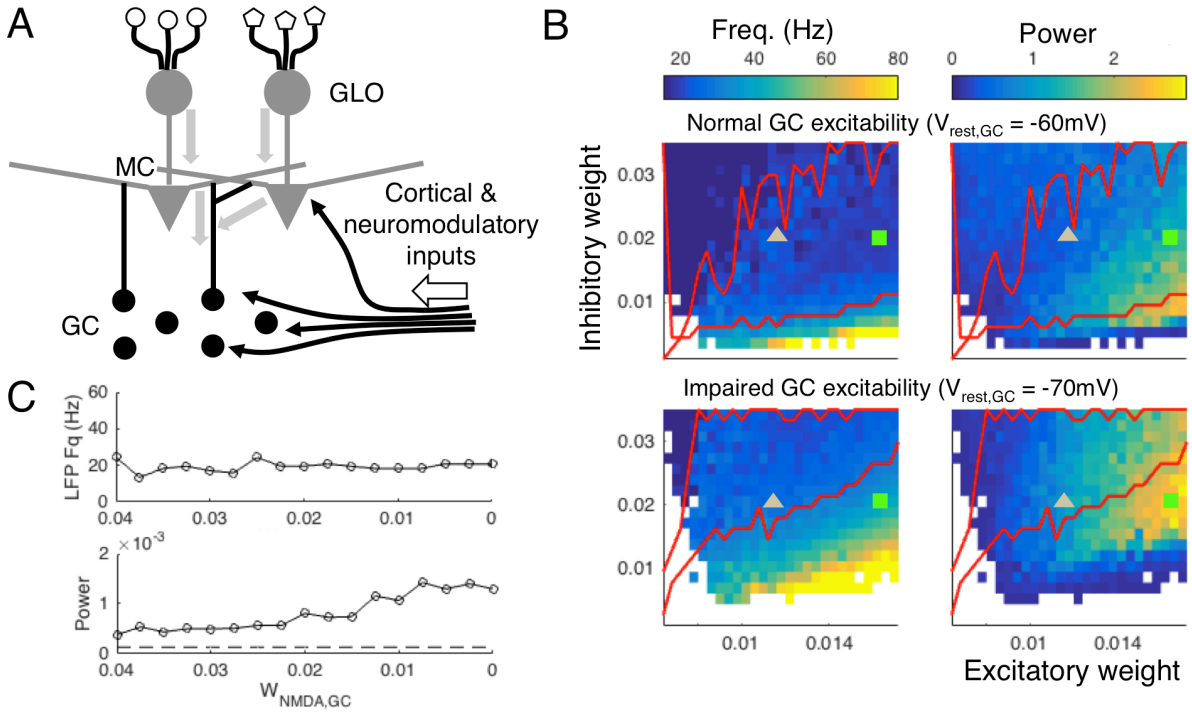

Figure 3.1. Modeling predictions. A: Schematic of olfactory bulb circuitry. Glomeruli (GLO) innervated by unique receptors receive sensory inputs which are conveyed to mitral cells (MCs). Sensory (thick gray arrows) and cortical/neuromodulatory feedback (thin black arrows) both converge onto granule cells (GCs). **B:** Modeling results (Osinski and Kay, 2016) showing odor-induced LFP power and frequency landscapes under normal (top) and impaired (bottom) GC excitability conditions. The y-axis is inhibitory weight, which represents the strength of inhibition from GCs to MCs, and the x-axis shows excitatory weight, which represents the strength of sensory input to MCs. The boundary of the beta regime (20 – 30 Hz) is drawn in red. White regions had power less than or equal to the noise floor, which was defined as the maximum power of the residual oscillation due to common inputs to MCs when inhibition is removed. The MC stimulation due to strong (high volatility) and weak (low volatility) odorant stimuli at constant inhibitory weight are marked by a green square and gray triangle, respectively. In the normal condition (top) the evoked beta frequency is fairly stable with respect to sensory input strength and both low (gray triangle) and high (green square) volatility odorants induce beta oscillations. In the impaired condition (bottom) the GC resting potential ($V_{rest,GC}$ in the model) remains at -70 mV, and the evoked beta frequency is less stable over the same range of inputs. In this condition, the high volatility odorant (green square) generates high power low gamma oscillations, while the low volatility odorant (gray triangle) induces higher power beta oscillations that it did in the normal condition. **C:** (Top) Beta oscillation frequency remains stable as the strength of the NMDA current from GC to MC ($W_{NMDA,GC}$ in the model) is gradually reduced to 0, because they are sustained by the N-type voltage gated channel current. (Bottom) In this particular simulation, the LFP power increases as NMDA is reduced because the system is over-inhibited for high values of $W_{NMDA,GC}$. The dashed line indicates power of the noise floor due to common excitation without inhibition. (Figures adapted and edited from Osinski and Kay (2016), with permission.)

The model predicted that GC excitability influences the stability of OB LFP oscillation frequency. Beta oscillations were generated over a wide range of parameters when GCs were in a high state of excitability, providing sustained graded inhibition onto MCs. Decreasing GC excitability destabilized the LFP frequency, such that stronger stimuli would drive oscillations out of the beta regime, while weaker stimuli could actually induce higher power beta. The bi-directional effect on beta oscillation power was a consequence of shifting the balance of excitation and inhibition onto MCs. This is illustrated in Figure 3.1B, which shows the range of LFP frequencies generated by the simulated MC-GC dendrodendritic network as a function of sensory input to MCs and strength of GC-MC inhibition in normal and impaired GC excitability conditions. Two points illustrate the predicted effects of low volatility (weak odor, low excitatory weight) and high volatility (strong odor, high excitatory weight) odorants on the LFP under these two conditions. Under normal conditions, a high volatility odorant (green square) induces beta oscillations with relatively high power, and a low volatility odorant (gray triangle) induces lower power beta oscillations (Figure 3.1,B top). Under impaired GC excitability conditions, the strong odorant induces high power low gamma frequency oscillations instead of beta oscillations (Figure 3.1,B bottom). Conversely, the weak odorant induces higher power beta oscillations than it did under normal GC excitability. Thus, the model predicts that for strong odors, a drug that lowers GC excitability should attenuate the power of beta oscillations, but for weak odors the same drug should enhance the evoked beta oscillations.

Our model also predicted which channels and currents maintain beta vs. gamma oscillations. Beta oscillations could be sustained in the model by graded inhibitory currents, mediated primarily by voltage-dependent calcium channels (VDCCs), even when NMDA currents were blocked (Figure 3.1C). Gamma oscillations, however, could not be maintained in the model without intact NMDARs, which matched results showing that APV, an NMDAR antagonist, blocks gamma oscillations in the OB of waking mice (Lepousez and Lledo, 2013b).

3.1.2 Overview of pharmacological experiments

We tested the predictions of our model experimentally by infusing drugs into the OB that modulate GC excitability in several ways. Muscarinic receptors are found in high density in the EPL, where GCs synapse onto MC lateral dendrites and at moderate densities in the GC layer (Fonseca et al., 1991; Lein et al., 2007). Muscarinic receptor agonists can both inhibit or excite GCs by differential activation of M1 or M2 receptors (Castillo et al., 1999; Mandairon et al., 2006; Smith and Araneda, 2010; Li and Cleland, 2013) and can influence their excitability by modulating afterdepolarization (Nickell and Shipley, 1993; Pressler et al., 2007b). When we infused scopolamine, a muscarinic antagonist, into the ventromedial OB prior to an odor sampling session, beta oscillations were decreased in response to a high volatility odorant and increased in response to a low volatility odorant. Furthermore, we found that infusion of APV, an NMDAR antagonist, suppressed gamma but not beta oscillations. Both of these results align well with the model's predictions. Injection of oxotremorine, a muscarinic agonist produced more variable

results, but in some rats we observed a tendency for OB gamma and beta to be suppressed, possibly due to over-inhibition. Although beta oscillations require intact connections between OB and PC (Neville and Haberly, 2003b; Martin et al., 2006b), we found that PC beta oscillations show a degree of independence in power, and coherence between the OB and PC is relatively unaffected by decreasing beta in the OB. Together, these results confirm our model predictions and reveal a more nuanced picture of the generation of beta oscillations in the olfactory system than was previously understood.

3.2 Methods

Subjects were 8 adult male Sprague-Dawley rats (350 - 450 g; purchased from Envigo (Harlan)), maintained in the colony room on a 14 –10 h light/dark schedule (lights on at 08:00 CST). Two rats were used for pilot studies to determine drug dosages. Six rats were used for the data as reported. Rats were housed singly after electrode implantation and had access to unlimited food and water for the course of the experiments. All animal procedures were done with approval and oversight by the University of Chicago Animal Care and Use Committee with strict adherence to AAALAC standards.

3.2.1 Electrode implants

Before each surgery, rats were given a subcutaneous injection of ketamine cocktail (35 mg/kg ketamine, 5 mg/kg xylazine, and 0.75 mg/kg acepromazine).

Anesthesia was maintained by checking for reflexes every 15 min and administering intraperitoneal injections of ketamine. Bipolar stainless steel formvar insulated electrodes (100 μm wire; ~1 mm vertical tip separation) were placed in the left anterior OB (8.9 mm anterior to bregma, 1.5 mm lateral, average depth 3 mm), left aPC (0.5 mm anterior to bregma, 3.0 mm lateral, 15° angle, average depth 8 mm), and right ventromedial OB (8.5 mm anterior to bregma, 1.5 mm lateral, average depth 4 mm) as shown in Figure 2A. A cannula guide (Plastics One C315, 26 gauge, 5 mm guide with 0.75 mm internal injection cannula projection) with two stainless steel electrodes attached on either side of the shaft was implanted in the left ventromedial OB (8.2 mm anterior to bregma, 1.5 mm lateral, average depth 2.5 mm). Bipolar electrodes were vertically positioned across the ventral mitral cell layer in the OB and across the layer 2/3 pyramidal cell layer in the aPC by orienting the electrode perpendicular to the cell layer and lowering it until the LFP was reversed across the two leads of the bipolar electrode. The cannula was inserted into the GCL by observing a reduction in the amplitude of the LFP after lowering past the dorsal mitral cell layer. Internal cannula depths determined *post mortem* are shown in Figure 2D. Reference and ground wires attached to stainless steel screws were secured to the skull over the left cerebellum and right occipital lobe respectively (see REF & GND Fig. 2A). Additional screws were used for securing the headstage to the skull. Connector pins for each lead were inserted into a round plastic receptacle (Ginder Scientific, Ottawa, Canada), and the assembly was embedded in dental acrylic (See Fig. 3.2E). Rats were allowed to recover for 2 weeks after surgery before beginning the experimental protocol.

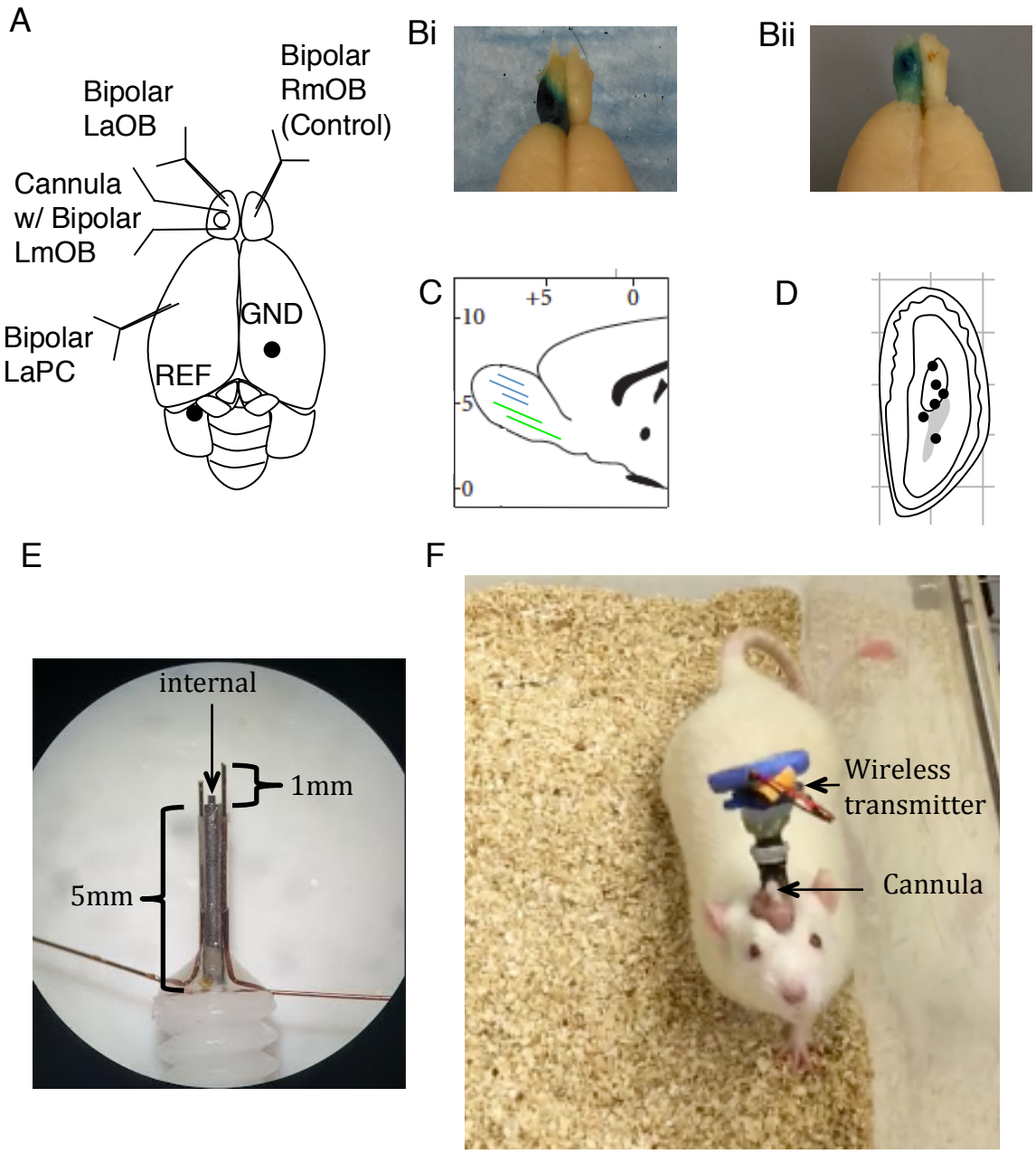

Figure 3.2. Electrode placement and drug spread. A: Schematic showing electrode and cannula placements. **B:** Two representative examples showing spread of methylene blue dye (injected just before perfusion) localized to the left OB. **C:** Schematic sagittal slice showing approximate anterior-posterior spread of drug (blue lines) as determined by spread of methylene blue dye. (The two green lines correspond to the two rats with large contralateral scopolamine effects whose means are colored green in Figure 6C.) **D:** Schematic coronal section of LmOB showing approximate internal cannula tip depths determined via Prussian Blue reaction. **E:** Close-up of of cannula guide, internal cannula projection, and cannula electrodes. **F:** Fully recovered rat with wireless transmitter plugged into implant. A metal collar is tightened to ensure a firm connection. A battery is taped to the top of the wireless transmitter. The cannula cap is indicated.

3.2.2 Verification of electrode placements and drug spread

After experiments were complete, rats were deeply anesthetized with a euthanizing dose of Urethane (1g/kg), and methylene blue dye was injected into the cannula at the same rate and volume used for drugs during experiments (4 μL, at 1 μL/min). Dye could not be injected into one rat due to cannula blockage. Current was passed between each electrode and the ground screw, thus depositing iron residue at the tips of the stainless steel wires. The brain was fixed via intracardial perfusion, and electrode tips were marked using the Prussian Blue reaction. Prior to sectioning, brains were extracted from the skull, the electrode array was removed, and the brains were sunk in 30% sucrose (0.1 M phosphate buffered formal saline) for two days and then flash frozen in isopentane cooled to -40deg. OB cannula placements were confirmed by visual examination of coronal slices showing electrode tracks and the blue stain marking the electrode tips (Fig. 3.2D). The spread of methylene blue dye across rats is shown in in Fig. 3.2B,C.

3.2.3 Drugs and dosages

We used three drugs in this study: scopolamine (Sigma Aldrich, MW 339.81g/mol), oxotremorine (Sigma Aldrich, MW 322.19 g/mol), and APV (Sigma Aldrich, 197.13 g/mol). We ran pilot experiments on 2 rats (not including the 6 rats used for the study) to determine the appropriate dose of these drugs. For our initial choice of Scopolamine dose we followed (Mandairon et al., 2006), who used a low concentration of 7 mM and a high concentration of 38 mM. In our pilot experiments,

we found no effect of low concentration on beta power and small effects at the higher dose. We found that a slight increase to 50 mM produced much stronger effects. In this study we refer to 38mM as the low concentration and 50mM as the high concentration. We did not use the 7 mM dose, because we wanted to limit the number of drug conditions planned for each subject. For APV we tried to follow Leposez & Lledo (2013) who infused 0.25 mM and 1 mM for high and low concentrations. However, both of these doses caused seizures in our rats. We found that 100 μM was a safe dose that still produced significant effects. For oxotremorine, we followed Bendahmane et al. (2016) and Smith et al. (2015) who used 10 μM and 30 μM doses. No significant effects were seen at 10 μM, but 30 μM produced strong effects (though they were not always consistent, see Results). Higher concentrations tended to induce seizures.

Initially, we intended to use low and high doses of each drug, but because oxotremorine and APV produced seizures at higher doses and showed little effect at lower doses in our pilot study, and the need to limit the number of infusions for each subject, we only used low doses of oxotremorine and APV for this study. There were no seizures induced by scopolamine in our pilot rats, even at concentrations higher than those used in the present study.

3.2.4 Experimental design

After full recovery from surgery, rats were habituated to odors for one day before the start of experiments to eliminate novelty effects. Drugs were freshly mixed immediately before each experiment. At the start of the experiment, rats

were plugged into a Multichannel Systems wireless transmitter headstage (W16-HS) and then placed in a clean polycarbonate cage with fresh bedding. A battery to power the headstage was taped to the top of the assembly as shown in Figure 3.2E. Each experiment started with 5 minutes of free behavior recording to obtain a baseline LFP used to normalize the odor evoked gamma and beta oscillations. Afterwards, 4 μL of drug or saline was infused into the left OB at a rate of 1 μL/min. If the cannula was clogged, then 2 μL of saline was carefully injected by hand to clear the blockage. In some cases the cannula became permanently clogged (possibly due to scar tissue and glial cell buildup) and no further sessions could be run, resulting in partial data for those subjects. A control session with saline injection was performed after every two drug sessions to track any systematic changes in the LFP from day to day. The order of drug sessions was balanced across rats.

Drug effects often started immediately after or even during the infusion (Fig. 3.3C), so we began odor presentations immediately after infusion. Two odorants were used in this study, Ethyl-2-methylbutyrate (EMB, Sigma Aldrich) and Geraniol (GER, Sigma Aldrich). EMB has a high volatility (theoretical vapor pressure-VP- at 25^{o} C of 7.86 mm Hg) and elicits high amplitude beta oscillations, while GER has a low volatility (VP 0.0133 mm Hg) and elicits smaller beta oscillations (Lowry and Kay, 2007b). Odors were presented in blocks of 24 trials with ~20 s between trials (total 48 trials). These odor blocks spanned the two phases of an apparent biphasic scopolamine effect (see Figs 3.3 & 3.4). For each trial, an odor soaked cotton swab was held under the rat's nose for two or three sniffs (as judged by the presenter). In two of the rats, we also used an interleaved odor presentation design, where EMB

and GER were alternated on each presentation for a total of 48 trials, producing 12 trials of a given odor for each half of the experiment. Interleaving the odor presentations did not change the main results of the experiment. The drug and odor order were balanced across all 6 rats. The timeline of the odor block presentation experiment is depicted in Figure 3.4B.

3.2.5 Electrophysiology

All data were recorded wirelessly using Multichannel Systems 32-channel basic wireless recording system, using a 16-channel headstage (W16-HS) with a digital sampling rate of 2 kHz. To power the headstage a small battery was secured to the top of the assembly with tape as shown in Figure 3.2E. Each lead was recorded with reference to a skull screw above the left cerebellum (see REF in Fig. 3.2A). A ground screw was placed over the right posterior cortex. Approximate odor onset times were recorded with a 5V TTL pulse triggered by the experimenter pressing a button just before the rat took its first sniff. Brain signals and events were recorded with MC Rack software (http://www.multichannelsystems.com/downloads/software).

3.2.6 Spectral analysis

For each rat, we assessed the quality of signals from the two leads from each brain area. We chose the lead with the cleanest signals and most prominent beta oscillations from each pair and used this lead for analysis across the entire set of experiments. All analysis was performed in MATLAB® R2015b. We filtered out

movement artifact (MATLAB 'designfilt' function using 'lowpassfir' with pass 4Hz, stop 8Hz, then applied with the filtfilt function) and subtracted it from the original data. We found that finite impulse response filters produced less prominent edge effects than infinite impulse response. We then extracted the odor presentation trials from the continuous LFP trace in 4-second windows starting from the button press at the start of each trial. We calculated power spectra for each trial using the multitaper method implemented in the Chronux version 2.11 toolbox for MATLAB (Bokil et al., 2010b), with a time-half-bandwidth of 2 and 3 tapers over a frequency range of 1 Hz to 100 Hz. This method multiplies each LFP trace with a series of tapers (Slepian sequences) and then averages them, which has the effect reducing spurious noise contributions. The Slepian sequences also possess desirable spectral concentration properties, which produce a more accurate measure of the underlying power spectrum (Bokil et al., 2010b). We divided the LFP power spectra into three bands: beta (15 – 30 Hz), low gamma (40 – 60 Hz), and high gamma (60 – 100 Hz). We discarded the first 4 trials of each 24 trial odor block, because beta often only comes on after the 3rd or 4th odor presentation, consistent with findings in Lowry and Kay (2007). We then averaged the power in each frequency band across the remaining 20 trials, and report the peak beta band power from the averaged power spectra.

To calculate coherence between OB and PC signals we used the coherencyc function in the Chronux toolbox. This function applies a multitaper coherence calculation to the entire 4s odor period for each trial and then averages across trials. We used 9 tapers with a time-half bandwidth of 5. We then applied Fisher's Z

transform of the coherence (Kay and Freeman, 1998; Kay and Beshel, 2010b), defined as $\tanh^{-1}$(coherence), to distribute the values from zero to infinity instead of zero to one.

3.2.7 Double normalization of power spectra

The LFP amplitudes differed across subjects and days, primarily due to differences in electrode placement and condition across subjects, electrode drift within subjects, and effects of repeated infusions. Normalizing the LFP power during odor presentations by baseline power alone was not sufficient to put the power values of different rats on the same scale for meaningful statistical comparisons, because different rats may show different degrees of odor-evoked oscillatory power increase even under normal conditions. These differences are often due to differences in electrode placement or quality. Therefore, we also compare the relative odor-evoked power changes under drug vs. saline conditions. Thus, we normalized each power spectrum first by the power in the 5 min baseline before the infusion and then by the power during odor presentations in the most recent saline session. The power in the 5 min baseline period was determined by dividing it into 4 s long non-overlapping windows and averaging the power of all these windows. Using the same length windows as for odor presentation ensured that the baseline spectrum had the same frequency resolution as the power of the odor presentation trials. Windows with significant movement artifacts were discarded. The saline sessions were also normalized by their baselines before being used as normalizations for the drug sessions.

3.2.8 Statistical methods

5-way unbalanced ANOVA was conducted for scopolamine and oxotremorine sessions separately using the MATLAB anovan function. Factors were subject, saline/drug, odor identity, odor block, and frequency band. For APV sessions we conducted a 4-way ANOVA, because odor blocks were combined for analysis of these sessions. An unbalanced design was used because some rats had missing sessions, either due to the cannula becoming permanently blocked or a drug causing seizures even at lower doses (these data were excluded). In addition, in some cases there were different numbers of repetitions (uniform odor blocks had rep = 20, interleaved odor blocks had rep = 10, after excluding the first 4 trials in each block).

When ANOVAs were significant, we performed post-hoc t-tests between each saline and drug pair using the mean for each rat. There were 2 (odors) x 2 (odor blocks) x 3 (frequency ranges) = 12 comparisons for each drug, giving us a Bonferroni correction factor of 12, and setting the significance threshold at $p < 0.05/12 \approx 0.004$. (For APV, we found no differences across odor blocks, so the trials were treated as a single block, with the number of comparisons reduced to 6, $p < 0.008$. See *Results- Effects of drugs on baseline LFP*.) Throughout the paper we present the data in violin plots (using MATLAB File Exchange function violin.m), which show a smoothed probability density distribution (using a Gaussian kernel) of the normalized power in beta, low gamma, and high gamma frequency bands averaged across all rats.

3.3 Results of pharmacological experiments

We designed the experiments to test the hypothesis that manipulating GC excitability would affect the amplitude of beta oscillations as predicted by our model (Fig. 3.1). Two drugs, scopolamine and oxotremorine, tested the effects of GC modulation by the muscarinic ACh receptor. A third drug, APV, tested our model's prediction that blocking NMDA receptors would decrease gamma but not beta oscillations.

3.3.1 Effects of drugs on baseline LFP

We timed odorant presentation to occur within the duration of the drug effects. To measure the duration of the drug effects, we recorded LFPs from 3 rats for 45 min after infusion without any odor presentations. Representative effects on the left medial OB (where the drug was infused) and right medial OB (a control) of a single rat are shown in Fig. 3.3A,B (end of infusion marked by vertical dashed line). To visualize the average effect we aligned the LFPs of each session to the end of infusion time, and averaged the 40 – 80 Hz gamma band power across subjects (Fig. 3.3C, gray traces). All three drugs typically began to take effect during infusion. APV (100 μM) had a highly consistent effect in every session, nearly abolishing gamma for over 20 minutes post infusion (Fig. 3.3Ciii). The muscarinic drugs, however, had more complex effects.

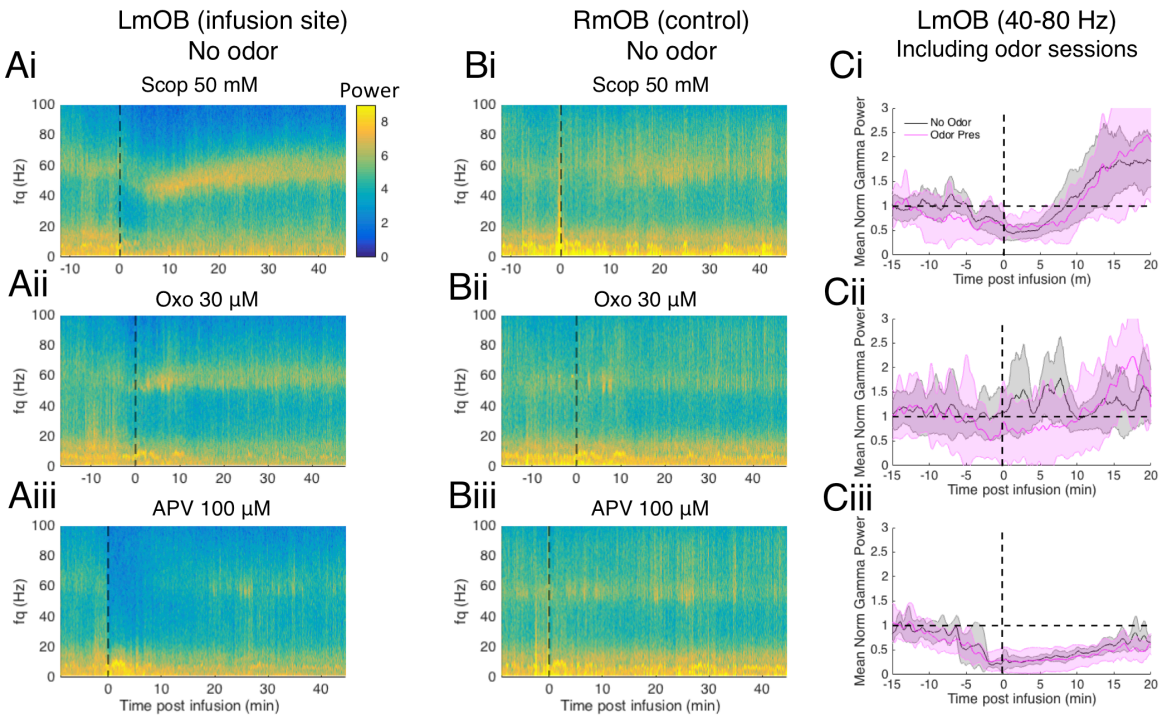

Figure 3.3. Temporal effects of drugs on OB LFP power. A: Representative spectrograms of LmOB LFP after infusion of scopolamine (Ai), oxotremorine (Aii), and APV (Aiii) into the LmOB without any odor presentations. Vertical dashed lines indicate end of infusion (time to complete the infusion varied slightly from session to session). **B:** Spectrograms of contralateral (RmOB) LFP activity corresponding to the sessions in A. **C:** Mean gamma (40 – 80 Hz) power averaged over no odor (gray) and odor presentation (pink) sessions aligned to end of infusion time (vertical dashed lines indicate end of infusion). Power was normalized by the average baseline power (indicated by horizontal dashed line). Scopolamine and APV had fairly consistent effects across subjects, but oxotremorine effects were highly variable.

Scopolamine infusion produced a consistent biphasic effect on the LFP, starting with a strong suppression of LFP power across gamma and beta frequencies, followed by a "rebound" boost in low gamma power, which slowly dissipated as gamma crept up to the baseline gamma frequency over about 20 min (Figures 3.3Ai and 3.3Ci). We measured the duration of the early phase as the time that the average broadband gamma (40 – 80 Hz) power took to return to pre-infusion baseline gamma power levels, which we found to be ~7-8 mins after the

end of infusion (Fig. 3.4A). Because of this biphasic effect we designed the odor presentations to fit into two blocks, each lasting about 7-8 minutes (24 presentations spaced by roughly 20s each), so that the first block covers the first phase while the second block covers the second phase. In Figure 3.4C we show the spectrograms of scopolamine (50 mM) infusion followed by odor presentation sessions in 4 rats to confirm that the first odor block (green line) and second odor block (red line) bracketed this transition. We used the same odor block design for all sessions to avoid introducing new variables, but since APV did not show biphasic

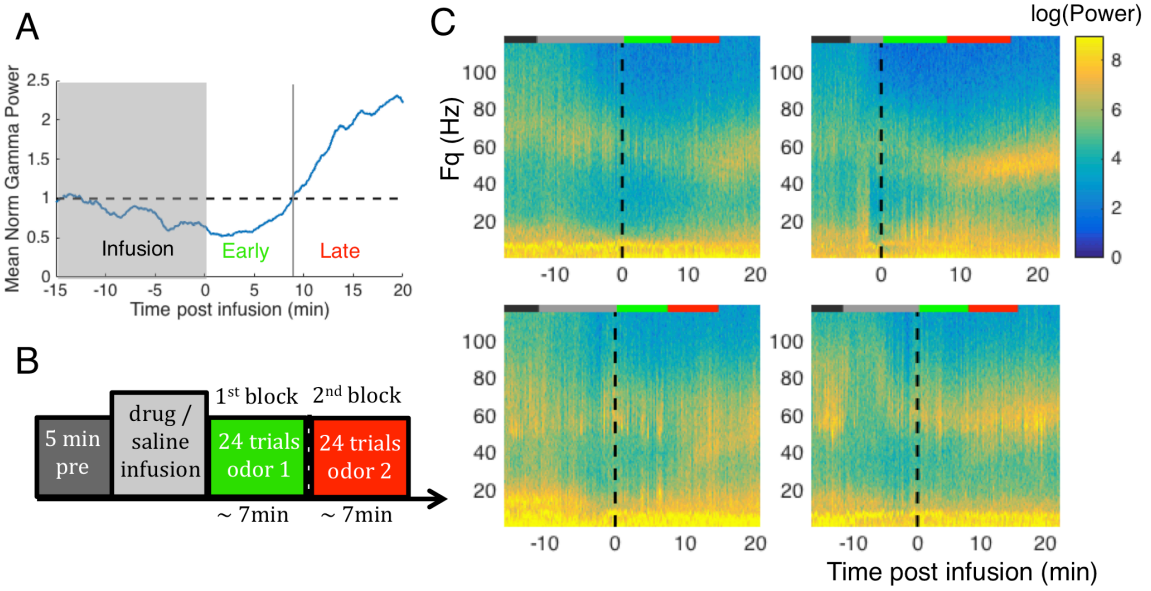

Figure 3.4. Determining average duration of early phase scopolamine effect in LmOB. A: Mean normalized power in the LmOB gamma band (40-80Hz) from all scopolamine sessions aligned by the end of infusion time-points. The infusion period (gray block) differed in duration from session to session (see methods). Dashed horizontal line is the baseline gamma power before infusion (power was normalized by baseline, so baseline is at 1). We interpret the early phase of scopolamine as the time post infusion it takes for mean gamma power to return to baseline (marked by vertical line), which is about 7-8min **B:** Odor presentation experimental timeline. The 1st block overlaps with the early phase of scopolamine effect, the 2nd block with the late phase. **C:** Example spectrograms of scopolamine (50 mM) sessions in 4 rats. Vertical black dashed lines indicate end of infusion. Colored lines at the top of each plot indicate the duration of each step in the experiment using same color scheme as the timeline in B. In each of these plots, the 1st (green) and 2nd (red) odor blocks bracket the transition between the two phases of the scopolamine effect. Odor evoked beta and gamma oscillations can be seen in some of the plots. In these plots, the 2nd odor block starts just before the onset of the rebound gamma (scopolamine effect phase 2).

effects we combined the APV data from both blocks.

While the scopolamine and APV effects were fairly consistent from session to session, the oxotremorine effects were highly variable. In the early sessions without odor presentations, oxotremorine tended to increase gamma power (Fig. 3.3Cii, gray trace), but in 70% of the odor presentation sessions oxotremorine reduced gamma power (Fig. 3.3Cii, pink trace). In those sessions, gamma suppression was followed by a rebound gamma increase, similar to the scopolamine sessions. Because of this, we used the same odor block design for oxotremorine as scopolamine. Oxotremorine is known to produce excitatory and inhibitory effects in the OB through differential activation of M1 and M2 receptors (Smith et al., 2015, see *Discussion*), and this may in part be responsible for the highly variable effects on gamma. We include oxotremorine data here for completeness, but we admit that more work must be done to dissect its effect on OB oscillations.

3.3.2 Muscarinic receptors

Our previous modeling work (Osinski and Kay, 2016) predicted that reducing GC excitability would lift the frequency of LFP oscillations induced by strong odors out of the beta regime into the low gamma range but would leave LFP oscillations evoked by weak odors in the beta regime with possibly some increase in power (Fig. 3.1B). To test these effects, we infused scopolamine (38 mM & 50 mM), a nonselective muscarinic antagonist with twice the affinity for M2 as for M1 receptors (Bolden et al., 1992), through a cannula positioned in the GC layer (Fig. 3.2D). Muscarinic drugs are known to modulate GC excitability in a complex manner

(Castillo et al., 1999; Mandairon et al., 2006; Pressler et al., 2007b; Devore and Linster, 2012b; Li and Cleland, 2013; Smith et al., 2015). With scopolamine, our intention was to prevent heightened excitability states from occurring, thus placing GCs in an impaired excitability state, as described in the modeling results in Figure 1B. We chose one high volatility odorant, ethyl-2-methylbutyrate (EMB), and one low volatility odorant, geraniol (GER), to probe the effects induced by strong and weak odors, respectively. As described earlier (Fig. 3.4), we divided odor presentation sessions into two blocks of 24 trials each lasting ~7-8 minutes to cover the biphasic scopolamine effect on the background LFP.

3.3.2i Results from a single scopolamine session

We first take a close look at a representative scopolamine (50 mM) session and its associated saline session from a single rat (Fig. 3.5), and then we examine the summary statistics of all the scopolamine sessions across all rats (Fig. 3.6). Figure 3.5A shows single trials of EMB- and GER-evoked oscillations in LaOB, LmOB (infusion site), RmOB, and LaPC after saline and scopolamine (50 mM) infusions. In these sessions, EMB was presented in the 1st odor block and GER in the 2nd. EMB evoked prominent beta oscillations on all channels after saline infusion (labeled β, Fig 3.5Ai). LaOB beta was typically smaller in amplitude than LmOB, consistent with other recordings in our laboratory, possibly because anterior OB receives fewer feedback fibers than more posterior parts or simply because the increased curvature in the anterior end of the bulb reduces the coherence of the laminar cortical field. After scopolamine 50 mM infusion, the EMB-evoked LaOB and LmOB

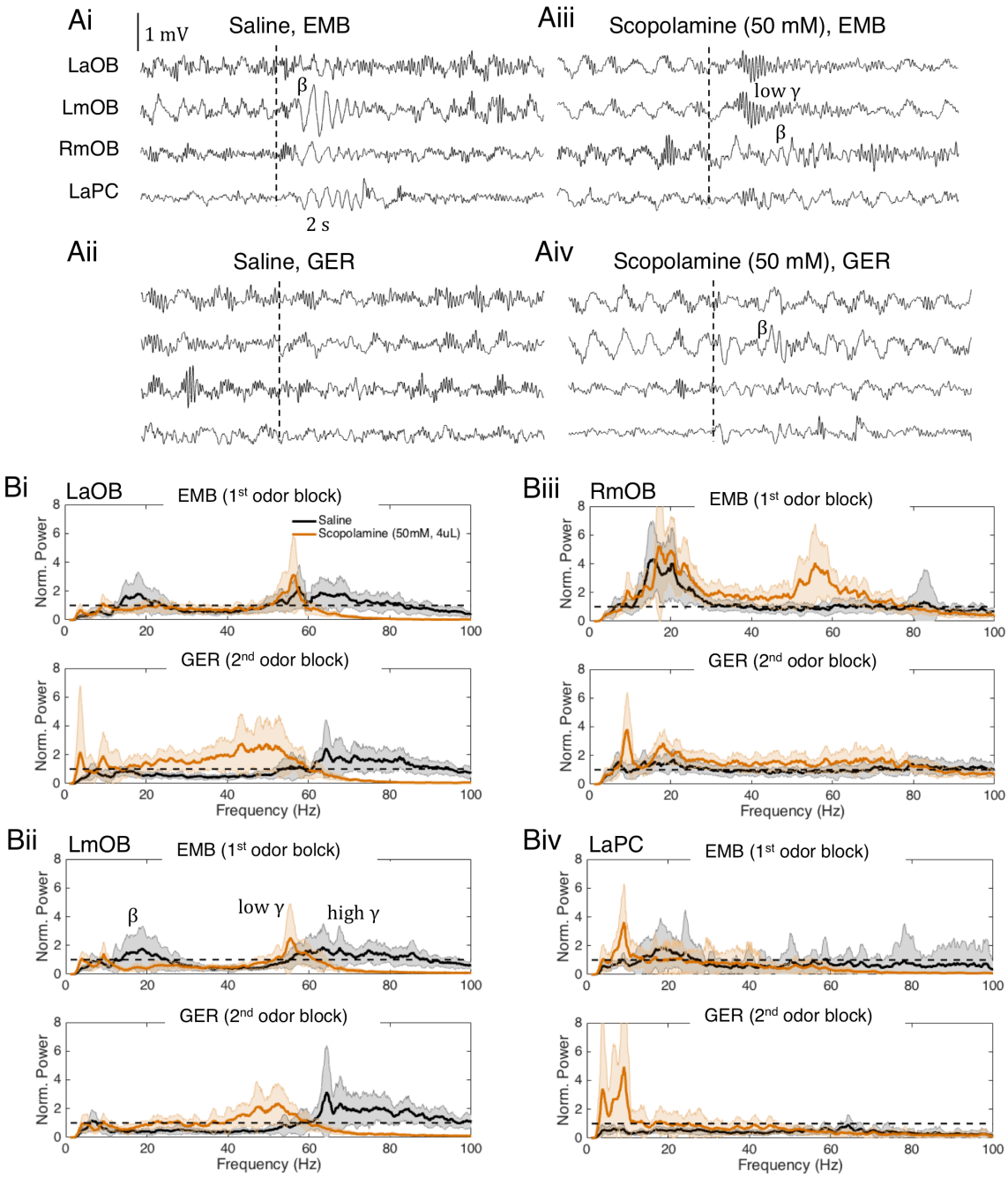

Figure 3.5. Representative scopolamine session and associated saline session from a single rat. A: Representative LFP traces during EMB (top) and GER (bottom) presentations in LaOB, LmOB, RmOB, and LaPC after saline (left) and scopolamine (right) infusions from a single rat. Twenty such trials are used to produce the power spectra in B. Odor presentation times are indicated by dashed vertical lines. In this session the EMB-induced beta in the LOB (labeled β) was visibly abolished and appeared to be replaced by a low gamma oscillation (labeled low γ). This occurred in 9 out of 12 of the scopolamine (50 mM) sessions and 4 out of 12 of the scopolamine (38 mM) sessions across the 6 rats. Beta persisted in the RmOB after scopolamine infusion. **B:** Mean power spectra of LaOB (Bi), LmOB (Bii), RmOB (Biii), and LaPC (Biv). For each brain region we show the LFP power spectra during EMB (top) and GER (bottom) presentation after saline (black) and scopolamine (orange) infusion. Power was normalized by the pre-infusion baseline, represented by the horizontal dashed line at 1. In the LmOB EMB spectrum (Bii, top) we annotate the beta (β), low gamma (low γ), and high gamma peaks (high γ).

beta oscillations were abolished and appeared to be replaced with a high power low gamma frequency oscillation (labeled low γ, Fig. 3.5Aiii). The contralateral (RmOB) beta oscillation, where no drug was delivered, was still present (labeled β, Fig. 3.5Aiii). GER did not evoke visible beta oscillations under the saline condition (Fig. 3.5Aii), but did evoke visible beta oscillations after scopolamine infusion (Fig. 3.5Aiv). In these trials the apparent opposite effect of scopolamine on EMB- and GER- evoked beta oscillations followed our model predictions of a bidirectional effect (Fig. 3.1B).

Figure 3.5B shows the average power spectra (normalized by baseline) of the single sessions from which the representative trials in Figure 3.5A were taken. The average power in the beta frequency range for LaOB and LmOB during the 1st odor block (EMB) is noticeably reduced, and a peak in the low gamma frequency band appears after scopolamine infusion (Fig 3.5Bi,ii, top; peak at ~55 Hz). This low gamma peak represents the low gamma oscillation that appears to occur in place of the beta oscillation, seen in the LFP trace in Fig 4Bii. There is also an increase in broadband low gamma in the 2nd odor block (GER). Unlike the 1st odor block however, this increase in low gamma is most likely not odor-evoked, but a consequence of the rebound gamma increase that occurs in the later phase of the scopolamine effect as shown in Figures 3.3 & 3.4. The distinction between the gamma frequencies in the EMB- and GER-induced LFP spectra may be related to the two different gamma subtypes, gamma1 and gamma2, noted by Kay (2003) (see *Discussion*). There was a small increase in GER-evoked beta under scopolamine in the representative trial shown in Figure 3.5Aiv, and, on average, the GER-evoked

beta power was slightly elevated relative to baseline for this session (Fig. 3.5Bi,ii, bottom). The LaPC showed negligible effects of EMB-evoked (Fig. 3.5Biv, top) and GER-evoked (Fig. 3.5Biv, bottom) beta following scopolamine infusion. Because PC tends to produce beta frequency activity spontaneously (Poo and Isaacson, 2009b), the baseline normalized LaPC beta was fairly low even when there was a visibly evoked beta oscillation. All three regions in the left hemisphere show a persistent decrease in high gamma oscillations lasting through both phases of the scopolamine effect. Although this occurred to some degree in 4 of 6 rats, the effect overall was not significant (see Fig. 3.6). In the RmOB there was no effect on beta power but a surprising increase in low gamma power following scopolamine infusion in this rat (Fig. 3.5Biii). There were prominent contralateral effects in approximately half of the rats, and this is discussed in more detail later (see Fig. 3.6C). We present this representative data set from a single rat because the replacement of beta by low gamma oscillations following scopolamine infusion could only be inferred by looking at the individual LFP traces themselves (comparing Fig. 3.5Bi and Fig. 3.5Biii), and not from summary statistics.

3.3.2ii Scopolamine effects in the OB

We now turn to address drug effects across all rats for low and high doses of scopolamine on the beta (15 – 30 Hz), low gamma (40 – 60 Hz), and high gamma (60 – 100 Hz) frequency bands. In order to put power values from different rats on the same scale we normalized the LFP power by both pre-infusion baseline and saline power (see *Methods*). 5-way ANOVAs were computed, with subject, drug treatment

(saline vs. drug), odor, frequency band, and block (early vs. late) as factors for each electrode location and drug concentration. The results of post hoc t-tests between the means of the saline and drug sessions for each rat and electrode location are reported in Fig. 3.6. As described in *Methods*, the Bonferroni correction on post hoc tests sets the significance threshold at $p < 0.004$ for drugs that showed a biphasic effect. For these and all subsequent descriptions of the drug effects, we first present the results of our ANOVA analyses, including the effects of all factors. After that, for electrode locations that show significant main effects or interactions involving the drug treatment, we present post hoc comparisons. Other effects (odor, subject, frequency band) have been extensively covered in our previous reports (Lowry and Kay, 2007b; Kay et al., 2009b; Kay, 2014b; Frederick et al., 2016a).

Effects on the left OB (treatment side) were similar across the two drug concentrations. For the low concentration (38 mM) scopolamine treatment, we found significant main effects of all five factors on LFP power in both sites in the OB (LmOB: subject p=7.4e-8, η^2 0.16; drug p=0.0019, η^2 0.03; odor p=1.03e-7, η^2 0.11; block p=0.0076, η^2 0.0003; frequency band p=7.77e-5, η^2 0.07; LaOB: subject p=0.0324, η^2 0.05; drug p=0.0389, η^2 0.02; odor p=1.00e-6, η^2 0.12; block p=0.0434, η^2 0.003; frequency band p=0.00001, η^2 0.08). Some of these effects were expected because of our prior knowledge about how the volatility of odors affects the power of beta oscillations (odor, band) and differences in electrode placement and therefore power of different oscillation frequencies across subjects (subject). Importantly, there was also a significant interaction between drug and odor at the injection site only (LmOB: p=0.0366, η^2 0.15), plus additional interactions at that

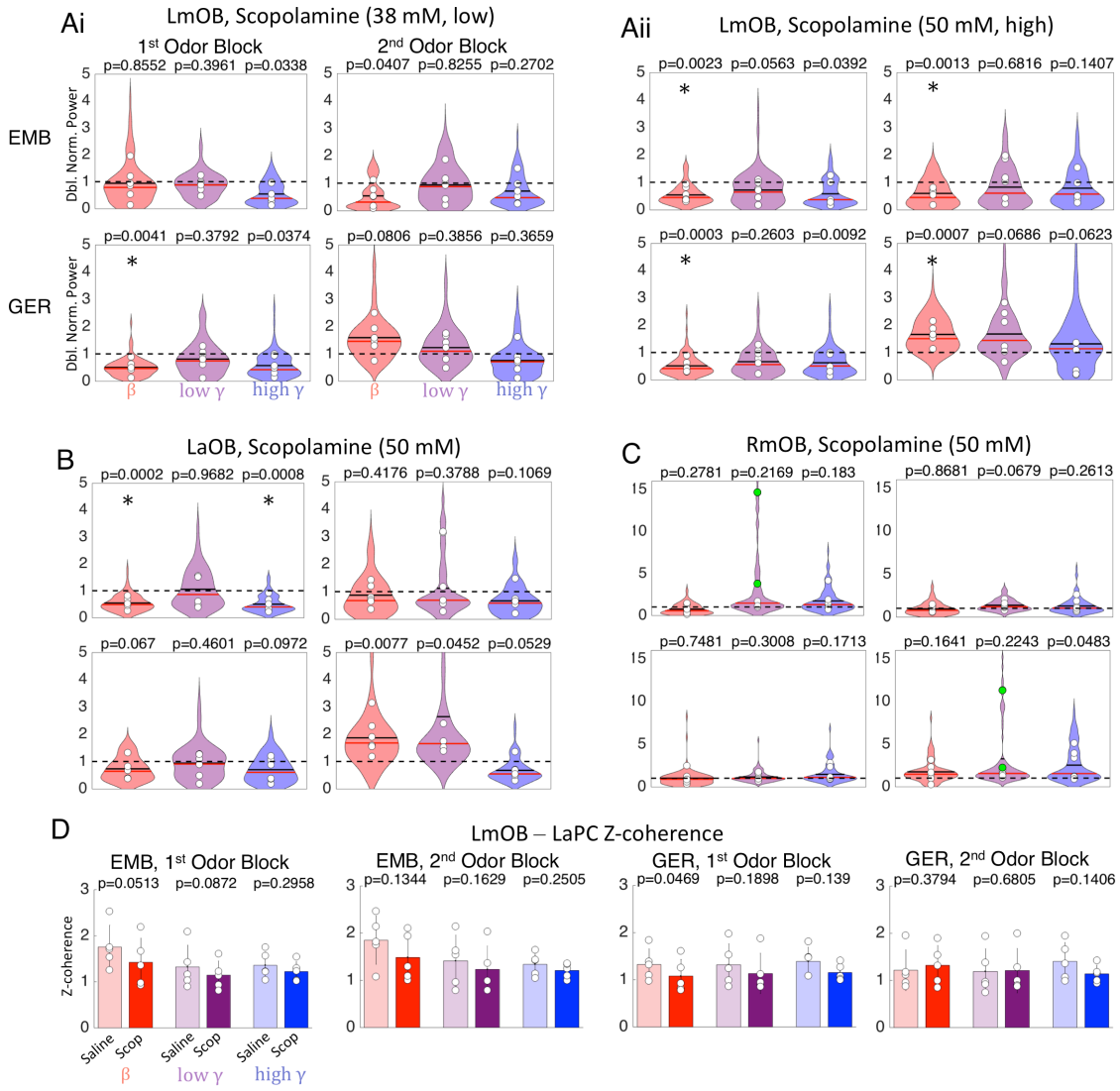

Figure 3.6. Scopolamine effects on odor induced LFP oscillations. A: Violin plots summarizing effects of low (38 mM, Ai) and high (50 mM, Aii) scopolamine doses on LmOB (infusion site) in all 6 rats for presentation of EMB (top) and GER (bottom) during 1st and 2nd odor blocks. White circles represent means of each rat. Power for each session was doubly normalized, first by baseline and then by its closest saline session (black dashed line). A value of 1 indicates no difference from the saline condition. Black solid horizontal lines on the violins show means for all rats; red horizontal lines are medians. Asterisks represent $p < 0.004$ for the post hoc comparisons between mean saline and drug for each rat. **B, C:** Violin plots summarizing effects of scopolamine (50 mM) on LaOB and RmOB (same annotations as A). Although the scopolamine effect in RmOB was not significant in the *post hoc* comparison across all rats, two rats showed very strong low gamma power (colored green for visualization). Note that the y-scale is increased for RmOB to fit the huge increase in low gamma power that occurred in one rat. **D:** Z-coherence between LmOB and LaPC under saline and scopolamine (50 mM) conditions was computed fro EMB and GER in both odor blocks.

site between subject and odor (p=0.0249, η^2 0.04), subject and frequency band (p=8.76e-7, η^2 0.17), odor and block (p=0.0447, η^2 0.01), and odor and frequency band (p=2.66e-6, η^2 0.10). Significant interaction effects for the LaOB were subject x band (p=2.04e-6, , η^2 0.22), odor x block (p=0.005, η^2 0.03), and odor x band (p=0.0007, η^2 0.07).

For the high concentration (50 mM) scopolamine treatment, we again found significant main effects for all five factors at the injection site (LmOB: subject p=1.93e-7, η^2 0.15; drug p=0.0020, η^2 0.03; odor p=2.57e-7, η^2 0.09; block p=0.0114, η^2 0.02; frequency band p=5.24e-5, η^2 0.07). We also found significant interactions between drug treatment and odor (p=0.0043, η^2 0.03) and drug treatment and block (p=0.0211, η^2 0.02), in addition to expected subject x band (p=1.93e-5, η^2 0.14) and odor x band (p=1.45e-6, η^2 0.09) effects. At the anterior OB recording site we did not find significant main effects of subject or odor, but we did find significant main effects of drug, block and frequency band (LaOB: drug p=0.0087, η^2 0.0001; block p=0.0327, η^2 0.004; band p=2.58e-5, η^2 0.11). At this site, we also found significant interaction terms involving drug treatment (drug x odor, p= 0.0154, η^2 0.03; drug x block, p=0.0066, η^2 0.03; drug x band, p=0.0031, η^2 0.03), plus additional interactions (subject x band, p=0.0006, η^2 0.16, and odor x band, p=0.0043, η^2 0.05) as expected.

Post hoc comparisons of drug vs. saline effects for each electrode site and frequency band shed more light on main effects and interactions. In the first odor block, LmOB beta power was significantly reduced for the high volatility odorant (EMB) only for the high scopolamine dose (50 μM, Fig. 3.6Aii top) but was

significantly reduced for both low and high doses when the low volatility odorant (GER) was presented (Fig. 3.6Ai,ii bottom). It is possible that the strong beta-evoking tendency of EMB may be counteracting the beta suppressing effects of scopolamine only at the low dose. GER evokes beta oscillations more weakly, and therefore the effect of scopolamine dominates even in the low dose.

In the second odor block, effects on beta power diverged between the strong and weak odors, confirming the bidirectional effect predicted by our model. For the high scopolamine dose in the second block (Fig. 3.6Aii), EMB-evoked beta was suppressed just as it was in the 1st odor block, but GER-evoked beta power was significantly increased. Similar trends are seen for the low scopolamine dose, though they did not pass our threshold for significance. The LaOB LFP power followed a pattern similar to LmOB, but only the reduction of beta in the 1st odor block was significant (Fig. 3.6B). The weaker effects in LaOB may be attributed to weaker overall beta signals in the anterior OB or possibly insufficient spread of the drug in some rats (Fig. 3.2Bi). The complete replacement of EMB-evoked beta by low gamma following scopolamine (50 mM) infusion (as seen in the single trials of Fig. 3.5A) was seen in 4 out of 12 scopolamine (38 mM) sessions and 9 out of 12 scopolamine (50 mM) sessions (sessions from both odor blocks), while in the sessions beta amplitude was either reduced or unaffected. The replacement of beta by low gamma can be inferred only from viewing the odor-evoked periods, not from the power over the entire 4s trial periods.

There were no significant effects of either low or high doses of scopolamine on the LmOB gamma bands during the odor exposure periods, though there was a

tendency for high gamma to be suppressed in during the 1st odor block, consistent with gamma suppression during the early phase of scopolamine in the no odor condition (Fig. 3.3). There was a significant reduction in LaOB high gamma power for EMB in the 1st odor block (Fig. 3.6B). Four of the 6 rats showed enhanced low gamma power in the 2nd odor block of high dose scopolamine, presumably due to the rebound low gamma intensification described in Figures 3.3 & 3.4. One possible reason why rebound gamma did not show a significant gamma increase in all rats is that odorants tend to increase beta while suppressing gamma (Buonviso et al., 2003b).

3.3.2iii Scopolamine effects in contralateral OB

As touched upon in Figure 3.5Bii, we noticed some strong but inconsistent contralateral effects in the gamma frequency bands following scopolamine infusion into the LmOB. The sessions of two rats in particular (both sessions where EMB was presented in block 1) had extremely high gamma power under scopolamine, especially in the low gamma band. The means of these two rats are colored green in the low gamma power bands of Figure 3.6C for the EMB 1st and GER 2nd odor blocks (same session). These are the same two rats that had the furthest posterior spread of dye in post-mortem inspection (two green lines in Fig 3.2C).

The results of the ANOVAs at the two different scopolamine concentrations showed no main effect of drug treatment on this side, but did show other significant main effects, as would be expected (38 mM scopolamine: odor, p=1.65e-6, η^2 0.12; band, p=7.63e-9, η^2 0.21; 50 mM scopolamine: odor, p=0.007, η^2 0.04; band,

p=0.0118, η^2 0.05). At both concentrations there was a significant interaction between drug and frequency band (38 mM: p=0.0025, η^2 0.06; 50 mM: p=0.0015, η^2 0.08), which is likely driven by the increase in low gamma power. We also found a significant odor x band interaction (38 mM: p=0.4.25e-7, η^2 0.18; 50 mM: p=0.0170, η^2 0.05).

The increase in low gamma power was not odor evoked, but persisted between odor presentations and lasted throughout the EMB and GER odor blocks. While the drug x band interaction was significant with a medium effect size, *post hoc* t-tests were not significant because of the wide variance across subjects. When the increase in low frequency gamma did occur, it was obvious to the eye, even during data acquisition. We suspect that in the sessions where there was a contralateral effect, some of the drug spread posteriorly into the anterior olfactory nucleus (AON). Contralateral projections through the anterior commissure linking the left AON to the right OB are known to exist (Nickell and Shipley, 1993), and it is possible that blocking muscarinic modulation of these fibers is driving the contralateral increase in gamma.

3.3.2iv Scopolamine effects in LaPC

In addition to LOB and ROB activity, LaPC activity was also recorded in each rat (Fig. 3.5A, bottom trace). One rat's LaPC data had to be discarded due to poor quality signals. The results of the ANOVAs showed the same effects for both drug doses. There were no significant effects of drug treatment, either as main effects or interactions (LaPC 38 mM: subject, p=2.23e-10, η^2 0.22; odor, p=4.25e-7, η^2 0.09;

band, p=9.68e-9, η^2 0.14; remaining NS. LaPC 50 mM: subject, p=3.29e-10, η^2 0.20; odor, p=1.55e-5, η^2 0.06; band, p=5.40e-10, η^2 0.16; remaining NS.). There were expected interactions that depend on differences across subjects and odors: subject x odor (38 mM: p=9.96e-6, η^2 0.09; 50 mM: p=0.0014, η^2 0.06), subject x band (38 mM: p=3.67e-8, η^2 0.18; 50 mM: p=1.31e-6, η^2 0.15), and odor x band (38 mM: p=5.53e-7, η^2 0.10; p=1.82e-6, η^2 0.09). These results show that there was no effect on aPC power in any of the frequency bands due to scopolamine action in the OB.

We had expected that a reduction in OB beta power by scopolamine would also reduce ipsilateral aPC beta power, because beta oscillations require intact bidirectional OB-PC connections (Neville and Haberly, 2003b; Martin et al., 2006b), and GCs receive most of their cortical inputs from the ipsilateral aPC. The results suggest that beta oscillations in the PC can be generated with some degree of independence from the OB, even though they still require intact projections from the bulb (at least under anesthesia, Neville and Haberly, 2003). This stability could be attributed to the PC's own tendency to generate beta frequency oscillations in response to odor stimulation. Indeed, a study by Poo and Isaacson (2009) found prominent PC beta oscillations in urethane-anesthetized rats, even when anesthesia depresses the feedback inputs into the OB.

We also computed the Z-coherence between OB and PC for scopolamine (50 mM) sessions and the associated saline sessions. A 5-way ANOVA showed significant main effects of subject, drug, odor, and frequency band (subject, p=1.44e-33, η^2 0.62; drug, p=0.0003, η^2 0.05; odor, p=3.61e-7, η^2 0.04; band, p=1.14e-6, η^2 0.04; block NS). The drug effect was different across subjects (subject x drug, p=0.0066, η^2

0.02), and there were other significant interactions not involving scopolamine treatment (subject x band, p=8.22e-6, η^2 0.06; odor x band, p=4.8e-7, η^2 0.04; remainder NS). While there was a significant effect of scopolamine overall as a slight reduction of coherence, none of the post hoc comparisons were significant (Fig. 3.6D). Thus, OB-PC beta coherence was still high even when beta was seemingly eliminated in the OB. This suggests that a small component at beta frequency persisted in the OB, even when beta power was suppressed to baseline levels by scopolamine, and that this is enough to support beta band coherence with the aPC.

3.3.2v Oxotremorine effects

To complement the antagonistic effects of scopolamine, we also infused a muscarinic agonist into the OB. We chose oxotremorine, because it has already been used in several studies of bulbar cholinergic modulation (Mandairon et al., 2006; Smith et al., 2015). We expected oxotremorine and scopolamine to have opposite effects, but oxotremorine produced inconsistent results (Fig. 3.3). While the results are somewhat equivocal, we include them here for completeness.

Results from our ANOVA analysis show that all factors show significant main effects at the injection site (LmOB: subject, p=0.0002, η^2 0.11; drug, p=0.0033, η^2 0.02; odor, p=1.46e-5, η^2 0.09; block, p=0.0173, η^2 0.02; band, p=0.0054, η^2 0.05). There were no significant interactions of any of the other factors with drug, but there were some other significant interactions: subject x band (p=0.0131, η^2 0.09), odor x block (p=0.0013, η^2 0.05), and odor x band (p=3.86e-5, η^2 0.05). At the anterior OB site, there were main effects only of drug and odor (LaOB: drug,

p=0.0019, η^2 0.06; odor, p=0.0028, η^2 0.06), no significant interactions with drug effects, but other significant interactions (odor x band, p=0.048, η^2 0.04; subject x band: p=0.0122, η^2 0.12; odor x band, p=0.0021, η^2 0.08).

As opposed to scopolamine, oxotremorine did significantly affect PC activity. We found significant main effects for all factors except odor block (LaPC: subject, p=0.0003, η^2 0.11; drug, p=0.0156, η^2 0.03; odor, p=0.0007, η^2 0.06; band, p=0.0002, η^2 0.10). There were no significant interactions with drug effects, but there were interactions between subject and odor (p=0.0360, η^2 0.04), subject and frequency band (p=0.0009, η^2 0.13), odor and block (p=0.0282, η^2 0.02), and odor and frequency band (p=0.0003, η^2 0.09). The contralateral OB also showed significant main effects, including a drug effect (RmOB: drug, p=0.0226, η^2 0.02; odor, p=1.70e-5, η^2 0.09; band, p=6.28e-11, η^2 0.25, remaining factors NS). No factors showed significant interactions with drug, but other interactions were significant: odor x block (p=0.0139, η^2 0.03) and odor x band (p=1.91e-7, η^2 0.15).

These effects played out in the *post hoc* analysis in somewhat confusing ways. Following oxotremorine (30 μM) infusion into LmOB, there was a significant decrease in LaOB beta power during presentation of GER in the 2nd block (Fig. 3.7A) and LmOB beta power during EMB in the 1st odor block (Fig. 3.7B). This was surprising, because scopolamine also blocked beta in the 1st EMB odor block, but increased beta in the 2nd GER odor block (Fig. 3.6Aii). So, the two drugs produced the same effect in the first block but opposite effects on GER in the second block. However, while scopolamine may have blocked EMB-induced beta by reducing GC GABA release to the point that oscillations could not be sustained, oxotremorine

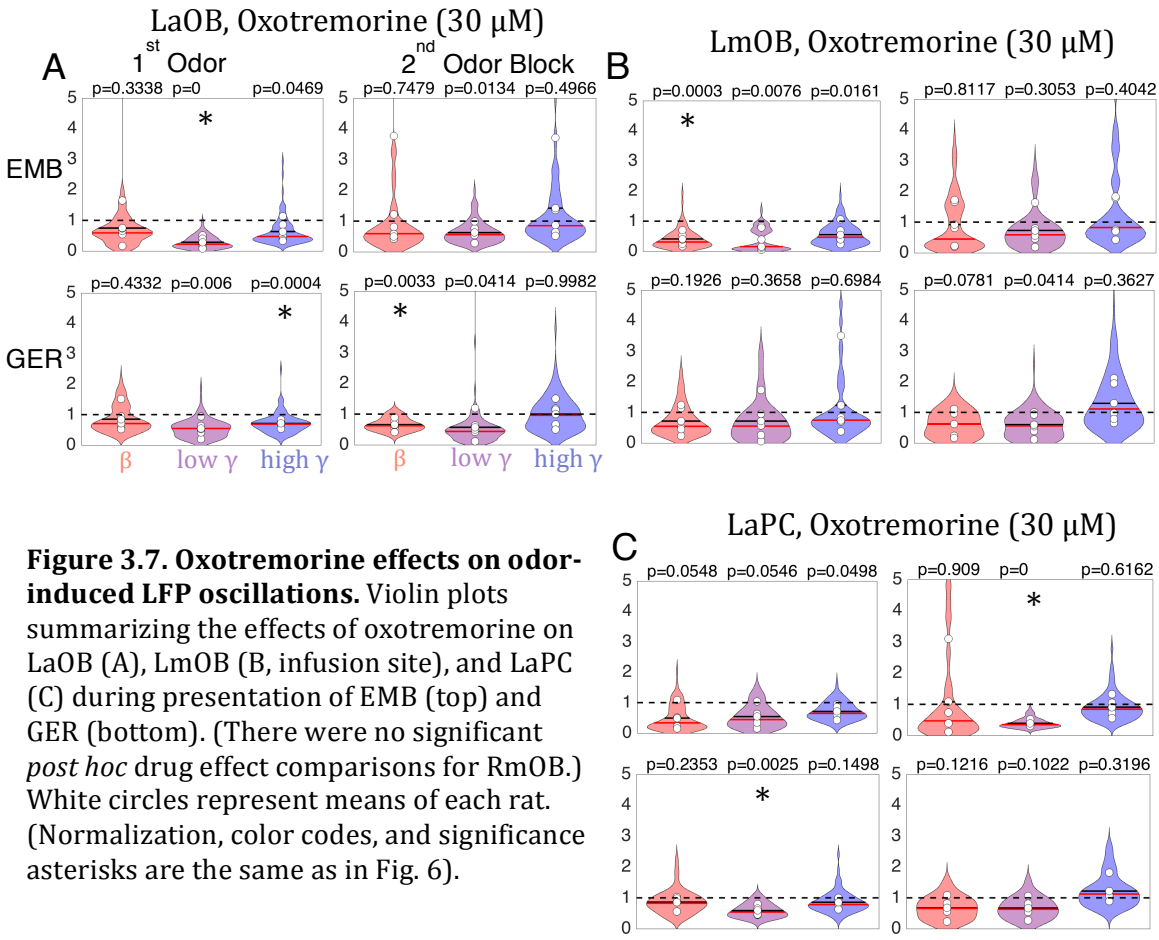

Figure 3.7. Oxotremorine effects on odor-induced LFP oscillations. Violin plots summarizing the effects of oxotremorine on LaOB (A), LmOB (B, infusion site), and LaPC (C) during presentation of EMB (top) and GER (bottom). (There were no significant *post hoc* drug effect comparisons for RmOB.) White circles represent means of each rat. (Normalization, color codes, and significance asterisks are the same as in Fig. 6).

may have blocked EMB-induced beta by driving excessive GABA release, tipping the balance in the other direction where inhibition dampens excitation too much. Such an effect was also seen in our model, where oscillations were only sustained in a range where there was a sufficient balance of excitation and inhibition. It is also possible that oxotremorine may inhibit GCs through action on M2 receptors or inhibit MCs themselves (Smith et al., 2015).

LaOB low gamma was significantly reduced in the 1st EMB odor block (close to significance in LmOB), and high gamma was reduced in the 1st GER odor block. As noted in Figure 3.3, oxotremorine tended to increase gamma power when no odor was present, but suppress it when odor was present. Interestingly, gamma

suppression in the LaPC was significant both for the 2nd odor block EMB presentations and 1st odor block GER presentations (Fig. 3.7D). *Post hoc* analyses of RmOB responses to oxotremorine infusion into LmOB showed no significant comparisons between saline and drug. Because of the inconsistent effects of oxotremorine (Fig. 3.3 Cii) and its likely non-specific effects (see *Discussion*) we refrain from making any strong conclusions about the effects of oxotremorine on beta oscillation generation in the OB.

3.3.3 NMDA receptors

We also tested another prediction of our model, that beta oscillations can be sustained independently of NMDAR currents, but that NMDAR currents are critical to sustain gamma oscillations. (In our model, beta oscillations rely critically on N-Type mediated Ca^{2+} currents.) We tested this prediction by infusing APV (100 μM), a selective NMDAR antagonist, into the LmOB. Because APV had a uniform effect lasting the entire session (Fig. 3.3Ciii), we combined data from the 1st and 2nd odor blocks, the results of which are summarized in Figure 3.8.

We analyzed the data with a 4-way ANOVA to test the influence of subject, drug, odor, and frequency band. At the injection site, all four factors showed significant main effects (LmOB: subject, p=0.0032, η^2 0.11; drug, p=0.0009, η^2 0.09; odor: p=2.98e-5, η^2 0.16; band, p=0.0002, η^2 0.15). APV treatment did not show significant interactions with any other factors at this site (subject x band, p=0.0137, η^2 0.13; odor x band, p=0.0004, η^2 0.13; remaining interactions NS). The main effects were somewhat different at the anterior OB site (LaOB: subject, NS; drug, p=0.0077, η^2

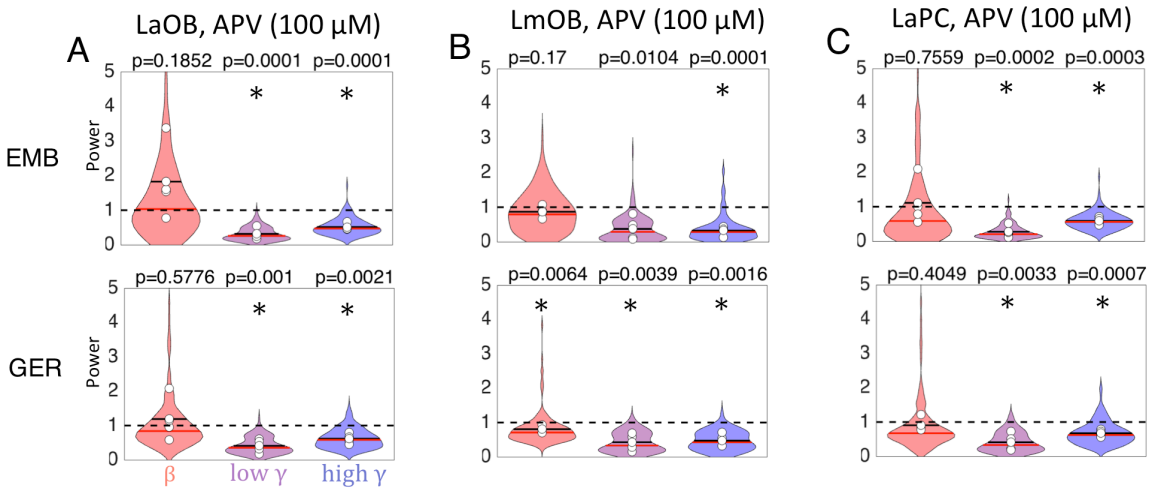

Figure 3.8. APV effects on odor-induced LFP oscillations. A: Violin plots summarizing effects of APV infusion into LmOB on LaOB in all 6 rats for presentation of EMB (top) and GER (bottom). 1st and 2nd odor blocks were combined for analysis of APV data (Fig. 3). (Symbols and normalization are the same as in Figs. 6 and 7.) Asterisks represent $p < 0.008$ (adjusted for 6 comparisons) for the post hoc T-tests between mean saline and drug for each rat. **B, C:** Violin plots summarizing effects of APV in LmOB (infusion site) and LaPC (same annotations as A). APV strongly suppresses gamma in all left hemisphere locations.

0.02; odor, p=8.93e-5, η^2 0.11; band, p=1.19e-7, η^2 0.34). APV treatment did show a significant interaction with frequency band at this site (p=0.0021, η^2 0.08), and there were some other interactions (subject x band, p=0.0337, η^2 0.08; odor x band, p=2.64e-5, η^2 0.17; other interactions NS).

As predicted by our model and in agreement with studies in mice (Lepousez and Lledo, 2013b), post hoc tests showed that LaOB and LmOB gamma oscillations were almost completely abolished (Fig. 3.8A,B). LaOB and LmOB beta power was largely unaffected, except for the LmOB GER presentations, which showed a small but significant decrease. It is possible that the decrease in LmOB beta for GER presentations reflects a stimulus dependent effect, similar to the contrasting effects

of EMB and GER seen during scopolamine infusion. However, we did not address this scenario in the model.

Analysis of the contralateral OB data showed no main or interaction effect of APV treatment (RmOB: odor, p=3.41e-5, η^2 0.11; band, p=1.51e-8, η^2 0.38; subject x band, p=0.0093, η^2 0.10; odor x band, 1.79e-6, η^2 0.22; remainder NS). We therefore omit the post hoc analysis. The ipsilateral aPC showed significant main effects for all factors (LaPC: subject, p=0.0011, η^2 0.13; drug, p=0.0344, η^2 0.03; odor, 0.0003, η^2 0.10; band, 2.01e-5, η^2 0.20). Interaction effects did not involve APV (subject x odor, p=0.0369, η^2 0.06; subject x band, p=0.0031, η^2 0.16; odor x band, p=0.0002, η^2 0.14; remainder NS).

Post hoc tests show that in contrast to the relative insensitivity of LaPC beta oscillations to scopolamine infusion into the LmOB, we found strong gamma suppression in LaPC after APV infusions into the LmOB (Fig. 3.8D), mirroring the effects in the OB.

3.4 Discussion

We tested two predictions of our previously published computational model (Osinski and Kay, 2016; Fig. 3.1): 1) beta oscillations are produced under conditions of heightened GC excitability, 2) beta oscillations can be generated independently of NMDA currents, while gamma oscillations cannot. We tested the first prediction by infusing muscarinic drugs into the OB (Figs. 3.3-3.7), and the second prediction by infusing APV, a selective NMDA antagonist (Figs. 3.3 & 3.8).

We found that scopolamine (50 mM) reduced EMB- and GER-evoked beta oscillations in the 1st odor block, but after a few minutes (in the 2nd odor block) we observed a divergent effect, where EMB-induced beta was suppressed and GER-induced beta was enhanced (Fig. 3.5A). The divergent effect in the 2nd odor block also aligns well with our model's predictions, that reducing GC excitation in strong stimulus input regimes (EMB) would decrease beta power and in weak stimulus input regimes (GER) would increase beta power. In 9 out of 12 of the scopolamine (50 mM) sessions, the EMB-evoked beta oscillation was replaced by a low gamma oscillation (Figs. 3.4A, 3.5Aii), as our model predicted for strong odors (green square Fig. 3.1B). The results of APV (100 μM) infusions also closely followed our model predictions (Fig. 3.7), knocking out gamma, but not beta, oscillations. However, oxotremorine (30 μM) effects were more difficult to interpret (Fig. 3.2 & 3.6). By also recording in LaPC and RmOB we were able to investigate the wider network that supports and is impacted by these oscillations across brain regions beyond the scope of the model. We found that PC beta oscillations were relatively insensitive to changes in OB beta power, but PC gamma oscillations were much more sensitive (Fig. 3.5D & 3.7D).

3.4.1 Complexity of muscarinic drug effects

Many studies of cholinergic modulation in the OB treat muscarinic receptors as modulators of GC excitability (Nickell and Shipley, 1993; Castillo et al., 1999; Martin et al., 2006b; Pressler et al., 2007b; Devore and Linster, 2012b; de Almeida et al., 2013b; Li and Cleland, 2013). Together these studies give the impression that

bulbar muscarinic receptors are exclusively involved in regulation of GC excitability, and this is indeed why we chose to use muscarinic drugs in this study. Although M1 and M2 receptors are found in highest density in the GC layer and external plexiform layers (where GCs form dendrodendritic synapses with MC lateral dendrites) they can be found throughout the OB (see Allen Mouse Brain Atlas CHRM1 & CHRM2 genes online; Fonseca et al., 1991; Lein et al., 2007). Therefore, our infusions of scopolamine are mostly targeting GCs and GC dendrites but to a lesser degree also targeting other cells as well.

Oxotremorine has been shown to have strong inhibitory effects on GCs and MCs in the main OB and excitatory effects on MCs and GCs in the accessory OB (AOB) through differential activation of M1 and M2 receptors (Smith and Araneda, 2010; Smith et al., 2015). Interestingly, Smith and Araneda also hypothesized that the direction of the effect may depend on the strength of input to GCs. They argued that when excitatory input onto GCs is weak, M2-mediated hyperpolarization is the predominant effect, reducing inhibition of MCs, but when excitatory input onto GCs is strong (*i.e.*, from excited MCs), the M1-mediated afterdepolarization will prevail, prolonging GC activation and increasing MC inhibition. There may be an interaction between oxotremorine effects on muscarinic receptors and strong odor stimulation triggering long lasting depolarizations in GCs (Egger et al., 2005b; Pressler et al., 2007b). These competing effects may explain the observed tendency for oxotremorine to increase gamma power when odors were absent, but decrease gamma when odors were present (Figs. 3.3Cii, 3.7).

Besides having opposite effects on M1 and M2 receptors, oxotremorine is also capable of activating nicotinic receptors, even though it is classified as a muscarinic agonist (Akk et al., 2005). Given the complexity of interactions, it is not altogether surprising that a drug as nonspecific as oxotremorine produces messy effects in an awake behaving animal, which itself is also most certainly releasing endogenous ACh during the recording session.

Scopolamine produced a biphasic effect in the LFP, first reducing broadband gamma power for ~7 min, followed by an intensification of low gamma while high gamma was still suppressed (Figs 3.3 & 3.4). The opposite effects on the two gamma bands in the 2nd phase may reflect the distinction between type 1 gamma, which depends on MC-GC interactions, and type 2 gamma, which may depend on GABAergic inhibition of GCs, as reported by Kay (2003). Although we ignored inhibition of GCs in our model for simplicity, it is quite possible that in reality scopolamine influences inhibition of GCs to produce contrasting effects on gamma 1 and gamma 2.

3.4.2 Spatial extent of gamma and beta oscillations

Gamma oscillations are thought to be more spatially localized to individual cortical areas and even parts of these areas, while beta oscillations are thought to represent a coordinated oscillation supported by bidirectional connections between OB and PC (Martin et al., 2006b; Kay et al., 2009b; Kay and Lazzara, 2010). Curiously, we found that aPC *beta* power was not significantly reduced when OB beta was reduced by scopolamine, but aPC *gamma* was significantly reduced when

ipsilateral OB gamma was suppressed by infusion of APV (Fig. 3.8D). It has long been known that oscillatory evoked potentials in PC depend on but are not driven by OB input (Freeman, 1968b), and APV desynchronizes MCs from population gamma coordination but does not suppress their firing. Thus, our results suggest that this input must be coordinated with the gamma rhythm in order for the PC to be capable of generating gamma spontaneously. On the other hand, this suggests that PC beta oscillations do not require beta band synchronized inputs from MCs, just some level of tonic excitation, or that the PC does not require very much beta band input from the OB (OB-aPC coherence was hardly affected under scopolamine). Future studies should address the mechanisms for beta vs. gamma generation in the aPC in order to understand this interesting dichotomy.

The effect of APV on anterior OB is very similar to that on medial OB, but with even more aggressive suppression of both gamma frequency bands (Fig. 3.8A,B). Although in some of the rats the drug did not appear to spread fully to the LaOB (see Fig. 3.2B), the gamma suppression was seen in all rats, suggesting that GCs in the more posterior bulb influence the activity of MCs in the anterior portion of the bulb. This aligns well with studies that have shown GCs to mediate between distant MCs via the long MC lateral dendrites, which can span the bulb (Migliore and Shepherd, 2008).

3.4.3 Contralateral effects

In some of the rats there were strong contralateral effects following scopolamine (Fig. 3.6C) and APV (Fig. 3.8C) infusions. We assume that these effects were not

caused by drug spreading into the RmOB, since dye spread was localized to the left side in all rats (Fig. 3.5E). Instead, we suspect that these effects were caused by drug spreading into the anterior olfactory nucleus (AON), which is innervated by fibers that link the two hemispheres through the anterior commissure. Indeed, those rats that had the most posterior dye spread (Fig. 3.2C) had the largest contralateral effects. Muscarinic modulation of anterior commissure fibers was reported by Nickell and Shipley (1993), who hypothesized that cholinergic inputs to MOB may modulate cross-bulbar information. The AON is known to densely innervate GCs (Price and Powell, 1970). Therefore, cross-bulbar communication may be regulated by fibers controlling GC excitability in both hemispheres. We are not aware of any studies relating NMDA-dependent modulation of cross-bulbar information, but our study suggests that this may also be possible. Though it was not our intention, our study provides motivation to more thoroughly study cross-bulbar mediation of gamma oscillations through cholinergic and NMDA dependent effects in the AON.

3.4.4 Implications for odor discrimination

Bulbar infusions of scopolamine have been shown to reduce spontaneous odor discrimination of closely related odorants (fine odor discrimination) in the absence of reinforcement learning (Mandairon et al., 2006; Chaudhury et al., 2009). Gamma and gamma-like oscillations have been functionally related to fine odor discrimination in honeybees, mice, and rats (Stopfer et al., 1997; Nusser et al., 2001b; Beshel et al., 2007). Therefore, it might be expected that bulbar scopolamine would reduce gamma oscillation power. Our model predicted, and we found, that

under scopolamine instead of gamma, beta oscillations were reduced or increased during strong or weak odor exposure, respectively. Because the same conditions that increase odor generalization (muscarinic block) also manipulate beta oscillations, it is possible that beta oscillations are also involved in fine odor discrimination. Thus far, however, the evidence does not support this inference; in the context of operant tasks under reinforcement learning, beta oscillations are either not increased or suppressed during fine odor discrimination (Beshel et al., 2007; Frederick et al., 2016a). However, it should be noted that muscarinic antagonist effects on odor perception appear to depend on the context of the behavioral evaluation (Mandairon et al., 2006).

3.4.5 The role of VDCCs in generating beta oscillations

The persistence of beta oscillations after APV infusion implicates VDCCs in supporting beta oscillations, because AMPAR currents alone could probably not maintain sufficiently strong MC inhibition to support beta oscillations when NMDARs are blocked. In our model we found that beta power would stay relatively constant for moderate NMDA current suppression, but would increase for stronger NMDA current suppression (Fig. 3.1C, bottom). This is because the combination of NMDA and VDCC currents over-inhibited MCs, and a reduction of NMDA current shifted the system closer to a balance of excitation and inhibition, resulting in higher power oscillations. Though not significant, it is interesting to note that the LaOB showed some beta increases (Fig. 3.8A), which could potentially be attributed to a

decrease in over-inhibition that occurs when NMDA is significantly blocked (assuming the system started in an over-inhibited state as shown in Fig. 3.1C).

An obvious next step would be to directly test the involvement of N-Type VDCCs in generating beta by infusing the N-type calcium channel blocker ω-conotoxin, but we leave this for future experiments. GCs are also known to express other VDCC subtypes, notably T-type channels which mediate Ca^{2+} spikes that can spread activity across the entire dendritic arbor to synchronize inhibition of all MCs connected to a given GC cell (Egger et al., 2005b). The role that VDCCs play in OB oscillations is still being researched, but our results suggest that they are necessary for switching between gamma and beta oscillatory states in OB granule cells.

3.4.6 Concluding Remarks

In summary, we found confirmation of our model's main predictions, that reduced GC excitability can have a bidirectional effect on the power of OB beta oscillations, and that OB beta oscillations can be sustained independently of NMDARs. Going beyond the scope of our model, we also recorded PC beta oscillations. Though PC and OB beta oscillations had nearly identical frequency (Lowry and Kay, 2007b; Kay and Beshel, 2010b), we found that reductions in OB beta power through reduced GC excitability were not accompanied by significant reduction in PC beta power. Furthermore, OB-PC coherence was also not significantly reduced, even when OB beta power was dramatically reduced. It is possible that an OB-PC loop was sustaining PC beta, even though the beta component in the OB was very small under these conditions. The drug is most likely

not targeting all GCs in the bulb equally, and some might be able to maintain an intact OB-PC loop. It is also possible that PC is just driving a small beta signal in the OB. Interestingly, a model of OB beta generation from a different group did not require OB and PC to coherently oscillate at beta frequency, but rather required a slow (theta frequency) modulation of GC excitability by PC inputs (David et al., 2015b). Our model also did not involve an oscillating PC, and the persistent beta coherence we found in experiments suggests that the existence of OB-PC beta coherence is not itself sufficient for generating full-blown OB beta oscillations. While intact bidirectional OB-PC connections are required to generate beta oscillations, the GCs appear to control OB beta power, and to mediate the transition from gamma to beta oscillations.

GCs can exert at least four distinct types of inhibition onto MCs (Mouret et al., 2009b). Dendrodendritic MC-GC connections can support local recurrent and lateral graded inhibition without GC somatic action potentials. But when GC action potentials are triggered, either by strong distal inputs or from MC or cortical inputs to the proximal dendrites near the soma, it is hypothesized that GCs switch to a global inhibition state, characterized by synchronous GABA release from all distal spines (Egger et al., 2005b; Egger, 2008b). The model developed by David et al. (2015) showed that switching between local and global inhibitory spiking GC states could drive transitions between gamma and beta oscillations, though the characteristics of GC firing patterns during beta oscillations have yet to be reported.

4. Measurements of extracellular potentials of olfactory bulb granule cell layer interneurons in awake behaving arts

4.1 Introduction

The modeling work (Osinski and Kay, 2016) and subsequent pharmacological experiments (Osinski et al., 2017) described in the past two chapters strongly argued that odor-evoked beta oscillations should occur during periods of heightened GC excitability. In these final experiments, we set out to characterize the firing patterns of individual GCs during beta oscillations. Although our model did not explicitly rely on spiking GCs, it implicitly assumed that GC firing would trigger the long lasting ADP (LLD) responsible for heightened GC excitability driving greater GABA release onto MCs resulting in sustained beta oscillations. In slice experiments GCs did not fire action potentials during the LLD (Egger et al. 2005; Pressler et al. 2007). These data, together with our model predictions, predict that GCs should fire at the onset of beta, but then remain inhibited throughout the duration of the excitability increase. As described below, we did indeed find such cells, but we also found a rich diversity of firing patterns possibly reflecting plasticity and different GCL cell types.

While this series of experiments was conducted to test the model's predictions, it was also exploratory in nature, as GCs have never been recorded in freely behaving rats before. The only recordings of GCs in awake animals to date were done under head-fixed conditions, and the correlation of firing patterns to the

LFP was not investigated (Cazakoff et al., 2014). We therefore expected these experiments would go beyond the scope of our model and reveal novel spike-field relationships of odor-evoked inhibitory cell activity.

4.2 Overview of experiments

For these experiments, 3 rats were successively implanted (about 2 months apart) with 32-channel Si probes (Cambridge Neurotech [model DBC2 probe]). Because the experiments were exploratory in nature, the experimental design evolved as more data were collected. Thus, not every rat performed the same experiments. The experiments are grouped into four categories, which are presented in Table 4.1 indicating which rats were used for each experiment.

Rat name	Single odor swab pres.	Multi-odor swab pres.	Nose-poke 1 odor full reward	Nose-poke 2 odor half reward
RK90 (Rat1)	EMB, GER, PP			
RK97 (Rat2)	EMB, GER, PP	EMB, GER, NA	EMB,GER	
RL16 (Rat3)	EMB, GER	EMB, GER, PP, NA	EMB, GER	EMB, PP

Table 4.1 Table of Si probe experiments showing which odors were used for each rat. For the Multi-odor swab pres. the order in which odors were presented is shown. EMB - Ethyl 2Methyl Butyrate (high volatility, VP 1.048 kPa), GER – Geraniol (low volatility, VP 0.0018 kPa), PP – Propyl Propionate (high volatility, VP 1.333), NA – Nonanoic Acid (low volatility, VP 0.0012 kPa).

The Single odor swab presentation experiments were the first experiments run on the rats and consisted of 30 presentations of an odorant-soaked cotton swab to a freely behaving rat in a clean cage with fresh bedding, much like the pharmacological experiment design (only one of the odors used in each session). The Multi-odor swab presentation experiments were similar except that multiple odorants were presented in a fixed interleaved order 30 times each (all odors in the same session). The order in which the odors were presented is shown in Table 4.1.

For the Nose-poke experiments, we trained rats to poke their noses into an odor port, which delivered odors using a computer controlled vacuum system and allowed us to measure the time at which rats poked their noses with an IR beam emitter-receiver system (see *Methods*). In the Nose-poke 1 odor full reward sessions, only a single odorant was used per session and each nose-poke was rewarded by a sugar pellet. In the Nose-poke 2 odor half reward sessions, the rat received one of two high volatility odors, EMB or PP. For the first half of the session both odors were rewarded, but rewards ceased for one of the odors half way through the session. This change in the experimental paradigm was designed to test the reward contingency of GCL neuron responses.

To analyze these data, I developed a python-based toolbox of analysis functions, which can be found in *Appendix II: Spike-Field Analysis Functions*. Wherever a specific function is used, I provide the name of the function so it can quickly be referenced in the toolbox.

4.3 Methods

Subjects were 3 adult male Sprague-Dawley rats (350 - 450 g; purchased from Envigo (Harlan)), maintained in the colony room on a 14 –10 h light/dark schedule (lights on at 08:00 CST). Rats were housed singly after electrode implantation. They had access to unlimited food and water for the course of the odor swab presentation experiments and were put on a restricted diet (80% of *ad libitum* weight) during the course of the nose-poke experiments. All animal procedures were done with approval and oversight by the University of Chicago Animal Care and Use Committee with strict adherence to AAALAC standards.

4.3.1 Electrode implants

32-channel Si probes (pictured in Fig. 4.1) were obtained from Cambridge Neurotech. Before each surgery, rats were given a subcutaneous injection of ketamine cocktail (35 mg/kg ketamine, 5 mg/kg xylazine, and 0.75 mg/kg acepromazine). Anesthesia was maintained by checking for reflexes every 15 min and administering intraperitoneal injections of ketamine. After ear bars were firmly in place, an incision was made along the sagittal suture from the anterior OB to the cerebellum and the skull was cleared of connective tissue. A small (~2 mm) hole was drilled over the left main OB and all bone and dura fragments carefully removed. Another hole was drilled over the right cerebellum for a ground screw and four more additional holes were drilled for support screws. All screws were then inserted.

Prior to surgery, a tiny amount of dental wax was placed in the rectangular notch of a vacuum chuck (obtained from Cambridge Neurotech) to improve adhesion to the body of the silicon probe. The vacuum chuck was fixed to a stereotaxic arm. The probe was carefully placed onto the vacuum chuck, with the flex cable covering all vacuum holes, and the probe body was gently nudged to adhere to the dental wax.

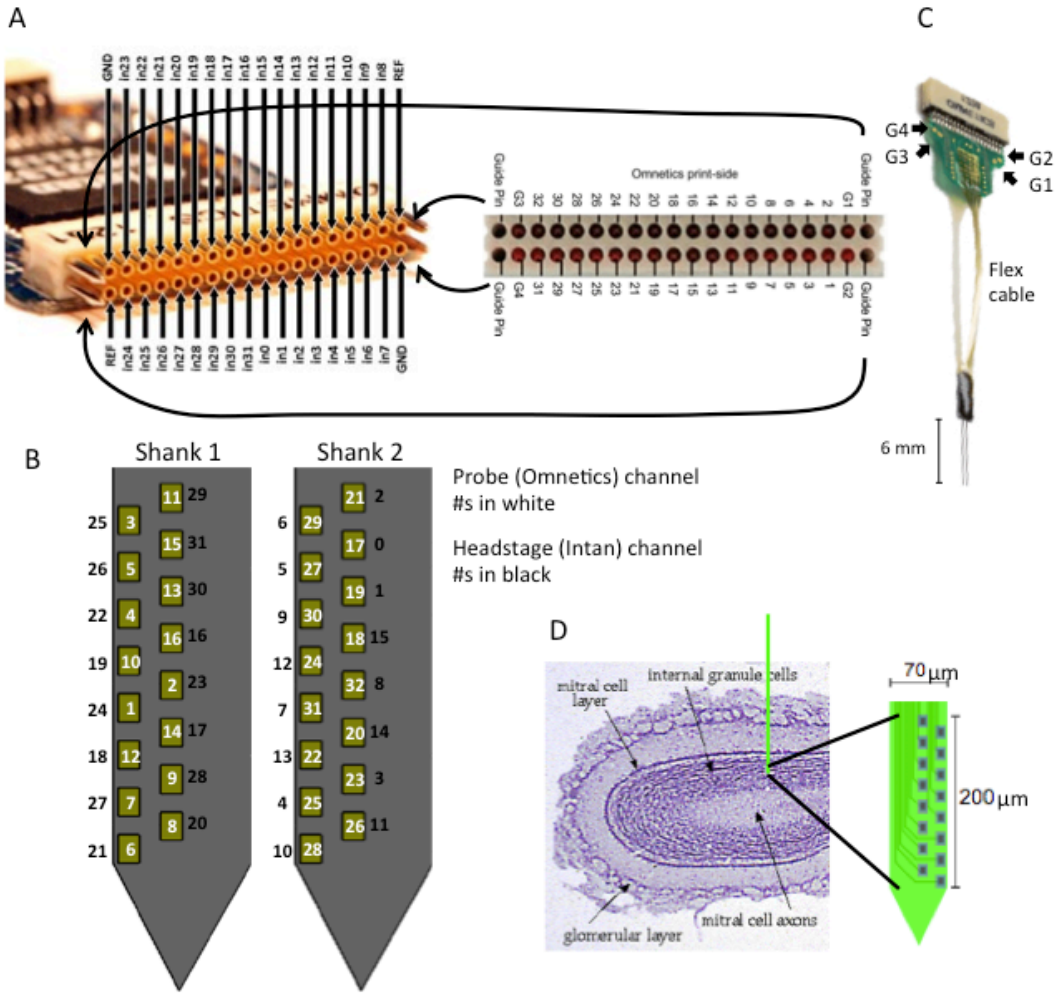

Figure 4.1 Probe channel mapping and dimensions. A) The Omnetics connectors of the probes (right) and connectors of the Intan headstages (left) use different numbering systems so one must be mapped to another. **B)** Channel mapping of probe to headstage connectors. **C)** Image of entire probe-connector assembly with ground pins marked. Only two ground pins were used. **D)** Probe dimensions and approximate position in GCL are shown. (Probe images provided by Cambridge Neurotech www.cambridgeneurotech.com, Intan headstage image from intantech.com/RHD2132_RHD2216_amp_board.html)

The vacuum alone was not strong enough to hold the omnetics connector, so the connector was taped to the arm of the vacuum chuck. Minor adjustments were made to the hinge of the vacuum chuck to ensure the probe was as vertical as possible.

The probe was lowered until it touched the surface of the brain and zero point was recorded. The probe shanks were so thin that the surface vasculature would often cause them to buckle, so micro adjustments were made to the stereotaxic arm until the probe slid into the brain tissue. Because the probe was so delicate, we wanted to avoid any unwanted movement of the probe, so we elected not to plug the probe in to monitor signals during probe insertion. Instead, the probe was inserted blindly to a depth of 1.5 mm relative to the zero point, which should place it within the dorsal GCL.

After placing the electrode, a few drops of Dura-Gel compound were mixed at 1:1 ratio. A droplet of the compound was pipetted into the hole to repair and reseal the durotomy. The Dura-Gel compound dries to a jelly-like consistency, cushioning the probe, and preventing dental cement from flowing into the hole. After the Dura-Gel dried, we coated the exposed probe shafts with Gorilla Glue, which improves adhesion of dental cement. Then we applied dental cement to the fix the probe in place, securing it to the nearest skull anchor screw.

Once the dental cement securing the probe had dried, a thin stainless steel wire, which was soldered to the ground pins on the probe's PCB board prior to surgery, was wrapped around the ground screw. The entire area was then encased in dental cement, with the flex cable folded inside and the omnetics connector aligned parallel to the rostral-caudal axis. After drying, the wound was cleaned and sutured, and the

rat received 0.1 mL Buprenex subcutaneously before being placed in a clean recovery cage. Rats were allowed to recover for 2 weeks after surgery before beginning the experimental protocol.

4.3.2 Data Acquisition

Raw data were digitized and amplified by an Intan RHD2132 headstage (http://intantech.com/RHD2132_RHD2216_amp_board.html), collected with an Open Ephys acquisition board (http://www.open-ephys.org/acq-board/) and preprocessed with Open Ephys GUI (http://www.open-ephys.org/gui/) on a computer running Windows 7. The 32 raw data signals were high pass filtered from 300 – 6000 Hz. One of these channels was also copied and low pass filtered from 1 – 300 Hz to obtain an LFP signal (see top of Fig. 4.2). We only used one channel for the LFP because the low pass signals from all the channels were virtually identical. The full data processing pipeline is depicted in Fig. 4.2.

4.3.3 Noise removal

The spike recordings suffered from several types of noise: Large deflections (> 20 standard deviations), small deflections (< 20 standard deviations), oscillatory noise, and single channel noise. Examples of each type of noise are depicted in Fig. 4.3. These had to be removed before clustering because they would dominate the principal components and render clustering ineffective. Below we describe each type of noise and procedures for its removal.

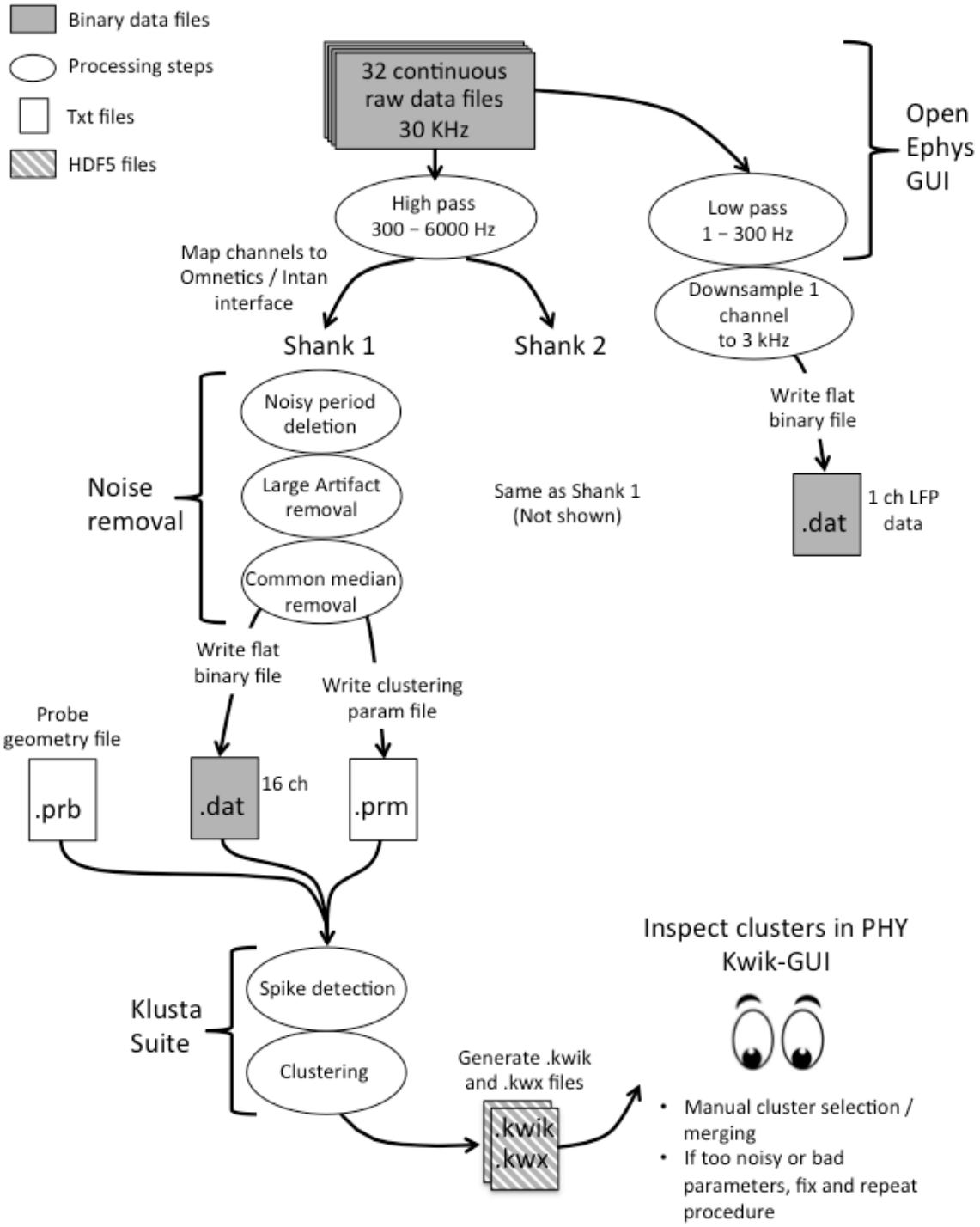

Figure 4.2 Spike data processing pipeline
High and Low pass filtering were performed during recording by Open Ephys, noise removal was performed by custom written python scripts, spike clustering was performed by the Klusta suite, and manual spike curating was performed through Phy Kwik-GUI.

4.3.3.i Large artifact removal

Large positive and negative deflections, several hundred std above the mean (Fig. 4.3A), were detected by a threshold (usually set to 20 std above mean) and replaced by zeroes symmetrically about the peak of the artifact up until the data reached ½ the standard deviation (ensuring no leftover peaks). The noise deflections in Figure 4.3A are coincide with the switching of the solenoids on each trial of the nose-poke experiment. We modified the artifact removal algorithm in the BARK toolbox developed by Kyler Brown (https://github.com/kylerbrown/bark) to apply the treatment to all channels simultaneously since large amplitude deflections on some channels would often be accompanied by smaller amplitude deflections on other channels that did not cross the threshold for removal.

4.3.3.ii Small artifact, oscillatory noise, and single channel noise removal

There were three types of noise that were too low in amplitude to be removed by thresholding: Small deflections (Fig. 4.3B, due to head movement), oscillatory noise (Fig. 4.3C), most likely originating from higher harmonics of 60 Hz noise that survived the high pass filter) and single channel noise (Fig. 4.3D, source unknown). These had to be detected by hand. Before clustering, the traces were inspected by eye to find obvious noisy periods. However, in many cases these noisy periods were not noticed until after the noise showed up in the clusters, leading to a process of clustering, notating noisy periods by eye, and re-clustering with noisy periods removed.

Sometimes we were unlucky to find a channel that produced many good spikes suddenly becoming noisy. When this was the case the noisy periods would be set to 0. Otherwise, any channel with substantial single channel noise was deleted completely. Removal of as many noise periods and channels as possible was crucial

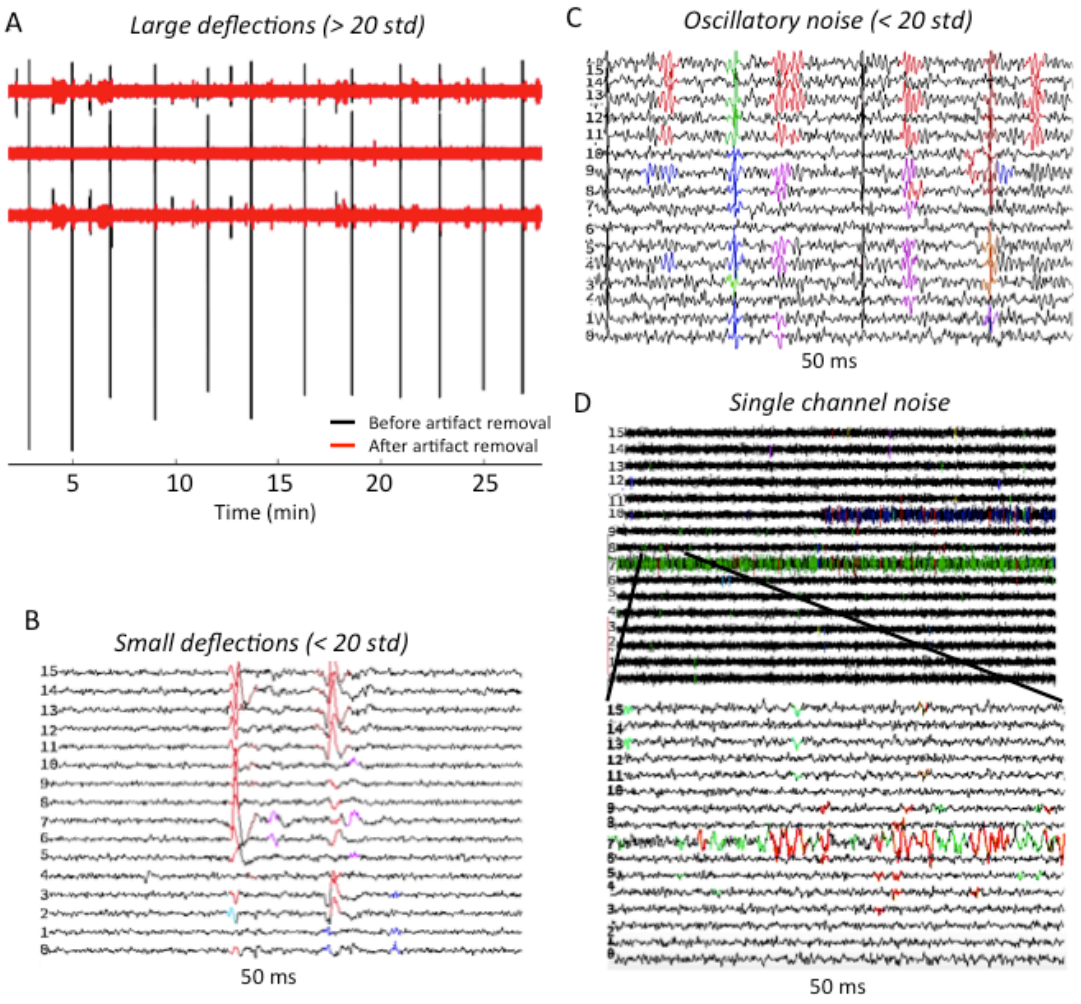

Figure 4.3 Examples of noise in neural recordings. A) High amplitude deflections (black) could easily be detected and removed with automated scripts. The large deflections in this particular example were caused by the switching of odor-delivery solenoid valves during a nose-poke experiment. The remaining small deflections after artifact removal (red) are neural spikes. **B, C)** Small noise deflections **(B)** and oscillatory noise **(C)** was harder to remove automatically without jeopardizing spikes of similar size. In the examples shown, these deflections are incorrectly classified as spikes (grouped by color). We therefore had to remove these periods by hand, often only noticing them after the data had been clustered. **D)** Single channels could suddenly become extremely noisy. If the noisy channel did not contribute many good spikes, it was deleted.

because any noise skewed the principle components, leading either to poor separation of clusters or to merging of too many clusters. The 2nd shank for Rat 3 appeared damaged, as it was very noisy on most channels and only produced a few small amplitude spike clusters, so we excluded the entire shank from the analysis.

4.3.3.iii Common median removal

Spike detection pipelines often include common average removal, where the mean signal at all time points is subtracted from each channel. This allows spikes to be better localized to individual channels. We used common median removal because the median is less sensitive than the mean to large fluctuations and has been shown to improve action potential detection on multielectrode arrays (Rolston et al., 2009). This step of preprocessing was crucial to identifying spatially localized spikes, because the high-passed channels covering such a small area had a great deal of common signal.

4.3.4 Spike detection and clustering via Klusta Suite

To extract unique spike clusters from our multichannel data, we used Klusta Suite (Rossant et al., 2016), a spike detection and clustering toolbox designed to cluster spikes recorded from arrays of arbitrarily large size. A detailed description of the toolbox can be found in the cited paper. Briefly, spikes are detected as spatiotemporally connected components across nearby channels via a two-threshold flood fill algorithm. The weak threshold defines the pool of channels

contributing to the cluster, while the strong threshold defines the largest spike in the group. The dual-threshold approach avoids spurious detection of small noise events that don't cross the strong threshold and ensures that spikes will not be erroneously split due to noise, because areas joined by weak threshold crossings are merged. The detected spike event groups are then clustered with the klustakwik2 algorithm, which employs a novel statistical method for high-dimensional cluster analysis termed the "masked EM algorithm." Much like the traditional EM algorithm, it fits data as a mixture of Gaussians, typically from just the first 3 PCA components, but uses a channel mask so that channels outside the mask do not contribute to cluster alignment. Once finished, klustakwik2 produces .kwik and .kwx files, both in HDF5 format, which contain all cluster information (see bottom of Fig. 4.2).

The Klusta suite has a one-sided threshold, and must therefore be run separately to detect negative and positive spikes. Although the Klusta suite authors found optimal values of 4 and 2 times the standard deviation for strong and weak spike detection thresholds, I found these values produced poor positive threshold clusters that appeared in small islands spread across the entire probe. I explored the parameters on a few small data sets and found better looking clusters with strong/weak values of 4.5 and 2 for negative spike detection and 4.5 and 1.5 for positive spike detection.

4.3.5 Probe files

The Klusta suite requires a probe file (extension .prb) that defines the probe geometry in order to group deflection from nearby channels with the flood-fill

algorithm. Although probe files in principle are able to contain multiple shanks, we designed separate prb files for each probe following advice on the klustaviewas@groups.google.com mailing list, which identified bugs in klustakwik2 when running for multiple probes. For this reason we run the entire data processing pipeline (Fig. 4.2) on each shank separately.

4.3.6 Manual spike sorting and merging

The clustering results must be inspected manually to isolate noise clusters from true spike clusters. We visualize the clustering results with the Phy Kwik-GUI (https://github.com/kwikteam/phy), which is designed to process the .kwik and .kwx files (bottom of Fig. 4.2). Noise clusters were identified on the basis of atypical waveforms, overly periodic correlograms, and unusual temporal organization (i.e. all spikes coming from a 2s slice of time). We also took care to remove misidentified positive/negative spikes (See Fig. 4.4). That is, when running for negative spikes,

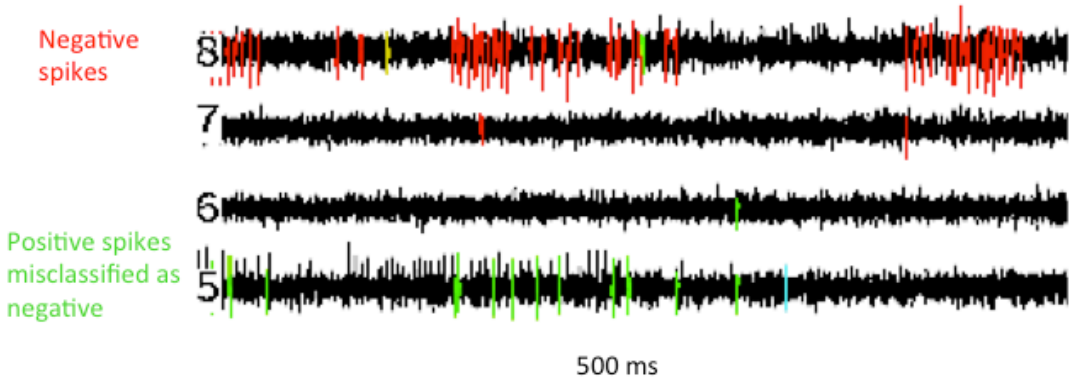

Figure 4.4 Negative and positive spikes. Example traces viewed in Phy Kwik-GUI showing negative spikes on channel 8 (red), and positive spikes on channel 5 (green) which were misclassified as negative. In this example positive and negative spikes occur on different channels, but they are also often found on the same channel.

any positive spike clusters that happen to accumulate are discarded, so as to avoid double counting in the positive spike cluster group.

After removing noise clusters from spike clusters we identify which clusters should possibly be merged on the basis of waveform similarity. Although the Phy Kwik-GUI has cluster merging capabilities, it would often freeze and crash, making the process overly tedious. Rather than endure these frustrations we performed cluster merging ourselves (see merge_clust in *Appendix II*). This approach proved superior because if the ISI after merging were to produce two humps instead of merging into a single seamless ISI, then the clusters could easily be left separate.

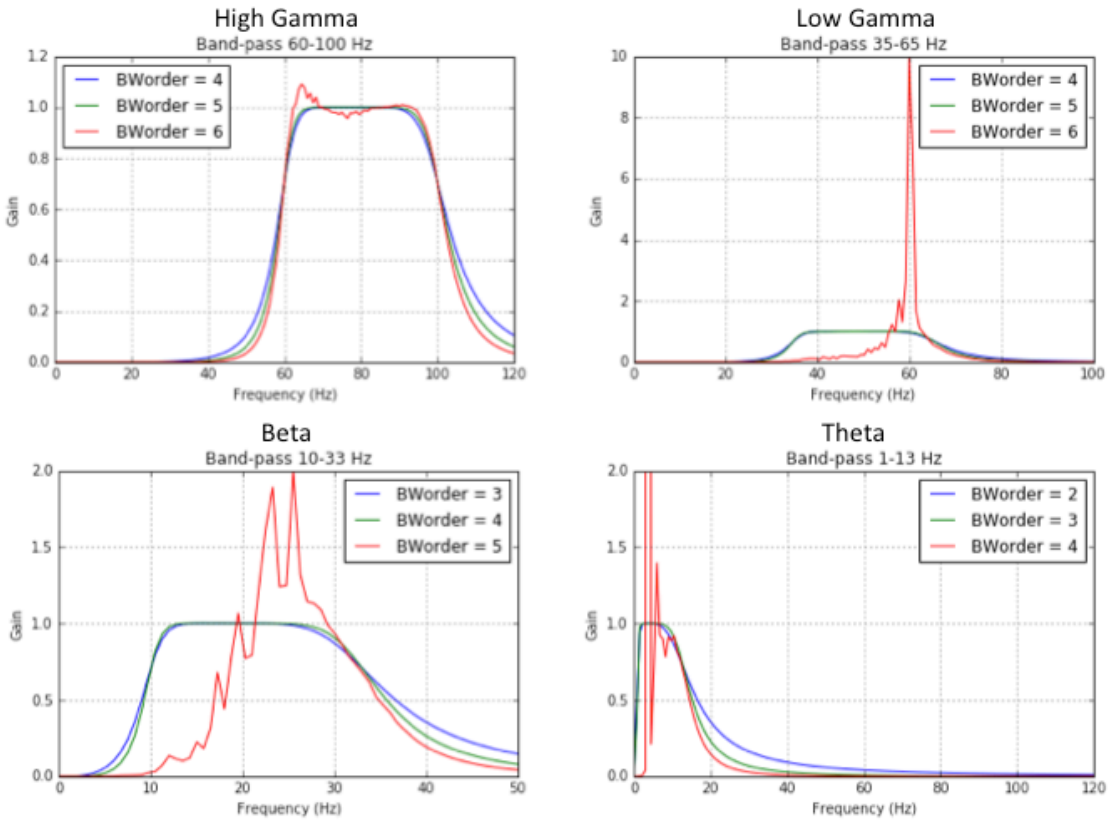

Figure 4.5 Design of Butterworth filters for gamma, beta, and theta frequency bands. For each band the filter order that gave the sharpest noiseless filter was chosen.

4.3.7 Design of Butterworth filters for theta, beta, and gamma frequencies

In order to isolate LFP activity in the theta, beta, and hi/lo gamma bands we used the butter function of the scipy.signal package. The order of the filters had to be chosen for each frequency band to generate smooth gain curves with the sharpest edges (Fig. 4.5). Optimal orders were theta: 3, beta: 4, hi/lo gamma: 5. After filtering, the envelope of the filters was obtained from the absolute value of the Hilbert transform of the filtered signals (see butter_env in *Appendix II*).

4.3.8 Spike- LFP phase histograms

To obtain the LFP oscillation phase we first filtered the LFP signal for the desired frequency band: either theta (4 – 15 Hz), beta (15 – 30 Hz), low (40 – 60 Hz) or high gamma (60 – 100 Hz). Then we took the Hilbert transform of the filtered LFP, represented as $H(x)$. The instantaneous phase of the filtered LFP signal was then calculated as

$$\phi_{inst} = \tan^{-1}\frac{Im(H(x))}{Re(H(x))}$$

The strategy for obtaining the spike-LFP phase histograms had to differ slightly for each frequency band because of their different temporal properties. Theta oscillations persist throughout the entire recording session, and therefore the spike-phase product was calculated for spikes in the entire recording session. Low and high gamma occur intermittently (usually at the peaks of theta oscillations), but because they are transitory, we had to restrict the calculation to periods with

gamma power above a certain threshold. By trial and error, I found 1.6 times the median gamma power to be a good threshold for gamma power strict enough to exclude most non-oscillatory periods, but generous enough to include smaller amplitude gamma oscillations.

Beta oscillations are also intermittent and transitory, but they are primarily odor evoked. Thus, we calculated beta phase histograms from thresholded regions restricted to odor periods. Since the power of beta oscillations spanned a narrower range than gamma, we used a stricter power threshold than for gamma of 0.4 times the median of the maximum beta power of each odor period. This ensured that only spikes during odor-evoked beta oscillations were used for the analysis. Reliable phase histograms could not be produced if cells fired less than 30 spikes in all odor periods combined and were thus excluded for this analysis (see spike_field_prod_with_rand and SPH_wrapper in *Appendix II*).

4.3.9 Finding peak LFP phase preference of spikes

We found that the phase histograms (as described above) were often sinusoidal or Gaussian. Rather than use just a Gaussian or sinusoid fit to find the phase at which cells fired the most, we calculated both Gaussian and sine fits, and chose the one with the lowest error. The argmax (x-value at which a function is maximum) of this fit was reported of the preferred phase of the cell. (See get_peak_phase_sinORgauss in *Appendix II*)

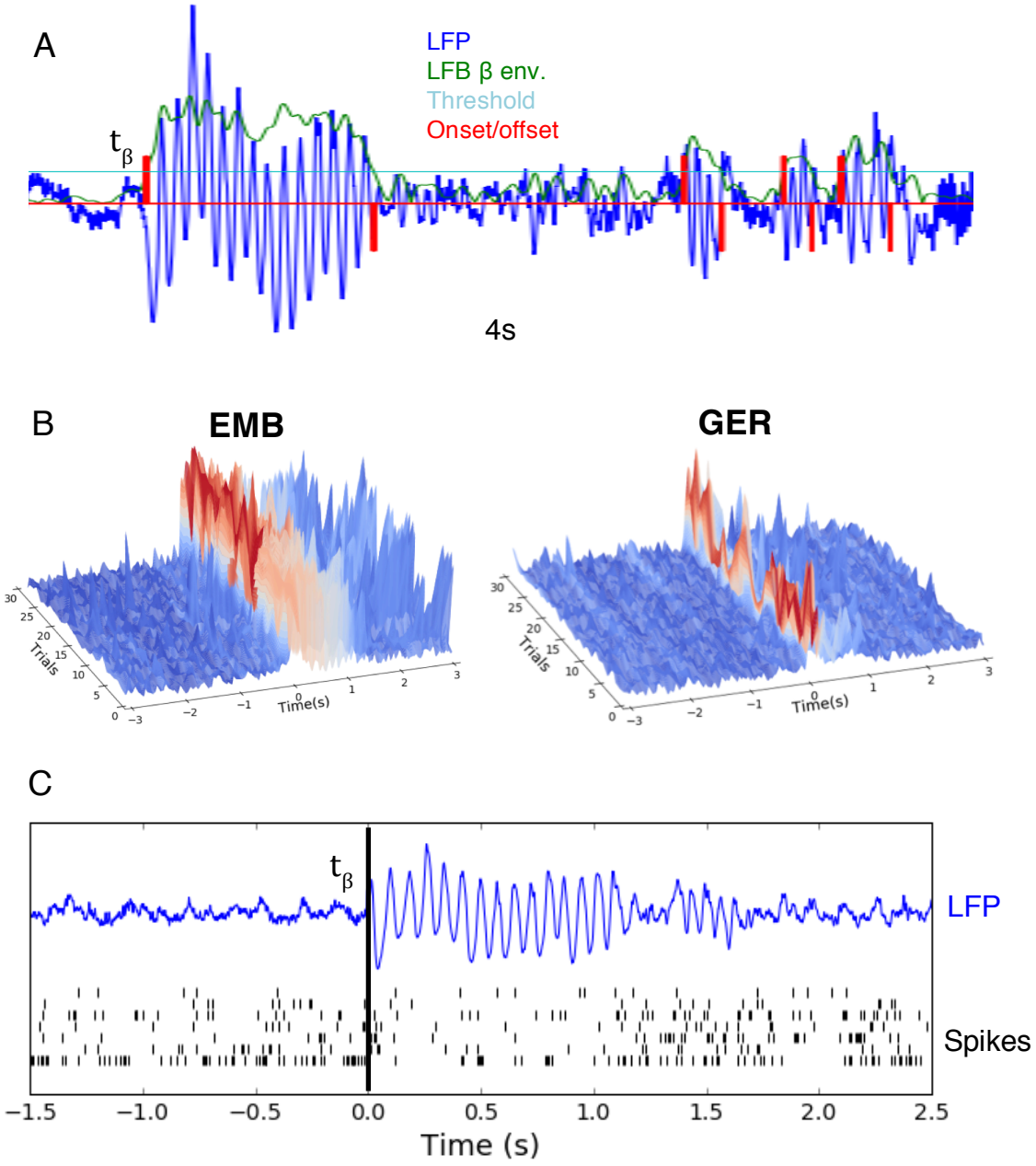

Figure 4.6 Aligning spikes to beta onset. A) An odor (EMB) presentation time window showing bandpass filtered LFP (blue), beta envelope (green), threshold (light blue), and beta onsets (red positive) and offsets (red negative). When multiple beta events were detected, only the first crossing of the beta envelope threshold in the was used to align spikes (labeled t_β). **B)** Representative beta filtered LFP envelopes for all 30 trials of EMB (left) and GER (right) presentations aligned to beta onset as described in **A**. Even though GER-induced beta oscillations are much lower in amplitude, most trials still appear well-aligned. **C)** Alignment of spike trains to beta onset (t_β) from 7 simultaneously recorded GCL neurons. In this example, some of cells were inhibited for ~1s following the onset of the beta oscillation.

4.3.10 Aligning spikes to beta oscillations

In the absence of any precise measure of stimulus onset for the odor swab presentation experiments, we aligned spikes to the onset of odor-evoked beta oscillations. Our procedure for aligning spikes to beta is depicted in Figure 4.6. For each trial we filtered the LFP to obtain the beta envelope and found the time at which the envelope first crosses a threshold in the window (t_β as illustrated in Fig. 4.6A). Here we used a threshold of 0.6 times the median of the max beta power in all odor periods, which was stricter than the one used for spike-field coherence calculations, below. The stricter threshold was primarily chosen because it resulted in higher peaks of the beta-aligned PSTH.

As can be seen in Fig. 4.6B, this alignment strategy produces consistently aligned beta LFP envelopes across all trials of an experiment for both high volatility and low volatility odor evoked beta oscillations (see align_spikes_to_beta in *Appendix II*).

4.3.11 Spike field coherence

Coherence is defined as

$$C_{X,Y} = \frac{P_{XY}^2}{P_{XX}P_{YY}}$$

, where P_{XY} is the cross power spectral density between signals X and *Y,* and P_{XX} and P_{YY} are the respective power spectral densities. This produces a value bounded between 0 and 1. To calculate coherence between any two signals both signals must have the same time resolution. For spike-field coherence (SFC), we bin spikes into

time bins of the time resolution of the LFP signal, which in our case is 3 kHz. We computed SFC with the python function scipy.signal.coherence (see spike_field_coh in *Appendix II*).

Because gamma and beta oscillations are transitory, the SFC had to be calculated during power thresholded periods. Our procedure for calculating SFC is

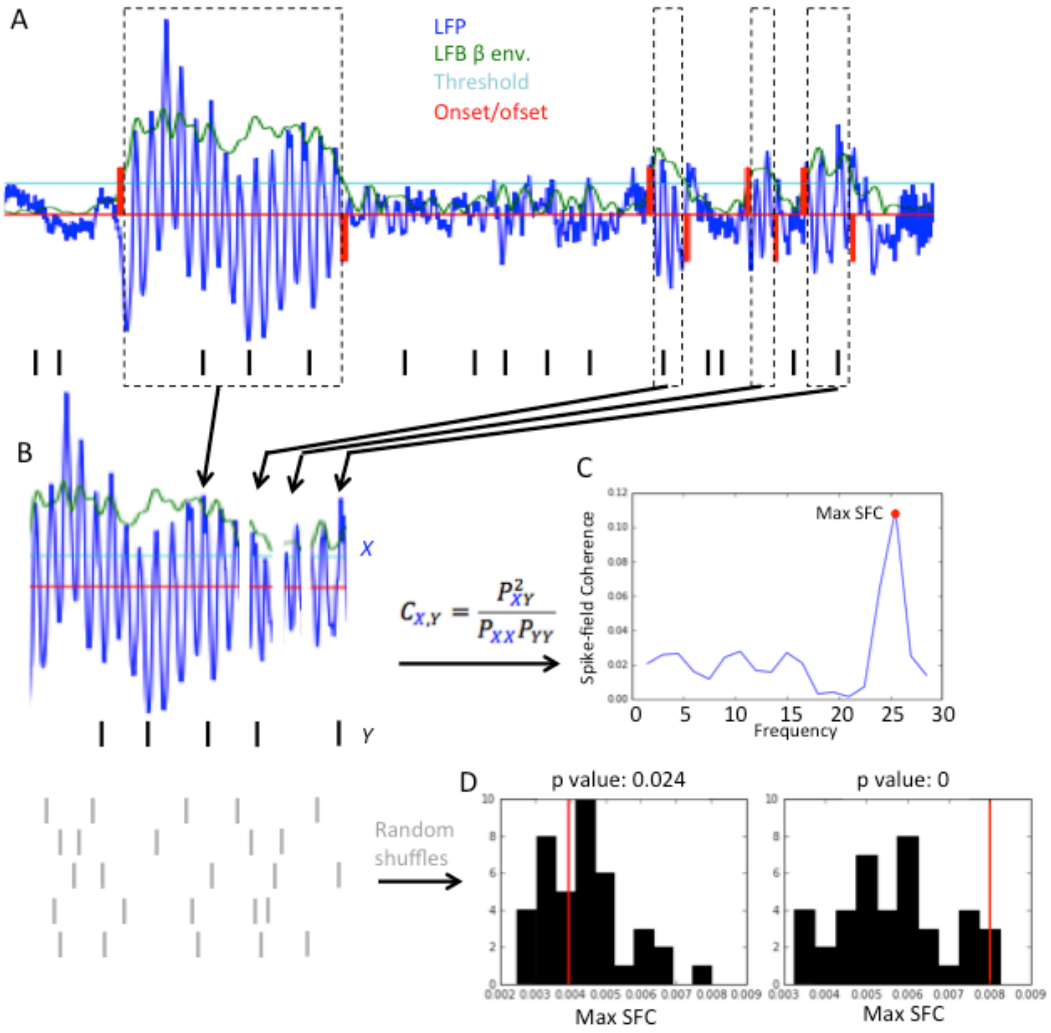

Figure 4.7 Diagram illustrating procedure for calculating spike-field coherence for beta oscillations. A) Beta oscillation periods are detected by threshold crossing of beta filtered LFP envelope. **B)** The LFP oscillation periods are stitched into a one dimensional array. The same is done for the spike times. Spike times are binned into same time resolution as LFP. **C)** The coherence between the binned spikes and LFP is computed as the ratio of cross spectral density to power spectral densities of LFP and spike trains. The maximum SFC is reported (red dot). **D)** The same procedure is produced for 50 random shuffles of the spikes. A 1-sided 1-sample T-test is used to determine if the true SFC is significantly higher than the mean SFC of the random shuffles.

schematically shown in Figure 4.7. The same thresholds were used as for the spike-phase histograms (Fig. 4.7A). We found that calculating the SFC for each thresholded period individually was not viable because most of the periods did not contain enough spikes to produce a statistically meaningful measure. Fixed windows could not be used for the calculations because inclusion of spikes during non-oscillatory periods drove the SFC down to chance levels. Therefore, we stitched all the thresholded LFP periods together, taking care to keep track of the cumulative start times of each period to adjust the corresponding spike times accordingly (Fig. 4.7B). The SFC was then computed and the argmax (x-value at which a function is maximum) of the coherence spectrum (Fig. 4.7C) was taken as the SFC of that cell (see SFC_wrapper in *Appendix II*).

Statistical significance of the SFC measure was measured by a 1-sample T-test (scipy.stats.ttest_1samp) to determine if the true SFC is significantly greater than the mean SFC of 50 random shuffles (Fig. 4.7D). The p-value of a one-sided T-test is just half that of the two-sided T-test, so we divided the output of scipy.stats.ttest_1samp by 2 and cells with SFC lower than the mean of the random shuffle were excluded. A significant threshold of 0.001 was used, though most cells that were significant had p-values < 1e-10.

We noticed that SFC calculations for low amplitude beta oscillations were biased by the fact that the low amplitude beta events were typically very short, some lasting less than one oscillatory cycle. When stitching together many such short events, as described above, we created a synthetic signal that artificially inflated the value of the SFC. Thus SFC values for low volatility odors GER and NA

were higher on average than the high volatility odors EMB and PP, even though phase histograms for the high volatility odors tended to appear more peaked. SFC should ideally be calculated on data segments of equal lengths, but because the GER and NA – evoked beta oscillations were usually brief and interspersed with gamma oscillations, while EMB and PP evoked beta oscillations appeared in long stretches, the data itself did not allow a fair comparison. For this reason, we only present SFC values for the high volatility odors.

4.3.12 Peri-stimulus time histograms

To calculate peri-stimulus time histograms (PSTH) spikes were binned into uniform bins over a window spanning each odor presentation. The spikes in each window were then aligned either to the onset of the beta oscillation, or to the nose-poke time if the rats were in an operant box. PSTHs of the aligned spikes were then calculated by binning spikes, averaging across trials, and dividing by the bin width to get units of rate (Hz). We used bin width of 200 ms for visualization of dynamics over several seconds, and 50 ms time bins for visualization of faster dynamics (See calc_PSTH in *Appendix II*).

4.3.13 Spike-Distance analysis

A spike distance metric was used to obtain a measure of the prediction accuracy of each cell recorded in the multi-odor presentation experiments. These experiments had 30 trials per odor, giving 90 spike trains total for the rat with 3 odors, and 120

spike trains total for the rat with 4 odors (Rats 2 & 3 in Table 4.1). All spike times were aligned to the onset of the odor evoked beta oscillation, and a 2s window starting 0. 2s before beta onset was used for this analysis. A python implementation of the Victor & Purpura (1993) spike distance metric was used to calculate the distance between every pair of spike trains at a fixed cost *q* (units 1/s), producing a symmetric distance matrix for each cell (see Fig. 4.8A for example distance matrices and distance_between_all_trials in *Appendix II*).

To obtain prediction accuracy from each distance matrix, the distances were grouped by odor and summed them for each trial, reducing a matrix of dimension N_{trials} x N_{trials} to a matrix of dimension N_{trials} x N_{odors}. The odor giving the shortest distance was taken as the predicted odor for that trial. The prediction accuracy is then the number of correctly predicted trials divided by the total number of trials. This was repeated for a range of cost values ranging from 1/(0.1ms) to 1/(2s) (The cost is the inverse of the time resolution).

As a sanity check, an alternative method of spike train classification based on correlation between spike trains and PSTHs on a subset of cells was also used. For this method, we first bin all spike times into 0.1 ms bins and then calculate the PSTH for each odorant (of a given cell), leaving one spike train out. We smooth the PSTH and the isolated spike train with a Gaussian of width W and compute the correlation coefficient between the smoothed spike train and smoothed PSTHs. The predicted odor of the spike train is the odor class of the PSTH with highest correlation to that spike train. If it is the same as the odor that actually produced the spike train, then the classification is correct. This is repeated for each spike train for a range of

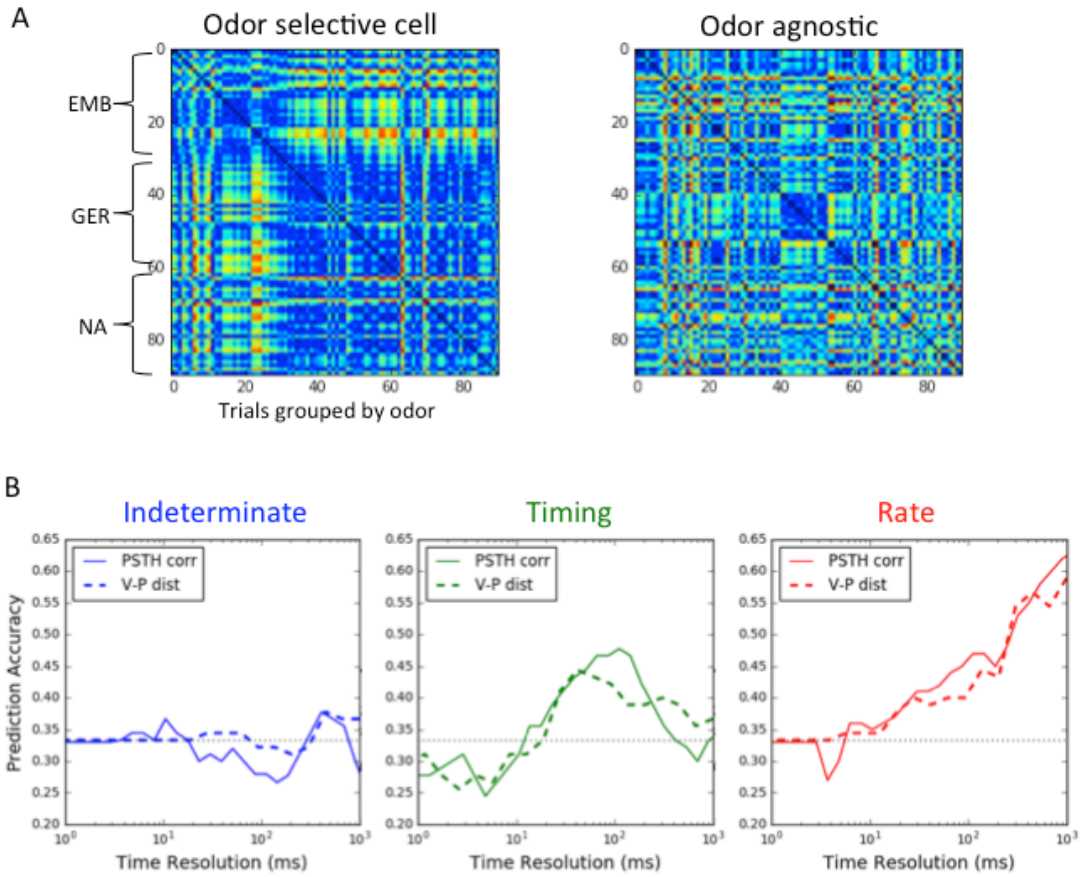

Figure 4.8 Computing odor prediction accuracy of individual cells using a spike distance metric analysis. A) Representative Victor-Purpura distance matrices for a cell with a preference for EMB (left), and another cell that showed no preference for the 3 odors presented. Although odors were interleaved in these experiments, the trials are rearranged to be grouped by odor in the distance matrices to facilitate the analysis and for visualization. **B)** Comparison of prediction accuracies obtained by the Victor-Purpura method (dashed) and alternate PSTH correlation based method (solid) for indeterminate (blue), timing (green), and rate (red) cells. For V-P method the time resolution is the inverse of the cost (1/q), but for PSTH corr method the timing resolution is the width of the smoothing Gaussian.

Gaussian bin widths W ranging from 1 ms to 2 s (the entire length of the window). Taking the width of the Gaussian as the timing resolution and calculating prediction accuracy as before, we found that this method produced results similar to the Victor-Purpura based method (Fig. 4.8B).

4.3.14 Visualization of neural population response trajectories

In order to visualize the evolution of the population response over time we performed dimensionality reduction. This analysis was performed for the multi-odor swab presentation experiments (2nd column of Table 4.1). Because individual trials were highly variable, we performed dimensionality reduction on the beta-onset-aligned PSTH instead of individual trials. PSTHs were computed with 100 ms

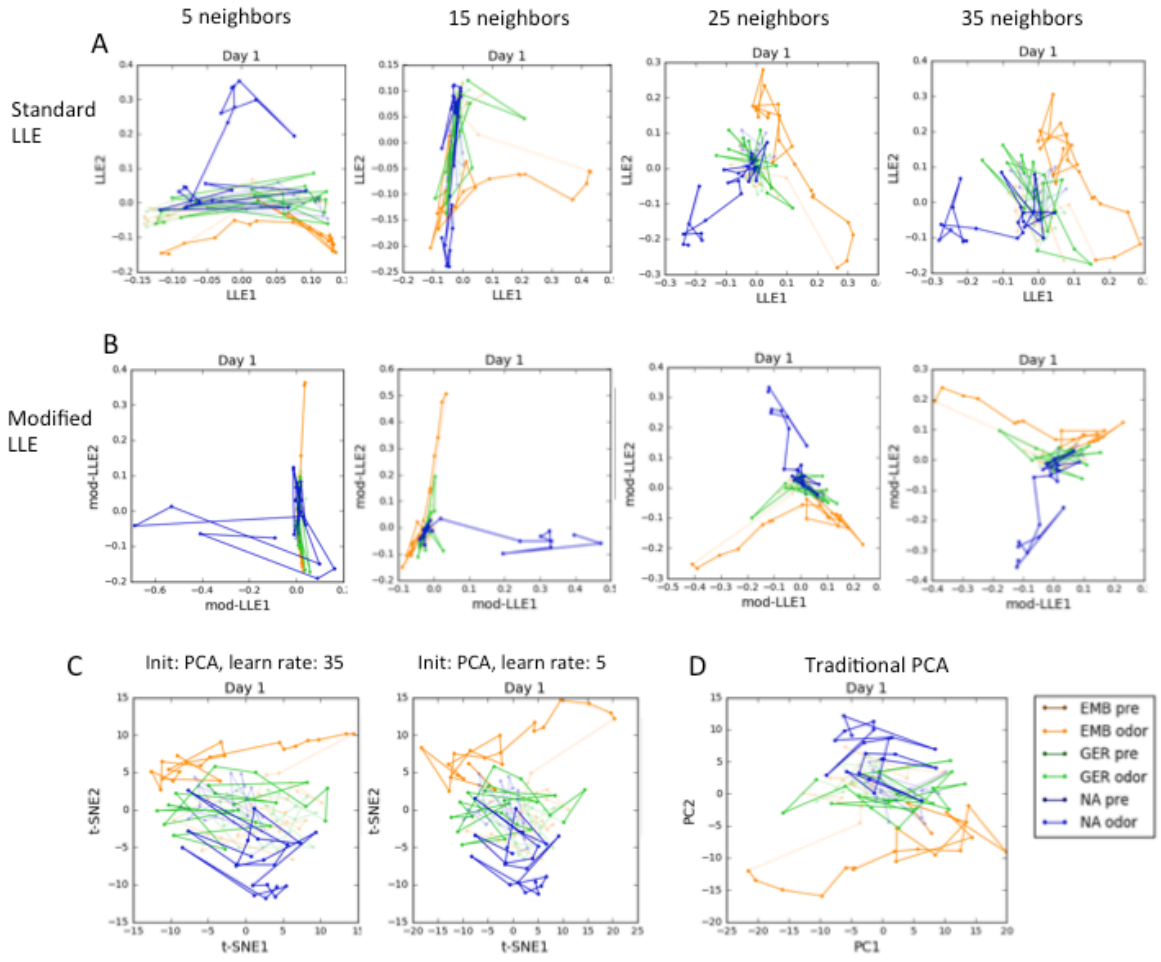

Figure 4.9 Comparison of dimensionality reduction techniques for visualizing response trajectories. Shown are Rat 2's neural population response trajectories to 3 odors (EMB – orange, GER – green, NA – blue) on Day 1 generated by standard LLE (**A**), modified LLE (**B**), t-SNE (**C**), and traditional PCA (**D**). A few parameter combinations are shown to illustrate the range of visualizations achieved with these methods. Color legend (in **D**) is same for all panels. Transparent and filled colors indicate pre and post beta onset respectively. In the end we found that LLE and t-SNE created trajectories of comparable or worse quality than PCA, so we decided to use PCA.

time bins over a 4s period from 2s prior to and 2s after beta onset. All PSTHs from a single day were organized into a single matrix with length(PSTH) x N_{odors} rows and N_{cells} columns.

We attempted several dimensionality reduction techniques on these matrices to find the best visualization. Following Stopfer et al. (2003), we tried locally linear embedding (LLE) and the more recently developed modified LLE (Zhang & Wang (no year listed on manuscript)) for a range of number of neighbors (see Fig. 4.9A ,B). LLE produced nice trajectories for 25 – 35 neighbors, but the modified LLE is too aggressive, so trajectories are difficult to see. We also tried t-distributed stochastic neighbor embedding (t-SNE) with many different parameter combinations (examples shown in Fig. 4.9C). For most parameter combinations t-SNE tended to fit the trajectories into a circular space, thus compressing them undesirably. We found best t-SNE trajectories using a PCA initialization and a low learning rate, but this is effectively the same as simply running PCA (compare Fig. 4.9C, right and Fig. 4.9D). In the end we found that LLE and straightforward PCA (Fig. 4.9D) produced comparable results. We chose to use LLE, and chose different numbers of neighbors for different data sets to obtain optimal separation and smoothness of trajectories.

4.3.15 Event time management

Event times for the cotton swab presentation experiments were initiated by a hand-held button. Event times in the nosepoke experiments were generated by a Med Associates SmartCTL DIG-716B control box. In both cases the events were 5V TTL pulses that were fed into the Open Ephys acquisition box via BNC cables.

Unfortunately, the event signals were often very noisy, perhaps due to cable noise or a fault within the acquisition box itself, resulting in repeated pulses rather than a single pulse at the onset and onset of each event. To isolate the pulses of interest we scanned the event files for onsets of pulse trains, recorded the time, then skipped 100 ms (determined by eye to be longer than all of the pulse noise trains), and continued the scan (see scandtrig_while in *Appendix II*).

In the nose-poke experiments, the Open Ephys system often registered completely spurious events when triggered by the Med Associates control box. Therefore, before scanning for event onsets, the nose-poke event times gathered by the Open Ephys system were matched to the event times stored by a Med Associates system running MedPC IV to ensure that every event was detected properly. The nose-poke experiments also suffered from a great deal of 60 Hz noise. We deleted most noisy periods while keeping most of the odor delivery periods intact. Care had to be taken to detect any overlaps between the removed periods and the event durations (see trim_events in App*endix II*).

4.3.16 Training rats to nose-poke

Rats 2 & 3 were trained to poke into an odor-port to receive sugar pellet rewards. Both rats learned the behavior in 3 days. A single trial consists of the following sequence: House light turns on, rat pokes nose, reward delivered if rat holds nose in nose-port for over 500 ms (or not if unrewarded), house light turns off 2s after nose-poke. If rat fails to poke nose in 5s, the houselights turns off for a 6s penalty and then another trial is initiated. The odor port was equipped with an IR sensor

that recorded times of nose-poke and nose-removal from the odor port. All automation was controlled by MedPC IV. We ran rats on two paradigms: (1) single odor full reward (3rd column in Table 4.1) - The experiment was set to terminate after 100 attempts, typically producing between 30 – 40 clean trials per sessions. (2) two odor half reward (4th column in Table 4.1) – For the first 60 attempted trials both odors were fully rewarded, then for the second 60 attempted trials the reward was removed for one of the odors.

We noticed that the 60 Hz noise often showed up between trials when the rat would investigate the hole through which the cable to the head-stage came in. Because of this we decided to delete all inter-trial periods and only cluster on trial periods, which are defined by each house-light ON/OFF event pair. Furthermore, the Open Ephys system tended to register spurious events, so we intersected Open Ephys events with internally generated MedPC IV events to ensure only true events were counted (as described in *4.3.13 Event time management*).

4.3.17 Odorant Delivery System

The odorant delivery system, depicted in Figure 4.10 is described in detail in Frederick et al. (2011). This system splits a clean air stream into a clean air stream and two odor streams gated by solenoids which pass through liquid odorants housed in test tubes. The solenoids control which odor is used, while a vacuum line gated by a different solenoid controls delivery to the odor port. Air is bubbled through an odor tube for 2 s before the vacuum line is closed so that odor delivery is

almost immediate (estimated delay is 60-100 msec). All solenoids are controlled by the Med Associates system.

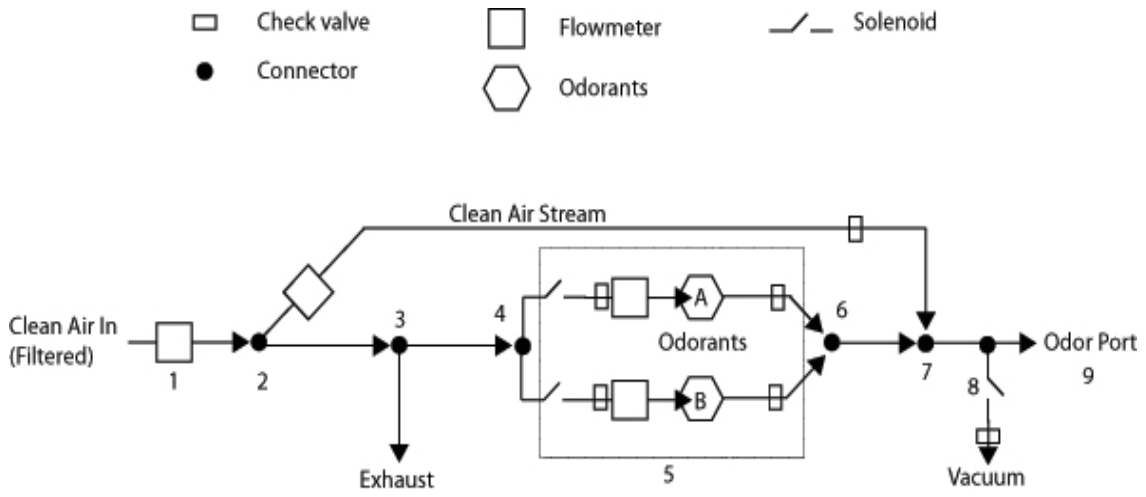

Figure 4.10 Odorant delivery system. Clean air enters the system after being passed through a carbon filter (1). The clean air is then split into a clean air stream (2) and two odor streams (4). An exhaust vent (3) prevents pressure problems. The odor streams pass through the odorants (5), which are housed in test tubes (A, B). The odorant streams then meet (6) and rejoin the clean air stream (7) at which point the odorized air has approximately 16% saturated vapor. If the vacuum line is open (8), the odorized air is diverted to an exhaust. If the vacuum line is closed, then the odorized air is able to flow into the odor port (9). Arrows indicate the direction of flow. Solenoids are controlled by a computer. All connectors, except the one for the vacuum, which used a T-connector, were Y-connectors. Check valves ensured flow direction throughout the system. Reproduced from Frederick et al. (2011) with permission.

4.4 Results of high-density Si probe recordings

4.4.1 Spike waveforms and baseline firing rates

Because each of the 32 channels of the high-density probes tended to detect at least one negative and one positive waveform, a typical recording session produced around 64 spike clusters. Figure 4.11A shows representative categories of negative spike waveforms obtained after successful clustering of clean data periods. Positive spikes falling into the same categories were also detected. Whether a spike is positive or negative is purely a consequence of geometry (where the cell is relative to the probe), as shown by 3D simulations of extracellular potentials (Buzsáki et al., 2012). We did not see any biphasic waveforms characteristic of axonal spikes, and thus we assumed that most recorded action potentials were somatic spikes in the GCL or somatic spikes from distant M/T cells.

Most of the detected clusters looked like the small single channel deflection shown in the upper left of Figure 4.11A. Although to some eyes these would appear to be nothing more than noise, these small deflections often showed strong stimulus dependent firing patterns. These clusters could represent distant single cells, but more likely represent multiunit activity mixed with noise, because these types of clusters often showed sub-millisecond ISIs. Larger spike waveforms usually had cleaner ISIs and correlograms with a clear refractory period. Unfortunately, the cells with large waveforms did not always respond to the odors we chose to present.

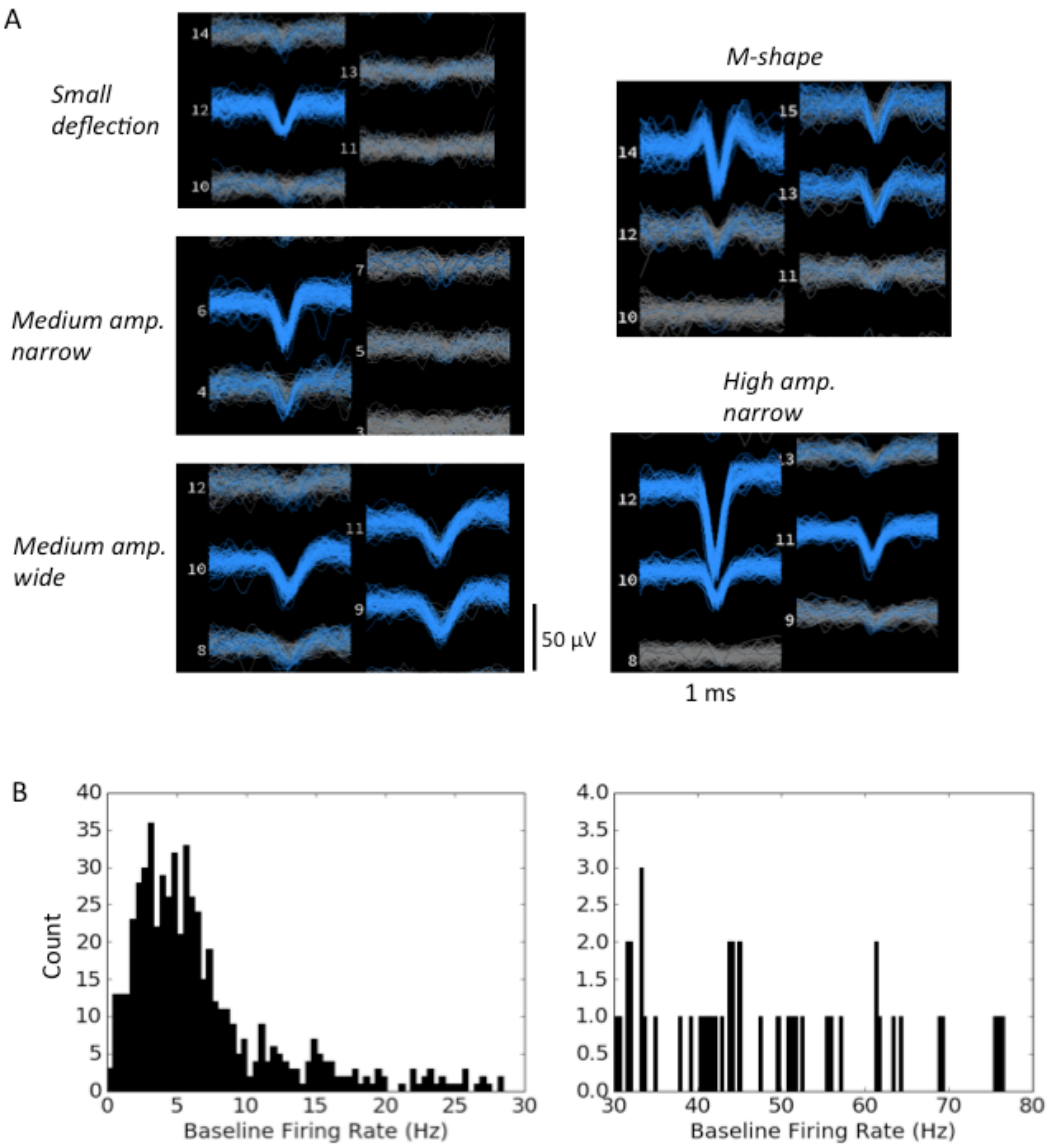

Figure 4.11 Spike waveforms and baseline firing rates. A) Representative negative action potential waveforms. Positive waveforms also can be organized into the same general categories. No biphasic waveforms characteristic of axons were found, thus we assume that most action potentials come form cell bodies in the GCL. **B)** Histogram of baseline firing rates for all GCL neurons included in this study (620 cells total, 206 from Rat 1, 260 from Rat 2, 154 from Rat 3). The majority of cells had baseline firing rates between 1 and 10 Hz. Only 51 cells had firing rates higher than 30 Hz (*right*), and these are most likely multiunit recordings.

We attempted to classify neural identity by waveform, but we found no consistently sortable classes of waveforms. This is probably because the probes are surrounded by GCL neurons from every angle, and the shape of electrophysiological

waveforms changes when viewed from different angles (Buzsáki et al., 2012). We did not find any spatial organization of different waveforms along the probe shaft. That is to say, in a given recording session, any of these waveforms could be found on any channel. We also did not find any clustering of waveforms by any of the response metrics we used in the present work.

The baseline firing rates of all GCL neurons included in this study (620 total) were calculated by averaging the rates computed from a 1 s window 2 s before each odor presentation. They varied quite drastically across cells, ranging approximately from 0.5 Hz to 70 Hz. However, as can be seen from the histogram of baseline firing rates shown in Figure 4.11B (*left*), the majority of cells fell within the 1 – 10 Hz range. Approximately 2/3rds of the cells in this range showed clear refractory periods. Only 51 out of 620 cells total had baseline firing rates > 30 Hz (Fig. 4.11B *right*), and these are most likely multiunits as their ISIs did not have clear refractory periods. The firing rates of GCs in slice have been reported to be very low, between 0.5 – 5 Hz (Cang & Isaacson, 2003), and recent recordings of GCs in awake head fixed mice showed rates of 1 – 10 Hz (Cazakoff et al. 2014). It is possible that the cells we recorded with lower firing rates are GCs, while those with moderate firing rates are a different class of interneurons or distant M/T cells (see *Discussion 4.5.1*).

4.4.2 Classification of spike responses during passive odor presentations

Because we did not have a precise measure of stimulus presentation during passive odor presentations, we aligned the spike responses during each odor presentation to the onset of the beta oscillation (See *Methods 4.3.10* and Fig. 4.6). We produced

peri-stimulus time histograms (PSTH) by averaging all the spike trains for a given odor and dividing by the bin width. By scanning through hundreds of PSTHs of individual cell responses from all three rats by eye we found that responses fell within 6 general categories, which are depicted in Figure 4.12. These categories consisted of two excitatory (E) type responses (transient Fig. 4.12A, and persistent Fig. 4.12B), two inhibitory (I) type responses (transient, Fig. 4.12D and persistent Fig. 4.12E), a mixed E/I response (Fig. 4.12C), and no rate modulation (Fig. 4.12F). The mixed response category further subdivided into three subcategories, E-I, E-I-E, and I-E, but only E-I-E is shown in Figure 4.12C. We did not find any clustering of response type with waveform or baseline firing rate because, as will be shown later, individual cells showed multiple response types to different odors and over subsequent days.

As mentioned in the introduction to this chapter, our model implicitly assumes that GCs would fire at the onset of beta, but remain inhibited for the duration of the beta oscillation. The existence of E-I and E-I-E responses confirms that this behavior really does occur in awake behaving rats in a subset of GCL neurons. Seven such cells with E-I responses to EMB are shown in Figure 4.6C along with the odor evoked beta oscillation, showing that cells are inhibited for $\sim$ 1s (most of the duration of the beta oscillation). Interestingly, the same cells appear to regain firing as a second smaller beta oscillation emerges, indicating that the inhibition of these cells is not a necessary condition for beta to emerge. The remaining response categories define a broader range of responses than the model could have predicted

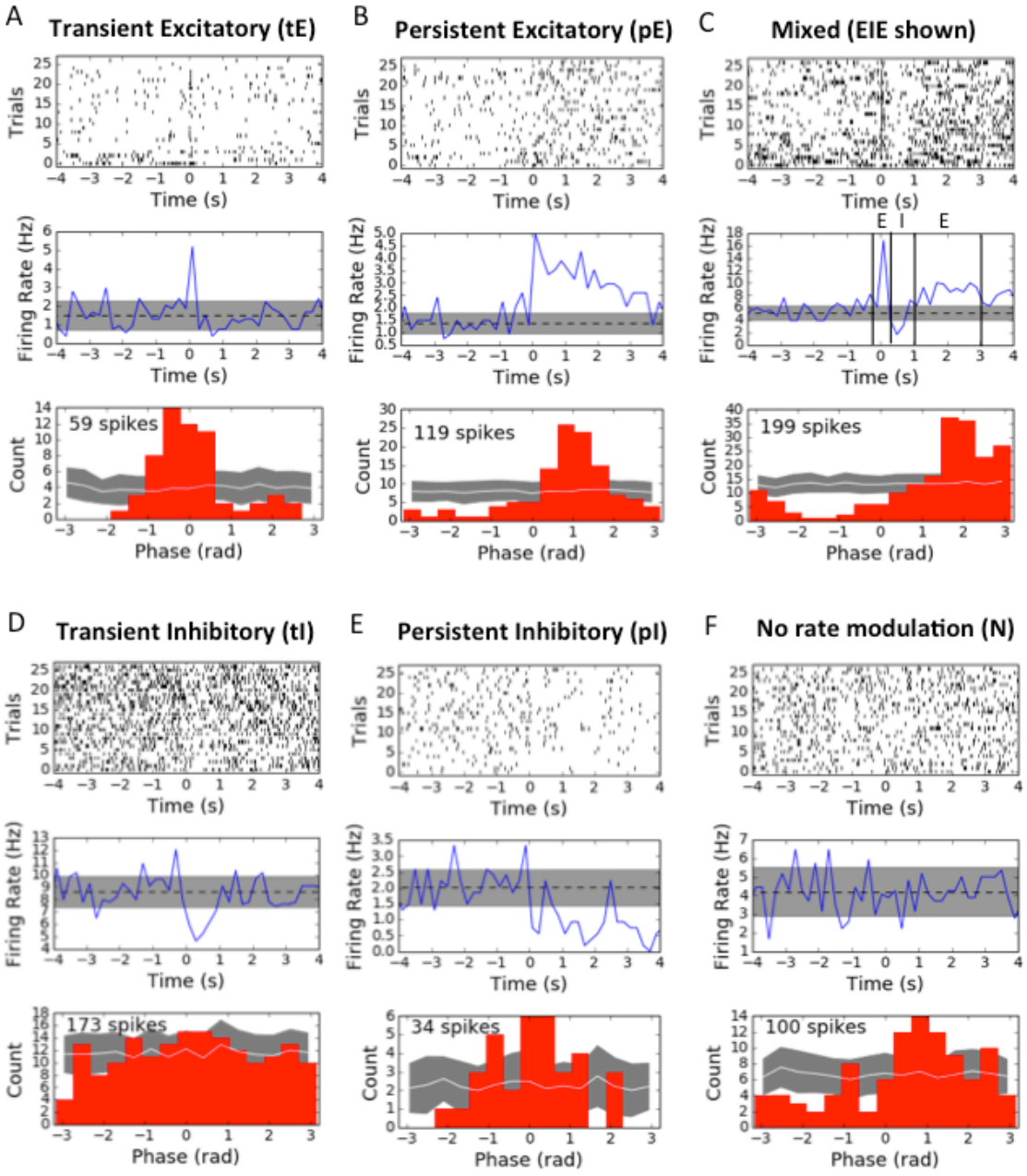

Figure 4.12 General response categories of GCL neurons. GCL neuron odor responses aligned to beta onset could be grouped into 6 major categories (**A – F**). Each sub-figure includes a raster plot (top), PSTH (middle), and spike – beta phase histogram (bottom). In the PSTH plots, the dashed line and gray region represent the mean and standard deviation of the baseline firing rate calculated from a 2 s window 2 s before beta onset. For the phase histograms the white line and gray region represents the mean and standard deviation of phase histograms calculated from 50 random shuffles of the same number of spikes. Subdivision defining the mixed response E-I-E are indicated on the PSTH plot (**C**).

and may reflect the diversity of inhibitory cell types in the GCL. The excitatory and inhibitory responses of different cells to the same odor may be due to inhibitory connections between GCL interneurons (Pressler & Strowbridge, 2006).

We were not only interested in the modulation of firing rate during beta oscillations, but also the modulation of spike timing in the form of phase locking. Thus, for each cell we also calculated spike-beta phase histograms (see *Methods 4.3.8*), which are shown in the bottom panel of each subfigure in Figure 4.12. In this example, all cells showed strong phase locking except for the cell with the tI response (Fig. 4.12D). Notably, the cell that showed no rate modulation (Fig. 4.12F) was still phase locked to beta, suggesting that cells could potentially carry independent information in their rate and timing by participating in different dynamical states.

4.4.3 Variability of responses of well-isolated cells across odors and days

In the previous sections, we discussed experiments in which we presented only one odor at a time, thus we could not investigate the responses of individual cells to different odors. In the multi-odor swab presentation experiments (2nd column of Table 4.1), we interleaved several different odors per session in a fixed order (see 2nd column of Table 4.1 for order of odor presentations). We performed sessions on four consecutive days to investigate the day-to-day variations of individual cells that might be held across days. In both Rats 2 & 3 we found clusters that responded differently to different odors.

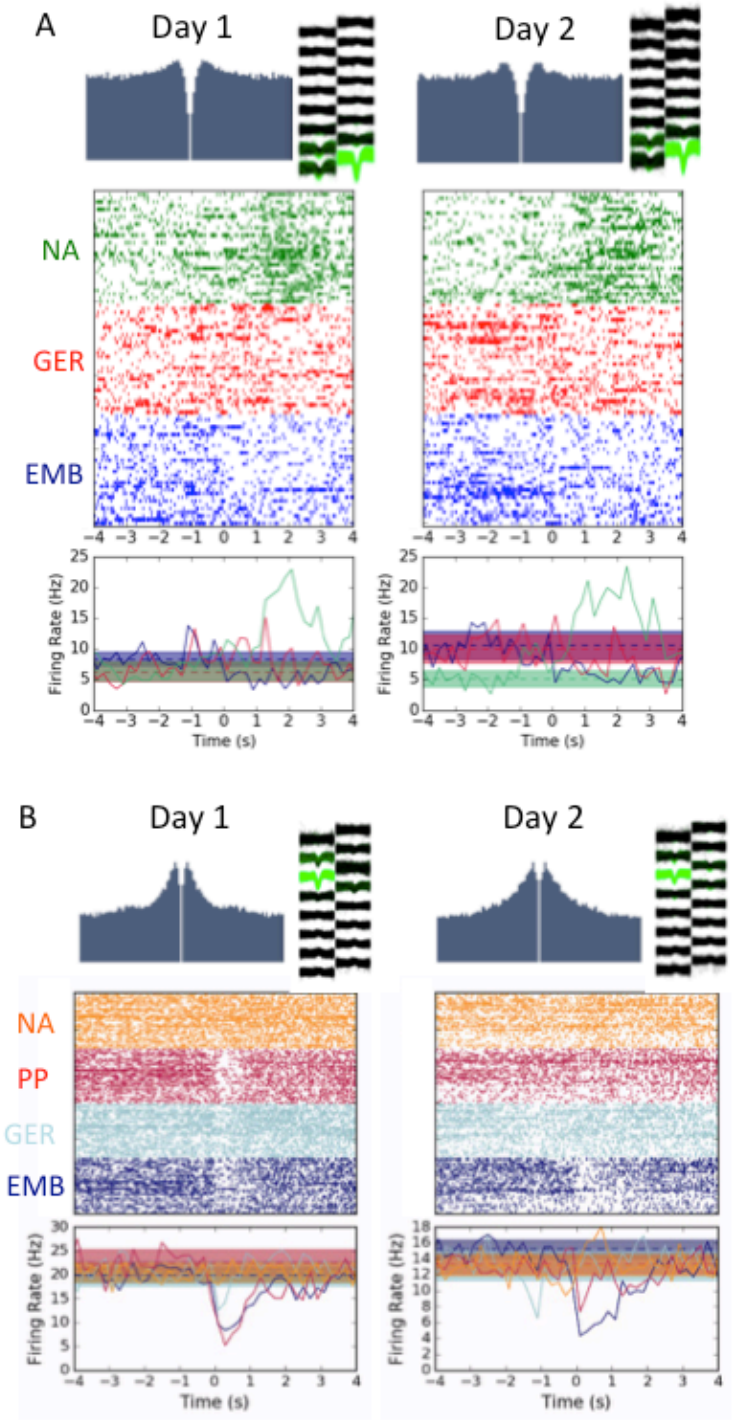

Figure 4.13 GCL neuron responses on consecutive days. Example odor responses on two consecutive days of a cell from Rat 2 (**A**) and Rat 3 (**B**). For each day the correlogram and spike waveforms (top), raster plots grouped by odor (middle), and PSTH per odor (bottom) are shown. Correlograms were calculated 1 ms bins in a 50 window ms.

To illustrate the variability of responses within clusters of spikes from individual cells or multiunit responses, Rat 2 had a cluster with a strong persistent excitation for NA, but a persistent inhibition for EMB and GER (Fig. 4.13A), and Rat 3 had a cluster with strong inhibition to EMB and PP, a slight inhibition to GER, and no response to NA (Fig. 4.13B). The responses for these clusters appeared to be maintained on the 2nd day, but both of these clusters were lost after the 2nd day. By the presence of a refractory period in the correlogram for the Rat 2 example (Fig. 4.13A, top) we feel confident that all the spikes in this cluster came from the same cell, but the lack of a clear refractory period in the Rat 3 example correlogram indicates that the cluster likely contains spikes from multiple cells or possibly some noise. The signals in Rat 3 were generally noisier, and the clustering procedure appeared to miss some spikes on Day 2, resulting in gaps in the raster plots, although the shape of the histogram remained the same. It is interesting to note that the Rat 2 cell seemed to maintain inhibition after odorant was presented, because the baseline firing rate for the NA presentation was lower than the other two (NA is the last in the sequence for this rat). Also, it is interesting that the example cluster for Rat 3 seems to scale its inhibitory response by the volatility of the odorant (see VP of each odorant in Table 4.1).

A small subset of clusters maintained the same waveform and correlogram over 3-4 days, leading us to believe that we were holding the same cell (or small group of cells) over these days. Figure 4.14 shows the raster plot, PSTH, and phase histograms of one such cell from Rat 2. This cell was only sensitive to EMB, but the response of this cell appeared to progress from an I-E type response on Day 1, to a

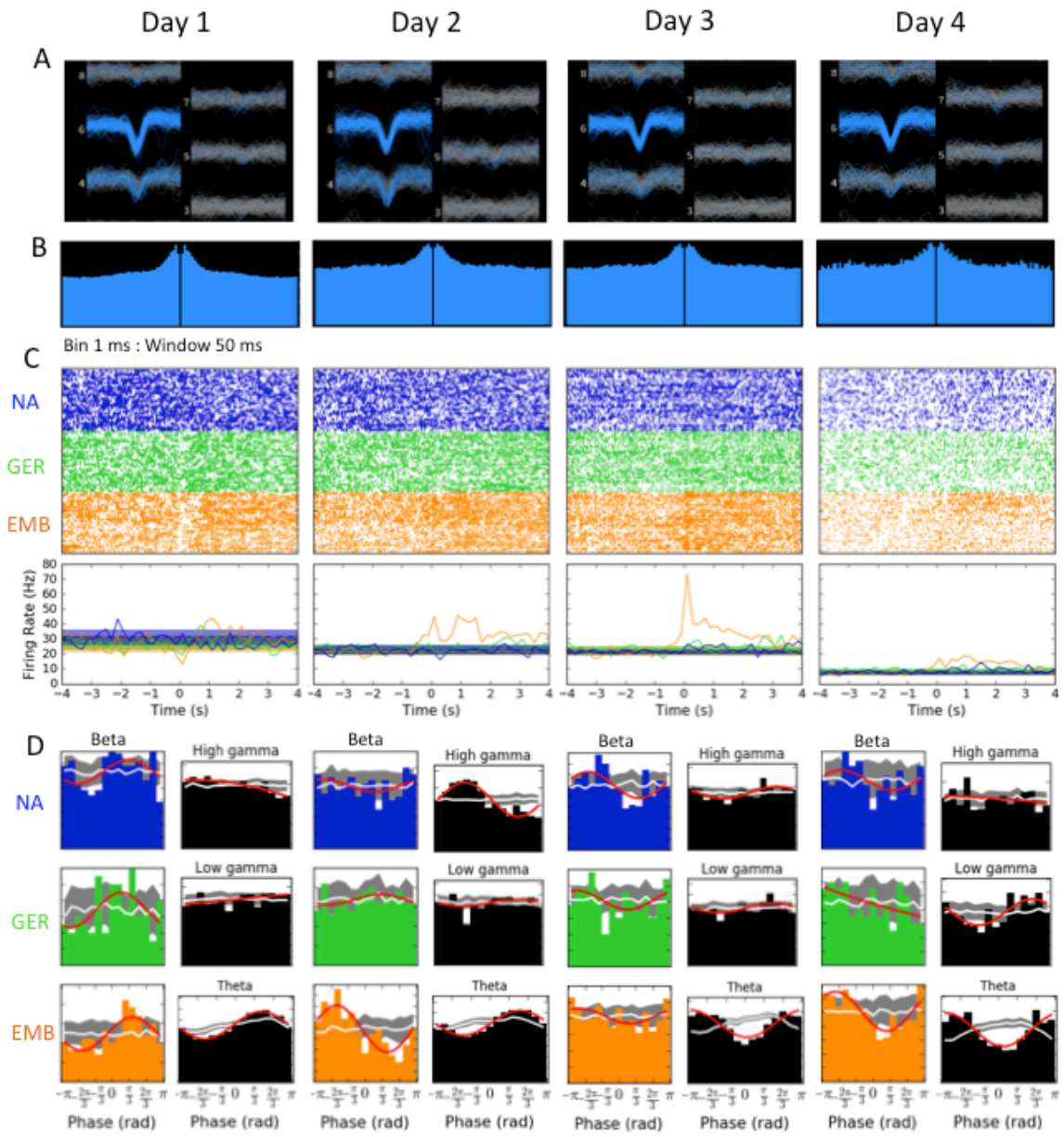

Figure 4.14 Firing rate and phase locking of single GCL neuron held over multiple days. Waveforms **(A)** and correlogram **(B)** of a single cluster appear fairly consistent across 4 consecutive days. Traces included in this cluster are colored blue. Correlogram was produced with bin size of 1 ms over a 50 ms window. The peak at small correlation time reflects the tendency of these spikes to arise in bursts. Lack of clear refractory periods indicates possible noise or multiple cells contributing to this cluster. **C)** Beta onset-aligned spike raster plots (top) and corresponding PSTH (bottom) grouped and colored by odor. The PSTH on Day 1 shows an inhibitory-excitatory response for EMB (orange), but for Days 2 and 3 the response is purely excitatory. Day 4 still shows persistent excitatory response, but firing rate is over twice as low as other days, probably due to failure of spike detection algorithm to detect all spikes. **D)** Spike - phase histograms of beta, high/low gamma, and theta filtered LFPs. Spike – beta phase histograms was calculated separately for each odor (colored as in the raster plots) while phase histograms for gamma and theta (in black) were calculated for entire recording session. Best fit (red line), mean (white line) and standard deviation (gray filled) of 50 random shuffles.

persistent excitatory response on Day 2, to an even more prominent excitatory response on Day 3. On Day 4 the firing rate was much lower, most likely because the cell had drifted away from the probe so that not every spike was detected. In addition to this striking evolution of the odor response over days, this cluster showed changes in LFP phase preferences across days (Fig. 4.14D). The beta phase preference for EMB (Fig. 4.14D orange, bottom) was near 90° on Day 1, but on all other days was clearly negative. It is not likely that the LFP polarity changed due to movement between days because the probe did not span a cortical layer. This cluster did not show a strong gamma phase preference, except for high gamma on Day 2 and a low gamma preference on Day 4. The theta phase preference appeared to change from 90° on Days 1&2 to 180° on Days 3&4. Interestingly, the mean beta

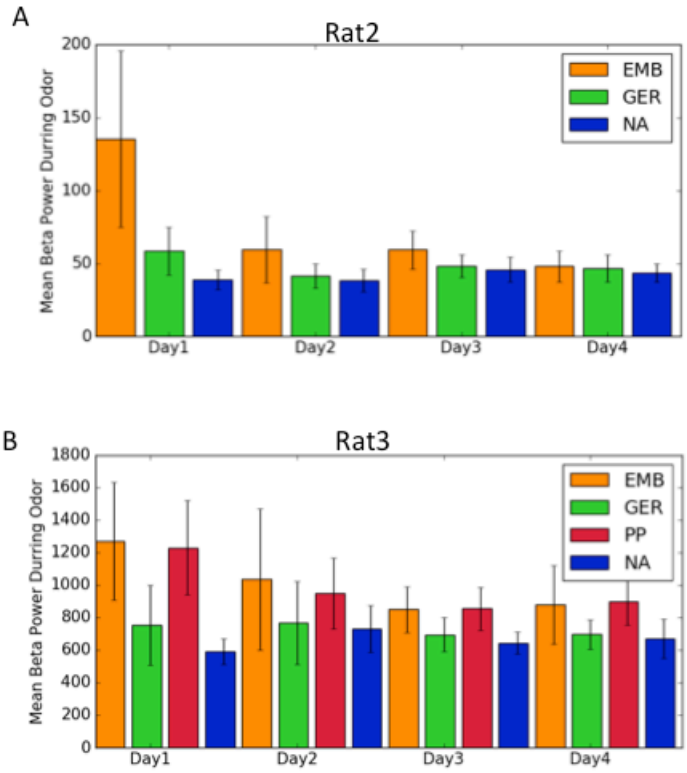

Figure 4.15 Mean odor evoked beta power on consecutive days. Mean LFP beta band (15 – 35 Hz) power for each odor and day of the multi-odor swab presentation experiments for Rat 2 **(A)** and Rat 3 **(B)**. Error bars are from 30 trials each.

power recorded during each odor presentation drops significantly after Day 1 for high volatility odors, while the beta power for low volatility odors remains roughly the same across all days (Fig. 4.15). This could reflect some form of familiarization with the procedure, or a change in odor sampling strategy, perhaps as the rats learn to take shallower or shorter sniffs of the high volatility odors.

4.4.4 Evolution of population response trajectories over time

We simultaneously recorded ~60 – 80 neurons per session in Rat 2 and ~30 – 40 neurons per session in Rat 3 (which had missing shank 2 due to noise). In addition to looking at the responses of individual cells, we wanted to investigate the responses at the population level. Inspired by work of Stopfer, et al. (2003), we computed response trajectories and visualized them using locally linear embedding (LLE, see *Methods 4.3.14*). Unlike Stopfer et al. (2003), we computed the trajectories using PSTHs across all trials rather than individual trials or averaged triplets as they did. The number of neighbors used for LLE must be tuned to produce the most visually clear trajectories. By trial and error, we found optimal values of 25 and 14 numbers of neighbors for Rat 2 and Rat 3 populations, respectively. Thus, by reducing dimensionality across a large number of cells we could represent the activity of all cells in just two dimensions.

The trajectories for each odor used in the multi-odor swab presentation experiments are shown in Figure 4.16. Transparent and filled colors indicate pre- and post-beta onset respectively. For Rat 2, LLE produced clearer trajectories than PCA. On Days 1 & 2 for Rat 2 the EMB-induced population trajectory (orange)

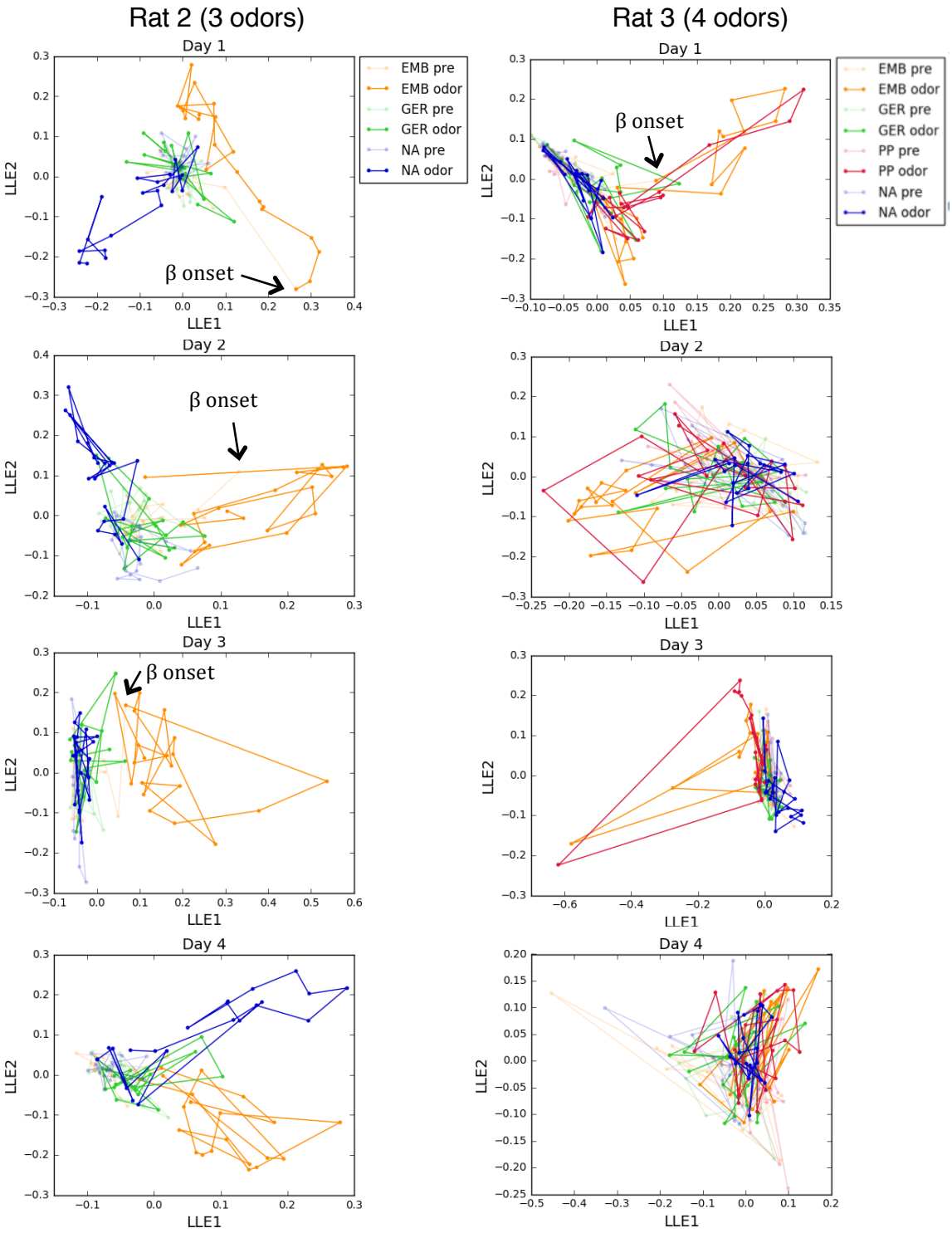

Figure 4.16 Trajectories obtained from LLE decomposition of PSTHs across the entire neural population. The trajectories cover the period starting 2s prior to beta onset (transparent colors) to 2s after beta onset (filled colors) in 100 ms time steps. Although most of the trajectories are rather noisy and angular, a relatively smooth path emerges for EMB (orange) on Day 1 of Rat 2 (*left*). It is clear in this plot that the trajectory diverges at the onset of beta oscillation (transition from light to filled orange color, β onset marked by arrow). After ~800 ms the trajectory returns closer to its original starting point, but continues to wander away from it, as the full responses can last up to 3s. The two high volatility odors (EMB & PP) tend to overlap for Rat 3 (*right*).

clearly diverges from its pre-beta onset baseline path immediately at the onset of beta. The NA trajectory (blue) also tends to diverge, but it does so more slowly, as can be seen by the overlap of light and dark blue trajectories. This may be due to a genuine later onset of NA activity, or simply due to the fact that NA induced much smaller beta oscillations making alignment to them less precise. The EMB trajectory does not return to baseline in the 2s post beta onset, suggesting that the population response lasts longer than 2s. GER trajectories do not diverge much from pre-beta onset paths, because most of the cells in Rat 2 were insensitive to GER. On Day 3, the EMB trajectory (orange) diverges sharply from its pre-beta onset path, reflecting a very strong excitatory and inhibitory EMB responses by many cells on this day. We point out that one of the cells in this population is the same cell shown in Figure 4.14 that had such a strong excitatory response to EMB on Day 3.

Even though we tried to optimize the visualizations, the best trajectories for Rat 3 (Fig. 4.16, right) were noisier and more angular than those of Rat 2. This is probably due to the lower number of neurons from Rat 3 (only 30 – 40). In comparison, Stopfer et al. 2003 needed over 100 cells to get smooth trajectories (personal communication). Nonetheless, we see that the trajectories for the two high volatility odorants, EMB (orange) and PP (red), tend to overlap with themselves more than the two low volatility odorants, especially in Days 1 & 3. This result echoes what we saw for the individual neuron in Fig. 4.13 B, where firing responses to both high volatility odors were strong inhibition. The Rat 3 EMB and PP responses appear shorter-lived than the Rat 2 responses to EMB, as they sharply diverge and then return close to baseline within the 2s. The Day 4 trajectories are

overlapping, possibly due to signal degradation and noise that led to poor clustering. It appears that on a population level, the GCL neuron population sampled for Rat 3 is more sensitive to odor volatility than odor identity, because the odors within each volatility class overlap. This supports the idea that GCL neurons might be broadly tuned to odors, because they receive inputs from MCs from across the bulb and strong centrifugal drive from higher order areas.

4.4.5 Cells that are strongly phase locked to gamma oscillations tend not to be phase locked to beta oscillations.

As seen in Figures 4.12 & 4.14 some phase histograms are obviously peaked, and others are not. To quantify the degree of phase locking across our entire data set we computed the spike-field coherence (SFC) between spikes and the LFP filtered for either beta or gamma bands (see Fig. 4.7 and *Methods 4.3.11*). In Figure 4.17, we plot beta SFC vs low and high gamma SFC for all cells in the data set responding to high volatility odors. Because the beta SFC for low volatility odors tended to be biased due to short beta epochs (explained in *Methods 4.3.11*) we only present high volatility results. Each point represents a cell (or multi-cell cluster), and each cell with significant beta coherence (as determined by 1 sided, 1 sample T-test) is colored red. For each of these plots, the upper right quadrant tends to be unpopulated. That is, cells with high beta coherence tend not to have high gamma coherence.

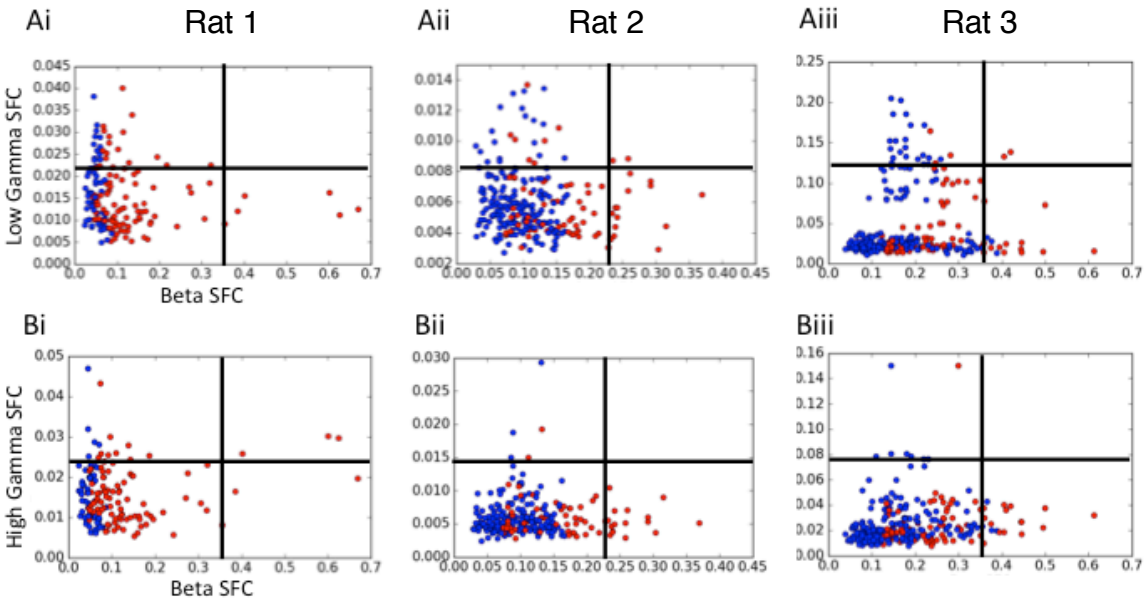

Figure 4.17 Plotting beta SFC vs high and low gamma SFC. Spike-beta coherence vs spike-low gamma (A) and spike-high gamma (B) coherence for every cell in the data set responding to high volatility odors. Each plot is divided into quadrants. Very few cells fall in the upper right quadrant. Cells with significant beta coherence are colored red.

It is possible that cells with higher beta coherence represent a different subtype than cells with higher gamma coherence, but they did not cluster with any of the other response properties that we measured. Spike – gamma coherence was quite low (< 0.02) for all cells except for a subpopulation in Rat 3, which had much greater low gamma SFC than the other rats (Fig. 4.17 Aiii). It is possible that the cells with greater low gamma coherence are distant MCs, because these cells are known to have fairly high gamma coherence.

4.4.6 GCL neurons show heterogeneous beta LFP phase preferences

The preferred beta phase of each cell (or multi-cell cluster) was calculated by fitting a Gaussian or a sinusoid (whichever gave the best fit) to the phase histogram and

taking the argmax (see red curves on phase histograms in Fig. 4.14 D and *Methods 4.3.9*). In Figure 4.18A we count the preferred phases for all cells recorded in each rat (white bars count only those cells with significant SFC). A phase of 0^o corresponds to the peaks of the beta oscillation, while 180^o ($\pm \pi$) corresponds to the troughs (Fig. 4.18B). Curiously, the preferred phases for Rat 1 were all peaked around just above 0^o, but those for Rats 2 & 3 were more heterogeneous. Although the total population of Rats 2 & 3 showed preferred phases towards 180^o ($\pm \pi$), most of the phase preferences for cells with significant beta SFC were between 0 and 180^o. It is possible that the LFP in Rat 1 was reversed relative to the LFP in Rats 2 and 3 if the probe for rat one was somehow crossing a layer, but it is unlikely as the probes were lowered to the same depth for all rats, and the GCL LFP should be of consistent polarity (phase reverses when crossing the EPL).

Figure 4.18 C shows that cells had roughly the same preferences for all odor-induced beta oscillations in Rat 1. The phase preference was consistent over long time intervals as well, as evidenced by the two EMB sessions that were recorded 3 weeks apart. The beta phase preferences in Rats 2 & 3 differed more across odors. In particular, cells in Rat 3 responded to GER and NA with 180^o phase preferences, but responded to PP with a peak phase preference just under 90^o. This suggests that odors of different volatilities could possibly drive some GCL neurons at different phases of beta oscillations. It is possible that phase preferences were heterogeneous in Rats 2 & 3 because the probes detected different inhibitory subtypes in the GCL, while the phase preferences were more similar in Rat 1 because the probe happened to be placed near a nest of similar cells types. Rat 1 only had single odor

sessions, while Rats 2&3 had multiple odors interleaved in a session, so it also can't be ruled out that the succession of different odors caused the more heterogeneous phase preferences.

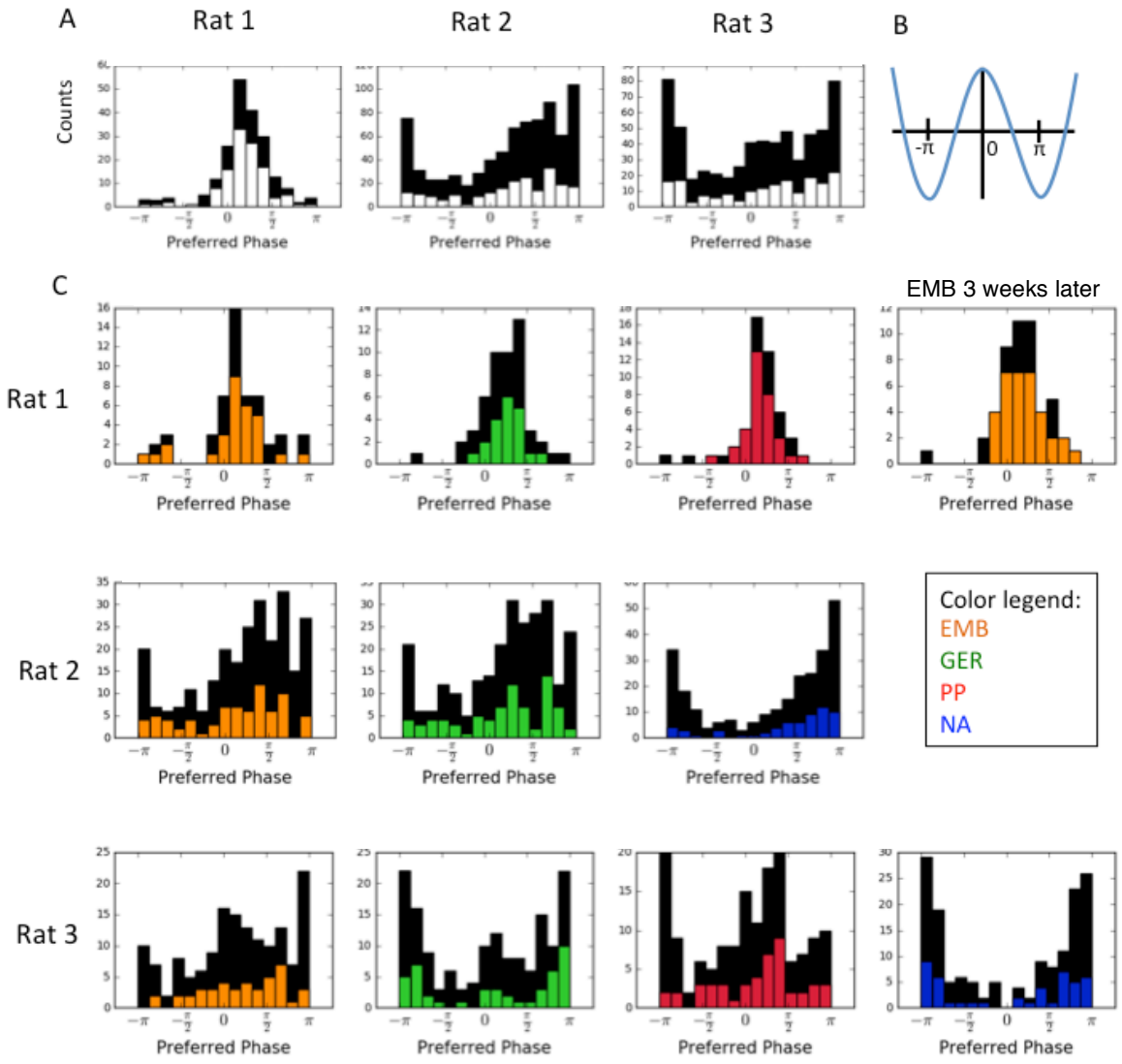

Figure 4.18 Preferred phases for all recorded cells in each rat A) Preferred phase pooled across all odorants for each rat. Black bars represent SFC of the entire cell population. White bars represent cells with significant beta SFC. **B)** Schematic showing phase convention used. **C)** Preferred phase grouped by odor for each rat. Black bars represent SFC of the cell population recorded for that odor. Colored bars represent the cells with significant beta SFC for that odor. For these plots, data for Rat 1 is taken from single odor blocks (only one day per odor). Data for Rats 2 & 3 was pooled across the four days of interleaved presentations and grouped by odor.

4.4.7 Prediction accuracies from spike distance metrics distinguish between timing and rate cells

Continuing with the multi-odor swab presentation data of Rats 2 & 3, we next investigated how well we could decode odor identity from the neural firing patterns. We chose to do this by computing the Victor-Purpura (1993) distance metric between all spike train pairs and then determining the predicted odor of each spike train as the odor that evoked the spike trains giving the shortest average distance (see *Methods 4.3.13* for more detail). The prediction accuracy was then simply calculated as the number of correct spike train predictions divided by the total number of spike trains. The spike distance was calculated for a range of timing resolutions, from 0.1ms to 2s (the entire spike train window). At fine timing resolution, the timing of individual cells influences the distance metric, but at course timing resolutions only the total number of spikes contribute. Therefore, this analysis allows us to identify cells that carry odor identity information in the timing of their responses and cells that carry odor information only in the number of spikes they fire.

Using this approach, we found three classes of odor selectivity, which we refer to as non-informative, timing, and rate cells. Non-informative selectivity did not successfully distinguish between the odors presented. Timing selectivity showed peak prediction accuracy at an intermediate timing resolution. Rate selectivity had peak prediction accuracy when the timing resolution was the size of the window, so the only information available to distinguish between odors is the number of spikes. A representative of each of these types is shown in Figure 4.8B.

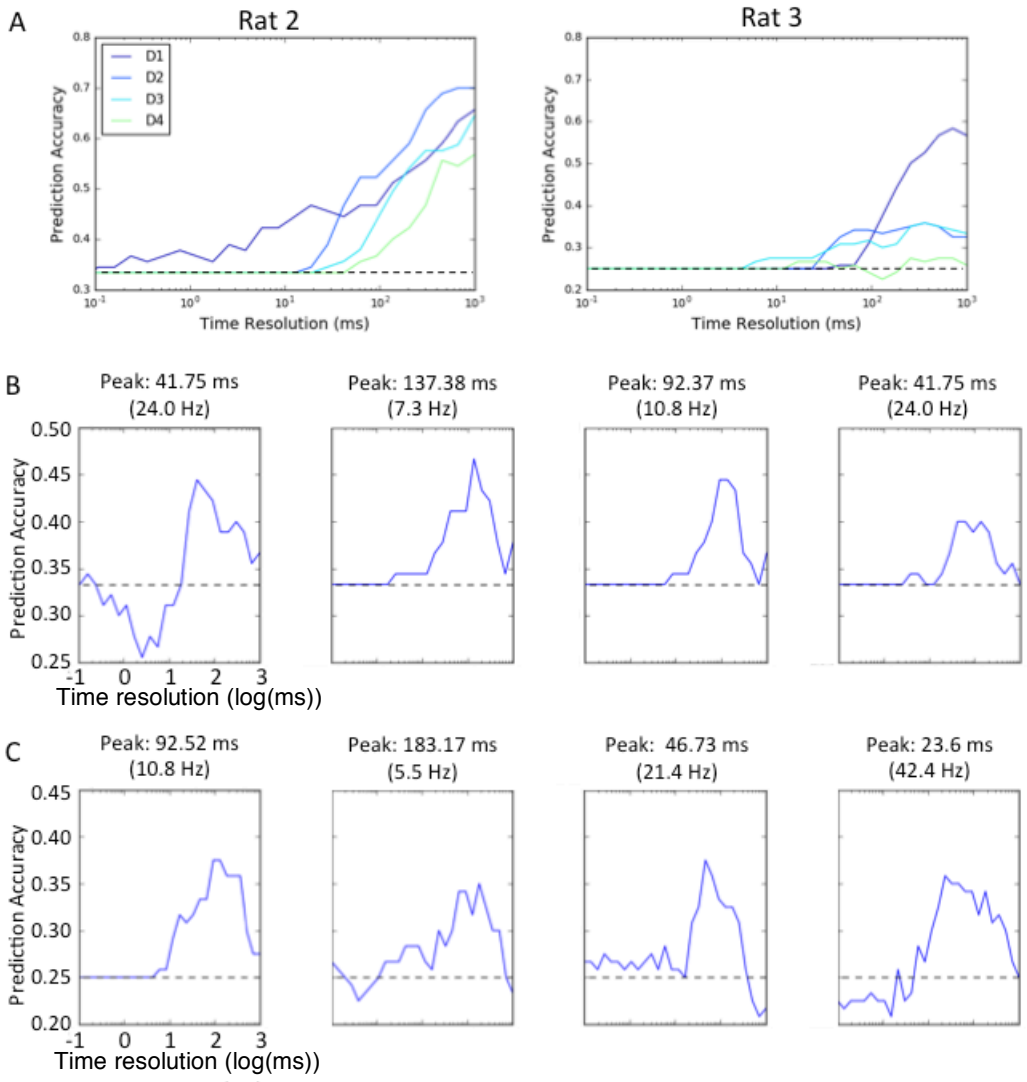

Figure 4.19 Prediction accuracy of cell populations and individual cells. A) Odor prediction accuracies of the entire recorded population recorded in Rat 2 (left) and Rat 3 (right) were obtained from the mean distance matrix across all cells. Dashed black line represents chance. **B)** Prediction accuracies as a function of time resolution for 4 representative timing cells in Rat 2. The time resolution and corresponding frequency for each peak prediction accuracy are indicated. Dashed black line represents chance. **C)** Same as **B**, but for Rat 3.

Because we used a very small stimulus space for these experiments (only 3 odors for Rat 2 and 4 odors for Rat 3), it is likely that some of the indeterminate cells would have shown discriminable responses had we used more odors.

With only three odors used for Rat 2 and four odors used for Rat 3, the chance prediction accuracies were 33% and 25% respectively. Most of the peak

prediction accuracies for rate and timing cells were below 50%. Rate cells produced the highest accuracies with a maximum of only 60%. These values are rather low when compared to prediction accuracies using similar methods in cortical neurons (Mackevicius et al., 2012). The prediction accuracies for the entire population, obtained from the mean distance matrix across all cells, were rate-like for Rat 2 (Fig. 4.19A, *left*). The population prediction accuracy for Rat 3 (Fig. 4.19A, *right*) cells was poor because many of the cells have accuracies below chance due to temporary drops in spike detection (See *Discussion* section 4.5.4 for explanation).

Although the prediction accuracies from the whole population were maximum for rate-like classification, quite a few individual cells in both rats showed timing selectivity (23% of cells in Rat 2, and 15% of cells in Rat 3). Examples of four such cells are shown in Figure 4.19B,C. The majority of these timing cells showed peak prediction accuracies at timing resolutions corresponding to beta and theta frequencies, and some even at gamma frequencies (like the rightmost cell in Fig. 4.19C). This means that for these cells, variations in spike timing on beta and theta time scales convey the most information about odor identity. Although these experiments were not designed with this analysis in mind, this analysis reveals a tantalizing link between spike timing, LFP frequencies, and odor identity.

4.4.8 Alignment of spikes to nose-poke reveals early phase of GCL neural responses locked to behavior

We trained Rats 2 & 3 to poke their noses into an odor port hooked up to a computer controlled odorant delivery system (Fig. 4.10, and see *Methods 4.3.17*).

The odor port was equipped with an IR detector, giving us a behaviorally relevant time point with which to align our signals. In the nose-poke 1 odor full reward sessions (3rd column of Table 4.1) we used only one odor per session and rewarded each successful nose-poke with a sugar pellet. For these sessions, the data for Rat 3 was contaminated with so much 60 Hz noise that very few trials were salvageable, so we only present results for Rat 2. In the odor swab presentations experiments, the rats stayed plugged into their headstages because the cable had plenty of slack to absorb the twists caused by locomotion. But during the nose-poke experiments the rats would frequently unplug themselves as they would nudge their heads into corners and press the headstage against the wall of the operant cage. The unplugged periods (Fig. 4.20A) were easily removed via simple thresholding and deletion, but repeated unplugging and re-plugging could slightly shift the probe, causing some cells to be lost and introducing new cells over the duration of the recording session.

Figure 4.20B shows that beta oscillations were reliably evoked by EMB shortly after the rat poked its nose into the odor port. The average latency of beta oscillation onset with respect to nosepoke time was ~150 ms for EMB and ~100 ms for GER, which is shorter than the latency our lab has seen when rats are performing Go/No-Go or Two Alternative Choice operant tasks (~250 msec). The decreased latency may be related to the absence of a decision period. Figure 4.20B also shows a period of fast investigative sniffing roughly coinciding with the dark period. This behavior was more common in the nose-poke experiments than the cotton swab presentation experiments, likely because rats get more active in the dark periods

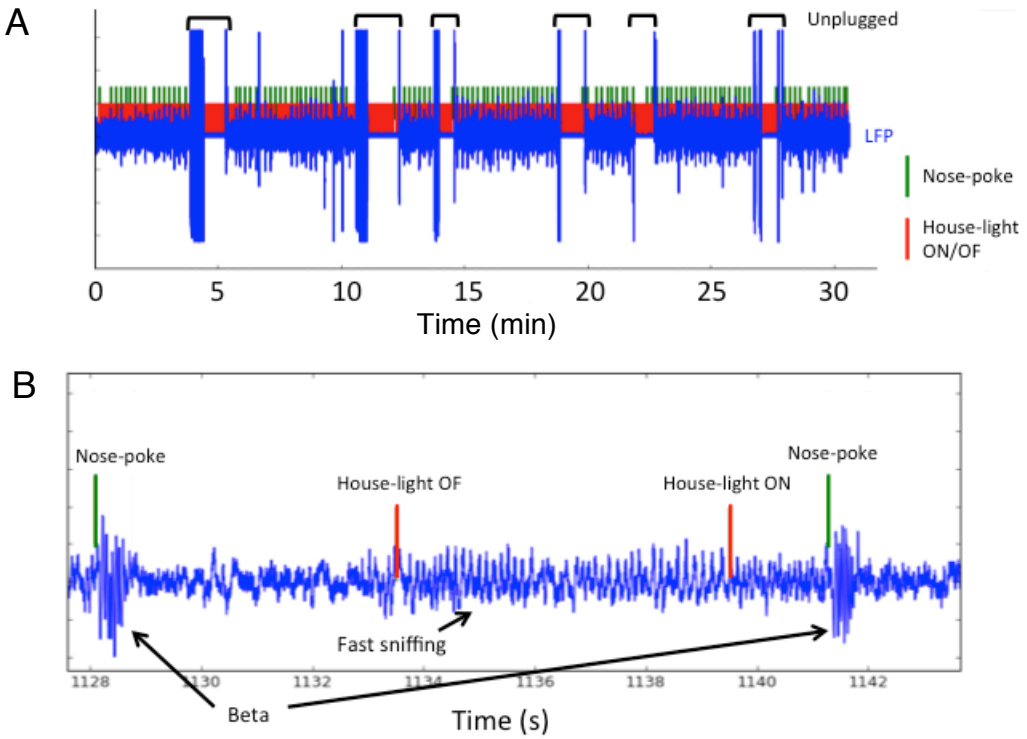

Figure 4.20 Raw LFP and event times during a nose-poke experiment A) LFP signal during the entire duration of one nose-poke recording session. The rat would frequently come unplugged from the tethered headstage as it explored the operant box. Individual house-light ON/OFF events. **B)** A zoomed in 15 s trace of the session in **B** shows that beta oscillations are reliably evoked almost immediately after the rat pokes its nose. The trace also shows fast investigatory sniffing, which often initiates when the house-light turns off.

between trials and the operant box was a more enriched environment than the cage in which swabs were presented.

In Figure 4.21A we show representative PSTHs for all the different types of nose-poke aligned responses to GER (Fig. 21Ai) and EMB (Fig. 21Aii). For these PSTHs we used a time bin of 50 ms to see finer grained dynamics than the PSTH in previous plots. Using this finer temporal resolution, we saw that many of the cells fired spikes that were precisely timed to the moment of nose-poke (top two rows of Fig. 4.21Ai,ii). Most cells that fired at nose-poke showed a brief return to baseline and then elevated activity for some portion of the beta period (second row of Fig. 4.21Ai,ii). Others cells were excited or inhibited only with the onset of beta (3rd and

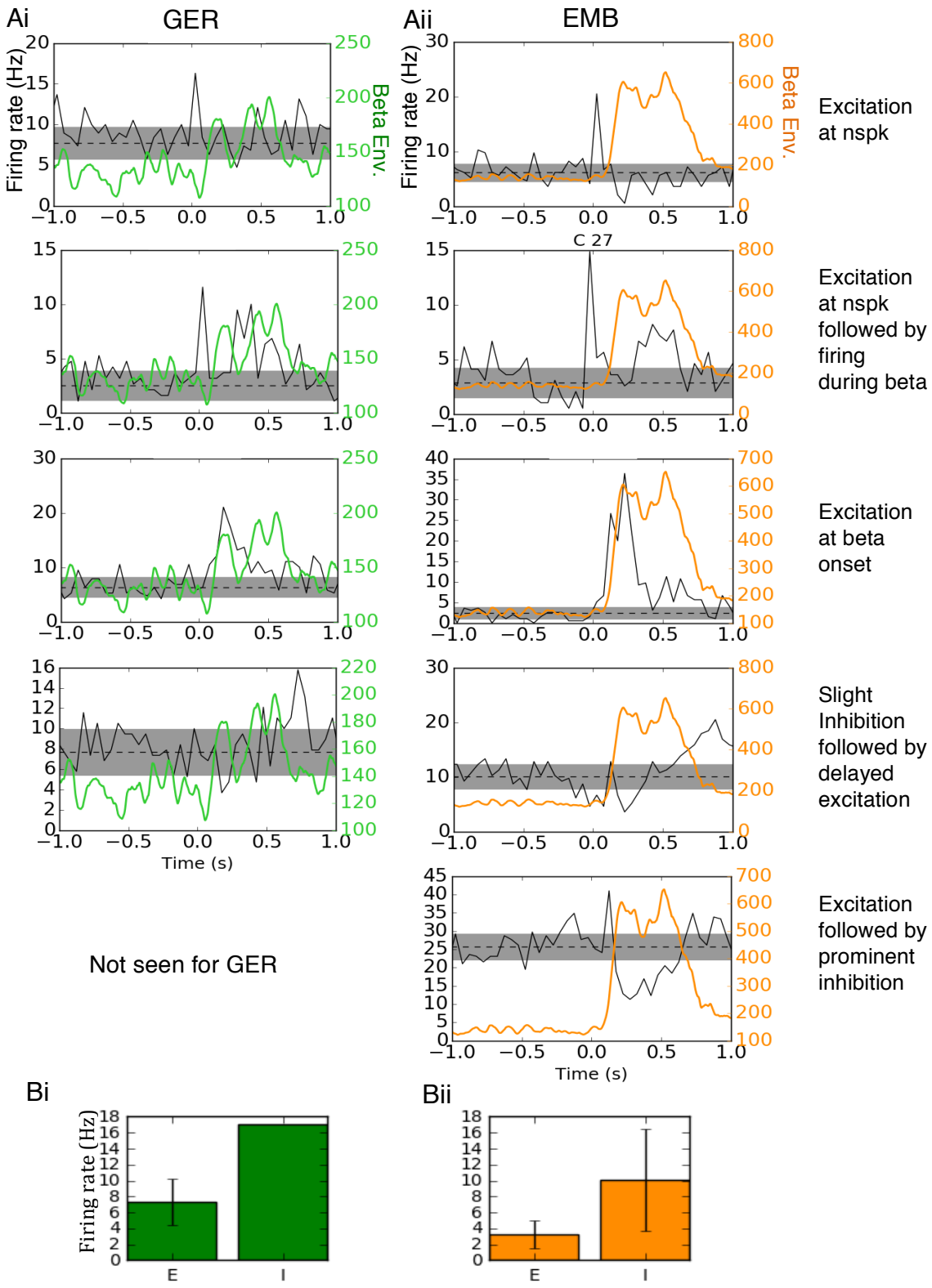

Figure 4.21 Average nose-poke aligned responses of GCL neurons to GER and EMB. A) Representative nose-poke aligned responses of individual cells for GER **(Ai)** and EMB **(Aii)** stimulation. Dashed line and gray area represent mean and standard deviation of baseline firing rate. Responses to GER did not show any prominent inhibition. **B)** Comparison of mean firing rates of cells that showed excitatory (E) and inhibitory (I) responses to GER **(Bi)** and EMB **(Bii)**. Only one cell had an inhibitory response to GER.

4th rows from the top of Fig. 4.21Ai,ii), and yet others showed mixed responses (bottom row of Fig. 4.21Aii). The EMB session produced 60 cells (or multi-cell clusters) total, 22 of which had no response, 9 fired at nose-poke, 8 were excited at beta onset, and 21 showed inhibitory or mixed responses. The GER session produced 68 cells (or multi-cell clusters) total, 42 of which had no change in firing rate, 12 fired at nose-poke, 13 were excited with beta onset, and only 1 showed a slight inhibitory response. Interestingly, cells that showed excitatory responses (grouping transient and persistent responses together) tended to have lower baseline firing rates than cells that showed inhibitory responses (Fig. 21Bi,ii). An exciting possibility is that the higher firing rate cells are being inhibited by the lower firing rate cells. In future work we will look at correlations in the firing patterns of these cells to see if such a relationship exists.

One might suspect that different responses might occur at different locations in the GCL. Excitatory and inhibitory responses were found distributed across the probe leads, but as shown in Figure 4.22, a diverse array of responses was detected within a localized region in the GCL. Excitatory and inhibitory responses in nearby GCL neurons could arise from local inhibitory connections between the cells. Although we have not yet looked, it would be interesting to see if there are any correlations in the firing patterns in nearby cells with such opposing responses.

The precise locking of spikes to nose-poke suggests that GCL neurons may not only be odor sensitive, but also part of a network of cells involved in motivated behavior. Our model predicted that GCs should spike before beta onset to drive the long lasting depolarization, which in turn increases GC excitability and sustains

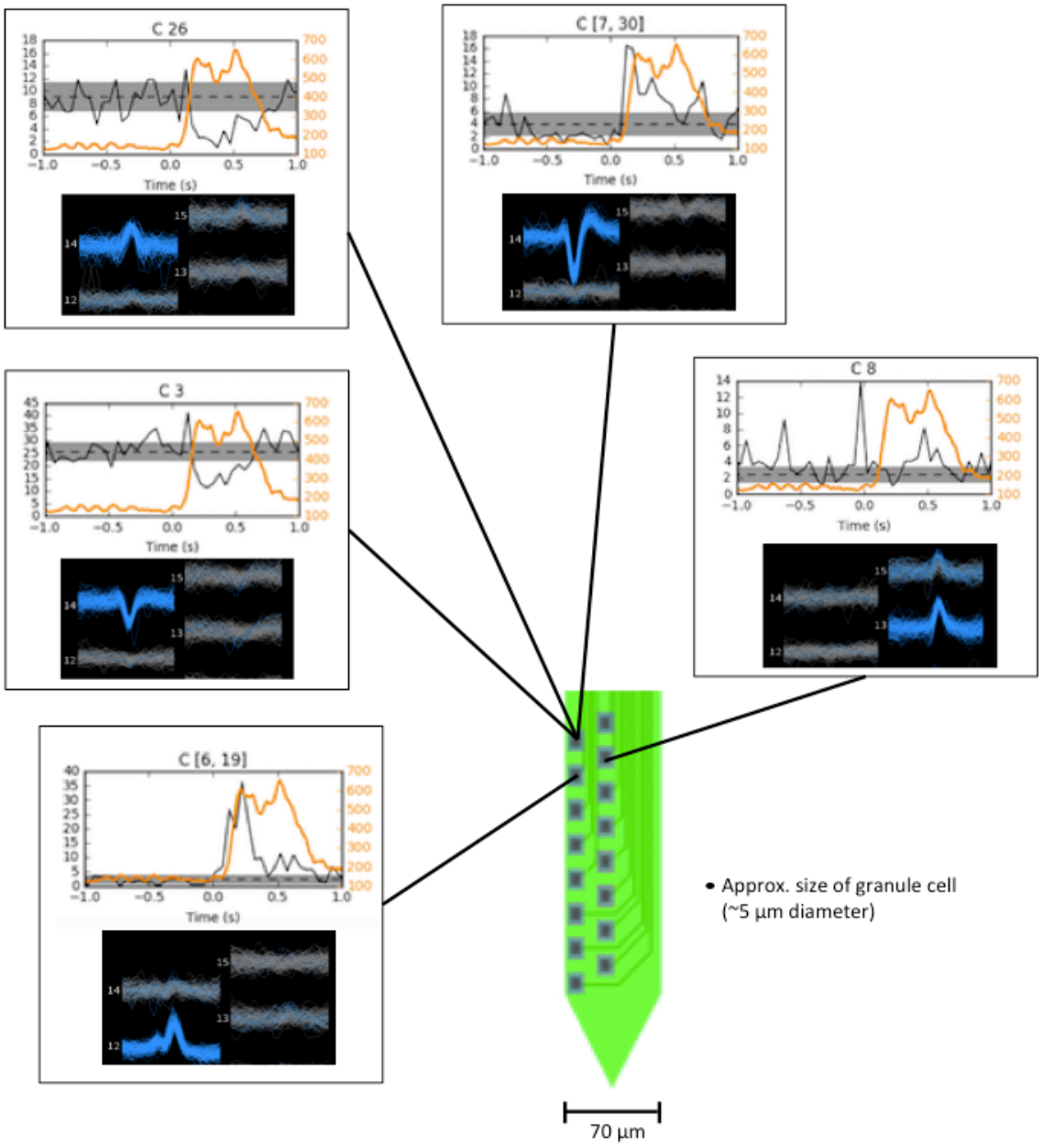

Figure 4.22 Diverse cell responses are detected in a small region of the probe. During the nose-poke single odor full reward EMB session the upper region of one of the shanks detected a particularly diverse collection of responses and waveforms. This suggests that nearby GCL neurons can have very different responses. Approximate size of granule cell is included for scale.

GABA release. Although the origins of the impulse that excites GCL neurons precisely at nose-poke are unknown, it is possible that it originates from cortical top-down inputs rather than sensory stimulation. A simple control to test this idea would be to include some blank trials during the session to check if the nose-poke locked GCL responses could be evoked without an odorant stimulus. Such a result would suggest that a motivated behavior might facilitate beta oscillation generation by centrifugally stimulating a subpopulation GCL neurons.

4.4.9 Results of Nose-poke 2-odor half-reward experiments

In a final set of nose-poke experiments we used two high volatility odors, EMB and PP. Both odors were rewarded fully for the first half of the session, but the reward for PP was discontinued for the second half of the session. Only Rat 3 performed these sessions (4th column of Table 4.1). The goal of these experiments was to answer the question, does the presence or absence of a reward influence odor evoked GCL neuron activity?

These experiments came with three challenges: (1) They were designed after the rat had already been implanted for ~4 months, so the signal quality was greatly reduced, and (2) the probe in Rat 3 was particularly sensitive to 60 Hz noise which the operant box frequently introduced into the signal. This had to be removed before clustering or else clusters were themselves composed of noise (see *Methods*). (3) The rat would frequently unplug itself, and this caused cells to be lost and new ones to be introduced over the course of the experiment. This can be seen in Figure 4.23A, which shows the firing rates of all cell across the entire experiment (with

noise and inter-trial periods removed). It appears that a sudden increase in most of the cells firing rates occurs just before the 2nd unplugging event, but this may just be due to a shifting of the probe closer to a group of cells.

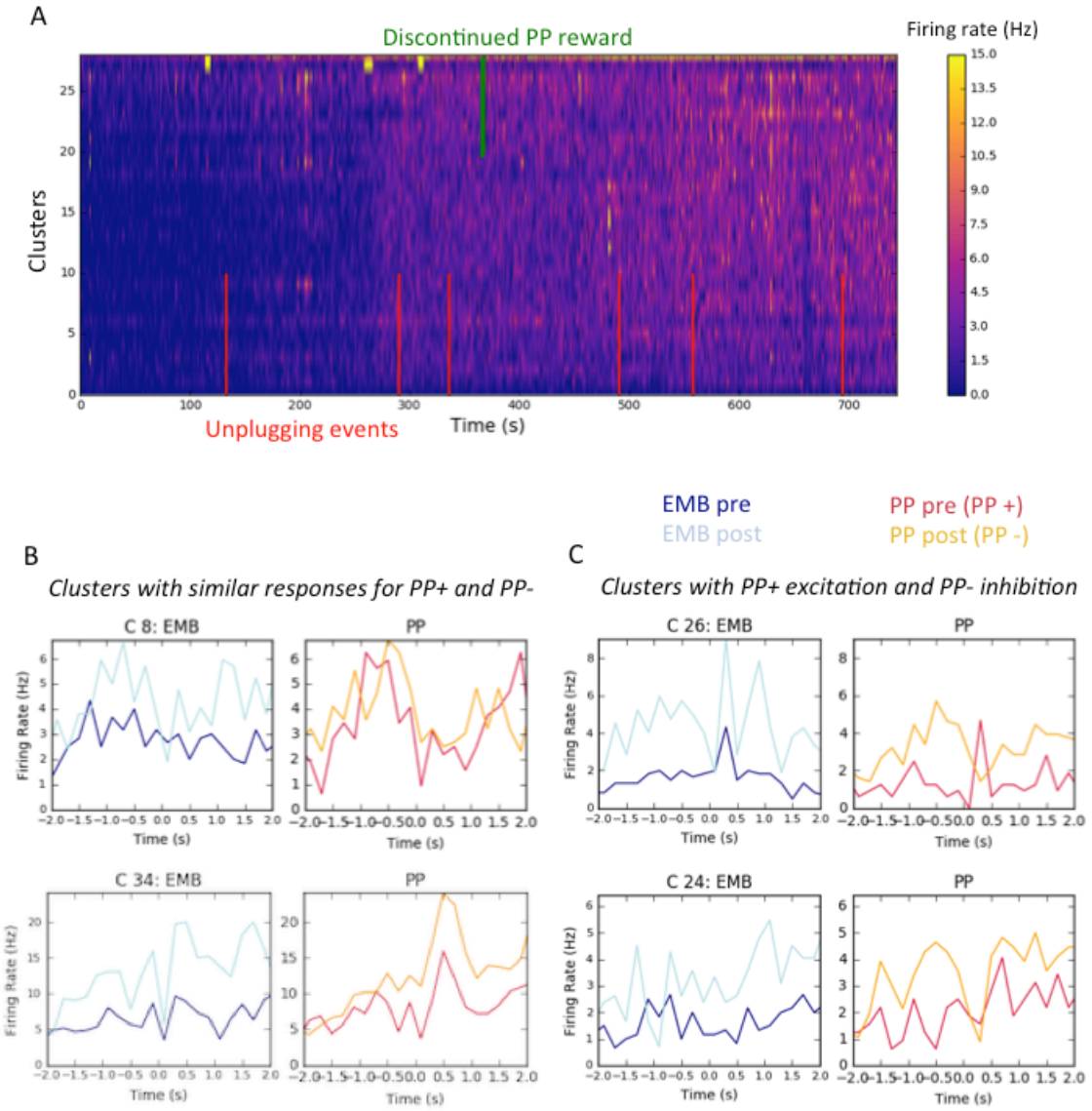

Figure 4.23 Some GCL neuron responses show reward contingency A) Firing rates of all clusters recorded for the nose-poke 2 odor half reward session. Although a few clusters show more consistent firing rates across the experiment, the firing rates for most of the clusters starts very low (1 – 3 Hz). The overall increases in firing rate seem to line up with the unplugging events (red vertical lines), which suggests that most of the clusters are corrupted by movement of the probe. A green vertical line marks the point at which PP reward was discontinued. **B)** Example PSTHs of two clusters that showed similar responses for both EMB and PP before and after PP reward discontinuation. **C)** Example PSTHs of two clusters that selectively showed inhibitory responses to PP-, but similar response for EMB pre and post PP reward discontinuation. PSTHs computed with 200 ms bins. (PP+ rewarded PP, PP- unrewarded PP)

Despite these significant limitations, we found some cells that showed compelling responses. In Figure 4.23B,C we computed PSTHs from trials before and after discontinuing PP reward. These PSTHs used the wider 200 ms bins. We refer to the rewarded PP trials as PP+ and unrewarded PP trials as PP-. We found some cells that showed similar responses for both EMB and PP before and after the reward discontinuation, so these cells were not sensitive to the change in reward (Fig. 4.23B). But surprisingly, some cells appeared to be inhibited only for PP after the reward was removed (Fig. 4.23C). The EMB responses, on the other hand, showed similar trends before and after (except for an overall increase in firing rate due to the clustering artifact described above). Out of 28 cells recorded for this session, 10 of them selectively showed inhibition for PP-. Although the data quality of this final experiment was poor, the results provide exciting preliminary data to serve as motivation for future experiments.

4.5 Discussion

In this series of experiments we recorded extracellular potentials using 32-channel Si probes implanted in the GCL of rats who participated in four different odor presentation experiments (Table 4.1). The results of our experiments show that GCL neurons produce odor specific responses that may evolve over time (Figs. 4.12-4.14 & 4.16). Cells with high gamma coherence tend to have low beta coherence and *vice versa* (Fig. 4.17). In one rat, the preferred beta oscillation phase across the whole recorded population was close to 90^{o}, but the other two rats showed more

heterogeneous phase preferences across GCL neurons (Fig. 4.18). Interestingly, some of the cells' responses carry more odor identity information in their timing, while others carry more in their rate (Fig. 4.19). In one rat, we showed that reward contingency may also influence the polarity of responses (Fig. 4.23). Together, these results demonstrate that GCL neuron responses are quite diverse and may help represent the meaning of odors on various time scales.

4.5.1 Possible approaches to identifying GCL neurons

In classical multichannel electrophysiology, different neurons can often be identified by the shape of their waveforms across multiple channels. This is usually possible because cortical neurons are organized in layers and the probe remains a fixed distance from the layer or contains channels that span the layer. In our case this was not viable because our probes were located within the GCL and were surrounded by GCL neurons from all sides. Simulations of the shape of extracellular potentials have shown that recorded spike shape differs greatly depending on where the probe is relative to the soma (Buzsáki et al., 2012). However, the relative lack of clearly biphasic waveforms suggested to us that we are recording from GCL neurons and not M/T cell axons. We could not be sure what type of neuron we were recording from the waveform shape, and thus we referred to all recorded neurons as GCL neurons to avoid misidentification.

Although identifying neuronal types by waveform was not possible, there are other features that may differentiate between cell types, at least on a functional level. One such feature is baseline firing rate. Our GCL neurons had a wide range of

baseline firing rates, but most fell within 1 – 10 Hz as shown in Figure 11B. Unlike the fast spiking interneurons found in neocortex, OB GCs typically fire at low rates (Cang and Isaacson, 2003a; Cazakoff et al., 2014). Two other known GCL interneuron subtypes, Blanes cells and deep short axon cells, also fire at similarly low rates (Pressler and Strowbridge, 2006; Burton and Urban, 2015). M/T cells typically fire spontaneously around 10 - 20 Hz (Kay & Laurent, 1999), though some tufted cells may fire faster around 30 - 40 Hz (Fukunaga et al, 2012; Igarashi et al., 2012). Thus, the slowest firing cells might be GABAergic GCL neurons, cells firing at moderate rates and clear refractory periods might be distant MCs somatic potentials, and the fastest firing cells may be distant tufted cells, if a refractory period is present, or otherwise multiunit combinations of the mentioned cell types.

Another feature that may help us distinguish between cell types is phase locking to gamma oscillations. It is known that M/T cells can be strongly phase locked to gamma and often fire in bursts (Eeckman and Freeman, 1990; Kay and Laurent, 1999). Thus a cell that fires 10 – 30 Hz bursts locked to gamma and has a refractory period in its ISI might be a M/T cell. We noticed that cells with high SFC between spikes and gamma oscillations had lower SFC between spikes and beta (Fig. 4.17). Some cells with high gamma SFC also have baseline firing rates near that of MCs. The sub-population of cells in Rat 3 that had particularly strong low gamma SFC might in fact be M/T cells.

4.5.2 Plasticity of GCL neuron responses over days

Several GCL neurons were well isolated and close enough to the probe that they could be recorded over days. Some of these cells showed the same response from day to day, but others showed changes in both their firing rate and LFP phase preferences (Fig. 4.14). GCL neurons receive dense contralateral innervation and neuromodulatory inputs (Kiselycznyk et al., 2006; Mouret et al., 2009a; Illig, 2011), which we hypothesize can drive context-dependent changes in their responses that may mirror those seen in mitral/tufted cells responses (Pager, 1978; Bhalla & Bower, 1997; Kay & Laurent, 1999; Rinberg et al., 2006; Doucette & Restrepo, 2008). For the multi-odor swab presentation experiments conducted on consecutive days, the contextual change may be the onset of familiarity (especially going from day 1 to day 2), because both rats were unfamiliar with the odor presentation protocol on day 1. This hypothesis may be supported by the fact that the mean beta power for high volatility odors (EMB in Rat 2, EMB & PP in Rat 3) was high on the first day, then dropped significantly on days 2 & 3. Since beta oscillations are thought to increase when nasal airflow rate is high (Fourcaud-Trocmé et al., 2011b), the decrease in beta LFP power could reflect a change in odor sampling strategy, perhaps as the rats learn to take shallower or shorter sniffs of high volatility odors.

4.5.3 Tuning of GCL neural responses to odor identity vs odor volatility

To visualize the odor response of the entire recorded GCL neuron population we performed LLE, following Stopfer et al. (2003), which produced trajectories in a 2D

space that evolved in time (Fig. 4.16). Although the trajectories for Rat 3 are somewhat messy, it appears that the trajectories for the two high volatility odors overlapped more closely with each other than with the two low volatility odors. This suggests that GCL neural responses might be more sensitive to odor volatility than odor identity. Unfortunately, we only used one high volatility odor for Rat 2, so we cannot confirm this in another rat. The only other study to date that recorded GCs in awake rats found GC responses to be more broadly tuned when awake than under anesthesia (Cazakoff et al., 2014). As GCs receive inputs from M/T cells across the bulb due to the long M/T cell lateral dendrites, such broad odor tuning of GCs would be expected.

4.5.4 Reasons for relatively low prediction accuracies from distance metric

Using a distance metric with varying temporal resolution to compare spike trains elicited by different odors, some cells were found to distinguish better between odors when distances were computed at fine temporal resolution (which we called timing cells), while others performed better when the total number of spikes was counted (which we called rate cells) (Figs. 4.8, 4.19). However, as described in the results, these values are rather low when compared to studies in cortical neurons, which used the same approach (Mackevicius et al., 2012), especially when looking at the population prediction accuracy (Fig. 4.19A), which is close to 100% for cortical neurons. One reason this may be the case is that these cells, being presumed inhibitory neurons that receive inputs from many MCs, may have broad response tuning, as was found to be the case for GCs (Cazakoff et al. 2014), so they respond

similarly to multiple odorants. Indeed, we showed an example of such a cell in Fig. 4.13B. For the cells that showed strong responses to only one odor, there was still a great deal of trial-to-trial variability. Because rats were behaving freely, they did not always sniff the odor swabs in the same way, sometimes turning their heads away while other times trying to lick or bite the swab, so the evoked responses could be modulated by behavioral factors independent of the odors, causing within class spike trains to vary quite a bit.

Another reason for low prediction accuracies is that many of the clusters with nice waveforms that passed our criteria for inclusion were later found to suffer from a clustering artifact. These clusters appeared to drop out or drastically reduce in firing rate at some point of the recording, likely due to movement of the probe causing the waveform to change and thus the clustering algorithm to lose the cell, and then come back. Such artificial changes in firing rates could drive prediction accuracies below chance, as spike trains elicited by different odors could become more similar to each other than those elicited by the same odor simply because spikes are missing. In future work we will remove the segments of time where cells drop out.

4.5.5 Reward contingency of GCL neuron responses: The bigger picture

During the reward modulation experiment some GCL neurons appeared to switch the polarity of their response from excitatory to inhibitory when an odor became unrewarded (Fig. 4.23). Although only one rat participated in this experiment, this

result provides exciting preliminary data for future studies. Previous studies have shown that a switch between which of the two odors is rewarded in a Go/No-Go task causes MCs to switch the polarity of their divergent responses (Doucette and Restrepo, 2008). Several other studies have also shown strong context modulation of M/T cells responses (Pager, 1978; Bhalla & Bower, 1997; Kay & Laurent, 1999). Although we used a simpler task than these studies (most studies used a Go/No-Go task), our results may be the first demonstration of context modulation of GCL neurons to date. Contextual meaning most likely arises from a wider neural network than the OB alone and probably relies on centrifugal inputs into the OB (Rinberg et al., 2006; Mouret et al., 2009a). Since most of these inputs target the GCL, we expected that GCL neurons should show some degree of context modulation. Although the OB is known to host adult born dopaminergic cells (Bonzano et al., 2016), these exist primarily in the GLO layer and are thought to be involved in sensory gain control and not reward modulation. Rather, OB reward modulation might function in a similar way as it does in the basal ganglia-thalamo-cortical loop, with the OB playing a similar role as a thalamus (Kay and Sherman, 2007).

5. Conclusion

5.1 Summary of results

I have presented a three-part body of work consisting of computational modeling (Osinski & Kay, 2016), pharmacological experiments (Osinski et al. 2017), and electrophysiological recordings (manuscript in preparation). The common thread through each of these is the role that OB GCs play in generating beta oscillations. The modeling work showed that OB beta oscillations could be sustained by VDCC-mediated synaptic currents in the MC-GC dendrodendritic network. Importantly, in this model beta oscillations could not be sustained by heightened GC excitability alone, but relied on an appropriate convergence of sensory input and centrifugal feedback onto GCs that increased their excitability. The model led to two main predictions. The first prediction suggested that there can be a divergent influence on the power of beta oscillations for low and high sensory input regimes when GC excitability is reduced. The second prediction is that beta oscillations are sustained primarily through VDCC-mediated currents independent of NMDA-mediated currents. Although the model didn't explicitly include GC somatic spikes, it implicitly assumed that GCs should fire spikes just before beta oscillation onset because their excitability is driven by an afterdepolarization current following a somatic spike.

In the pharmacological experiments, we found evidence for the two predictions. Infusion of scopolamine, which depresses GC excitability by blocking

muscarinic receptors, reduced the power of beta oscillations elicited by a strong (high volatility) odorant, but enhanced beta oscillations evoked by a weaker (low volatility) odorant (Fig. 3.6). The agreement with the model was not exact, because the biphasic effect of scopolamine (Fig. 3.3 & 3.4) was not captured by the model. This complex effect could be due to the influence of scopolamine on other muscarinic receptors throughout the bulb. Evidence for the second prediction was found when infusion of the NMDAR receptor antagonist APV did not significantly reduce beta oscillation power, but aggressively blocked gamma (Fig. 3.8).

In the high-density electrophysiological recordings, we also found evidence for the implied assumption of our model, namely that GCs would fire just before or at the onset of beta oscillations (Figs. 4.6C, 4.12A, 4.21). Some of the cells firing before the onset of beta were actually tightly locked to the time at which the rat poked its nose into an odor port (Fig. 4.21), suggesting that GCL neurons are behaviorally modulated. A rich diversity of other response types was also detected, indicating that our model assumptions were too simplistic (as is the case for most models). We point out that, in our model only a fraction of GCs had to participate in the beta oscillation, leaving open the possibility that other cells could be involved in another process during the beta oscillation. The GCL is home to many inhibitory subtypes, which may lead to more complex inhibitory cell responses. Interestingly, we found that some GCL neurons better discriminated between odors using the number of spikes, while others convey more information in the timing of their responses (Fig. 4.19), which we referred to as timing cells and rate cells. In

experiments where rats were trained to poke their noses into an odor port we found evidence for behaviorally modulated GCL responses.

5.2 Future directions

Over the course of the experiments presented here I left many stones unturned, especially for the high-density multichannel electrophysiological recordings of GCL neurons. I now discuss some avenues for continuing this work. Some of the contents of this section are redundant with what was said in previous discussion sections, but are included here for completeness.

5.2.1 Combining pharmacology and high density probe recordings

High-density Si probes attached to cannulas already exist, thus we could combine pharamacological manipulation and high-density recording to ensure that the effect that muscarinic drugs scopolamine and oxotremorine actually inhibit and excite GCL neurons as we expect. We could also expand to other drugs because the GCL receives a wide array of neuromodulatory inputs, and their effects on GCL activity in awake animals are not yet known. One such drug to use would be the N-type Ca^{2+} channel blocker, ω-conotoxin. Although the infusion of APV supported the model prediction that N-type VDCCs drive beta oscillations, it was not direct. To directly test the involvement of N-Type VDCCs we can infuse ω-conotoxin and then present odors.

5.2.2 Identifying GCL neuron types

Although I was not able to successfully identify different GCL neuron types in the present work, in section *4.5.1* I provided some suggestions on how to better discriminate between GCL cell types. The presence of rate and timing cells (as described in section *4.4.7*), suggests a functional distinction between two types of GCL neurons. I have not yet attempted to cluster timing and rate cells by other features such as waveform, phase preference, or baseline firing rates. Furthermore, I noticed that cells with inhibitory type responses tended to have higher baseline firing rates (Fig. 4.21). The higher firing rate cells may be distant M/T cells, and if this is the case then, they should also be phase locked to gamma.

5.2.3 Population level analysis of GCL neural responses: can we find cells working together?

Except for the population trajectories described in section 4.4.4, most of the analysis of the GCL neuron responses were on a cell-by-cell basis. Because we have many simultaneously recorded cells, we can perform a great deal of population level analysis. The simplest of these would be to look at pairwise correlations especially between nearby cells with opposite responses, like the ones shown in Figure 4.22. Does one always fire before the other? Do they fire on complementary phases of a beta oscillation, or are they completely uncorrelated?

Another possibility is to take an information theoretic approach. Such an analysis could potentially reveal highly informative firing patterns across cells,

suggesting that they may be participating in a dynamical state. It could also tell us whether the responses of cells are redundant, independent, or synergistic (carrying more information together than alone). However, because we don't have many trials (30 at most), there is a lot of trial-to-trial variability, and the stimulus space used in the experiments was quite small (only 3 or 4 odors), information theoretic analysis might not be viable for these recordings. Because the cells in the recorded population are not sensitive to every odor, future experiments should use more odorants to make it more likely that a cell will respond. Recordings should also be performed immediately after recovery from surgery to ensure highest signal quality.

5.2.4 Recording GCL neural responses during reward contingency experiments

Although the reward contingency experiment was only conducted in one rat, it served as a preliminary experiment to stimulate future work. The responses of OB M/T cells are known to be highly contextually modulated (Pager, 1978; Bhalla & Bower, 1997; Kay & Laurent, 1999). Because GCs receive dense cortical and neuromodulatory inputs, it is likely that this contextual modulation is mediated by GCs. Future implanted rats will be trained on Go/No-Go and 2-alternative choice tasks, which involve more cognitive processing than the simple rewarded nose-poke task used in this work. With these experiments, we will come closer to understanding the neural process that gives meaning to odors.

APPENDIX

Appendix I: Derivation of $[Ca]_{baseline}$

Because in the absence of MC spikes I_N has a non-zero activation even for resting potentials as low as -75 mV there is a constant Ca^{2+} current which sustains an internal $[Ca]$ which we call $[Ca]_{baseline}$. In order to prevent $[Ca]_{baseline}$ from driving tonic inhibition of MCs we subtract it in the calculation of $P_{release}$, as shown in Table 2.1. We derive $[Ca]_{baseline}$ by solving the steady state equation for $[Ca]$ evaluated at $V_{rest,dGC}$,

$$\tau_{Ca}[\dot{Ca}] = -[Ca] + \rho_{Ca}(I_{NMDA} + I_N) = 0 \qquad (A1)$$

$$[Ca] = \rho_{Ca} \cdot I_N = \rho_{Ca} \cdot W_N \bar{m}_N \frac{10^{-4}}{10^{-4} + [\mathrm{Ca}]} [E_{Ca(N)} - V_{rest,dGC}]$$

Note that in the absence of MC spikes the steady state of $I_{NMDA}$is 0 and the steady state of m_N is $\bar{m}_N$ evaluated at $V_{rest,dGC}$. Now we have a quadratic expression in $[Ca]$,

$$[Ca]^2 + 10^{-4}[Ca] - 10^{-4}\rho_{Ca} W_N \bar{m}_N \left[E_{Ca(N)} - V_{rest,dGC}\right] = 0 \qquad (A2)$$

which has the following solution

$$[Ca] = \frac{-10^{-4} \pm \sqrt{10^{-8} - 4 * 10^{-4}\rho_{Ca} W_N \bar{m}_N \left[E_{Ca(N)} - V_{rest,dGC}\right]}}{2} \qquad (A3)$$

$$[Ca] \approx \pm\sqrt{-10^{-4}\rho_{Ca} W_N \bar{m}_N \left[E_{Ca(N)} - V_{rest,dGC}\right]}$$

In the approximation we take advantage of the fact that the second term in the square root is of order $1 >> 10^{-4} >> 10^{-8}$. Now we must recognize that E_{Ca} itself is a logarithmic function of $[Ca]$, and thus an analytical solution here is not tractable.

Instead, $[Ca]_{baseline}$ is found as the value for which the left hand side (LHS) and right hand side (RHS) of the following equation intersect

$$V_{rest,dGC} + \frac{[Ca]^2{}_{baseline}}{10^{-4}\rho_{Ca}W_N\bar{m}_N} = \frac{RT}{zF} ln \frac{[Ca]_{out}}{[Ca]_{baseline}} \qquad (A4)$$

In practice this is achieved by finding the index of the minimum of abs(LHS – RHS), giving a value for $[Ca]_{baseline}$ which agrees well with the steady state internal [Ca] of all 720 simulated GCDs. One should note that this method breaks down if $[Ca]_{baseline}$ reaches or overshoots $[Ca]_{th}$ because in that case $P_{release}$ will be 0 or negative. We keep our model parameters in a range where this problem is not encountered.

Appendix II: Spike-Field Analysis Functions

Available on github: https://github.com/boleszek/NeuroAnalysisFunctionsPython

```
"""
Created on Sat Jun 24, 2017
@author: Boleszek Osinski, Kay Lab, University of Chicago

These functions were originaly designed to analyze spikes and LFPs
- detected with 32-channel 2-shank Si probes (Cambridge Neurotech)
- digitaly recorded using OpenEphys software

Data formats:
- Continuous data must be converted to flat binary .dat format to be analyzed
- Spike timing data are stroded in hdf5 format kwik files generated by klustakwik2

"""

import numpy as np
from scipy.signal import butter, hilbert, filtfilt, coherence
from scipy import stats
import random



def align_spikes_to_beta(no,nop,thb_sc,LFPb_env,SPK,odor_periods,sf):
    # This function aligns spike times to onset of beta oscillation determined by threshold
    # If no > 1 then the function will divide trials up into each odor
    # NOTE: This function assumes the odor presentations were interleaved if no>1!
    ########################################################
    # INPUTS:
    # no              -  number of odors
    # nop             -  number of presentations per odor
    # thb_sc          -  scaling of max beta envelope used to define threshold for beta onset
    # LFPb_env        -  List of beta envelope (per odor if no>1)
    # SPK             -  List of spike times for each cluster
    # odor_periods    -  List of start/stop times of each odor presentation
    # sf              -  Sampling freuqency
    ########################################################

    sssf = sf/10

    # Extract LFPb_env, in restricted odor periods
    # for determining acurate odor-evoked beta env integral and finding first real beta
    # trying to exclude noise-like deflections occurring at beggining of some trials
    sc1 = 0.8
    sc2 = 2
    start = odor_periods[0::2] - sc1*sf
    stop = odor_periods[1::2] + sc2*sf
    LFPb_env_op = exctract_LFP_trials(start,stop,nop*no,LFPb_env)
    #benv_integral = [np.sum(LFPb_env_op[i]) for i in range(nop*no)]
    #sindbei=np.argsort(benv_integral) # sorted inds of beta envelope integral
    # Get rid of edge effects by setting envelope on either edge = 0!!!
    # This will also allow detection of suprathresh at start of window!
    for i in range(nop*no):
        LFPb_env_op[i][0:50] = 0
        LFPb_env_op[i][-50:] = 0

    if no == 1:
        # Get index of threshold on beta power
        #thb = thb_sc*np.max(LFPb_env) # threshold on entire data set (good for EMB data)
        thb = thb_sc*np.median([np.max(LFPb_env_op[i]) for i in range(nop)])
        startb_op = list()
        for i in range(nop):
```

```
        yo = LFPb_env_op[i] >= thb
        # find first nonzero element (should correspond to beta onset)
        # If there is no detectable beta, then use lower thresh
        if sum(yo.nonzero()[0]) == 0:
            yo = LFPb_env_op[i] >= thb/2
        if sum(yo.nonzero()[0]) == 0:
            yo = LFPb_env_op[i] >= thb/2.5
        if sum(yo.nonzero()[0]) == 0:
            yo = LFPb_env_op[i] >= thb/3
        startb_op.append(yo.nonzero()[0][0]) # this is in ssLFP time!


    # Extract LFP, LFPb_env, and spikes in extended odor periods (to include baseline)
    scext1 = 6 #s
    scext2 = 6
    start = odor_periods[0::2] - scext1*sf
    stop = odor_periods[1::2] + scext2*sf
    LFPb_env_op_ext = exctract_LFP_trials(start,stop,nop,LFPb_env)
    #ssLFP_op_ext = exctract_LFP_trials(start,stop,nop,ssLFP)
    SPK_op_ext = exctract_SPK_trials(start,stop,nop,SPK)
    # adjust startb_ob indices for extended windows
    startb_op_ext = [startb_op[i]+sssf*(scext1-sc1) for i in range(nop)]

    # Align spikes to beta env thresh crossing for extended windows
    SPK_op_ext_aligned = []
    for i in range(nop):
        SPKtmp = list()
        for s in range(len(SPK)):
            # align spikes to startb_op_ext
            SPKtmp.append(SPK_op_ext[i][s] - startb_op_ext[i]*10)
        SPK_op_ext_aligned.append(SPKtmp)
else:

    # Get index of threshold on beta power for each odor
    #thb = []
    #for o in range(no):
    #    thb.append(thb_sc[o]*np.max(np.hstack(LFPb_env_op[o::no])))
    #print('using global max per odor')
    thb = []
    for o in range(no):
        # use the median of max values to minimize scaling by outliers
        thb.append(thb_sc[o]*np.median([np.max(LFPb_env_op[o::no][i]) for i in range(nop)]))

    startb_op = []
    for o in range(no):
        inds = np.arange(o,nop*no,no)
        startb_op_temp = []
        for i in range(nop):
            yo = LFPb_env_op[inds[i]] >= thb[o]
            # find first nonzero element (should correspond to beta onset)
            # If there is no detectable beta, then use lower thresh
            if sum(yo.nonzero()[0]) == 0:
                yo = LFPb_env_op[inds[i]] >= thb[o]/2
            if sum(yo.nonzero()[0]) == 0:
                yo = LFPb_env_op[inds[i]] >= thb[o]/2.5
            if sum(yo.nonzero()[0]) == 0:
                yo = LFPb_env_op[inds[i]] >= thb[o]/3
            startb_op_temp.append(yo.nonzero()[0][0]) # this is in ssLFP time!
        startb_op.append(startb_op_temp)

    # Extract LFP, LFPb_env, and spikes in extended odor periods (to include baseline)
```

```
        scext1 = 6
        scext2 = 6
        start = odor_periods[0::2] - scext1*sf
        stop = odor_periods[1::2] + scext2*sf
        LFPb_env_op_ext = exctract_LFP_trials(start,stop,nop*no,LFPb_env)
        #ssLFP_op_ext = exctract_LFP_trials(start,stop,nop*no,ssLFP)
        SPK_op_ext = exctract_SPK_trials(start,stop,nop*no,SPK)
        # adjust startb_ob indices for extended windows
        startb_op_ext = []
        for o in range(no):
            startb_op_ext.append([startb_op[o][i]+sssf*(scext1-sc1) for i in range(nop)])

        # Align spikes to beta env thresh crossing for extended windows
        SPK_op_ext_aligned = []
        for o in range(no):
            SPK_op_ext_aligned_temp = []
            inds = np.arange(o,nop*no,no)
            for i in range(nop):
                SPKtmp = list()
                for s in range(len(SPK)):
                    # align spikes to startb_op_ext
                    # startb_op_ext is in ssLFP time!
                    SPKtmp.append(SPK_op_ext[inds[i]][s] - startb_op_ext[o][i]*10)
                SPK_op_ext_aligned_temp.append(SPKtmp)
            SPK_op_ext_aligned.append(SPK_op_ext_aligned_temp)

    return SPK_op_ext_aligned, LFPb_env_op, LFPb_env_op_ext, startb_op_ext

def align_spikes_to_beta_general(LFPb_env,SPK,thb_sc,op_start,op_stop,wind_restrict,wind_extend
    # This function aligns spike times to onset of beta oscillation determined by threshold
    # It is more generalized than the first version of this function:
    # - allows user to set restricted and extended window adjustment params
    # - designed to just run on the entire data. No spilitting into groups
    #   (if different thb_sc are needed for different events then simply run function with diff
    # - does not assume interleaved odor presentations
    ########################################################
    # INPUTS:
    # LFPb_env       -  List of beta envelope. (1D array)
    # SPK            -  List of spike times for each cluster. (list of dim #clusters)
    # thb_sc         -  scaling of max beta envelope used to define threshold for beta onset
    # op_start       -  List of odor period start times
    # op_stop        -  List of odor period stop times
    # wind_restrict  -  [start,stop] pair of vallues in (s) added to start/stop of each trial w
    #                   closer to the actual beta events. Used in beta onset detection step. st
    # wind_extend    -  [start,stop] pair of vallues in (s) added to start/stop of each trial w
    #                   The output of the function uses the extended window. start is usuall a
    # sf             -  Sampling freuqency (Hz)
    #
    # Written by Boleszek Osinski, Kay Lab (2017)
    ########################################################

    # start and stop bettwe be the same length!
    assert len(op_start) == len(op_stop)
    nop = len(op_start)

    sssf = sf/10

    #-------- Extract LFPb_env in restricted odor periods --------#
    # for determining acurate odor-evoked beta env integral and finding first real beta
    # trying to exclude noise-like deflections occurring at beggining of some trials
    start = np.array(op_start) + wind_restrict[0]*sf
```

```
    stop = np.array(op_stop) + wind_restrict[1]*sf
    LFPb_env_op_rest = exctract_LFP_trials(start,stop,nop,LFPb_env) # this functions assumes LFI
    # Get rid of edge effects by setting envelope on either edge = 0!
    # This will also allow detection of suprathresh at start of window!
    for i in range(nop):
        LFPb_env_op_rest[i][0:50] = 0
        LFPb_env_op_rest[i][-50:] = 0

    #-------- Detect beta onset for each trial in restricted windows --------#
    # Get index of threshold on beta power (single threshold using median power of all trials)
    thb = thb_sc*np.median([np.max(LFPb_env_op_rest[i]) for i in range(nop)])
    startb_op = list()
    for i in range(nop):
        yo = LFPb_env_op_rest[i] >= thb
        # find first nonzero element (should correspond to beta onset)
        # If there is no detectable beta, then use lower thresh
        if sum(yo.nonzero()[0]) == 0:
            yo = LFPb_env_op_rest[i] >= thb/2
        if sum(yo.nonzero()[0]) == 0:
            yo = LFPb_env_op_rest[i] >= thb/2.5
        if sum(yo.nonzero()[0]) == 0:
            yo = LFPb_env_op_rest[i] >= thb/3
        startb_op.append(yo.nonzero()[0][0]) # this is in ssLFP time!


    #--------- Extract LFPb_env, and spikes in extended windows --------#
    start = np.array(op_start) + wind_extend[0]*sf
    stop = np.array(op_stop) + wind_extend[1]*sf
    LFPb_env_op_ext = exctract_LFP_trials(start,stop,nop,LFPb_env)
    SPK_op_ext = exctract_SPK_trials(start,stop,nop,SPK)
    # adjust startb_ob indices for extended windows
    startb_op_ext = [startb_op[i]+sssf*(-wind_extend[0]-wind_restrict[0]) for i in range(nop)]

    #-------- Align extended window spikes to beta env thresh crossing --------#
    SPK_op_ext_aligned = []
    for i in range(nop):
        SPKtmp = list()
        for s in range(len(SPK)):
            # align spikes to startb_op_ext
            SPKtmp.append(SPK_op_ext[i][s] - startb_op_ext[i]*10) # rescaling back by 10 to be
        SPK_op_ext_aligned.append(SPKtmp)

    return SPK_op_ext_aligned, LFPb_env_op_rest, LFPb_env_op_ext, startb_op_ext

def align_spikes_to_events(SPK_trials,event_times,event_ID = []):
    # This function aligns spike times in SPK_trials to event_times
    # NOTE: This function assumes that event_times are in same units as SPK!
    ########################################################
    # INPUTS:
    # SPK_trials    -  List of spike times in each trial (length Ntrials, with Ncell sublists)
    # event_times   -  List of event times (length Ntrials), must be same units as SPK_trials
    # event_ID      -  List of unique numeric event IDs (i.e. unique odors). (length Ntrials)
    #                       If nothing provided, assume all events same type
    #
    # Written by Boleszek Osinski, Kay Lab (2017)
    ########################################################

    assert len(SPK_trials) == len(event_times)
    nc = len(SPK_trials[0]) # number of cells

    if len(event_ID) == 0:
```

```
        # assume only 1 type of event
        event_ind_list = [np.arange(0,len(event_times))] # put it in a list so len(event_ind_li
        uid = []
    else:
        assert len(SPK_trials) == len(event_ID)
        uid = np.unique(event_ID) # names of unique events
        event_ind_list = []
        for i in range(len(uid)):
            event_ind_list.append(np.where(event_ID == uid[i])[0])

    # Align spikes to event times. There will be multiple groups if >1 type of event
    SPK_trials_aligned = []
    for i in range(len(event_ind_list)): # this groups things by unique events
        SPKtmp_group = list()
        for j in event_ind_list[i]: # this idexes over the individual events in each group
            SPKtmp_cells = list()
            for c in range(nc):
                # align spikes to event_times
                SPKtmp_cells.append(SPK_trials[j][c] - event_times[j])
            SPKtmp_group.append(SPKtmp_cells)
        SPK_trials_aligned.append(SPKtmp_group)

    return SPK_trials_aligned, uid

def butter_env(order, low, high, signal):
    # This function bandpass filters the signal between low and high frequencies using butterwo
    # Returns filtered signal, envelope, and phase determined by hilbert transform
    # INPUTS:
    # order    - order of butterworth filter
    # low      - low lim of fq band (Hz/nyq)
    # high     - high lim of fq band (Hz/nyq)
    # signal   - signal to be filtered
    # NOTE: low and high fq band cutoffs must be divided by nyquist frequncy!
    ######################################
    b, a = butter(order, [low, high], btype='bandpass')
    filt_signal = filtfilt(b, a, signal)
    # Amplitude of analytic signal is the envelope
    hilb_filt_signal = hilbert(filt_signal)
    filt_signal_env = np.abs(hilb_filt_signal)
    # The instantaneous phase corresponds to the phase angle of the analytic signal
    filt_signal_ph = np.angle(hilb_filt_signal)
    return filt_signal, filt_signal_env, filt_signal_ph

def calc_PSTH(no,nop,bw,edges,SPK_op_ext_aligned):
    # This function calculates PSTH for aligned spikes
    # If no > 1 then the function will divide trials up into each odor
    # This function has hard coded values
    # NOTE: This function assumes the odor presentations were interleaved if no>1!
    ######################################################
    # INPUTS:
    # no                -  number of odors
    # nop               -  number of odor presentations
    # bw                -  bin width (s)
    # edges             -  edges in time used to calculate histogram for PSTH
    # SPK_op_ext_aligned -  embedded lists of beta-aligned spikes. This is output from align_sp
    ######################################################

    if no == 1:
        PSTH = []
        PSTH_trim = [] # trim 2s from start and end of PSTH (where there are missing spikes due
        PSTH_blmn = []
```

```
        PSTH_blstd = []
        trim = int(2/bw - 1) # number of indices of PSTH corresponding to 2s
        for s in range(len(SPK_op_ext_aligned[0])):
            hist_temp_sum = np.zeros(len(edges)-1)
            for i in range(nop):
                hist_temp,crap = np.histogram(SPK_op_ext_aligned[i][s],edges)
                hist_temp_sum += hist_temp
            PSTH.append(hist_temp_sum/(nop*bw))
            PSTH_trim.append(PSTH[s][trim:-trim])
            PSTH_blmn.append(np.mean(PSTH_trim[s][0:int(3/bw)]))
            PSTH_blstd.append(np.std(PSTH_trim[s][0:int(3/bw)]))
    else:
        PSTH = []
        PSTH_trim = [] # trim 2s from start and end of PSTH (where there are missing spikes due
        PSTH_blmn = []
        PSTH_blstd = []
        trim = int(2/bw - 1) # number of indices of PSTH corresponding to 2s
        for o in range(no):
            PSTH_temp = []
            PSTH_trim_temp = []
            PSTH_blmn_temp = []
            PSTH_blstd_temp = []
            for s in range(len(SPK_op_ext_aligned[0][0])):
                hist_temp_sum = np.zeros(len(edges)-1)
                for i in range(nop):
                    hist_temp,crap = np.histogram(SPK_op_ext_aligned[o][i][s],edges)
                    hist_temp_sum += hist_temp
                PSTH_temp.append(hist_temp_sum/(nop*bw))
                PSTH_trim_temp.append(PSTH_temp[s][trim:-trim])
                PSTH_blmn_temp.append(np.mean(PSTH_trim_temp[s][0:int(3/bw)]))
                PSTH_blstd_temp.append(np.std(PSTH_trim_temp[s][0:int(3/bw)]))
            PSTH.append(PSTH_temp)
            PSTH_trim.append(PSTH_trim_temp)
            PSTH_blmn.append(PSTH_blmn_temp)
            PSTH_blstd.append(PSTH_blstd_temp)

    return PSTH, PSTH_trim, PSTH_blmn, PSTH_blstd

def calc_PSTH_general(nue,bw,edges,SPK_trials_aligned,blwin):
    # Unlike calc_PSTH, which includes hard coded values specifc to the beta-aligned analysis,
    # This function calculates PSTH for aligned spikes aligned to generalized events (no hard c
    # If nue > 1 the function will calculate PSTH for each event type
    ########################################################
    # INPUTS:
    # nue                -  number of unique types of events (i.e. different odors)
    # bw                 -  bin width (s)
    # edges              -  edges in same unit as spikes used to calculate histogram for PSTH
    # SPK_trials_aligned -  embedded lists of beta-aligned spikes. This is output from align_sp
    # blwin              -  [start,stop] baseline window (same units as spikes) to determine ba
    ########################################################

    blstart = np.where(edges > blwin[0])[0][0] # first index greater than start
    blstop = np.where(edges < blwin[1])[0][-1] # last index less than stop

    if nue == 1:
        SPK_trials_aligned = [SPK_trials_aligned] # put it in a list so it is indexed in the sa

    PSTH = []
    PSTH_blmn = []
    PSTH_blstd = []
    for n in range(nue):
```

```
        PSTH_temp = []
        PSTH_blmn_temp = []
        PSTH_blstd_temp = []
        nev = len(SPK_trials_aligned[n]) # number of events (trials) in group n
        for s in range(len(SPK_trials_aligned[n][0])): # iterate over cells
            hist_temp_sum = np.zeros(len(edges)-1)
            for i in range(nev):  # iterate over events in a group
                hist_temp,crap = np.histogram(SPK_trials_aligned[n][i][s],edges)
                hist_temp_sum += hist_temp
            PSTH_temp.append(hist_temp_sum/(nev*bw)) # normalize to Hz
            PSTH_blmn_temp.append(np.mean(PSTH_temp[s][blstart:blstop]))
            PSTH_blstd_temp.append(np.std(PSTH_temp[s][blstart:blstop]))
        PSTH.append(PSTH_temp)
        PSTH_blmn.append(PSTH_blmn_temp)
        PSTH_blstd.append(PSTH_blstd_temp)

    return PSTH, PSTH_blmn, PSTH_blstd

def classify_PSTH(PSTH,bw):
    # This function breaks the aligned PSTH into 3 parts:

    # 0.4s arround the stimulus onset (alignement point)
    # 0.6s after that (completing first s after stim onset)
    # 2s after that
    # Note: these values are assuming that bw = 0.2s!


    # The response in each of these time periods is classified as exited (1), inhibbited (-1),
    # or no change from baseline (0). This is represented by class_vec

    # Note: PSTH must have clean edges! PSTH is assumed to have even number of points and > 3s l

    # Take 1st 3s as baseline
    blmn = np.mean(PSTH[0:int(3/bw)])
    blstd = np.std(PSTH[0:int(3/bw)])

    half = int(len(PSTH)/2)

    class_vec = [0,0,0]

    # t1 is bin width
    t2 = 0.6 # s after t1
    t3 = 2.2 # s after t2

    if np.mean(PSTH[half-1:half+1]) > blmn + 1.3*blstd: # a little stricter criterion for the ti
        class_vec[0] = 1
    if np.mean(PSTH[half-1:half+1]) < blmn - 1.3*blstd:
        class_vec[0] = -1
    if np.mean(PSTH[(half+1):(half+1+int(t2/bw))]) > blmn + blstd:
        class_vec[1] = 1
    if np.mean(PSTH[(half+1):(half+1+int(t2/bw))]) < blmn - blstd:
        class_vec[1] = -1
    if np.mean(PSTH[(half+1+int(t2/bw)):(half+1+int((t2+t3)/bw))]) > blmn + blstd:
        class_vec[2] = 1
    if np.mean(PSTH[(half+1+int(t2/bw)):(half+1+int((t2+t3)/bw))]) < blmn - blstd:
        class_vec[2] = -1

    # Naming:
    # [0,0,0] unmodulated (U)
    # [1,0,0] transient excitation (tE)
    # [-1,0,0] transient inhibition (tI)
```

```
    # [0,1,0] delayed transient excitation (dtE)
    # [0,-1,0] delayed transient inhibition (dtI)
    # [1,1,1] persistent excitation (pE)
    # [-1,-1,-1] persistent inhibition (pI)
    # [0,0,1],[0,1,1] delayed persistent excitation (dpE)
    # [0,0,-1],[0,-1,-1] delayed persistent inhibition (dpI)
    # [1,-1,0] EI
    # [1,-1,1] EIE
    # [-1,1,0] IE
    # [-1,1,-1] IEI
    # remaining patterns might be ignored

    return class_vec

def distance_between_all_trials(SPK_op,ot_inds,start,stop,q,sf):
    # This function uses the victor & purpura distance metric to produce a
    # distance matrix between all spike train pairs in SPK_op within a window
    # defined by start and stop.
    # If list of multiple cells is provided then dist mat is calculated seperately for each cel
    ############################
    # INPUTS:
    # SPK_op      - must be an embedded list with 1st level - odor, 2nd level - trials, 3rd lev
    # ot_inds     - predifined 2 x no*ntr matrix of odor and trial indices
    # start       - start time of window (s)
    # stop        - stop time of window (s)
    # q           - cost per unit time to move a spike (as defined by victor & purpura)
    # sf          - sampling frequency (to convert spike trains to units of s)
    ############################
    from victor_purpura import distance # victor_purpura.py must be in same directory!
    # the victor_purpura module must be in path

    nc = len(SPK_op[0][0])
    nt = ot_inds.shape[1]
    dist_mat = []
    for c in range(nc):
        #print('Calculating all distances from cell '+str(c)+'...')
        dist_mat_temp = np.zeros((nt,nt))
        for i in range(nt):
            si = SPK_op[int(ot_inds[0,i])][int(ot_inds[1,i])][c]/sf
            si = si[np.logical_and(si > start,si < stop)]
            for j in np.arange(i,nt):
                sj = SPK_op[int(ot_inds[0,j])][int(ot_inds[1,j])][c]/sf
                sj = sj[np.logical_and(sj > start,sj < stop)]

                dist_mat_temp[i,j] = distance(si, sj, q)
                dist_mat_temp[j,i] = dist_mat_temp[i,j] # matrix is symmetric
        dist_mat.append(dist_mat_temp)

    return dist_mat

def extract_from_mpc(mpc_fname,token,stop=None):
    # This function extracts data from variable 'token' up until 'stop', and converts it into a
    # INPUTS:
    # mpc_fname  - medPC file name
    # token       - sThe variable whose data is to be extracted
    # stop       - The variable at which to stop (if nothing provided the extraction will keep
    # OUTPUTS:
    # numdat     - 1D numeric array
    ######################################

    # load string data into strdat
```

```
    strdat = []
    with open(mpc_fname, 'r') as f:
        for line in f:
            if token in line:
                for line in f: # now you are at the lines you want
                    if stop in line: # Run until you hit stop variable
                        break
                    else:
                        strdat.append(line)

    # convert string sata into numeric data
    numdat = np.empty(0)
    for i in range(len(strdat)):
        temp = strdat[i].split()[1:] # skip the first entry, which is an index
        temp = np.array(temp,dtype = float) # convert to numeric array
        numdat = np.concatenate((numdat,temp))

    numdat = numdat[numdat>0] # get rid of any trailing 0s

    return numdat

def exctract_LFP_trials(start,stop,nop,ssLFP):
    # INPUTS:
    # start      -       start time of extraction window (samples)
    # stop       -       stop time of extraction window (samples)
    # nop        -       number of odor presentations (usually 30)
    # ssLFP      -       sub sampled LFP

    ssLFP_op = list()
    for i in range(nop):
        # remember, LFP is subsampled by 10
        ssLFP_op.append(ssLFP[int(start[i]/10):int(stop[i]/10)])

    return ssLFP_op

def exctract_SPK_trials(start,stop,nop,SPK):
    # INPUTS:
    # start      -       start time of extraction window (samples)
    # stop       -       stop time of extraction window (samples)
    # nop        -       number of odor presentations (usually 30)
    # SPK        -       1 x nclusters list of spike times (samples)

    SPK_op = list()
    for i in range(nop):
        SPKtmp = list()
        for s in range(len(SPK)):
            # find spk times in odor periods. Don't save spikes within 10 smaples of the stop
            # to avoid later indexing issues when indexing last element of subsampled array
            sind = np.array(np.where((SPK[s] > start[i]) & (SPK[s] < (stop[i]-10))))
            sind = sind.astype(int) # convert type to int
            SPKtmp.append(SPK[s][sind]-start[i]) # subtract away start time of odor period
        SPK_op.append(SPKtmp)

    return SPK_op

def fft_integrate_power_in_band(signal,Fs,fstart,fstop):
    # This function calculates FFT power spectrum of signal and integrates the power in chosen j
    # INPUTS:
    # signal   - continuous signal
    # Fs       - sampling frequency (Hz)
    # fstart       - start of fq band
```

```
    # fstop       - stop of fq band
    ####################################
    N = len(signal)
    T = 1.0 / Fs #(s)
    signal_FFT = np.fft.fft(signal)
    signal_PWR = 2.0/N * np.abs(signal_FFT[0:int(N/2)])

    f = np.linspace(0.0, 1.0/(2.0*T), N/2) # define freuqency vector
    fstart_ind = np.where(f>fstart)[0][0]
    fstop_ind = np.where(f>fstop)[0][0]

    sumpwr = np.sum(signal_PWR[fstart_ind:fstop_ind]) # sum power

    return signal_PWR, sumpwr, f, fstart_ind, fstop_ind

def find_matching_files(ddir,match_str_list):
    # This function finds all the folders in data directory ddir with names that includes the el
    # match_str_list
    import os
    ddir_list = os.listdir(ddir)
    dfold_list = []
    for file in ddir_list:
        for i in range(len(match_str_list)):
            if match_str_list[i] in file:
                dfold_list.append(file)
    return dfold_list

def get_FR(spikes,bw,sf,maxt):
    # spikes     -     vector of spike times
    # bw         -     bin window (s)
    # sf         -     sampling fq
    # maxt       -     max time bin
    bins = np.arange(0,maxt,bw)
    [fr,bleh] = np.histogram(spikes/sf,bins)
    fr = fr/bw # convert counts to rate
    return fr

def get_peak_phase_sinORgauss(data,edges):
    # Fits a sine and a gaussian to a histogram of the spike-phase product values in "data" bin
    # Returns the phase at the peak value of the fit with the lowest error.
    # INPUTS:
    # data      -  list of spike-phase products
    # edges     -  edges from -pi to pi for binning data into histogram
    from scipy.optimize import curve_fit
    import math

    # Define sine function
    def sinfunc(x, *p):
        #A, w, p, c = p # if w (fq) is not fixed
        A, p, c = p # fixed w
        #return A * np.sin(w*x + p) + c
        return A * np.sin(x + p) + c

    # Define gaussian
    def gauss(x, *p):
        A, mu, sigma = p
        return A*np.exp(-(x-mu)**2/(2.*sigma**2))

    edge_step = edges[1]-edges[0]
    hist, bin_edges = np.histogram(data, edges)
    bin_centres = edges[0:-1]+edge_step/2
```

```
    # p0sin is the initial guess for the fitting coefficients (A, w, p, c)
    #p0sin = [np.max(hist), 1, 0, np.max(hist)/2]
    # p0sin is the initial guess for the fitting coefficients (A, p, c)
    p0sin = [np.max(hist)/2, 0, np.max(hist)]

    # p0gauss is the initial guess for the fitting coefficients (A, mu and sigma)
    p0gauss = [np.max(hist), bin_centres[np.argmax(hist)], 0.5]

    try:
        coeff_sin, var_matrix_sin = curve_fit(sinfunc, bin_centres, hist, p0=p0sin, maxfev = 10(
        coeff_gauss, var_matrix_gauss = curve_fit(gauss, bin_centres, hist, p0=p0gauss, maxfev =

        # Get the fitted curve
        hist_fit_sin = sinfunc(bin_centres, *coeff_sin)
        hist_fit_gauss = gauss(bin_centres, *coeff_gauss)

        mse_sin = np.mean(np.square(hist_fit_sin-hist)) # mean sqared error of sine fit
        mse_gauss = np.mean(np.square(hist_fit_gauss-hist)) # mean sqared error of gaussian fit

        if mse_sin < mse_gauss:
            peak_phase = math.degrees(bin_centres[np.argmax(hist_fit_sin)]) # peak phase in degr
            mse = mse_sin
            hist_fit = hist_fit_sin
        else:
            peak_phase = math.degrees(bin_centres[np.argmax(hist_fit_gauss)]) # peak phase in d(
            mse = mse_gauss
            hist_fit = hist_fit_gauss

        peak_phase = np.round(peak_phase,decimals=1)
    except:
        # if both fits fail to evaluate then the hist is probably bad, but save the peak phase
        peak_phase = np.round(math.degrees(bin_centres[np.argmax(hist)]),decimals=1)
        mse = np.nan
        hist_fit = np.nan


    if peak_phase == 0:
        peak_phase = np.abs(peak_phase) # sometimes 0 is returned as -0.0

    return peak_phase, mse, hist, hist_fit

def load_spikes_from_kwik(dfile, clust_choice, use_clust_choice):
    '''
    Inputs : dfile        - file directory (including filename)
             clust_choice - list of cluster labels you want to extract
             use_clust_choice - if 1 t

    Outputs: SPK          - list of spike times (in samples) for each cluster
    '''
    import h5py
    with h5py.File(dfile,'r') as D:
        # for viewing contents of folders
        # dv=D['/channel_groups/0/spikes/time_samples']
        # for i in iter(dv):
            # print(i)
        time_samples = D.get('/channel_groups/0/spikes/time_samples')
        np_time_samples = np.array(time_samples)
        cluster_labels = D.get('/channel_groups/0/spikes/clusters/main')
        np_cluster_labels = np.array(cluster_labels) # label of each individual spike
        cluster_names = D.get('/channel_groups/0/clusters/main')
```

```
        np_cluster_names = np.array(cluster_names) # name of each cluster category
        # must additionally convert from <U2 to int32
        np_cluster_names = np_cluster_names.astype('int32')

    SPK = []
    if use_clust_choice == 1:
        for i in clust_choice:
            temp_ind = np.squeeze(np.array(np.where(np_cluster_labels == i)))
            SPK.append(np_time_samples[temp_ind])
        # redefine cluster names as the clust_choice, since those are the clusters we chose, dul
        np_cluster_names = clust_choice.copy()
    else:
        for i in range(len(np_cluster_names)):
            temp_ind = np.squeeze(np.array(np.where(np_cluster_labels == np_cluster_names[i])))
            SPK.append(np_time_samples[temp_ind])
    return SPK, np_cluster_names

def load_waveforms_with_merge_and_down(foldername,cl_chan,cl_names,dlim):
    # - This function loads spike waveforms and masks that were exported by get_spike_waveforms_
    # - It assumes .npy files with 'wv_clust' in the waveform filename and 'msk_clust' in the m
    # - If multiple cl_names exist it will merge their waveforms
    #
    # Dependencies:
    # find_matching_files
    #
    # INPUTS:
    # foldername    -  folder where files are stored
    # cl_chan       -  the channel that the clusters refer to (a single number)
    # cl_names      -  the names of the clusters (can be > 1)
    # dlim          -  downsampling limit (if nspikes > dlim), then downsample to dlim spikes
    ###############################################################################

    if isinstance(cl_names,list):
        # need to merge waveforms
        WFfile_list = find_matching_files(foldername,['wv_chan'+str(cl_chan)])
        MSKfile_list = find_matching_files(foldername,['msk_chan'+str(cl_chan)])
        WV_list = []
        MSK_list = []
        for c in range(len(cl_names)):
            wv_name = WFfile_list[c]
            msk_name = MSKfile_list[c]
            WV_list.append(np.load(foldername+'/'+wv_name))
            MSK_list.append(np.load(foldername+'/'+msk_name))
        # concatenate waveforms and masks (this effectively merges them, although doesn't prese
        WV = WV_list[0] #initialize
        MSK = MSK_list[0] #initialize
        for i in np.arange(1,len(cl_names),1):
            WV = np.vstack((WV,WV_list[i]))
            MSK = np.vstack((MSK,MSK_list[i]))
    else:
        # No need to merge waveforms
        # The output of find_matching_files is inside of a list, so I have to index by [0]
        wv_name = find_matching_files(foldername,['wv_chan'+str(cl_chan)+'_clust'+str(cl_names)
        msk_name = find_matching_files(foldername,['msk_chan'+str(cl_chan)+'_clust'+str(cl_name
        WV = np.load(foldername+'/'+wv_name)
        MSK = np.load(foldername+'/'+msk_name)

    ns = len(MSK)
    if ns > dlim:
        # take a random, NON REPEATING, sample of the data of size dlim
        rand_inds = random.sample(range(ns), dlim) # this function is awesome! Non-repeating :)
```

```
        WV = WV[rand_inds,:,:]
        MSK = MSK[rand_inds,:]

    return WV, MSK

def merge_clust(SPK,clust_names,merge,cchan=[]):
    # This function merges the clustets listed in merge.
    # It deletes the individual clusters and appends the new one
    # INPUTS:
    # SPK         -  list of spike times
    # clust_names -  list of cluster names (ordered in same way as SPK)
    # merge       -  list of clusters to be merged
    # cchan       -  cluster channel. This is optional since we may not need it in some cases
    ####################################

    # merge to the first cluster in group
    ord_inds = []
    for i in range(len(merge)):
        temp_inds = []
        for j in merge[i]:
            temp_inds.append(clust_names.index(j))
            ord_inds.append(clust_names.index(j)) # also add to ord_inds for later deletion
        SPK_merged = []
        for d in temp_inds:
            SPK_merged = np.sort(np.hstack((SPK_merged,SPK[d])))
        # append merged cluster to SPK list and new clust name
        SPK.append(SPK_merged)
        clust_names.append(merge[i])

    # only edit cchan if it is supplied as an ndarray
    if isinstance(cchan,np.ndarray):
        for i in range(len(merge)):
            # the chan of first cluster should be same as all others in a merge unit. Just use j
            cchan = np.append(cchan,cchan[clust_names.index(merge[i][0])]) # must use np.append
        ord_inds = sorted(ord_inds,reverse=True) # sort from largest to smallest to facilitate d
        for d in ord_inds:
            cchan = np.delete(cchan,d)

    # delete the unmereged clusters
    ord_inds = sorted(ord_inds,reverse=True) # sort from largest to smallest to facilitate dele
    for d in ord_inds:
        del SPK[d]
        del clust_names[d]

    return SPK, clust_names, cchan

def prediction_accuracy_from_dist(dist_mat,no,nop):
    # This function caluclates the prediction accuracy for each category in the distance matrix
    # the summed distance within category to outside of category. Minimum distance is considered
    # no   -  number of odors (stimulus categories)
    # nop  -  number of presentations per odor
    #########
    # Output - accuracy (dim ncells)

    #print('Calculating prediction accuracies...')

    nc = len(dist_mat) # assuming there is a dist_mat for each cell
    nt = dist_mat[0].shape[0] # number total trials

    accuracy = []
    for c in range(nc):
```

```
        correct_prediction = 0

        for t in range(nt):
            current_category = int(np.floor(t/nop))
            total_dist = np.zeros((no,1))
            for o in range(no):
                # sum all trials for each stimulus category
                total_dist[o] = sum(dist_mat[c][t,o*nop:(o+1)*nop])
                # Normalize total_dist by number of trials per category
                # Note: must not include diagonals (within category ntrials = nop-1)
                if o == current_category: # if current trial is within category, divide by nop-1
                    total_dist[o] = total_dist[o]/(nop-1)
                else:
                    total_dist[o] = total_dist[o]/nop

            current_prediction = np.argmin(total_dist) # category with minimum distance is the p
            if current_prediction == current_category:
                correct_prediction += 1

        accuracy.append(correct_prediction/nt)
    return accuracy

def predict_accuracy_from_PSTHcorr(SPK_op,ot_inds,start,stop,wg,sf):
    # - As an alternative to the victor-purpura method, this function calculated distance by cor
    # correlation between Gaussian filtered versions of individual spike trains and PSTHs for ea
    # - Filtering means convolution, and to do this the spikes have to be binned into time bins
    # - After correlations are computed, the predicted class the class of PSTH that gives max co
    ############################
    # INPUTS:
    # SPK_op      - must be an embedded list with 1st level - odor, 2nd level - trials, 3rd leve
    # ot_inds     - predifined 2 x no*ntr matrix of odor and trial indices
    # start       - start time of window relative to beta onset (s)
    # stop        - stop time of window relative to beta onset (s)
    # wg          - width of Gaussian (in s)
    # sf          - sampling frequency (to convert spike trains to units of s)
    ############################

    from copy import deepcopy

    bw = 1/10000 # bin width (s)
    edges = np.arange(start, stop, bw) # for binning spikes into 0.1ms bins
    # gaussian same length as spike train, but centered in middle of time window
    gx = np.linspace((start-stop)/2,(stop-start)/2,len(edges)-1)
    gaussian = np.exp(-(gx/wg)**2/2)

    nc = len(SPK_op[0][0])
    nt = ot_inds.shape[1]
    no = len(np.unique(ot_inds[0]))
    nop = np.sum(ot_inds[0]==0);

    corr_mat = []
    accuracy = []

    for c in range(nc):
        # save matrices for later calculating PSTH
        SPK_matrices = [[] for o in range(no)] # empty list for each odor
        for i in range(nt):
            si = SPK_op[int(ot_inds[0,i])][int(ot_inds[1,i])][c]/sf
            si = si[np.logical_and(si > start,si < stop)]
            si = np.histogram(si,edges)[0] # spikes bin into 0.1ms bins
            SPK_matrices[int(ot_inds[0,i])].append(si)
```

```
        correct_prediction = 0
        corr_mat_temp = np.zeros((nt,no))
        for i in range(nt):
            current_category = int(np.floor(i/nop))
            # Get current spike train
            si = SPK_op[int(ot_inds[0,i])][int(ot_inds[1,i])][c]/sf
            si = si[np.logical_and(si > start,si < stop)]
            si = np.histogram(si,edges)[0] # spikes binned into 0.1ms bins
            # delete the current spike train from corresponding SPK matrix
            SPK_matrices_cpy = deepcopy(SPK_matrices) # make copy that will be edited each trial
            del SPK_matrices_cpy[int(ot_inds[0,i])][int(ot_inds[1,i])]
            # Compute corr between Gaussian filtered spike train and Gaussian filtered PSTH per
            for o in range(no):
                PSTH = np.mean(np.array(SPK_matrices_cpy[o]),axis=0)
                PSTH = np.convolve(PSTH,gaussian,mode = 'same')
                si = np.convolve(si,gaussian,mode = 'same')
                corr_mat_temp[i,o] = np.corrcoef(si,PSTH)[0,1] # off diagonal element

            current_prediction = np.argmax(corr_mat_temp[i,:]) # category with max corr is the p
            if current_prediction == current_category:
                correct_prediction += 1
        accuracy.append(correct_prediction/nt)
        corr_mat.append(corr_mat_temp)

    return corr_mat, accuracy

def scandtrig_while(dtrig,skipdp):
    '''
    Unfortunately, the TTL pulses sometimes have multiple closely spaced repeats.

    This function scans the digital trigger (dtrig) to find the onsets of each
    repeated pulse train, then skips a time skipdp (in samples) and starts
    scanning again until no more triggers are detected

    NOTE: This function is meant to analyze OpenEphys event data triggered by
    MedPC TTL.

    NOTE: skipdp must be big enough that the algorithm skips over the repeats
    ,but small enough that it does not skip too far and miss the next real pulse!

    Boleszek Osinski (2017)
    Kay Lab, University of Chicago
    '''

    dtrig_clean = [dtrig[0]] # start with first pulse
    ind = dtrig_clean # initialize
    ii = 0
    while len(ind)>0:
        # prev_ind will update each time new pulse is detected
        prev_ind = dtrig_clean[ii]
        # start scan skipdp after prev_ind to skip over the transients
        ind = np.where(dtrig>(prev_ind+skipdp))[0]
        if len(ind)>0:
            dtrig_clean.append(dtrig[ind[0]]) # append the 1st pulse at index ind[0]
        ii = ii+1

    return dtrig_clean

def SFC_wrapper(SPK_op,LFPb_op,sssf,no,nop,startb_op,stopb_op,nrand):
    # This is a wrapper for spike_field_coh. It accepts single odorant and multiple odorant dat
```

```
# where no is number of odorants. This wrapper also alows you to choose to use the full odor
# presentation period or a specified list of periods (usually where beta power is a bove a t
# for calculating SFC, by seting use_full_op_for_sfc to 1 or 0
##########################################
# INPUTS:
# SPK_op              -  embeded list of spike times during odor pres (ordered by 1st index
# LFPb_op             -  embeded list of filtered LFP (ordered by 1st index pres, 2nd index
# sssf                -  sub sampled sampling frequency
# no                  -  number of odors
# nop                 -  number of presentations
# startb_op           -  start of thresholded periods (only used if use_full_op_for_sfc = 1,
# stop_op             -  stop of thresholded periods (only used if use_full_op_for_sfc = 1)
# nrand               -  number of spike shuffles for SFC noise floor
##########################################

nspk = len(SPK_op[0]) # number of cells

# if using a single odorant we don't need extra for loop (which may generate empty dimensior
if no == 1:

    # first we must concatenate all beta or odor periods and spike times into long vectors

    # use beta thresholded regions only!
    LFPb_cat = np.empty(0) # initialize array which will concatenate all beta periods
    SPKb_cat = [None]*nspk
    for s in range(nspk):
        cumulative_time_shift = 0 # cumulative shift in time to concatenate spike times bec
        SPKb_cat[s] = np.empty(0)
        for i in range(nop):
            # extract spikes for each start/stop pair of the thresholded region
            for b in range(startb_op[i].size):
                if np.isscalar(startb_op[i]): # if scalar don't index by b (only one beta i
                    current_start = startb_op[i] # only saving this to realign spikes for 1
                    bool_array =(SPK_op[i][s] > startb_op[i]) & (SPK_op[i][s] < stopb_op[i]
                    if s == 0: # concatenate LFPb only for first s (since s is over spikes)
                        LFPb_cat = np.append(LFPb_cat,LFPb_op[i][int(startb_op[i]/10):int(s
                else:
                    current_start = startb_op[i][b] # only saving this to realign spikes for
                    bool_array =(SPK_op[i][s] > startb_op[i][b]) & (SPK_op[i][s] < stopb_op
                    if s == 0: # concatenate LFPb only for first s (since s is over spikes)
                        LFPb_cat = np.append(LFPb_cat,LFPb_op[i][int(startb_op[i][b]/10):int
                sind = np.array(np.where(np.squeeze(bool_array)))
                if sind.size > 0: # trouble dealing with empty arrays
                    # concatenate spike times into single vector (used for SFC)
                    SPKb_cat[s] = np.append(SPKb_cat[s],SPK_op[i][s][0][sind]+cumulative_tir
                if np.isscalar(startb_op[i]): # update time_shift
                    cumulative_time_shift = cumulative_time_shift+stopb_op[i]-startb_op[i]
                else:
                    cumulative_time_shift = cumulative_time_shift+stopb_op[i][b]-startb_op[:
    # NOTE: must subtract 2 different start times! Current start, and past start!

    # Compute SFC (with rand)
    SFCb = []
    SFCb_max = []
    SFCb_rand = []
    SFCb_rand_max = []
    for i in range(nspk):
        f, Cxy = spike_field_coh(SPKb_cat[i],LFPb_cat,sssf)
        SFCb.append(Cxy)
        Cxyrand = [];
        for r in range(nrand):
```

```
            randSPK = 10*len(LFPb_cat)*np.random.random(SPKb_cat[i].size)
            f, Cxy = spike_field_coh(randSPK,LFPb_cat,sssf)
            Cxyrand.append(Cxy)
        SFCb_rand.append(Cxyrand)
        SFCb_max.append(np.max(SFCb[i][1:30]))
        rand_max_tmp = []
        for r in range(nrand):
            rand_max_tmp.append(np.max(SFCb_rand[i][r][1:30]))
        SFCb_rand_max.append(rand_max_tmp)

else:

    # first we must concatenate all beta or odor periods and spike times into long vectors

    LFPb_cat = []
    SPKb_cat = []
    for o in range(no):
        LFPb_cat_o_temp = np.empty(0) # initialize array which will concatenate all beta pe
        SPKb_cat_o_temp = [None]*nspk
        inds = np.arange(o,nop*no,no)
        for s in range(nspk):
            cumulative_time_shift = 0 # cumulative shift in time to concatenate spike times
            SPKb_cat_o_temp[s] = np.empty(0)
            for i in range(nop):
                # extract spikes for each start/stop pair of the thresholded region
                for b in range(startb_op[o][i].size):
                    if np.isscalar(startb_op[o][i]): # if scalar don't index by b (only one
                        current_start = startb_op[o][i] # only saving this to realign spike
                        bool_array =(SPK_op[inds[i]][s] > startb_op[o][i]) & (SPK_op[inds[i
                        if s == 0: # concatenate LFPb only for first s (since s is over spi
                            LFPb_cat_o_temp = np.append(LFPb_cat_o_temp,LFPb_op[inds[i]][int
                    else:
                        current_start = startb_op[o][i][b] # only saving this to realign sp
                        bool_array =(SPK_op[inds[i]][s] > startb_op[o][i][b]) & (SPK_op[ind
                        if s == 0: # concatenate LFPb only for first s (since s is over spi
                            LFPb_cat_o_temp = np.append(LFPb_cat_o_temp,LFPb_op[inds[i]][int
                    sind = np.array(np.where(np.squeeze(bool_array)))
                    if sind.size > 0: # trouble dealing with empty arrays
                        # concatenate spike times into single vector (used for SFC)
                        SPKb_cat_o_temp[s] = np.append(SPKb_cat_o_temp[s],SPK_op[inds[i]][s
                    if np.isscalar(startb_op[o][i]): # update time_shift
                        cumulative_time_shift = cumulative_time_shift+stopb_op[o][i]-startb_
                    else:
                        cumulative_time_shift = cumulative_time_shift+stopb_op[o][i][b]-sta
                        # NOTE: must subtract 2 different start times! Current start, and p
        # save concatenated LFBb and SPKb
        LFPb_cat.append(LFPb_cat_o_temp)
        SPKb_cat.append(SPKb_cat_o_temp)


    # Compute SFC (with rand)
    SFCb = []
    SFCb_max = []
    SFCb_rand = []
    SFCb_rand_max = []
    for o in range(no):
        SFCb_o_temp = []
        SFCb_max_o_temp = []
        SFCb_rand_o_temp = []
        SFCb_rand_max_o_temp = []
        for i in range(nspk):
```

```
                f, Cxy = spike_field_coh(SPKb_cat[o][i],LFPb_cat[o],sssf)
                SFCb_o_temp.append(Cxy)
                Cxyrand = [];
                for r in range(nrand):
                    randSPK = 10*len(LFPb_cat[o])*np.random.random(SPKb_cat[o][i].size)
                    f, Cxy = spike_field_coh(randSPK,LFPb_cat[o],sssf)
                    Cxyrand.append(Cxy)
                SFCb_rand_o_temp.append(Cxyrand)
                SFCb_max_o_temp.append(np.max(SFCb_o_temp[i][1:30]))
                rand_max_tmp = []
                for r in range(nrand):
                    rand_max_tmp.append(np.max(SFCb_rand_o_temp[i][r][1:30]))
                SFCb_rand_max_o_temp.append(rand_max_tmp)
            SFCb.append(SFCb_o_temp)
            SFCb_max.append(SFCb_max_o_temp)
            SFCb_rand.append(SFCb_rand_o_temp)
            SFCb_rand_max.append(SFCb_rand_max_o_temp)

    return SFCb, SFCb_max, SFCb_rand, SFCb_rand_max

def SPH_wrapper(SPK_op,LFPb_ph_op,sssf,no,nop,startb_op,stopb_op,nrand):
    # This function calculates spike phase product between spike times and LFP phase
    # The function is adapted to deal with single odorant and multiple interleaved odorant data
    ########################################
    # INPUTS:
    # SPK_op              -  embeded list of spike times during odor pres (ordered by 1st index
    # LFPb_ph_op          -  embeded list of LFP phase (ordered by 1st index pres, 2nd index ce
    # sssf                -  sub sampled sampling frequency
    # no                  -  number of odors
    # nop                 -  number of presentations
    # startb_op           -  start of thresholded periods
    # stop_op             -  stop of thresholded periods
    # nrand               -  number of spike shuffles for random phase noise floor
    ########################################

    ncell = len(SPK_op[0])# number of cells

    if no == 1:
        SPHprod = list() # SPHprod will have length = len(SPK)
        RPHprod = list() # same as SPHprod but for random spikes
        for s in range(ncell):
            SPHprod_temp = list()
            RPHprod_temp = list()
            for i in range(nop):
                # extract spikes for each start/stop pair of the thresholded region
                for b in range(startb_op[i].size):
                    if np.isscalar(startb_op[i]): # if scalar don't index by b (only one beta i
                        current_start = startb_op[i] # only saving this to realign spikes for 1
                        bool_array =(SPK_op[i][s] > startb_op[i]) & (SPK_op[i][s] < stopb_op[i]
                    else:
                        current_start = startb_op[i][b] # only saving this to realign spikes fo
                        bool_array =(SPK_op[i][s] > startb_op[i][b]) & (SPK_op[i][s] < stopb_op
                    sind = np.array(np.where(np.squeeze(bool_array)))
                    if sind.size > 0: # trouble dealing with empty arrays
                        # concatenate spike-phase products
                        [SFprod,RFprod] = spike_field_prod_with_rand(SPK_op[i][s][0][sind],LFPb_
                        SPHprod_temp.append(SFprod)
                        RPHprod_temp.append(RFprod)
            # save spike-phase products for each cluster
            if len(SPHprod_temp) == 0:
                # np.hstack is unable to deal with empty entries (stupid)
```

```
                SPHprod.append(np.empty( shape=(0, 0) )) # must add empty ARRAY (not LIST) for
                RPHprod.append(np.empty( shape=(0, 0) )) # must add empty ARRAY (not LIST) for
            else:
                SPHprod.append(np.hstack(SPHprod_temp))
                RPHprod.append(np.hstack(RPHprod_temp))
    else:

        SPHprod = []
        RPHprod = []
        for o in range(no):
            SPHprod_o_temp = list() # SPHprod_o_temp will have length = len(SPK)
            RPHprod_o_temp = list() # same as SPHprod_o_temp but for random spikes
            inds = np.arange(o,nop*no,no)
            for s in range(ncell):
                SPHprod_temp = list()
                RPHprod_temp = list()
                for i in range(nop):
                    # extract spikes for each start/stop pair of the thresholded region
                    for b in range(startb_op[o][i].size):
                        if np.isscalar(startb_op[o][i]): # if scalar don't index by b (only one
                            current_start = startb_op[o][i] # only saving this to realign spikes
                            bool_array =(SPK_op[inds[i]][s] > startb_op[o][i]) & (SPK_op[inds[i]
                        else:
                            current_start = startb_op[o][i][b] # only saving this to realign sp
                            bool_array =(SPK_op[inds[i]][s] > startb_op[o][i][b]) & (SPK_op[inds
                        sind = np.array(np.where(np.squeeze(bool_array)))
                        if sind.size > 0: # trouble dealing with empty arrays
                            # concatenate spike-phase products
                            [SFprod,RFprod] = spike_field_prod_with_rand(SPK_op[inds[i]][s][0][s
                            SPHprod_temp.append(SFprod)
                            RPHprod_temp.append(RFprod)
                # save spike-phase products for each cluster
                if len(SPHprod_temp) == 0:
                    # np.hstack is unable to deal with empty entries (stupid)
                    SPHprod_o_temp.append(np.empty( shape=(0, 0) )) # must add empty ARRAY (not
                    RPHprod_o_temp.append(np.empty( shape=(0, 0) )) # must add empty ARRAY (not
                else:
                    SPHprod_o_temp.append(np.hstack(SPHprod_temp))
                    RPHprod_o_temp.append(np.hstack(RPHprod_temp))
            SPHprod.append(SPHprod_o_temp)
            RPHprod.append(RPHprod_o_temp)

    return SPHprod, RPHprod

def spike_field_coh(spike_times,field,sssf):
    # This function uses the scipy.signal.coherence function. Must be imported
    # Assuming spike times are given in units of samples.
    # Also assuming LFP is subsampled by 10
    # This function bins spike times in bins of LFP sampling time, then computes coherence
    bw = 10
    bins = np.arange(0,10*len(field),bw)
    [binned_spikes,bleh] = np.histogram(spike_times,bins)
    if len(binned_spikes) < len(field): # ensure binned spikes and LFP are same len
        binned_spikes=np.append(binned_spikes,0) # add zero to end
    elif len(binned_spikes) > len(field):
        binned_spikes=np.delete(binned_spikes,0) # delete 1st element
    f, Cxy = coherence(binned_spikes, field, sssf, nperseg=2000)
    # higher nperseg --> finer fq resolution
    return f, Cxy

def spike_field_prod_with_rand(spikes,field,nrand):
```

```
    # This function indexes field by spikes AND by nrand random arrays the same length as spikes
    # NOTE: this function assumes that spikes are sampled 10x higher than field
    # spike sample times must be subsampled and rounded to index ssLFP envelope
    ssinds = np.rint(0.1*np.array(spikes)) # round to nearest integer
    ssinds = ssinds.astype(int) # convert type to int
    SFprod = field[ssinds]
    # Do the same for nrand randomly generated spike trains as a control
    RFprod = [] # initialize list that will store nrand random spike-field products
    for n in range(nrand):
        randinds = field.size*np.random.sample(spikes.size)
        randinds = randinds.astype(int) # convert type to int
        RFprod.append(field[randinds])
    return SFprod, RFprod

def trim_events(odor_periods,trim):
    # odor periods    -    list of all odor periods in samples (start and stop are consecutive)
    # trim            -    list of start and stop samples of noisy periods, ordered from latest

    from itertools import compress # used for indexing with booleans

    ALLstart = odor_periods[0::2]
    ALLstop = odor_periods[1::2]
    for i in range(len(trim)):
        # detect overlap of odor periods with trim periods (hopefully there aren't any!)
        ovlap = list(compress(ALLstart, (np.array(ALLstart) > trim[i][0]) & (np.array(ALLstart)
        if ovlap != []:
            print('Overlap detected! Setting odor period start '+str(ovlap)+' to trim start '+st
            yo=np.where(np.array(ALLstart) == ovlap)
            ALLstart[int(yo[0])] = trim[i][0]-1 # add -1 so that there is no overlap
        # subtract away the trimmed period
        ALLstart_shift = [a - (trim[i][1]-trim[i][0]) for a in ALLstart if a > trim[i][1]] # dou
        ALLstart = list(compress(ALLstart,np.array(ALLstart) < trim[i][1])) # redifeine ALLstart
        ALLstart = ALLstart + ALLstart_shift # add the 1st and 2nd parts of ALLstart

        ovlap = list(compress(ALLstop, (np.array(ALLstop) > trim[i][0]) & (np.array(ALLstop) < t
        if ovlap != []:
            print('Overlap detected! Setting odor period stop '+str(ovlap)+' to trim start '+str
            yo=np.where(np.array(ALLstop) == ovlap)
            ALLstop[int(yo[0])] = trim[i][0]-1 # add -1 so that there is no overlap
        # subtract away the trimmed period
        ALLstop_shift = [a - (trim[i][1]-trim[i][0]) for a in ALLstop if a > trim[i][1]] # downs
        ALLstop = list(compress(ALLstop,np.array(ALLstop) < trim[i][1])) # redifeine ALLstop as
        ALLstop = ALLstop + ALLstop_shift # add the 1st and 2nd parts of ALLstop

    # redefine odor periods
    odor_periods[0::2] = np.array(ALLstart)
    odor_periods[1::2] = np.array(ALLstop)
    return odor_periods
```

Bibliography

Akk G, **Milescu LS**, **Heckmann M**. Activation of heteroliganded mouse muscle nicotinic receptors. *J Physiol* 564: 359–76, 2005.

de Almeida L, **Idiart M**, **Linster C**. A model of cholinergic modulation in olfactory bulb and piriform cortex. *J Neurophysiol* 109: 1360–77, 2013.

Amini B, **Clark JW**, **Canavier CC**. Calcium dynamics underlying pacemaker-like and burst firing oscillations in midbrain dopaminergic neurons: a computational study. *J Neurophysiol* 82: 2249–2261, 1999.

Atallah B V, **Scanziani M**. Instantaneous modulation of gamma oscillation frequency by balancing excitation with inhibition. *Neuron* 62: 566–77, 2009.

Balu R, **Pressler RT**, **Strowbridge BW**. Multiple modes of synaptic excitation of olfactory bulb granule cells. *J Neurosci* 27: 5621–32, 2007.

Baszczak M, **Kasicki S**. A single compartment neuron model with activity-dependent conductances during NMDA induced activity. [Online]. *Acta Neurobiol Exp (Wars)* 65: 183–90, 2005. http://www.ncbi.nlm.nih.gov/pubmed/15960304.

Bathellier B, **Lagier S**, **Faure P**, **Lledo P-M**. Circuit properties generating gamma oscillations in a network model of the olfactory bulb. *J Neurophysiol* 95: 2678–91, 2006.

Bendahmane M, **Ogg MC**, **Ennis M**, **Fletcher ML**. Increased olfactory bulb acetylcholine bi-directionally modulates glomerular odor sensitivity. *Sci Rep* 6: 25808, 2016.

Beshel J, **Kopell N**, **Kay LM**. Olfactory bulb gamma oscillations are enhanced with task demands. *J Neurosci* 27: 8358–8365, 2007.

Bhalla US, **Bower JM**. Multiday Recordings from Olfactory Bulb Neurons in Awake Freely Moving Rats: Spatially and Temporally Organized Variability in Odorant Response Properties. *J Comput Neurosci* 4: 221–256, 1997.

Bokil H, **Andrews P**, **Kulkarni JE**, **Mehta S**, **Mitra PP**. Chronux: a platform for analyzing neural signals. *J Neurosci Methods* 192: 146–51, 2010a.

Bonzano S, **Bovetti S**, **Gendusa C**, **Peretto P**, **De Marchis S**. Adult Born Olfactory Bulb Dopaminergic Interneurons: Molecular Determinants and Experience-Dependent Plasticity. *Front Neurosci* 10: 189, 2016.

Boyd AM, **Sturgill JF**, **Poo C**, **Isaacson JS**. Cortical Feedback Control of Olfactory Bulb Circuits. .

Brea JN, **Kay LM**, **Kopell NJ**. Biophysical model for gamma rhythms in the olfactory bulb via subthreshold oscillations. .

Brunel N, **Wang X-J**. What determines the frequency of fast network oscillations with irregular neural discharges? I. Synaptic dynamics and excitation-inhibition balance. *J Neurophysiol* 90: 415–30, 2003.

Buonviso N, **Amat C**, **Litaudon P**, **Roux S**, **Royet J-P**, **Farget V**, **Sicard G**. Rhythm sequence through the olfactory bulb layers during the time window of a respiratory cycle. *Eur J Neurosci* 17: 1811–1819, 2003

Burton SD, **Urban NN**. Rapid Feedforward Inhibition and Asynchronous Excitation Regulate Granule Cell Activity in the Mammalian Main Olfactory Bulb. *J Neurosci* 35: 14103–14122, 2015.

Buzsáki G, **Anastassiou CA**, **Koch C**. The origin of extracellular fields and currents — EEG, ECoG, LFP and spikes. *Nat Rev Neurosci* 13: 407–420, 2012.

Bywalez WG, **Patirniche D**, **Rupprecht V**, **Stemmler M**, **Herz AVM**, **Pálfi D**, **Rózsa B**, **Egger V**. Local postsynaptic voltage-gated sodium channel activation in dendritic spines of olfactory bulb granule cells. *Neuron* 85: 590–601, 2015.

Cang J, **Isaacson JS**. In vivo whole-cell recording of odor-evoked synaptic transmission in the rat olfactory bulb. *J Neurosci* 23: 4108–4116, 2003b.

Castillo PE, **Carleton A**, **Vincent JD**, **Lledo PM**. Multiple and opposing roles of cholinergic transmission in the main olfactory bulb. *J Neurosci* 19: 9180–9191, 1999.

Cazakoff BN, **Lau BYB**, **Crump KL**, **Demmer HS**, **Shea SD**. Broadly tuned and respiration-independent inhibition in the olfactory bulb of awake mice. *Nat Neurosci* 17: 569–76, 2014.

Cenier T, **Amat C**, **Litaudon P**, **Garcia S**, **Lafaye de Micheaux P**, **Liquet B**, **Roux S**, **Buonviso N**. Odor vapor pressure and quality modulate local field potential oscillatory patterns in the olfactory bulb of the anesthetized rat. *Eur J Neurosci* 27: 1432–40, 2008.

Cenier T, **David F**, **Litaudon P**, **Garcia S**, **Amat C**, **Buonviso N**. Respiration-gated formation of gamma and beta neural assemblies in the mammalian olfactory bulb. *Eur J Neurosci* 29: 921–30, 2009.

Chaudhury D, **Escanilla O**, **Linster C**. Bulbar acetylcholine enhances neural and perceptual odor discrimination. *J Neurosci* 29: 52–60, 2009.

Chen WR, **Xiong W**, **Shepherd GM**, **Haven N**. Analysis of Relations between NMDA Receptors and GABA Release at Olfactory Bulb Reciprocal Synapses Section of Neurobiology. 25: 625–633, 2000.

Chess A, **Simon I**, **Cedar H**, **Axel R**. Allelic inactivation regulates olfactory receptor gene expression. [Online]. *Cell* 78: 823–34, 1994.

David F, **Courtiol E**, **Buonviso N**, **Fourcaud-Trocme N**. Competing mechanisms of gamma and beta oscillations in the olfactory bulb based on multimodal inhibition of mitral cells over a respiratory cycle. *eNeuro* (November 12, 2015).

Desmaisons D, **Vincent JD**, **Lledo PM**. Control of action potential timing by intrinsic subthreshold oscillations in olfactory bulb output neurons. [Online]. *J Neurosci* 19: 10727–37, 1999.

Devore S, **Linster C**. Noradrenergic and cholinergic modulation of olfactory bulb sensory processing. *Front Behav Neurosci* 6: 52, 2012.

Doucette W, **Restrepo D**. Profound Context-Dependent Plasticity of Mitral Cell Responses in Olfactory Bulb. *PLoS Biol* 6: e258, 2008.

Eeckman FH, **Freeman WJ**. Correlations between unit firing and EEG in the rat olfactory system. [Online]. *Brain Res* 528: 238–44, 1990.

Egger V. Synaptic sodium spikes trigger long-lasting depolarizations and slow calcium entry in rat olfactory bulb granule cells. *Eur J Neurosci* 27: 2066–2075, 2008.

Egger V, **Svoboda K**, **Mainen ZF**. Mechanisms of lateral inhibition in the olfactory bulb: efficiency and modulation of spike-evoked calcium influx into granule cells. [Online]. *J Neurosci* 23: 7551–8, 2003.

Egger V, **Svoboda K**, **Mainen ZF**. Dendrodendritic synaptic signals in olfactory bulb granule cells: local spine boost and global low-threshold spike. *J Neurosci* 25: 3521–30, 2005.

Evans RC, **Maniar YM**, **Blackwell KT**. Dynamic modulation of spike timing-dependent calcium influx during corticostriatal upstates. *J Neurophysiol* 110: 1631–45, 2013.

Fisahn A. Distinct Roles for the Kainate Receptor Subunits GluR5 and GluR6 in Kainate-Induced Hippocampal Gamma Oscillations. *J Neurosci* 24: 9658–9668, 2004.

Fonseca MI, **Aguilar JS**, **Skorupa AF**, **Klein WL**. Cellular mapping of m2 muscarinic receptors in rat olfactory bulb using an antiserum raised against a cytoplasmic loop

peptide. *Brain Res* 563: 163–170, 1991.

Fourcaud-Trocmé N, **Courtiol E**, **Buonviso N**. Two distinct olfactory bulb sublaminar networks involved in gamma and beta oscillation generation: a CSD study in the anesthetized rat. *Front Neural Circuits* 8: 88, 2014.

Fourcaud-Trocmé N, **Courtiol E**, **Buonviso N**, **Voegtlin T**. Stability of fast oscillations in the mammalian olfactory bulb: experiments and modeling. *J Physiol Paris* 105: 59–70, 2011.

Frederick DE, **Brown A**, **Brim E**, **Mehta N**, **Vujovic M**, **Kay LM**. Gamma and beta oscillations define a sequence of neurocognitive modes present in odor processing. *J Neurosci* 36: 7750–7767, 2016.

Freeman WJ. Effects of surgical isolation and tetanization on prepyriform cortex in cats. *J Neurophysiol* 31: 349–57, 1968.

Freeman WJ. *Mass Action in the Nervous System*. New York: Academic Press, 1975.

Freeman WJ, **Schneider W**. Changes in Spatial Patterns of Rabbit Olfactory EEG with Conditioning to Odors. *Psychophysiology* 19: 44–56, 1982.

Friedman D, **Strowbridge BW**. Both electrical and chemical synapses mediate fast network oscillations in the olfactory bulb. *J Neurophysiol* 89: 2601–10, 2003.

Fukunaga I, **Herb JT**, **Kollo M**, **Boyden ES**, **Schaefer AT**. Independent control of gamma and theta activity by distinct interneuron networks in the olfactory bulb. *Nat Neurosci* 17: 1208–16, 2014.

Gire DH, **Schoppa NE**. Long-term enhancement of synchronized oscillations by adrenergic receptor activation in the olfactory bulb. *J Neurophysiol* 99: 2021–5, 2008.

Gourévitch B, **Kay LM**, **Martin C**. Directional Coupling From the Olfactory Bulb to the Hippocampus During a Go / No-Go Odor Discrimination Task. (2010). doi: 10.1152/jn.01075.2009.

Gray CM, **Skinner JE**. Centrifugal regulation of neuronal activity in the olfactory bulb of the waking rabbit as revealed by reversible cryogenic blockade. *Exp Brain Res* 69, 1988.

Higley MJ, **Sabatini BL**. Calcium signaling in dendritic spines. *Cold Spring Harb Perspect Biol* 4: a005686, 2012.

Hines ML, **Morse T**, **Migliore M**, **Carnevale NT**, **Shepherd GM**. ModelDB: A Database to Support Computational Neuroscience. *J Comput Neurosci* 17: 7–11.

Igarashi KM, **Ieki N**, **An M**, **Yamaguchi Y**, **Nagayama S**, **Kobayakawa K**, **Kobayakawa R**, **Tanifuji M**, **Sakano H**, **Chen WR**, **Mori K**. Parallel Mitral and Tufted Cell Pathways Route Distinct Odor Information to Different Targets in the Olfactory Cortex. *J Neurosci* 32: 7970–7985, 2012.

Illig K. Corticofugal projections from the anterior olfactory nucleus target olfactory bulb principal cells. *Nat Preced* Available, 2011.

Inoue T, **Strowbridge BW**. Transient activity induces a long-lasting increase in the excitability of olfactory bulb interneurons. *J Neurophysiol* 99: 187–99, 2008.

Isaacson JS. Mechanisms governing dendritic gamma-aminobutyric acid (GABA) release in the rat olfactory bulb. *Proc Natl Acad Sci U S A* 98: 337–42, 2001.

Isaacson JS, **Strowbridge BW**. Olfactory reciprocal synapses: dendritic signaling in the CNS. [Online]. *Neuron* 20: 749–61, 1998.

Ito I, **Bazhenov M**, **Ong RC**, **Raman B**, **Stopfer M**. Frequency transitions in odor-evoked neural oscillations. *Neuron* 64: 692–706, 2009.

Jahr CE, **Stevens CF**. Voltage dependence of NMDA-activated macroscopic conductances predicted by single-channel kinetics. *J Neurosci* 10: 3178–3182, 1990.

Kay L. Circuit oscillations in odor perception and memory. [Online]. *Odor Mem Percept* 208, 2014.

Kay LM. Two species of gamma oscillations in the olfactory bulb: dependence on behavioral state and synaptic interactions. *J Integr Neurosci* 2: 31–44, 2003.

Kay LM. Circuit oscillations in odor perception and memory. *Prog Brain Res* 208: 223–251, 2014b.

Kay LM, **Beshel J**. A beta oscillation network in the rat olfactory system during a 2-alternative choice odor discrimination task. *J Neurophysiol* 104: 829–39, 2010

Kay LM, **Beshel J**, **Brea J**, **Martin C**, **Rojas-Líbano D**, **Kopell N**. Olfactory oscillations: the what, how and what for. *Trends Neurosci* 32: 207–14, 2009.

Kay LM, **Freeman WJ**. Bidirectional processing in the olfactory-limbic axis during olfactory behavior. *Behav Neurosci* 112: 541–553, 1998.

Kay LM, **Laurent G**. modulation of mitral cell activity in behaving rats.

Kay LM, **Lazzara P**. How Global Are Olfactory Bulb Oscillations? *J Neurophysiol* 104: 1768–1773, 2010.

Kay LM, **Sherman SM**. An argument for an olfactory thalamus. *Trends Neurosci* 30: 47–53, 2007.

Kiselycznyk CL, **Zhang S**, **Linster C**. Role of centrifugal projections to the olfactory bulb in olfactory processing. *Learn Mem* 13: 575–9, 2006.

Kurahashi T, **Menini A**. Mechanism of odorant adaptation in the olfactory receptor cell. *Nature* 385: 725–9, 1997.

Lagier S, **Carleton A**, **Lledo P-M**. Interplay between local GABAergic interneurons and relay neurons generates gamma oscillations in the rat olfactory bulb. *J Neurosci* 24: 4382–92, 2004.

Lagier S, **Panzanelli P**, **Russo RE**, **Nissant A**, **Bathellier B**, **Sassoè-Pognetto M**, **Fritschy J-M**, **Lledo P-M**. GABAergic inhibition at dendrodendritic synapses tunes gamma oscillations in the olfactory bulb. *Proc Natl Acad Sci U S A* 104: 7259–64, 2007.

Laing DG, **MacKay-Sim A**. Olfactory adaptation in the rat [Online]. *Olfaction Tast. V*.

Lakatos P. An Oscillatory Hierarchy Controlling Neuronal Excitability and Stimulus Processing in the Auditory Cortex. *J Neurophysiol* 94: 1904–1911, 2005.

Legendre P, **Rosenmund C**, **Westbrook GL**. Inactivation of NMDA channels in cultured hippocampal neurons by intracellular calcium. [Online]. *J Neurosci* 13: 674–84, 1993.

Lein ES, **Hawrylycz MJ**, **Ao N**, **Ayres M**, **Bensinger A**, **Bernard A**, **Boe AF**, **Boguski MS**, **Brockway KS**, **Byrnes EJ**, **Chen L**, **Chen L**, **Chen T-M**, **Chi Chin M**, **Chong J**, **Crook BE**, **Czaplinska A**, **Dang CN**, **Datta S**, **Dee NR**, **Desaki AL**, **Desta T**, **Diep E**, **Dolbeare TA**, **Donelan MJ**, **Dong H-W**, **Dougherty JG**, **Duncan BJ**, **Ebbert AJ**, **Eichele G**, **Estin LK**, **Faber C**, **Facer BA**, **Fields R**, **Fischer SR**, **Fliss TP**, **Frensley C**, **Gates SN**, **Glattfelder KJ**, **Halverson KR**, **Hart MR**, **Hohmann JG**, **Howell MP**, **Jeung DP**, **Johnson RA**, **Karr PT**, **Kawal R**, **Kidney JM**, **Knapik RH**, **Kuan CL**, **Lake JH**, **Laramee AR**, **Larsen KD**, **Lau C**, **Lemon TA**, **Liang AJ**, **Liu Y**, **Luong LT**, **Michaels J**, **Morgan JJ**, **Morgan RJ**, **Mortrud MT**, **Mosqueda NF**, **Ng LL**, **Ng R**, **Orta GJ**, **Overly CC**, **Pak TH**, **Parry SE**, **Pathak SD**, **Pearson OC**, **Puchalski RB**, **Riley ZL**, **Rockett HR**, **Rowland SA**, **Royall JJ**, **Ruiz MJ**, **Sarno NR**, **Schaffnit K**, **Shapovalova N V.**, **Sivisay T**, **Slaughterbeck CR**, **Smith SC**, **Smith KA**, **Smith BI**, **Sodt AJ**, **Stewart NN**, **Stumpf K-R**, **Sunkin SM**, **Sutram M**, **Tam A**, **Teemer CD**, **Thaller C**, **Thompson CL**, **Varnam LR**, **Visel A**, **Whitlock RM**, **Wohnoutka PE**, **Wolkey CK**, **Wong VY**, **Wood M**, **Yaylaoglu MB**, **Young RC**, **Youngstrom BL**, **Feng Yuan X**, **Zhang B**, **Zwingman TA**, **Jones AR**. Genome-wide atlas of gene expression in the adult mouse brain. *Nature* 445: 168–176, 2007.

Lepousez G, **Lledo P**. Odor discrimination requires proper olfactory fast oscillations in awake mice. *Neuron* 80: 1010–1024, 2013b.

Lepousez G, **Valley MT**, **Lledo P-M**. The impact of adult neurogenesis on olfactory bulb circuits and computations. *Annu Rev Physiol* 75: 339–63, 2013.

Li G, **Cleland TA**. A two-layer biophysical model of cholinergic neuromodulation in olfactory bulb. *J Neurosci* 33: 3037–3058, 2013.

Li G, **Cleland TA**. A coupled-oscillator model of olfactory bulb gamma oscillations. *PLOS Comput Biol* 13: e1005760, 2017.

Li Z, **Hopfield JJ**. Modeling the olfactory bulb and its neural oscillatory processings. *Biol Cybern* 61: 379–392, 1989.

Linster C, **Cleland TA**. Glomerular microcircuits in the olfactory bulb. *Neural Netw* 22: 1169–73, 2009.

Linster C, **Menon A V**, **Singh CY**, **Wilson D a**. Odor-specific habituation arises from interaction of afferent synaptic adaptation and intrinsic synaptic potentiation in olfactory cortex. *Learn Mem* 16: 452–9, 2009.

Lowry CA, **Kay LM**. Chemical factors determine olfactory system beta oscillations in waking rats. *J Neurophysiol* 98: 394–404, 2007.

Ma M, **Luo M**. Optogenetic activation of basal forebrain cholinergic neurons modulates neuronal excitability and sensory responses in the main olfactory bulb. *J Neurosci* 32: 10105–16, 2012.

Mackevicius EL, **Best MD**, **Saal HP**, **Bensmaia SJ**. Millisecond precision spike timing shapes tactile perception. *J Neurosci* 32: 15309–17, 2012.

Malnic B, **Hirono J**, **Sato T**, **Buck LB**. Combinatorial receptor codes for odors. *Cell* 96: 713–23, 1999.

Manabe H, **Mori K**. Sniff rhythm-paced fast and slow gamma-oscillations in the olfactory bulb: relation to tufted and mitral cells and behavioral states. *J Neurophysiol* 110: 1593–1599, 2013.

Mandairon N, **Ferretti CJ**, **Stack CM**, **Rubin DB**, **Cleland TA**, **Linster C**. Cholinergic modulation in the olfactory bulb influences spontaneous olfactory discrimination in adult rats. *Eur J Neurosci* 24: 3234–3244, 2006.

Martin C, **Beshel J**, **Kay LM**. An olfacto-hippocampal network is dynamically involved in odor-discrimination learning. *J Neurophysiol* 98: 2196–205, 2007.

Martin C, **Gervais R**, **Hugues E**, **Messaoudi B**, **Ravel N**. Learning modulation of odor-induced oscillatory responses in the rat olfactory bulb: a correlate of odor recognition? *J Neurosci* 24: 389–397, 2004.

Martin C, **Gervais R**, **Messaoudi B**, **Ravel N**. Learning-induced oscillatory activities correlated to odour recognition: a network activity. *Eur J Neurosci* 23: 1801–10, 2006.

Martin C, **Ravel N**. Beta and gamma oscillatory activities associated with olfactory memory tasks: different rhythms for different functional networks? *Front Behav Neurosci* 8: 218, 2014.

Matsutani S, **Yamamoto N**. Centrifugal innervation of the mammalian olfactory bulb. *Anat. Sci. Int.* (2008). doi: 10.1111/j.1447-073x.2007.00223.x.

Mazzoni A, **Lindén H**, **Cuntz H**, **Lansner A**, **Panzeri S**, **Einevoll GT**. Computing the Local Field Potential (LFP) from Integrate-and-Fire Network Models. *PLoS Comput Biol* 11: e1004584, 2015.

Migliore M, **Cavarretta F**, **Hines ML**, **Shepherd GM**. Distributed organization of a brain microcircuit analyzed by three-dimensional modeling: the olfactory bulb. *Front Comput Neurosci* 8: 50, 2014.

Migliore M, **Shepherd GM**. Emerging rules for the distributions of active dendritic conductances. *Nat Rev Neurosci* 3: 362–70, 2002.

Migliore M, **Shepherd GM**. Dendritic action potentials connect distributed dendrodendritic microcircuits. *J. Comput. Neurosci.* (2008). doi: 10.1007/s10827-007-0051-9.

Mombaerts P, **Wang F**, **Dulac C**, **Chao SK**, **Nemes A**, **Mendelsohn M**, **Edmondson J**, **Axel R**. Visualizing an olfactory sensory map. [Online]. *Cell* 87: 675–86, 1996.

Mouret A, **Murray K**, **Lledo PM**. Centrifugal drive onto local inhibitory interneurons of the olfactory bulb. *Ann N Y Acad Sci* 1170: 239–254, 2009.

Nagayama S, **Takahashi YK**, **Yoshihara Y**, **Mori K**. Mitral and Tufted Cells Differ in the Decoding Manner of Odor Maps in the Rat Olfactory Bulb. *J Neurophysiol* 91: 2532–2540, 2004.

Neville KR, **Haberly LB**. Beta and gamma oscillations in the olfactory system of the urethane-anesthetized rat. *J Neurophysiol* 90: 3921–30, 2003.

Nickell WT, **Shipley MT**. Evidence for presynaptic inhibition of the olfactory commissural pathway by cholinergic agonists and stimulation of the nucleus of the diagonal band. *J Neurosci* 13: 650–659, 1993.

Nusser Z, **Kay LM**, **Laurent G**, **Homanics GE**, **Mody I**. Disruption of GABAA Receptors on GABAergic Interneurons Leads to Increased Oscillatory Power in the Olfactory Bulb Network [Online]. *J Neurophysiol* 86: 2823–2833, 2001a.

Nusser Z, **Kay LM**, **Laurent G**, **Homanics GE**, **Mody I**. Disruption of GABA(A) receptors on GABAergic interneurons leads to increased oscillatory power in the olfactory bulb network. *J Neurophysiol* 86: 2823–2833, 2001b.

Osinski B, **Kim A**, **Xiao W**, **Mehta NM**, **Kay LM**. Pharmacological manipulation of olfactory bulb granule cell excitability modulates beta oscillations: Testing a model. *bioRxiv* (2017). doi: 10.1101/234625.

Osinski BL, **Kay LM**. Granule cell excitability regulates gamma and beta oscillations in a model of the olfactory bulb dendrodendritic microcircuit. *J Neurophysiol* 116: 522–39, 2016.

Pager J. Ascending olfactory information and centrifugal influxes contributing to a nutritional modulation of the rat mitral cell responses. *Brain Res* 140: 251–269, 1978.

Peace ST, **Johnson BC**, **Li G**, **Kaiser ME**, **Fukunaga I**, **Schaefer AT**, **Molnar AC**, **Cleland TA**. Coherent olfactory bulb gamma oscillations arise from coupling independent columnar oscillators. *bioRxiv* (November 3, 2017). doi: 10.1101/213827.

Petreanu L, **Alvarez-Buylla A**. Maturation and death of adult-born olfactory bulb granule neurons: role of olfaction. *J Neurosci* 22: 6106–13, 2002.

Poo C, **Isaacson JS**. Odor representations in olfactory cortex: “sparse” coding, global inhibition, and oscillations. *Neuron* 62: 850–61, 2009a.

Pressler RT, **Inoue T**, **Strowbridge BW**. Muscarinic receptor activation modulates granule cell excitability and potentiates inhibition onto mitral cells in the rat olfactory bulb. *J Neurosci* 27: 10969–81, 2007a.

Pressler RT, **Strowbridge BW**. Blanes cells mediate persistent feedforward inhibition onto granule cells in the olfactory bulb. *Neuron* 49: 889–904, 2006.

Price JL, **Powell TPS**. An electron-microscopic study of termination of afferent fibres to olfactory bulb from cerebral hemisphere. *J Cell Sci* 7: 157–187, 1970.

Rall W, **Shepherd GM**. Theoretical reconstruction of field potentials and dendrodendritic synaptic interactions in olfactory bulb [Online]. *J Neurophysiol* 31: 884–915, 1968.

Ravel N, **Chabaud P**, **Martin C**, **Gaveau V**, **Hugues E**, **Tallon-Baudry C**, **Bertrand O**, **Gervais R**. Olfactory learning modifies the expression of odour-induced oscillatory responses in the gamma (60-90 Hz) and beta (15-40 Hz) bands in the rat olfactory bulb. *Eur J Neurosci* 17: 350–358, 2003.

Rinberg D, **Koulakov A**, **Gelperin A**. Sparse Odor Coding in Awake Behaving Mice. *J Neurosci* 26: 8857–8865, 2006.

Rojas-Líbano D, **Frederick DE**, **Egaña JI**, **Kay LM**. The olfactory bulb theta rhythm follows all frequencies of diaphragmatic respiration in the freely behaving rat. *Front Behav Neurosci* 8, 2014.

Rojas-Líbano D, **Kay LM**. Olfactory system gamma oscillations: the physiological dissection of a cognitive neural system. *Cogn Neurodyn* 2: 179–94, 2008.

Rojas-Líbano D, **Kay LM**. Interplay between sniffing and odorant sorptive properties in the rat. *J Neurosci* 32: 15577–89, 2012.

Rolston JD, **Gross RE**, **Potter SM**. Common median referencing for improved action potential detection with multielectrode arrays. In: *Proceedings of the 31st Annual International Conference of the IEEE Engineering in Medicine and Biology Society: Engineering the Future of Biomedicine, EMBC 2009*. 2009, p. 1604–1607.

Rossant C, **Kadir SN**, **Goodman DFM**, **Schulman J**, **Hunter MLD**, **Saleem AB**, **Grosmark A**, **Belluscio M**, **Denfield GH**, **Ecker AS**, **Tolias AS**, **Solomon S**, **Buzsaki G**, **Carandini M**, **Harris KD**. Spike sorting for large, dense electrode arrays. *Nat Neurosci* 19: 634–641, 2016.

Schoppa NE, **Kinzie JM**, **Sahara Y**, **Segerson TP**, **Westbrook GL**. Dendrodendritic inhibition in the olfactory bulb is driven by NMDA receptors. *J Neurosci* 18: 6790–6802, 1998.

Shepherd GM. Synaptic organization of the mammalian olfactory bulb. *Physiol Rev* 52: 864–917, 1972.

Smith RS, **Araneda RC**. Cholinergic Modulation of Neuronal Excitability in the Accessory Olfactory Bulb. *J Neurophysiol* 104: 2963–2974, 2010.

Smith RS, **Hu R**, **DeSouza A**, **Eberly CL**, **Krahe K**, **Chan W**, **Araneda RC**. Differential Muscarinic Modulation in the Olfactory Bulb. *J Neurosci* 35: 10773–85, 2015.

Stopfer M, **Bhagavan S**, **Smith BH**, **Laurent G**. Impaired odour discrimination on desynchronization of odour-encoding neural assemblies. *Nature* 390: 70–74, 1997.

Urban NN, **Sakmann B**. Reciprocal intraglomerular excitation and intra- and interglomerular lateral inhibition between mouse olfactory bulb mitral cells. *J*

Physiol 542: 355–67, 2002.

Yu GZ, **Kaba H**, **Okutani F**, **Takahashi S**, **Higuchi T**, **Seto K**. The action of oxytocin originating in the hypothalamic paraventricular nucleus on mitral and granule cells in the rat main olfactory bulb. [Online]. *Neuroscience* 72: 1073–82, 1996.

Zeng S, **Li B**, **Zeng S**, **Chen S**. Simulation of spontaneous Ca2+ oscillations in astrocytes mediated by voltage-gated calcium channels. *Biophys J* 97: 2429–37, 2009.

Zhang S, **Ehlers M**, **Bernhardt J**, **Su C**, **Huganir R**. Calmodulin mediates calcium-dependent inactivation of N-methyl-D-aspartate receptors [Online]. *Neuron* 21: 443–453, 1998.

Zufall F. The Cellular and Molecular Basis of Odor Adaptation. *Chem Senses* 25: 473–481, 2000.